THE UNIVERSITY OF CHICAGO

ELECTROSTATICS AND HYDRODYNAMICS IN CONTINUUM-SCALE SIMULATIONS: NUMERICAL APPROACHES AND APPLICATIONS

A DISSERTATION SUBMITTED TO
THE FACULTY OF THE PRITZKER SCHOOL OF MOLECULAR ENGINEERING
IN CANDIDACY FOR THE DEGREE OF
DOCTOR OF PHILOSOPHY

BY
JIYUAN LI

CHICAGO, ILLINOIS
MARCH 2020

For my mother, father and sisters

TABLE OF CONTENTS

LIST OF FIGURES

ACKNOWLEDGMENTS

I would like to thank my advisor, Professor Juan de Pablo, for his profound impact on this dissertation. He knows my strength and weakness so well and has always put me in the most comfortable spot so that I can realize my full potential.

I would also like to give special thanks to, Xujun Zhao, Xikai Jiang and Abhinendra Singh, who I have worked closely to develop the numerical methods and applications in this dissertation. Without them, this journey would be much harder if not impossible. I am also grateful to Professor Juan Hernandez-Ortiz who has played a big role in teaching me numerical methods and transport phenomena, and to Professor Jian Qin and Professor Karl Freed for serving as great mentors and inspiring me to be more passionate and disciplined.

I would also like to thank my friends and colleagues who have supported me along the way, in no particular order: Lucas Antony, Gurdaman Khaira, Kyle Hoffmann, Abelardo Ramirez-Hernandez, Marat Andreev, Rui Zhang, Hadi Ramezani-Dakhel, Mike Webb, Nick Jackson, Minirosadat (Sanaz) Sadati, Ivan Lyubimov, Yamil Colon, Jose (Adrian) Martinez-Gonzalez, Julio C. Armas-Perez, Nader Taheri Qazvini, Daniel Reid, Johnny Alfaro, Weiwei Chu, Ye Zhou, Alec Bowen, Ashley Guo, Emre Sevgen, Cody Bezik, Gustavo Andres Vazquez Montoya, Viviana Palacio Betancur, Joshua Leqieu, Andres Cordoba, Joshua Moller, Meng Shen, Ming Han, and Heyi Liang, Aria Coraor, Chuting Deng, Chuqian Chen, Lu Li, Jiajing Li, Hao Wu, Jialu Liu and Ruyi Wang.

Lastly, I would like to thank my mother, Yufang Lei, my father, Xiangqian Li and my two incredible sisters, Qianqian Li and Tingting Li for always supporting my decisions and trying their best to help me pursuing my dream. I dedicate this work to all of you.

ABSTRACT

Electrostatic and hydrodynamic interactions have profound impact on the structural and dynamic properties of a vast set of colloidal and biological systems. However, challenges are presented toward developing efficient numerical methods to describe these interactions due to their long-range and many-body nature. In this work, we develop several numerical models to describe electrostatic interactions with the consideration of the polarization effect in dry/deionized systems, to model hydrodynamic interactions and their coupling with thermal fluctuations for Brownian particles in suspensions, and to simulate the electrokinetic phenomena for charged particles suspended in ionic solutions. We then apply these efficient numerical approaches on several applications. First, we combine an evolutionary optimization strategy CMA-ES with a particle dynamics simulator based on the electrostatics models and successfully obtain the charges on granular polarizable particles based on a given set of experimental trajectories. Second, we examine the structure and dynamics of hydrodynamically interacting finite-size Brownian particles in a spherical cavity and systematically study how lubrication, long-range hydrodynamics, particle volume fraction and shape affect the equilibrium structure and the diffusion behavior of these confined particles. The observations from this study suggest that the shape of biomolecules, particles and polymers could determine their mobility and diffusion inside cells and tissues. Lastly, we examine the effect of electrostatic polarization on the dynamics of hydrodynamically interacting particles during sedimentation in unconfined and confined Stokes fluids. It is found that as particles agglomerate because of the electrostatic interactions and polarization effects, their collective motions are concomitantly modified by hydrodynamic interactions and fluid flows. It is also found that, when sedimenting in a confined geometry, dynamics of charged polarizable particles are strongly affected by the dielectric permittivities of the particle, fluid, and the confining geometry. These findings serve as a fundamental build up to understand the effect of hydrodynamic and electrostatic interactions on a wide range of applications including dynamics of biological entities in vascular environments and particle dynamics during water

filtration and purification.

CHAPTER 1

INTRODUCTION

Electrostatic and hydrodynamic interactions are ubiquitous in nature and technology. Examples include DNA molecules that are usually negatively charged due to their sugar-phosphate backbones, microfluidics that are used to precisely control the transport and self-assembly of colloidal particles, and Janus membranes that are used to harvest power from salinity gradient, etc. Although these two interactions can influence the structural and dynamic properties of materials in profound ways, they present challenges toward developing efficient numerical methods to describe them due to their long-range and many-body nature. And classical descriptions of these two interactions may break down and need additional corrections under certain circumstances. For example, in the case of describing the electrostatic interactions between charged objects in dry or deionized solvent, Coulombic energy can be insufficient when the dielectric polarization effect is significant. In another case of describing electrostatic interactions in ionic solution, Poisson-Boltzmann (PB) theory and Debye-Huckle equation (Linearized PB) are widely used to include the ionic screening effect, however, the underlying assumption of these theories can be invalid in many modern applications such as nanofluidics that are only 10nm wide in the confined dimension.

In this dissertation, we present several new numerical approaches and implementations to tackle the electrostatic and hydrodynamic interactions to while overcoming the limitations of classical theories. The dissertation, is organized into eight main chapters, among which, Chapter 2 - 5 describe the numerical methods to solve electrostatic and hydrodynamic interactions and Chapter 6 - 9 present the applications studied using the numerical methods proposed.

In Chapter 2, we derive an analytical, perturbative theory of the polarization and the electrostatic interactions by relying on a generalized image method. The theory considers an ensemble of dielectric spheres of arbitrary charges, sizes and dielectric permittivity immersed in a continuum dielectric medium. We validate and measure the accuracy of the theory

by comparing its predictions to full-blown numerical solutions. Then we demonstrate the importance of polarizability for clusters of dielectric spheres, as well as a periodic crystal of charged dielectric spheres arranged into a NaCl-type lattice. This analytical framework for understanding the consequences of polarization will enable molecular simulations of large systems of polarizable particles.

In Chapter 3, we present a numerical approach to solve the polarization and electrostatic interactions based on boundary integral methods. The approach overcomes the limitations of the analytical theory in Chapter 2 and allows calculations of the polarization effect in an ensemble of arbitrary-shaped dielectric objects within confined/unconfined systems. We first formulate the governing PDE, i.e., Poisson equation, in terms of integral equations which are then solved using the Boundary Element Method (BEM) to avoid explicitly including the embedding space exterior to the bodies. Then we employ a parallel computational approach that relies on using scalable open source libraries and utilizes a kernel-independent Fast Multipole Method (FMM) to evaluate the integrals in $O(N)$ operations, with $O(N)$ memory cost, thereby substantially improving the scalability and efficiency of computational integral methods. And finally, we demonstrate the accuracy, efficiency, and scalability of the proposed approach using several test cases and show that it can enable highly efficient and accurate simulations.

In Chapter 4, we present an efficient $O(N)$ computational approach to model the dynamics of hydrodynamically interacting Brownian particles confined in arbitrary geometries. A parallel finite element Stokes' solver is the center of the algorithm. Once it is combined with the General geometry Ewald-like method (GgEm), a mid-point time integration scheme and a Chebyshev polynomial approximation, for the fluctuation-dissipation theorem, results in an scalable algorithm - the pFE-GgEm algorithm. The pFE-GgEm algorithm shows excellent parallel performance (linear) as a function of the number of CPUs. We validate the algorithm by comparing its solutions to theoretical solutions in a simple geometry (for the Stokes' solver), and by calculating the diffusion coefficients of slit-confined DNA molecules

(for the mid-point scheme, eigenvalues of the diffusion tensor and the Chebyshev polynomial approximation). It is also shown that the pFE-GgEm algorithm is capable of handling complex geometries under non-equilibrium conditions by studying the behavior of DNA chains under an elongational flow in a cross-channel geometry. And finally, the proposed algorithm is combined with the Immersed Boundary method, the IB-pFE-GgEm approach, to simulate finite-size particles of arbitrary shape confined in any geometries.

In Chapter 5, we present a numerical approach to describe the electrokinetic phenomena in confined ionic solutions. Conventionally, the PB theory is usually used to calculate the electric potential and Helmholtz-Smoluchowski theorem is commonly utilized to model the electroosmotic flow. And these methods are based on assumptions of thin electric double layer (EDL) and equal number of co-ions and counterions in the bulk. However, these methods are no longer valid to describe the electrokinetic phenomena in systems where the thickness of EDL is comparable to the channel size in the confined dimension and leads to imbalanced co- and counter ions. We attempt to overcome these limitations by directly solve the Poisson equation for electrostatic potential, the Stokes equations for fluid field and the Nernst-Planck equation for ion concentration. The proposed approach is then validated against analytical and other numerical solutions for several test systems. It is found that the proposed approach can successfully recover the diffusion and convection process of continuum ionic field as well as its interactions with the electrostatic field.

In Chapter 6, we combine an evolutionary optimization strategy CMA-ES with a particle dynamics simulator, which utilizes the electrostatic energy model presented in Chapter 2 and Chapter 3, to obtain the charges on granular polarizable particles based on a given set of experimental trajectories. The proposed strategy is demonstrated in the context of several problems. In the first problem, the initial position and velocities of all particles are given, and the algorithms are used to infer the particles' charges. In the second and third problems, both the particles' charges and initial velocities are unknown, and it is shown that the evolutionary optimization can be used to successfully determine the particles' charges

and their initial velocities. In the fourth problem, the evolutionary optimization strategy is applied to extract the charges from experimentally observed trajectories, and the charges are found to be within the ranges reported in previous experimental measurements from the literature. The proposed strategy could be extended to more complex systems containing electrostatically charged granular particles and we envision that it can find applications in material property measurements and material designs.

In Chapter 7, we examine how lubrication, long-range hydrodynamics, particle volume fraction and shape affect the equilibrium structure and the diffusion of suspended spherical and cylinderical particles confined in a spherical cavity. It is found that once the particle volume fraction is greater than 10%, the particles start to form layered aggregates that greatly influence particle dynamics. Hydrodynamic interactions strongly influence the particle diffusion by inducing spatially dependent short-time diffusion coefficients, stronger wall effects on the particle diffusion towards the walls, and a sub-diffusive regime –caused by crowding– in the long-time particle mobility. The level of asymmetry of the cylindrical particles considered here is enough to induce an orientational order in the layered structure, decreasing the diffusion rate and facilitating a transition to the crowded mobility regime at low particle concentrations. The results discussed in this chapter offer fundamental insights into the diffusion and distribution of globular and fibrillar proteins inside cells.

In Chapter 8, we extend the study in Chapter 7 to the case of mixtures of spheres and cylinders. Indeed, in applications (e.g. cytoplasm or colloidal suspensions) one rarely deals with systems of pure mono-disperse spheres, and it is therefore of interest to consider how mixtures behave relative to their pure counterparts. It is found that introducing cylinders in a background of spheres, i.e. particles with a simple degree of anisotropy, has a pronounced influence on the structure and dynamics of the particles. First, increasing the fraction of cylinders induces a particle segregation effect, where spheres are pushed towards the wall and cylinders remain near the center of the cavity. This segregation leads to a lower mobility for the spheres relative to that encountered in a system of pure spheres at the same

volume fraction. Second, the diffusive-to-anomalous transition and the degree of anomaly – quantified by the power low exponent in the mean square displacement vs. time relation – both increase as the fraction of cylinders becomes larger. These findings are of relevance for studies of diffusion in the cytoplasm, where proteins exhibit a distribution of size and shapes that could lead to some of the effects identified in the simulations reported here.

In Chapter 9, we examine the effect of electrostatic polarization on the dynamics of hydrodynamically interacting particles during sedimentation in unconfined and confined Stokes fluids. This particular problem serves as a fundamental build up to understand the effect of hydrodynamic and electrostatic interactions on a wide range of applications including dynamics of biological entities in vascular environments and particle dynamics during water filtration and purification. It is found that charged particles with equal signs will form stable clusters depending on their charge ratio and the difference between dielectric permittivities of the particle and the fluid. Stability conditions for this cluster formation are inherited during the dynamical evolution of the sedimenting particles. As particles agglomerate because of the electrostatic interaction and polarization effect, their collective motions are concomitantly modified by HI and fluid flows. It is also found that, when sedimenting in a confined geometry, dynamics of charged polarizable particles are strongly affected by the dielectric permittivities of particles, fluid, and the confining geometry.

Finally, in Chapter 10, we present an overview summarizing the proposed numerical approaches and their applications. The general conclusion of this dissertation is that classical continuum theories may fail to describe the electrostatic and hydrodynamic interactions in varieties of soft matter systems and that we have developed alternative efficient numerical models instead to handle them.

CHAPTER 2

NUMERICAL APPROACH: AN ANALYTIC APPROACH TO DIELECTRIC POLARIZATION

2.1 Abstract

Surface charging or polarization can strongly affect the nature of interactions between charged dielectric objects, particularly when sharp dielectric discontinuities are involved. By relying on a generalized image method, we derive an analytical, perturbative theory of the polarization and the interactions between charged particles in many-body systems. The validity and accuracy of the theory are established by comparing its predictions to full-blown numerical solutions. The importance of polarizability is then demonstrated for clusters of dielectric spheres, as well as a periodic crystal of charged dielectric spheres arranged into a NaCl-type lattice. The analytical framework for understanding the consequences of polarization will enable molecular simulations of large systems of polarizable particles.

2.2 Introduction

Electrostatic interactions are ubiquitous in nature and technology [4, 5]. Free charges, such as ions, respond to applied electric fields by generating a net current, whereas uncharged materials become polarized and generate additional electric fields whose magnitude and effects on charged and uncharged objects are largely determined by the relative dielectric permittivity of the material and its surroundings.

The dielectric response to an applied field changes abruptly at an interface where surface charges accumulate when both sides of the interface respond differently. Charge accumulation can influence the interactions between dielectric objects in profound ways. Examples include the aggregation or dispersion of charged granular materials [6, 7], colloids [5], and nano-particles [8]. It also plays a central role in the clustering of dust involved in the early

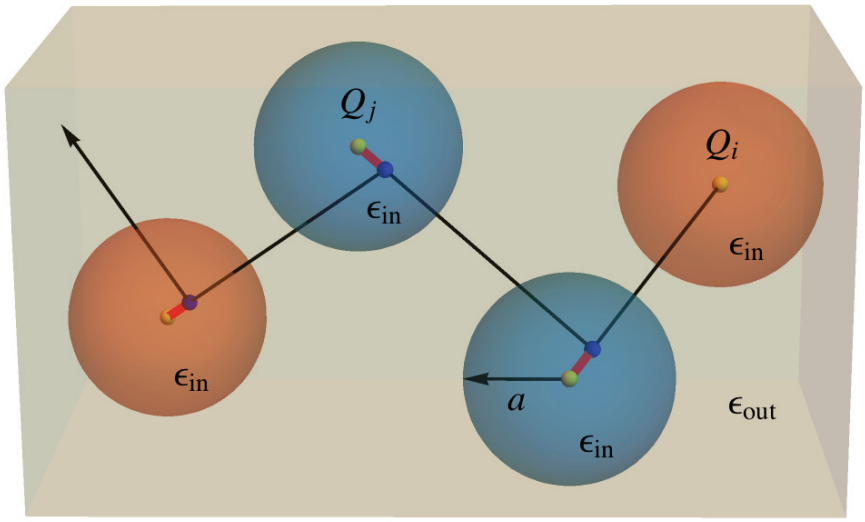

Figure 2.1: The continuum model for an ensemble of dielectric spheres. Blue dot: Kelvin image point. Red segment: Neumann image line representing polarization effects.

stages of planet formation [9, 10, 11].

Important efforts have sought to capture polarization effects in numerical calculations [12, 13, 14, 15, 16]. Some of the latest and more numerically-efficient approaches use explicit surface-charge elements to highlight the importance of polarization in charged colloidal particle assemblies [14,15]. Numerical methods, however, become unwieldy for studying polarization and its many consequences in large many-body system. This work presents a tractable and general analytical theory of many-body polarizability based on the extension of a multiple scattering formalism that obviates the need for surface charges and, instead, describes their overall influence of electrostatic interactions through analytical functions of only particle positions. As such, the theory is particularly well suited for description of many-body systems.

2.3 Models and methods

We consider an ensemble of dielectric spheres immersed in a continuum dielectric medium with dielectric permittivity ϵ_{out}, as illustrated in Fig. 2.1. A sphere i centered at $\mathbf{R}_i$ has dielectric constant $\epsilon_{in,i}$, radius a_i, and charge Q_i. The theoretical underpinnings of our pro-

posed approach are discussed in Refs. [17, 18]. For simplicity, the spheres have uniform radii and dielectric constants, but different charges at the centers. However, the new formalism applies for different sizes and dielectric permittivities. The electrostatic energy for an arbitrary particle configuration is given by a multiple scattering series with terms of increasing complexity that depend on the relative positions of an increasing number of particles [17, 18],

$$E = E_1 + E_2 + E_3 + E_4 + \dots \tag{2.1}$$

where $E_1 = \sum_i \frac{Q_i^2}{8\pi a_i}(\frac{1}{\epsilon_{\text{out}}} - \frac{1}{\epsilon_{\text{in}}})$ includes effectively contributions from Bohr solvation energies, which represent the interactions between the induced surface charges and the source charges at the centers of the spheres. The second term in the series, E_2, designates the effective two-body contributions, which equal the bare Coulomb energy between charges, $E_2 = \frac{1}{2}\sum_{i,j} \frac{Q_i Q_j}{4\pi\epsilon_{\text{out}}|\mathbf{R}_i - \mathbf{R}_j|}$. The term $E_3 = \sum_{i,k,j} \frac{Q_i Q_j}{8\pi\epsilon_{\text{out}}} \mathbf{I}_{ikj}$ includes the lowest-order polarization contributions to the energy, where the geometrical kernel I_{ikj} is given by

$$I_{ikj} = (1 - \frac{\epsilon_{\text{in}}}{\epsilon_{\text{out}}}) \int \frac{d\mathbf{S}_k}{4\pi|\mathbf{R}_i - \mathbf{r}_k|} \cdot \nabla_k \frac{1}{|\mathbf{r}_k - \mathbf{R}_j|}) \tag{2.2}$$

Here $d\mathbf{S}_k$ is the surface element of the kth particle, $\mathbf{r}_k$ is the position vector, and ∇_k is the gradient with respect to $\mathbf{r}_k$. The terms in E_3 include the interaction between the surface charges induced by each source charge on all other charges in the system, thereby representing the effective interaction between two charges as mediated by the polarization arising at spherical interfaces. In principle, the source charge and the field charge can reside on the same sphere, but the scattering surface must be associated with a distinct particle.

Similarly, E_4 represents the second-order polarization contributions due to the interaction between two charges mediated by two polarized surfaces. Higher order terms follow in a similar manner, and all include geometrical kernels of the form $I_{ik_1k_2j}$, $I_{ik_1k_2k_3j}$, etc., as defined in Appendix. 2.6.1 (Eq. (2.13)). The theory has the important feature that these kernels are analytic function of the particle positions, thereby enabling straightforward

calculation of the forces acting on all particles and facilitating a physical interpretation of individual terms in the expansion of Eq. (2.1).

A key extension of the theory, introduced in this work, is the summation of an infinite series of contributions in Eq. (2.1), resulting the conversion of two-dimensional integrals over surface charges into an equivalent form that involves considerably more tractable one-dimensional integrals over line charge densities. Ref. [18] and Appendix 2.6.1 show how the integral kernels I_{ikj}, I_{ikkj}, I_{ikkkj} ... with identical first (i) and last (j) indices and with repeated internal (k) indices can be re-summed altogether, yielding

$$I_{ikj} + I_{ikkj} + I_{ikkkj} + \cdots = \epsilon \frac{t}{\sqrt{R_{ik}R_{jk}}} (\delta_{f,t^2} - gt^{-2g} \int_0^{t^2} df\, f^{g-1}) \frac{1}{D_{ikj}}, \qquad (2.3)$$

where $\epsilon \equiv (\epsilon_{\text{in}} - \epsilon_{\text{out}})/(\epsilon_{\text{in}} + \epsilon_{\text{out}})$, $g \equiv 1/(1 + \epsilon_{\text{in}}/\epsilon_{\text{out}})$, $t \equiv a_k/\sqrt{R_{ik}R_{jk}}$, $D_{ikj} = (1 + f^2 - 2f\hat{\mathbf{R}}_{ik} \cdot \hat{\mathbf{R}}_{jk})^{1/2}$, and $\hat{\mathbf{R}}_{ik}$ and $\hat{\mathbf{R}}_{jk}$ are unit vectors pointing along the directions of $\mathbf{R}_{ik}$ and $\mathbf{R}_{jk}$ respectively. The term δ_{f,t^2} in parentheses represents the contribution from an image charge placed at the Kelvin point [19], which is conventionally used to represent the electrostatic field generated by the surface charge on a conducting sphere (see Fig. 2.1). The generalization here to describe the field produced by the dielectric spheres consists of a contribution from the image at the Kelvin point and augmented by an image line segment between the center of the sphere and the Kelvin point (see Fig. 2.1). The contribution from the line segment was first documented by Neumann [20] over 130 years ago, and has been rediscovered several times [21, 22, 23] in different contexts, including the description of hydrodynamic interactions between small spherical particles in the neighborhood of large spherical particles [24]. Our work derives the analytic generalization of this image line charge construct to describe the many-body electrostatic interaction energy for a system with an arbitrary number of spherical particles – a generalization that is required for the evaluation of E_4, E_5, and all higher order contributions. In Appendix 2.6.1, iterative yet explicit expressions are provided for the kernels needed to evaluate these higher order many-body

interactions. The magnitude of subsequent terms in Eq. (2.1) decreases as the number of intervening scattering surfaces increases. The convergence rate is governed by the mismatch in the dielectric permittivity $\epsilon_{\text{in}}/\epsilon_{\text{out}}$, which determines the amount of surface charge, and the ratio between the sphere radius and the average inter-sphere separation, which measures the strength of electric field. The contributions $\tilde{E}_n(n > 2)$ to the total energy

$$E = E_1 + E_2 + \tilde{E}_3(g)\epsilon + \tilde{E}_4(g)\epsilon^2 + \dots \tag{2.4}$$

scale in the limit of large inter-particle separations as

$$\tilde{E}_n \simeq \frac{l_B}{d}(\frac{a}{d})^{3(n-2)}k_BT \tag{2.5}$$

where $l_B \equiv e^2/(4\pi\epsilon_{\text{out}}k_BT)$ is the Bjerrum length, a is the radius of the particles, and d is the average separation between particles. The exponent 3 arises because the dominant component of the polarization at large separations is given by the dipole moment, which is proportional to the volume of the particles. Note that here we use the standard definition for the Bjerrum length to illustrate the scaling dependence of energy on the different parameters. The actual system energy should scale quadratically with the charge per particle.

The polarization effects can be understood by considering a point charge Q_1 placed at $\mathbf{R}_1$, in the neighborhood of a dielectric sphere at the origin. The total electrostatic potential includes the Coulomb contribution and the contribution coming from the induced surface charge, which equals the sum of contributions from the Kelvin point and the Neumann line. The full expression for the electrostatic potential at position $\mathbf{R}_2$ is derived from Eq. (2.3). If the separations R1 and R2 are large, the dominant term is given by $Q_1\frac{\epsilon}{1+g}\frac{t^3}{\sqrt{R_1R_2}}\hat{\mathbf{R}}_2 \cdot \hat{\mathbf{R}}_1$, with $t \equiv a/\sqrt{R_1R_2}$ [18]. This is precisely the electrostatic field generated by a surface charge dipole $\frac{\epsilon}{1+g}Q_1t^3$. Higher order multipole terms may be constructed similarly, but the multipole expansion converges slowly at very short separations.

The field generated from a single scattering surface is greatly simplified in three limits:

(1) when the dielectric permittivity approaches infinity, $\epsilon_{\rm in} \to \infty$, the result reduces to that for a conducting sphere; (2) when the radius a asymptotically approaches infinity, the result reduces to that for a flat surface; and (3) when the electrostatic field acts on the source charge, the self-energy emerges in closed form, $Q_1^2 \epsilon \frac{t}{R}(\frac{1}{1-t^2} - \frac{g}{t^{2g}\mathbf{B}(t^2;g,0)})$, where $\mathbf{B}$ is the incomplete Beta function.

2.4 Results

We next illustrate examples showing the importance of polarization effects. First, consider the interaction between two identical dielectric spheres with charges Q_1 and Q_2 . The Born solvation energy E_1 only shifts the energy by a constant and is inconsequential to the present discussion. The bare Coulomb energy $E_2 = Q_1 Q_2 / R_{12}$ for two like charges is purely repulsive, while the dominant polarization contribution E_3 becomes attractive if the particle's dielectric constant $\epsilon_{\rm in}$ exceeds the medium value $\epsilon_{\rm out}$, this term can formally be written as

$$E_3 = (Q_1^2 + Q_2^2) \frac{f(a/R_{12};\epsilon)}{R_{12}} \tag{2.6}$$

The factor Q_1^2 (Q_2^2) originates from the interaction between the charge Q_1 (Q_2) and its image charges on particle 2 (1) The function $f(a, R)$ is given by Eq. (2.3), which depends on the details of surface charges, is negative (attractive), and is generally much smaller than unity.

The ratio between E_3 and E_2 may be written as $E_3/E_2 = (Q_1/Q_2 + Q_2/Q_1) f(a/R_{12};\epsilon)$. The interaction between the particles is therefore dominated asymptotically by the repulsive Coulomb contribution. However, E_3 may become more substantial than E_2 for sufficiently large charge asymmetry at short separations between the particles. This is confirmed by calculations presented in Fig. 2.2, for $Q_1 = Q_2 = 15$ and $\epsilon_{\rm in}/\epsilon_{\rm out} = 10$, where at small separations the energy becomes purely attractive, owing to the surface charge polarization. Our results agree quantitatively with those obtained by full-blown numerical solution of the surface charges, where indeed the lowest order polarization contribution E_3 captures much

of the polarization effect, and appears to be nearly 100 times faster than the numerical calculations.

A "phase" diagram designating the nature of two particle interactions is generated by varying the ratios $\epsilon_{\text{in}}/\epsilon_{\text{out}}$ and Q_1/Q_2. Fig. 2.2 demonstrates the existence of a widening window of attraction as $\epsilon_{\text{in}}/\epsilon_{\text{out}}$ or Q_1/Q_2 increases, since a growth in either of them favors a stronger polarization interaction. Fig. 2.2(a) suggests that different orders of polarization contributions exhibit an oscillatory convergent behavior, and that E3 alone is sufficient for small $\epsilon_{\text{in}}/\epsilon_{\text{out}}$, for which a closed-form expression is provided in Appendix 2.6.1.

We next consider aggregates of three particles, with charges Q_1, $Q_2 = -Q_1$ and Q_3 , arranged in a close-packed triangular configuration. The convergence rate of our theory is demonstrated in Fig. 2.3(a), and a stability diagram is presented in Fig. 2.3(b). The close-packed triangular configuration is unstable for all values of Q_3 in the absence of polarization effects, a consequence of the frustration experienced by particle 3 which repels particle 1 (2) for positive (negative) Q_3 . However, this frustration can be alleviated by sufficiently large polarization effects. Energy landscape and gradient calculations indeed show that increasing dielectric permittivity opens a stability window for finite Q_3 , and the region of stability is symmetric with respect to inverting the sign of Q_3.

For larger clusters with N particles, the number of n-body terms is given by combinatorial factors of order N^n , which raises concerns on convergence. Our calculations, however, indicate that the condition of charge neutral system at large separations improves the convergence rate for higher order terms. So the growth of the combinatorial factor poses no problems. This feature is demonstrated for the worst possible case, i.e., that of $N \to \infty$ particles. Thus, we calculate the cohesive energy for a crystal of charged, polarizable particles arranged into a NaCl lattice. The "cationic" and "anionic" particles have equal size and form close contacts. Furthermore, in practice, since most of the contributions retained formally involve terms that vanish essentially when the separation between spheres is high, a distance cutoff can be introduced to reduce the number of terms to be evaluated.

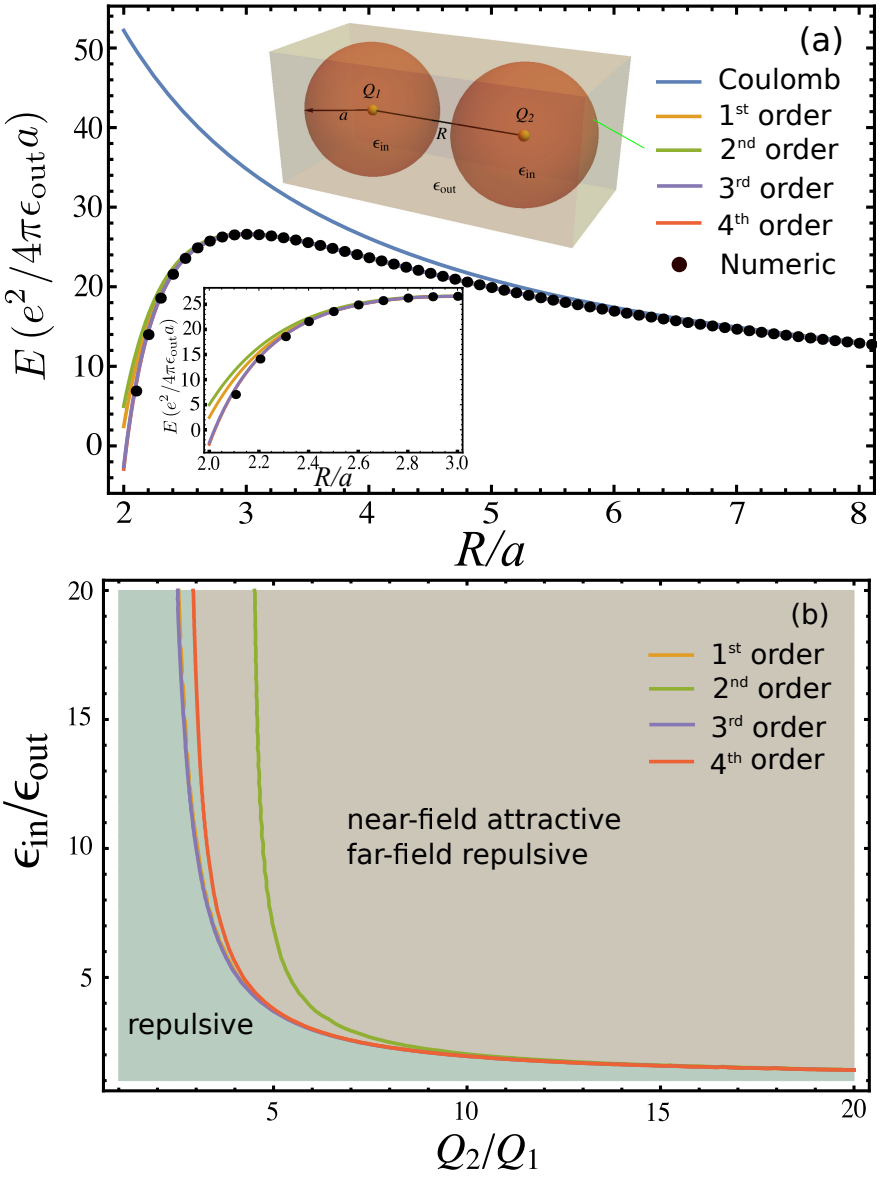

Figure 2.2: (a) Electrostatic energy between two dielectric spheres. Points: numerical solution [1]; lines: Coulomb (blue) and polarization (1st and 3rd order nearly overlap) contributions. Ratios of charges and permittivities: $Q_1 = Q_2 = 15$ and $\epsilon_{\rm in}/\epsilon_{\rm out}$ is 10. (b) Regimes of interactions: purely repulsive versus attractive at small separation. The first and third order theories nearly overlap.

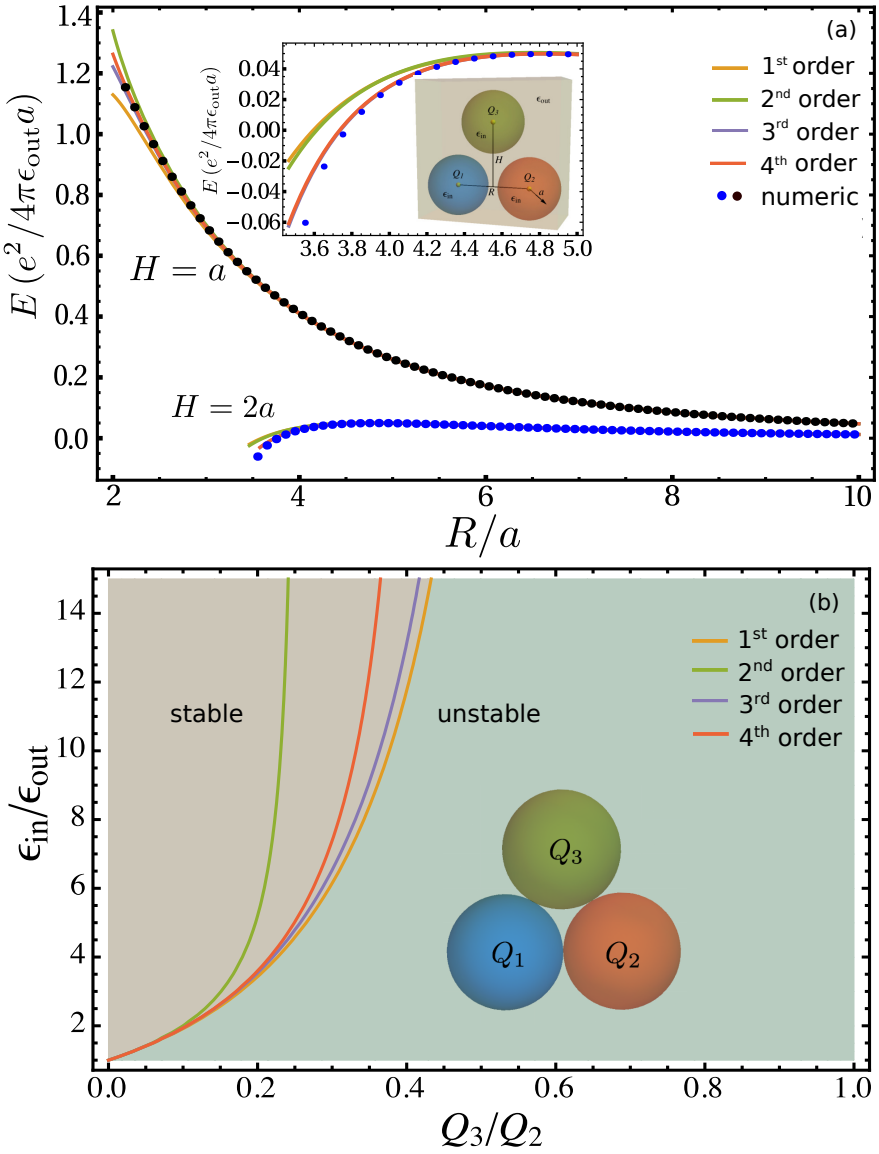

Figure 2.3: (a) Electrostatic energy between three spheres in a triangular arrangement ($Q_1 = -0.25$, $Q_2 = Q_3 = 1$, $\epsilon_{\rm in}/\epsilon_{\rm out} = 10$). Lines: predictions of multiple scattering theory; points: numerical solution. (b) Stability diagram for close contact triangular configuration with $Q_2 = -Q_1$

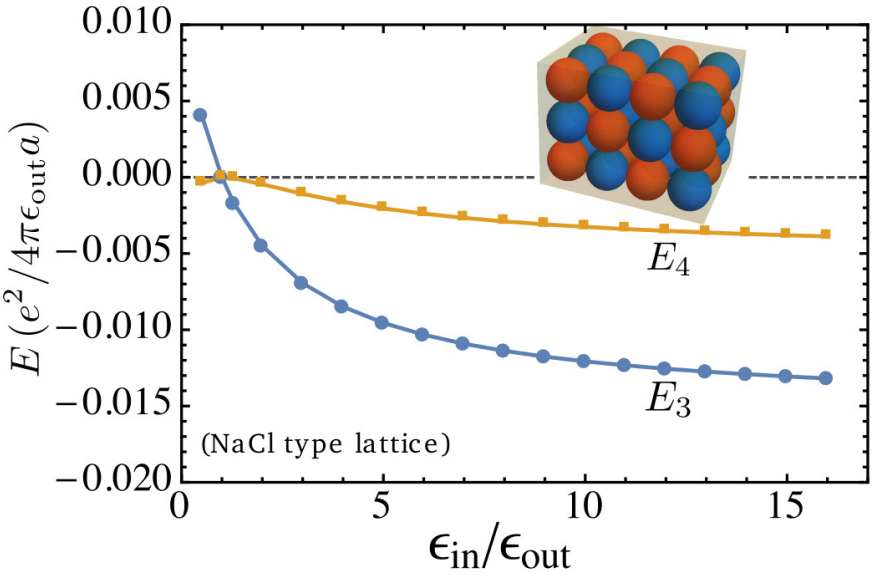

Figure 2.4: Electrostatic cohesive energy of a NaCl type lattice composed of charged, polarizable colloids, nano-particles, etc. The cations and anions have opposite charges and same radii, and form close contacts. Curves: first and second order polarization contributions.

The cohesive energy for ordinary crystals is the average Coulomb energy per site, the Madelung constant that equals -0.437 [25]. The many-body polarization corrections begin with E_3 , followed by E_4 , etc. This particularly system is interesting because the convergence rate with respect to order is low due to the large number of combinatorial factors and the long range nature of the Coulomb energy. We therefore examine these issues by studying the dependence of cohesive energy on system size and by extrapolating to an infinite lattice. The largest system considered contains 9^3 particles (Using an odd number of particles allows us to identify a particle at the center of the crystal and, to calculate the cohesive energy, we only need to evaluate the n-body terms to which this central point participates). Fig. 2.4 demonstrates that the first order contribution E_3 is negative for $\epsilon_{\rm in}/\epsilon_{\rm out} > 1$ and positive for $\epsilon_{\rm in}/\epsilon_{\rm out} < 1$. The second order contribution E_4 instead exhibits a maximum at $\epsilon_{\rm in}/\epsilon_{\rm out} = 1$ and is always negative. As expected, for the wide range of ϵ values investigated, E_3 is much smaller than E_2, and E_4 is even smaller, presumably due to massive cancellations from the crystal's symmetry at large distances. Our results represent the only available estimate of polarization effects in a nanocrystal, and additional, computationally-intensive convergence

studies should be pursued in the future. We postulate that the relative stability of different types of lattices might be altered by the contributions of E_3 and E_4 , particularly in the presence of defects.

2.5 Conclusions

In summary, we have developed an analytic perturbative approach for evaluating the polarization energy for a many-body collection of charged dielectric spheres embedded in a dielectric medium. The polarization-induced interactions between these spheres depend on the ratio of dielectric constants for the spheres and the medium, and the ratio of the distance between particles and the radii of the particles. In some cases, polarization completely alters the qualitative behavior; e.g., the interaction energy for a two-particle cluster can switch from repulsive to attractive, depending on the charge asymmetry and dielectric contrast. In other cases, polarization leads to stable configurations that otherwise could not occur in its absence, e.g., three-particle closepacked arrangements. The polarization energy of the largest system considered here, namely a densely packed ionic-crystal in the form of an NaCl lattice, allows us to predict a generalized, permittivity-dependent Madelung constant that goes beyond existing predictions based solely on Coulombic interactions. These calculations imply that the polarization energy can become quite significant for aggregates of highly polarizable objects, and is thus relevant for study of the stability and kinetics of charged granular materials, colloids, and nanoparticles. All the examples described here consider cases where the charges are placed at the center of particles, but the methodology can be readily applied to particles with arbitrary charge distributions to enable, in principle, investigations of the effects of polarization on the rotation of clusters of particles. The generalized image expansion introduced here could be further extended to describe the interactions among infinite dielectric cylinders, for which only the normal Kelvin images are needed. Furthermore, the methodology could also be applied to study the influence of electrostatic polarization on ion aggregation near a flat interface by representing the polarizable ion by a dielectric sphere,

and to study the polarization (image) effects on the ionic clouds surrounding a pair of highly charged interacting colloidal particles. Practical applications of our theory to clusters of specific systems, of course, will require inclusion of all other types of interactions.

For example, the presence of van der Waals interactions yields contributions whose magnitude in the lowest order depends on the ratio of the Hamaker constant A [4] to the product of charges. The relative importance of the polarization term follows from its ratio with the leading order Coulomb interaction. As our theory demonstrates, polarization effects generally involve many-body particle interactions whose magnitude we can now evaluate analytically. Such effects may help interpret the nature of nonpairwise additive interactions that have been discussed in the literature on colloidal materials [5]. Importantly, the energy expressions developed here only depend on the particle positions and are thus ideally suited for molecular dynamics simulations and theoretical work. A subsequent paper will compare our calculations with experimentally determined trajectories of charged dielectric objects.

2.6 Appendix

2.6.1 Multi-scattering formalism of electrostatic energy between dielectric particles

In what follows we provide explicit expressions for the electrostatic energy of an ensemble of dielectric spheres that are used in the main manuscript. The multi-scattering formalism of refs. [17, 18] expands the energy for an ensemble of dielectric spheres as a sum of terms of increasing complexity, which reads

$$E = E_1 + E_2 + E_3 + E_4 + \cdots \tag{2.7}$$

$$E_1 = \frac{1}{8\pi\epsilon_{\text{out}}} \sum_i \frac{Q_i^2}{a_i} \left(\frac{1}{\epsilon_{\text{out}}} - \frac{1}{\epsilon_{\text{in}}} \right) \tag{2.8}$$

$$E_2 = \frac{1}{8\pi\epsilon_{\text{out}}} \sum_{i,j} \frac{Q_i Q_j}{|\mathbf{R}_i - \mathbf{R}_j|} \tag{2.9}$$

$$E_3 = \frac{1}{8\pi\epsilon_{\text{out}}} \sum_{i,k,j} Q_i Q_j I_{ikj} \tag{2.10}$$

$$E_4 = \frac{1}{8\pi\epsilon_{\text{out}}} \sum_{i,k_1,k_2,j} Q_i Q_j I_{ik_1k_2j} \tag{2.11}$$

$$\ldots \tag{2.12}$$

Here, E_1 is equivalent to the Born solvation term, E_2 is the usual (bare) Coulomb energy, and E_3, E_4, etc. are polarization contributions. The indices i, j, k etc. run over all particles in the system. The kernels I_{ikj}, $I_{ik_1k_2j}$, etc. are integrals over the particle surfaces, and are given by

$$I_{ikj} = \left(1 - \frac{\epsilon_{\text{in}}}{\epsilon_{\text{out}}}\right) \int \frac{\mathrm{d}\mathbf{S}_k}{4\pi \left|\mathbf{R}_i - \mathbf{r}_k\right|} \cdot \nabla_k \frac{1}{\left|\mathbf{r}_k - \mathbf{R}_j\right|} \tag{2.13}$$

$$I_{ik_1k_2j} = \left(1 - \frac{\epsilon_{\text{in}}}{\epsilon_{\text{out}}}\right)^2 \int \frac{\mathrm{d}\mathbf{S}_{k_1}}{4\pi \left|\mathbf{R}_i - \mathbf{r}_{k_1}\right|} \cdot \nabla_{k_1} \int \frac{\mathrm{d}\mathbf{S}_{k_2}}{4\pi \left|\mathbf{R}_{k_1} - \mathbf{r}_{k_2}\right|} \cdot \nabla_{k_2} \frac{1}{\left|\mathbf{r}_k - \mathbf{R}_j\right|} \tag{2.14}$$

$$\dots \tag{2.15}$$

These terms can be understood as interactions between the i- and j-th particles mediated ('scattered') by the k_1-, k_2-th particles. The higher order terms $I_{ik_1k_2k_3j}$, $I_{ik_1k_2k_3k_4j}$ may be constructed analogously. Starting from the terms for E3, each higher order polarization energy term involves one additional surface integral. In Ref. [18], it is shown that these surface integral terms can be converted into one-dimensional line integrals. Specifically, note that

$$\begin{aligned} \mathcal{E}_{ikj} &= I_{ikj} + I_{ikkj} + I_{ikkkj} + \cdots \\ &= \epsilon \frac{t_k}{\sqrt{R_{ik}R_{kj}}} \left(\delta_{f,t^2} - gt^{-2g} \int_0^{t^2} \mathrm{d}f f^{g-1}\right) \frac{1}{\mathcal{D}_{ikj}} \end{aligned} \tag{2.16}$$

where $\epsilon \equiv \left(\epsilon_{\text{in}} - \epsilon_{\text{out}}\right) / \left(\epsilon_{\text{in}} + \epsilon_{\text{out}}\right), g \equiv 1/\left(1 + \epsilon_{\text{in}}/\epsilon_{\text{out}}\right), t = a/\sqrt{R_{ik_1}R_{k_2j}}$ and $\mathcal{D}_{ikj} = \left(1 + f^2 - 2f\hat{\mathbf{R}}_{ik} \cdot \hat{\mathbf{R}}_{jk}\right)^{1/2}$. The first term in the bracket represents a contribution from the image charge at the Kelvin point, and the second term represents a contribution from the

Neumann image line. By following the same analysis, it is further found that

$$\begin{aligned}
\mathcal{E}_{ik_1k_2j} =& \left(I_{ik_1k_2j} + I_{ik_1k_2k_2j} + I_{ik_1k_2k_2k_2j} + \cdots\right) \\
&+ \left(I_{ik_1k_1k_2j} + I_{ik_1k_1k_2k_2j} + I_{ik_1k_1k_2k_2k_2j+\cdots}\right) \\
&+ \left(I_{ik_1k_1k_1k_2j} + I_{ik_1k_1k_1k_2k_2j} + I_{ik_1k_1k_1k_2k_2k_2j+\cdots}\right) \\
&+ (\cdots)\cdots \\
=& \epsilon \frac{t_{k_1}t_{k_2}}{\sqrt{R_{ik_1}R_{k_2j}}} \left(\delta_{f_1,t_1^2} - g t_1^{-2g}\int_0^{t_1^2} \mathrm{d}f_1 f_1^{g-1}\right)\left(\delta_{f_2,t_2^2} - g t_2^{-2g}\int_0^{t_2^2} \mathrm{d}f_2 f_2^{g-1}\right)\frac{1}{\mathcal{D}_{ik_1k_2j}} \\
\equiv& \frac{\epsilon}{\sqrt{R_{ik_1}R_{k_2j}}}\mathcal{I}_1\mathcal{I}_2\frac{1}{\mathcal{D}_{ik_1k_2j}}
\end{aligned} \tag{2.17}$$

Here $t_1 \equiv a/\sqrt{R_{i,k_1}R_{k_1k_2}}$, and $t_2 \equiv a/\sqrt{R_{k_1,k_2}R_{k_2j}}$, In the last line, we have introduced the shorthand notation

$$\mathcal{I}_k \equiv \delta_{f_k,t_k^2} - g t_k^{-2g}\int_0^{t_k^2} \mathrm{d}f_k f_k^{g-1} \tag{2.18}$$

The kernel is given by $\mathcal{D}_{ik_1k_2j} = \left|f_1\hat{\mathbf{R}}_{ik_1} + \hat{\mathbf{R}}_{k_1k_2} + f_2\hat{\mathbf{R}}_{k_2j}\right|$. Similarly, for a generic term involving n bodies, we have

$$\mathcal{E}_{ik_1k_2\cdots k_{n-2}j} = \frac{\epsilon}{\sqrt{R_{ik_1}R_{k_{n-2}j}}}\mathcal{I}_1\mathcal{I}_2\cdots\mathcal{I}_{n-1}\frac{1}{\mathcal{D}_{ik_1k_2\cdots k_{n-2}j}} \tag{2.19}$$

It is shown in Ref. [18] that an iterative formula generates the kernel D_n involving n-particles

$$\mathcal{D}_n = \mathcal{D}_{n-1} + \left(f_{n-1}^2 + 2f_{n-1}c_{n,n-1}\right)\mathcal{D}_{n-2} + 2f_{n-1}\sum_{i=n-2}^{2} c_{n,i}\left(\prod_{j=i}^{n-2} f_j\right)\mathcal{D}_{i-1} \tag{2.20}$$

where $c_{n,n-1} \equiv \hat{\mathbf{R}}_{n,n-1}\cdots\hat{\mathbf{R}}_{n-1,n-2}$ represent the cosine of angle between vec- tors connecting two consecutive particle pairs. Using the above expressions, the total energy for a

system of polarizable spheres may be written

$$E = E_1 + E_2 + \frac{1}{8\pi\epsilon_{\text{out}}} \left(\sum_{ikj} Q_i Q_j \mathcal{E}_{ikj} + \sum_{ik_1k_2j} Q_i Q_j \mathcal{E}_{ik_1k_2j} + \cdots \right) \tag{2.21}$$

The terms in the bracket are the first order, the second order polarization contributions, etc.

Eq. (2.21) has been used in this manuscript for calculating polarization contributions to the energy of particle aggregates and NaCl-type lattices. For particle aggregates, the expressions provided above are sufficient. For the NaCl lattice, we have investigated the system size dependence for the cohesion energy systematically, and found that both the first and the second order polarization energies scale according to $1/L$, L being the size; a cubic system is used and L is the edge length normalized by particle diameter. The size dependence for $\epsilon_{\text{in}}/\epsilon_{\text{out}}$ is shown in fig. 2.5. The result can be fitted by the form $c_1 + c_2/L$. The values reported in the manuscript correspond to c_1, the extrapolated value for an infinite crystal.

The first order polarization energy for a two-particle case can be written compactly, and can be used to derive an explicit expression to the stability diagram. To see this, we note that the total energy for two particles can be written as

$$E = \frac{Q_1 Q_2}{4\pi\epsilon_{\text{out}} R} + \frac{\epsilon t}{8\pi\epsilon_{\text{out}} R} \left(Q_1^2 + Q_2^2 \right) \left(\frac{1}{1-t^2} - \frac{g}{t^{2g}} \mathbf{B}\left(t^2; g, 0 \right) \right) \tag{2.22}$$

where R is the separation distance between two spheres. For Q_1 and Q_2 of the same sign, the interaction is repulsive at large separations, and becomes attractive when $\mathrm{d}E/\mathrm{d}R = 0$. The solution R^* only depends on Q_1/Q_2 and $\epsilon_{\text{in}}/\epsilon_{\text{out}}$. The relation between Q_1/Q_2 and $\epsilon_{\text{i1}}/\epsilon_{\text{out}}$ at the stability boundary is obtained by setting $R^*\left(Q_1/Q_2, \epsilon_{\text{in}}/\epsilon_{\text{out}}\right) = 1/2$, i.e., by using the condition that the two particle touch each other. By direct differentiation, the critical relation can be resolved to be

$$\frac{Q_1}{Q_2} = D + \left(D^2 - 1 \right)^{1/2} \tag{2.23}$$

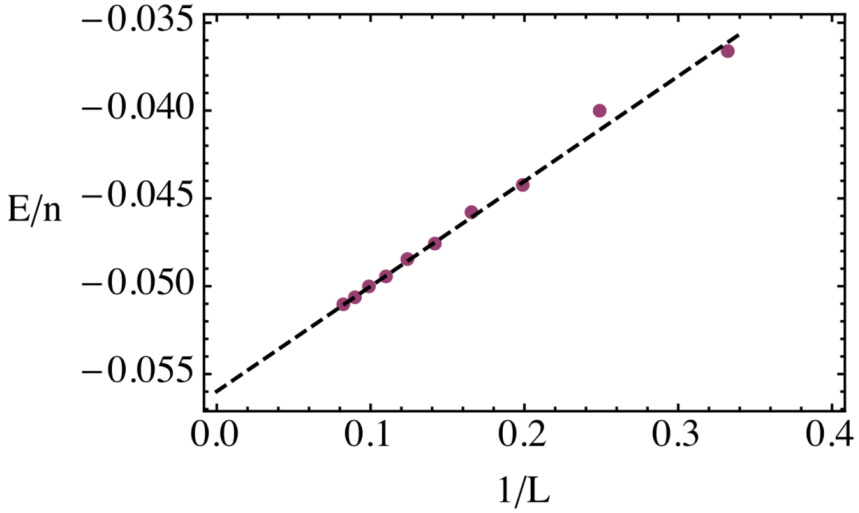

Figure 2.5: System size (L) dependence of the first order polarization energy for a NaCl-type lattice, with $\epsilon_{\text{in}}/\epsilon_{\text{out}} = 1.3$.

$$D = \frac{9(1+\epsilon)^3(\epsilon-1)^{-1}}{4(1+\epsilon)(1+4\epsilon) - 9\epsilon 4^{1/(1+\epsilon)}\mathbf{B}(1/4; g, 0)} \tag{2.24}$$

The above result can be used to generate the first order stability boundary curve in Fig. 2.2(b).

CHAPTER 3

NUMERICAL APPROACH: AN ACCELERATED NUMERICAL APPROACH TO DIELECTRIC POLARIZATION

3.1 Abstract

Large classes of materials systems in physics and engineering are governed by electrostatic interactions. Continuum or mesoscale descriptions of such systems can be cast in terms of integral equations, whose direct computational evaluation requires $O(N^2)$ operations, where N is the number of unknowns. Such a scaling, which arises from the many-body nature of the relevant Green's function, has precluded wide-spread adoption of integral methods for solution of large-scale scientific and engineering problems. In this work, a parallel computational approach is presented that relies on using scalable open source libraries and utilizes a kernel-independent Fast Multipole Method (FMM) to evaluate the integrals in $O(N)$ operations, with $O(N)$ memory cost, thereby substantially improving the scalability and efficiency of computational integral methods. We demonstrate the accuracy, efficiency, and scalability of our approach in the contest of an electrostatic problem involving polarizable dielectric bodies in an unbounded dielectric medium. The results from several test cases show that our proposed parallel approach, which is built on a kernel-independent FMM, can enable highly efficient and accurate simulations and allow for considerable flexibility in a broad range of applications.

3.2 Introduction

Massively parallel computer hardware, and the corresponding software, have enabled solution of increasingly complex problems in science and engineering. Such problems are often cast in terms of partial differential equations (PDEs). In many cases, it is convenient to formulate the PDEs in terms of integral equations, which can then be solved by relying on a variety of

numerical methods. For the particular case of boundary integral equations, the Boundary Element Method (BEM)[26] has found numerous applications in physical problems ranging from solids and fluids[27], to multiphase materials[28], heat transfer[29], electrostatics[12], and magnetostatics. For example, BEMs were used in fluid problems to study the motion and deformation of bubbles[30] and to determine the phase diagram of complex fluids[31]; BEMs have also been used to address three-dimensional (3D) linear elasticity problems involving particles embedded in a binder [32], and in crack analysis in 3D time harmonic elastodynamics[33]. BEMs are particularly well-suited for problems that involve bodies embedded in an infinite medium, with the boundary condition that the relevant potential decays to zero at infinity. If the embedding space is homogeneous and the governing equations for the underlying physics are linear, BEMs are frequently used in order to avoid explicitly including the embedding space exterior to the bodies. In this work, we consider this kind of problem as an explicit test case: dielectric bodies embedded in an infinite dielectric medium. However, our proposed method is widely applicable to problems in which the mathematical formulation can be cast in terms of a boundary integral equation.

In electrostatics, a class of problems is concerned with the electrostatic polarization of finite-size dielectric bodies embedded in an infinite dielectric medium. Free charges carried by these bodies, or free point charges in the medium, are sources of electrostatic fields. Because the relative permittivity of the medium is usually different from those of the bodies, the electrostatic field is discontinuous across the interface between a body and the medium. As a consequence, bound surface charges are induced on the interface to compensate for the discountinuity in the electrostatic field. In order to calculate the induced bound charges on the interface, a BEM was originally proposed using a variational approach[12] to solve the underlying Poisson equation . In numerical simulations of the polarizable bodies, BEMs have been used for stationary or mobile dielectrics[37, 38, 39, 40, 1]. A central aspect of this class of problems is the calculation of the distribution of bound surface charge density through solutions of a linear system of equations $Ax = b$, where A is a dense matrix whose

entries depend on the geometry of the dielectric bodies, x represents the induced bound surface charge density, and b represents contributions from free charges on the dielectric bodies, or free point charges in the exterior medium. The iterative Generalized Minimal Residual Method (GMRES)[41] provides an efficient numerical method to solve the resulting dense linear system of equations[42]. However, the matrix-vector multiplication in each GMRES iteration has a computational complexity of $O(N^2)$ in any direct implementation. In Refs. [1, 42], the matrix-vector multiplication is accelerated using a fast Ewald solver, i.e., the particle-particle particle-mesh method (PPPM or P^3M)[43], which offers a computational complexity of $O(NlogN)$.

In this work, we have developed an efficient and scalable parallel computational approach for BEMs that is built on the scalable parallel libraries libMesh (http://libmesh.github.io)[44] and ScalFMM (http://scalfmm-public.gforge.inria.fr)[45]. The boundary integrals are accelerated using a kernel-independent fast multipole method (FMM)[46] with $O(N)$ computational complexity. This kernel-independent FMM is an interpolation-based FMM that utilizes Chebyshev interpolation and low-rank approximation, and can also be used for kernels that are known only numerically. It was first developed for non-oscillatory kernels and later extended for oscillatory kernels[47]. Our approach to boundary integrals also adopts a matrix-free method that requires no explicit storage of a global matrix, thus enabling simulations with a memory cost of only $O(N)$. The corresponding software is is made freely available to potential users. In the remainder of this chapter, we first introduce the general boundary integral problem. We then discuss methods for the electrostatic problem, and our implementations of BEM; We apply our computational approach to several model problems and test its accuracy, efficiency, and scalability. We conclude with a summary and suggestions for future directions for improvements of the proposed approaches, and elaborate on several research areas and physical phenomena to which our approach could be applied.

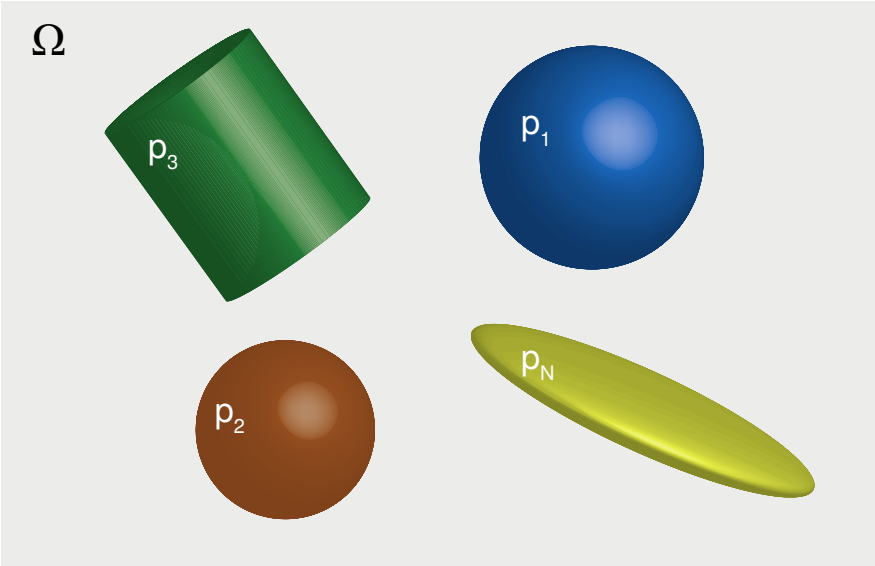

Figure 3.1: A schematic of general integral problems. Ω is the exterior region and the interior region Γ consists of different arbitrary-shaped bodies. $\Gamma = \bigcup_{i=1}^{P} p_i$, where P is the total number of bodies and p_i is the region occupied by ith body. The boundary the interior region is denoted as $\partial\Gamma$. Confined geometries can also be considered as shown in Fig. 3.2(b).

3.3 Methods

3.3.1 General integral problems

Many integral problems share similar configurations to those shown schematically in Fig. 3.1. Space is divided into an exterior region Ω and an interior region Γ consisting of the union of different bodies with arbitrary shapes, for example dielectric or ferroelectric/ferromagnetic bodies. It is assumed here that there are no intersections or contacts between any two bodies. In most problems, the solution is obtained from functions $f(\mathbf{r})$ obtained from the integral over the boundary of all bodies ($\partial\Gamma$) of a kernel $K(\mathbf{r}, \mathbf{r}')$ and a source function $g(\mathbf{r})$. The kernel is derived from a Green's function that represents the underlying physics of a delta-function source; thus

$$f(\mathbf{r}) = \int_{\partial\Gamma} K(\mathbf{r}, \mathbf{r}') g(\mathbf{r}')\, d^2 r'. \tag{3.1}$$

In numerical integration of the above integral using a Gaussian quadrature rule, $f(\mathbf{r}_i)$

can then in general be expressed as

$$f(\mathbf{r}_i) = \sum_{j=1}^{N} K(\mathbf{r}_i, \mathbf{r}_j)\sigma_j. \tag{3.2}$$

Equation (3.2) is exactly the type of summation for which the FMM is used, with $O(N)$ computational complexity rather than the $O(N^2)$ complexity that results from using the direct method over all points $\mathbf{r}_i$ and $\mathbf{r}_j$. The kernel-independent FMM enables fast computation of the integral with arbitrary kernels for a variety of problems.

3.3.2 Electrostatic problem

A large class of systems in materials science involve polarizable metal oxide colloidal or nanoparticles in a dielectric continuum. The presence of a particle exerts an electrostatic field on nearby particles, leading to their polarization, which then propagates throughout the entirety of the system in a cooperative manner. Under some circumstances, polarization interactions can in fact lead to attractive forces between charged particles having the same charge, a feature that has been revealed in striking detail for metalic oxide micro-particles[7]. Here we consider polarizable dielectric bodies p_i embedded in an infinite dielectric medium Ω. Dielectric polarization arises on the surface of the bodies when the relative permittivities of the bodies are different from that of the medium. Bound surface charges are then induced because of the discontinuity of the electrostatic field across the interfaces between bodies and medium. In the following, we first review key equations that facilitate implementation of the BEM. For details on the derivation of the method, we refer to Refs. [12, 1]. The relative permittivity of the medium is ϵ_m, the relative permittivity of ith body is ϵ_i, and the point charge carried by the i-th particle is Q_i. In this method, Q_i is represented by an equivalent surface free charge density σ_f on the surface of each body (see section IV.I in Ref. [1]). In the particular case of spherical bodies, $\sigma_f = Q_i/(4\pi r_i^2)$ on the ith body with radius r_i. The

induced bound surface charge density σ_b can then be calculated by solving

$$A\sigma_b = b, \tag{3.3}$$

where

$$A\sigma_b \equiv \bar{\epsilon}_i \sigma_b + \epsilon_0 \Delta\epsilon_i \mathbf{E}_b \cdot \mathbf{n}, \tag{3.4}$$

with

$$\mathbf{E}_b = \frac{1}{4\pi\epsilon_0} \int_{\partial\Gamma} \frac{\mathbf{r} - \mathbf{r}'}{|\mathbf{r} - \mathbf{r}'|^3} \sigma_b(\mathbf{r}')\, d^2\mathbf{r}'. \tag{3.5}$$

In the above equations, $\bar{\epsilon}_i = (\epsilon_i + \epsilon_m)/2$, $\Delta\epsilon_i = \epsilon_m - \epsilon_i$, ϵ_0 is the permittivity of vacuum, $\mathbf{n}$ is the outward-pointing normal unit vector at the interface between a body and the medium, and $\mathbf{E}_b$ is the electrostatic field that arises from the bound surface charge density σ_b. The integral is performed only on the surfaces of all dielectric bodies ($\partial\Gamma$). The right-hand side b in Eq. (3.3) is obtained from

$$b = (1 - \bar{\epsilon}_i)\sigma_f - \epsilon_0 \Delta\epsilon_i \mathbf{E}_f \cdot \mathbf{n}, \tag{3.6}$$

with

$$\begin{aligned} \mathbf{E}_f = \frac{1}{4\pi\epsilon_0} \Big(& \int_{\partial\Gamma} \frac{\mathbf{r} - \mathbf{r}'}{|\mathbf{r} - \mathbf{r}'|^3} \sigma_f(\mathbf{r}')\, d^2\mathbf{r}' \\ & + \int_{\Omega} \frac{\mathbf{r} - \mathbf{r}'}{|\mathbf{r} - \mathbf{r}'|^3} \frac{\rho_f(\mathbf{r}')}{\epsilon_m}\, d^3\mathbf{r}' \Big), \end{aligned} \tag{3.7}$$

where $\mathbf{E}_f$ is the electrostatic field that arises only from the free charges, σ_f is the surface free charge density on the surface of the dielectric bodies, and ρ_f is the volume free charge density in the medium Ω. In our examples, only free charges carried by the dielectric bodies are considered, and there are no free volume charges in the medium, so the second term in Eq. (3.7) is absent. Once we obtain the total surface charge density $\sigma = \sigma_f + \sigma_b$ and total electrostatic field $\mathbf{E} = \mathbf{E}_f + \mathbf{E}_b$ on the surface of the dielectric bodies ($\partial\Gamma$), the force vector

acting on the ith body, $\mathbf{F}_i$, can be calculated by a boundary integral over the surface of i-th body,

$$\mathbf{F}_i = \int_{\partial p_i} \mathbf{f}(\mathbf{r})\, d^2\mathbf{r} \tag{3.8}$$

where $\mathbf{f}(\mathbf{r})$ is the surface force density on the surface of the body,

$$\mathbf{f}(\mathbf{r}) = \epsilon_m \sigma \mathbf{E}(\mathbf{r}). \tag{3.9}$$

3.4 Implementations

In the electrostatic problem, because dielectric polarization occurs at the interface, only the surface of dielectric bodies, rather than their volume, is discretized with a triangular mesh using CUBIT. Constant monomial shape functions is used to approximate variables such as surface charges and electrostatic fields in each element. The boundary integration on each element is done using a one-point quadrature rule: the quadrature point in each element is set to be the centroid of that element, and the weight is the surface area corresponding to that element. If the dielectric bodies are spheres, the surface area is calculated analytically as the spherical area; if the dielectric bodies are not spheres, the surface area is approximated by the flat area of each triangular element. The point where variables are approximated in each element is set to be the same as the quadrature point. The linear system of equations Eq. (3.3) is solved using GMRES in a matrix-free form provided by libMesh and PETSc, i.e., we do not explicitly form the matrix A, rather, we define the action of matrix-vector multiplication $A\sigma_b$ that is used in each GMRES iteration. The most computationally expensive part in the matrix-vector multiplication is calculating the electrostatic fields, which is a boundary integral with the kernel multiplied by the surface charge densities [see Eqs. (3.5) and (3.7)]. In a direct method, the computational complexity of the matrix-vector multiplication is $O(N^2)$. In Refs. [1, 42], a fast Ewald solver is used to reduce the complexity to $O(NlogN)$; in our implementation, FMM is used to further reduce the complexity to $O(N)$.

In the following subsections, boundary integration and parallelization are presented.

3.4.1 Integrals accelerated by FMM

For the numerical implementation of the boundary integrals that arise when calculating electrostatic fields, we use Eq. (3.5) as an example for the discretization. The electrostatic field vector at the jth element that arises from the bound surface charge density is

$$\mathbf{E}_b^j = \frac{1}{4\pi\epsilon_0}\left(\sum_{k=1,k\neq j}^{N}\frac{\mathbf{r}_j-\mathbf{r}_k}{|\mathbf{r}_j-\mathbf{r}_k|^3}\sigma_b^k a_k + \sqrt{\frac{a_j}{\pi}}H_j\mathbf{n}_j\right), \tag{3.10}$$

where N is the total number of boundary elements (here also the Dof because of the constant monomial shape function used here), a_j and a_k are the surface areas of the j-th and k-th element, H_j is the mean curvature at j-th element, and $\mathbf{n}_j$ is the unit outward-pointing normal vector at the centroid of the j-th element. The first term in Eq. (3.10) is the contribution from all source elements except for the target element itself, and the second term is a correction term that replaces the original singular term when $j = k$. This approximate correction works reasonably well for arbitrary geometries (see section IV.B in Ref. [1]). For spherical surfaces, $H_j = 1/r$, where r is the radius of sphere to which the j-th element belongs; for cylindrical lateral surfaces, $H_j = 1/(2r)$, where r is the radius of the cylinder; for flat surfaces, $H_j = 0$, which means the correction term is zero.

The kernel used in the summation in Eq. (3.10) is

$$K(\mathbf{r}_i,\mathbf{r}_j) = \frac{\mathbf{r}_i-\mathbf{r}_j}{|\mathbf{r}_i-\mathbf{r}_j|^3}. \tag{3.11}$$

It is also from Eqs.(3.4) and (3.6) that the normal unit vector is associated with target points rather than source points, and is outside of the boundary integral. We also note that the above kernel in Eq. (3.11) is the spatial derivative of $1/r$ kernel. Because the $1/r$ kernel and its spatial derivatives, i.e. the forces from the $1/r$ potential, are already implemented

in ScalFMM, we can take advantage of its highly optimized algorithm specifically designed for the symmetric $1/r$ kernel to perform boundary integrals for the electrostatic problem, which is more efficient than our current implementation for the boundary integrals in the magnetostatic problem.

3.4.2 Parallelization

In our parallel implementation, we use a serial mesh, i.e. every processor has a copy of the boundary mesh, but the data structures, such as matrices and vectors, used to solve the linear system of equations are partitioned and distributed among all processors automatically in libMesh during the parallel solution using PETSc. A parallel mesh is needed only if storing mesh data on a each processor consumes too much memory, which may be the case for problems with billions of DoFs. We use METIS[55] as the partitioner for data structures associated with the mesh. For the electrostatic problem, only one partitioner is necessary and the main parallelization is implemented in building the right-hand side b, performing matrix-vector multiplication in each GMRES iteration, and calculating the force vectors on the dielectric bodies, i.e., every processor calculates its own contribution to the right-hand side, to the matrix-vector product, and to the force vectors.

For the parallelization of FMM in the electrostatic problem, one strategy is to partition only the source points, i.e., every processor has a copy of the coordinates of all target points on the boundary mesh, as well as coordinates, and normal unit vectors of only local source points. We then perform serial FMM calculations on every processor, which means that we first calculate the contributions from local source points to all target points. We then let all processors communicate and sum up contributions from every processor and assign integrated values to all target points. An alternative strategy would share a similar concept, but partition only target points and keeps on every processor a local copy of information from all source points. The specific choice between the above two strategies that is better suited for the problem at hand depends on whether the number of target points or number

of source points is largest. If the number of source (target) points is larger than that of target (source) points, we choose to partition the source (target) points, *i.e.,* the larger set of points, because this can reduce the computational time and the memory cost of storing particles on every processor. Most of the times we found the number of source points is larger than the number of target points, because the number of quadrature points is mostly larger than that of nodal points, so we choose to partition the source points in our parallel implementation. Since a constant monomial shape function is used here, the quadrature point (source point) in each element is also the point (target point) where variables, such as charge densities and electrostatic fields, are approximated, i.e. target points are the same as source points. In order to use the TSM model in ScalFMM and the strategy of partitioning only target/source points, all quadrature points are inserted into the octree first as target points, and then they are inserted into the same octree again as source points, along with information of associated physical values and quadrature weights. We then partition only the target points; each processor keeps a copy of all source points along with the information of physical values and quadrature weights, and we perform FMM in serial on every processor.

We also note that ScalFMM has its own strategy for parallelization of FMM, in which both target and source points are partitioned based on their Morton ordering[56]. The idea is to map 3D points in the octree to those in a 1D array based on the z-value of each point, and then to partition all points based on the index of their 1D representation. After partitioning, local points are inserted into the octree on each processor, and each processor then performs FMM and communicates with other processors[57]. This strategy consumes less memory than the previous two methods, but its implementation is more involved. Therefore, we have not considered it here, and will examine it in future developments of our computational approach, where we will also compare its parallel efficiency with methods that partition only target/source points. In the following section, we test our computational approach for the electrostatic problem by applying it to several model problems, and we compare the results with analytical solutions. These comparisons serve to demonstrate the accuracy, efficiency,

and scalability of our parallel approach.

3.5 Results and discussions

We verified our method and implementation with a few model calculations for which there are analytical as well as numerical literature solutions: specifically, two dielectric spheres with surface-bound free charges, and a sphere inserted in a cylindrical cavity in a dielectric medium. In addition, we tested our method on a model problem for which there exists no analytical solution in closed form, namely two dielectric cubes with uniform surface free charges. The results are shown in Fig. 3.2, and Fig. 3.2(a) shows the solution for the problem of two spherical dielectric bodies. We also varied the center-to-center distance between two spheres and calculated the electrostatic forces at each distance using our numerical approach and an analytical expression[59, 18] (see Fig . 3.3(a)). Figure 3.2(b) shows the solution for the dielectric sphere inside a cylindrical cavity in a dielectric medium. The polarization effect on the sphere is turned off by setting its relative permittivity to be the same as that of the medium; note that this problem is equivalent to that of a point charge inside a dielectric cylinder. Our results are in good agreement with analytical solutions as well as with previous numerical results from Ref. [12]. Figure 3.2(c) shows results for the two dielectric cubes. In particular, the bound surface charge densities accumulate on the corners and edges of the cubes, rather than on the faces with a max/min value of +/- 0.49. To better show the polarization effect on cubic faces, the color range is set to +/- 0.04 in Fig. 3.2(c).

Figure 3.3(a) shows the comparison between our numerical method and an analytical method of calculating body forces on two dielectric spherical bodies as a function of their center-to-center distance (particle separation). For the numerical method, the surface DoFs on each body are varied to test the accuracy, while the relative tolerance for the iterative solver GMRES is set to 10^{-5} in all cases (further decreasing the relative tolerance improves numerical results little). The relative errors for the body force are shown in Fig. 3.4. As the number of degrees of freedom increases, the relative errors decreases significantly when

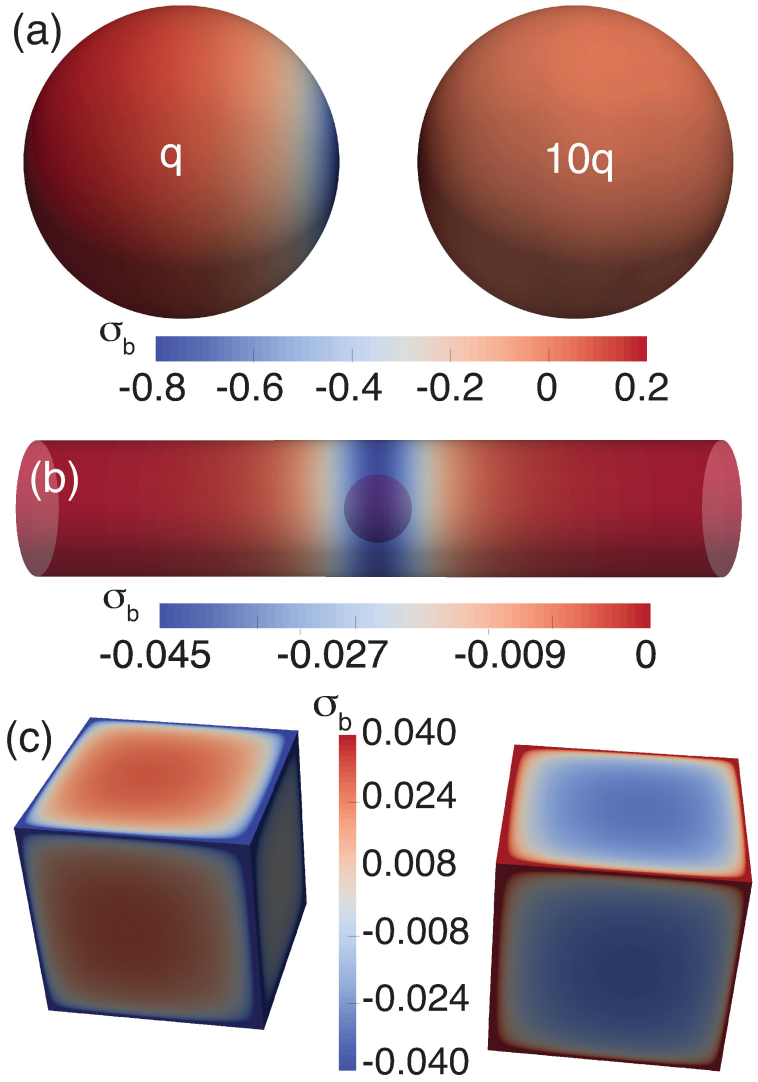

Figure 3.2: Model electrostatic problems for (a) two polarizable spherical dielectric bodies, (b) a polarizable dielectric sphere inside a cylindircal cavity in a dielectric medium, and (c) two polarizable dielectric cubes. The color maps show the induced *bound* surface charge density, (σ_b), in units of $q/(\epsilon_0 R^2)$. In (a), the two spheres have the same relative permittivity $\epsilon_1 = \epsilon_2 = 15$ and the same radius $r_1 = r_2 = R$, the relative permittivity of the medium is $\epsilon_m = 1$, the point charges are $Q_1 = 10q$ (body on the right), $Q_2 = q$ (body on the left), and the center to center distance is $d/R = 2.5$. In (b), the relative permittivities of the sphere and the cylindrical cavity are unity, while the relative permittivity of the medium is 2. The point charge on the sphere is q while the cylinder has no surface free charge density, the length and radius of cylinder is $10R$ and R; the radius of the sphere is $0.5R$ and its located at the center of the cylinder's axis. In (c), the side of cubes is R, the center to center distance is $d/R = 2.0$, the surface free charge densities are $-1/4\pi$ for the left cube and $1/4\pi$ for the right cube, and the relative permittivities of cubes and medium are the same as those in (a).

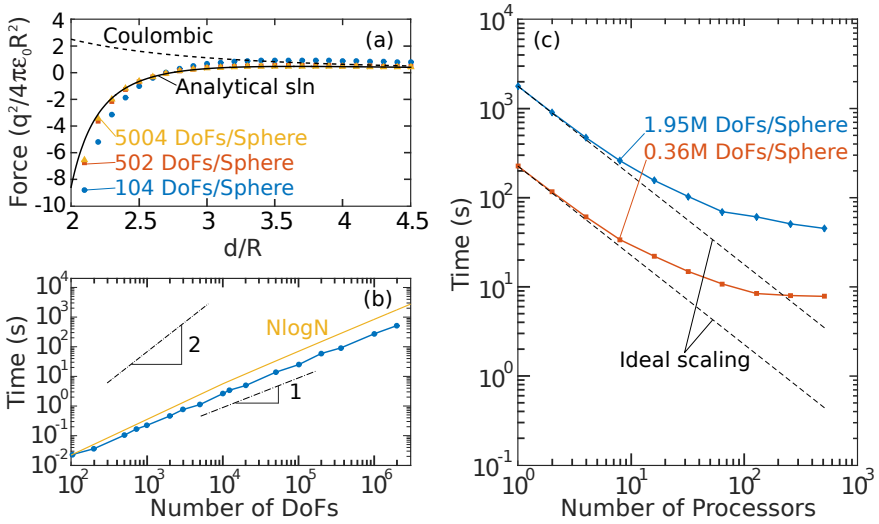

Figure 3.3: (a) Comparison between numerical and analytical results of calculating the electrostatic forces between two dielectric spherical bodies as a function of their center to center distance. Negative value means attractive force. (b) The scaling behaviors and computational time spent on solving for the surface bound charge densities and calculating body forces on particles using our numerical approach as a function of surface DoFs, tested on a single CPU core of Intel Xeon E5-1607 v3 @ 3.1GHz. The inset numbers 1 and 2 indicate the scaling of $O(N)$ and $O(N^2)$ respectively. For comparison purpose, it is assumed that the break-even point between $O(N)$ and $O(NlogN)$ is at 100 DoFs. (c) Strong scaling of solving the model electrostatic problem using our numerical approach tested on Blues at ANL.

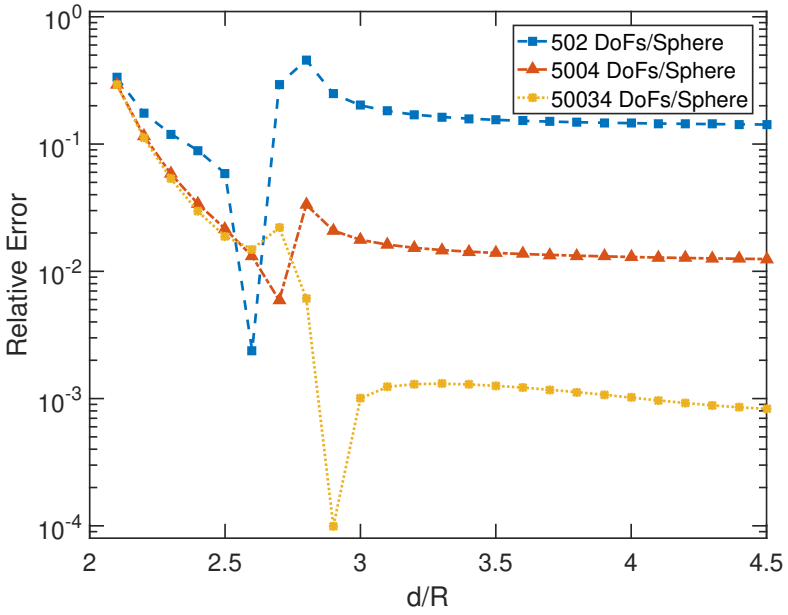

Figure 3.4: Relative errors of the body forces on unit dielectric spheres calculated from simulations compared to their analytical values for different DoFs/Sphere, as a function of center to center distance between two spheres.

$d/R \geq 2.8$. They decrease marginally when $d/R \leq 2.5$, and there are known difficulties in calculating forces accurately when two spheres are very close to each other because of large discretization errors, and adaptive mesh refinement is a technique to efficiently improve the accuracy in this situation[1]. The relative errors do not always decrease when $2.5 < d/R < 2.8$; under the same number of degrees of freedoms, for example 5004 DoFs/Sphere, they are even larger when $2.7 < d/R < 3.0$ than those when $d/R \geq 3.0$. This is because the body forces are nearly zero at these locations as shown by analytical solutions, and they are orders of magnitude smaller than those at other locations and thus more sensitive to discretization errors, which makes the relative errors large while the absolute error is very small.

Including polarization effects results in very different electrostatic interactions compared to those when only bare Coulombic interactions are included, especially when particle separations are small. These issues have been reported in past theoretical and numerical studies. In the particular case considered in Fig. 3.3, even though the surface free-charge densities on both bodies are all positive, the electrostatic interactions may exhibit attractive forces be-

tween the bodies when their center-to-center distance (d/R) is less than 2.74. Note that the bare Coulomb interaction consists of only repulsive forces, so it is crucial that the effects of dielectric polarization be included in calculations of electrostatic interactions for simulations of colloidal bodies, lest the underlying physics not be captured correctly.

Figure 3.3(b) shows the total computational time spent on assembling the right-hand-side of Eq. (3.3), solving the linear system of equations iteratively using GMRES, and calculating the body forces on one particle. As before, the order of Chebyshev polynomial is 5 in all cases. We can see that as surface DoFs increase, the computational time increases linearly, which is similar to that of the boundary integral using FMM in the magnetostatic simulation, and it confirms the $O(N)$ complexity of our method. In each case, because the distance between two particles is different from those in other cases, the box size for the octree is also different. The octree height in each case is tuned to achieve optical FMM performance, and the height generally increases as the surface DoFs increase. Compared to PPPM and the particle-mesh Ewald method[60] (PME) with $O(NlogN)$ complexity, FMM-based methods exhibit better computational complexity; Figure 3.3(b) shows that they have a clear advantage in high-performance computing of large-scale simulations with millions of unknowns. In addition, FMM-based methods are mesh-free approaches and more efficient for heterogeneous systems (*e.g.,* systems with electrostatic polarization), where the mesh-based approaches such as PPPM and PME that require an evenly spaced FFT-mesh become slow and memory-intensive[61].

Figure 3.3(c) shows strong scaling for up to 512 processors for solving the electrostatic problem when the surface DoFs on each particle are 0.36 M and 1.95 M. Overall, the computational times decrease as number of processor increases, and they are slightly larger than for ideal scaling when the number of processors is less than four. The difference between the computational time and ideal scaling increases as the number of processors increases. For the case with 0.36 M DoFs using 256 and 512 processors, the computational times were found to reach a plateau, while the strong scaling shows better performance for 1.95 M DoFs. In

order to investigate what prevented good scaling (*i.e.,* closer to ideal) for larger numbers of processors, we performed a detailed profiling of our code. We found that the time spent on inserting all source particles and FMM calculations on all source points dominate the total time, while the communication time spent on gathering all information of source points to every processor is much smaller. This observation shows that the plateau in strong scaling is the result of our parallel strategy of partitioning only target points and keeping a copy of all source points on every processor, so that all source points need to be inserted into the octree. This dominates the insertion time. In addition, FMM calculations have an $O(N)$ complexity, where $N = N_t/np + N_s$ since we only partition target points, N_t/np is the number of target points per processor and N_s is the number of all source points. In the electrostatic case, $N_t = N_s$ because of the one-point quadrature rule used in the boundary integration. So the FMM calculation time is dominated by calculations over source points, even if there are much fewer target points when the number of processors (np) is reasonably large. One strategy to recover better scaling for larger numbers of processors would be to create a separate partitioner for FMM, and to distribute both target and source points to every processor according to their Morton index. There will then be two partitioners in the simulation: one for FMM, and one for boundary elements. The challenge is then to create a mapping between the two partitioners to couple FMM with the boundary element calculation. Because our current parallel implementation shows very good scaling up to 128 processors, and quite good scaling for 1.95 M DoFs up to 512 processors, we believe our implementation is more than adequate for most applications. Further improvements to our parallel implementation will be performed in future work.

3.6 Conclusions

We have developed accurate, efficient, and scalable parallel computational approaches for integral problems based on the open source libraries libMesh and ScalFMM. The problems considered here all contain integrals of Green's functions over the boundary of the relevant

domains, which exhibit a computational complexity of $O(N^2)$ in direct implementations. To facilitate wider usage of these methods, we accelerated the computation of the boundary integrals using a kernel-independent FMM to achieve $O(N)$ computational complexity, and also with a memory cost of $O(N)$, resulting in significant gains in computational speed as well as in efficient memory utilization.

We note that FMMs have been used previously for boundary integrals and BEM[62, 63, 64], as well as combining with GMRES [32, 65]. However, there are few publicly available parallel codes using these techniques, in particular highly efficient and scalable ones. Our work is aimed at providing such a code framework, which we developed with the following features in mind: first, the code must run in parallel for large-scale problems with good parallel performances; second, it must be available for general distribution, at http://ime-code.uchicago.edu as part of the Continuum-Particle Simulation Suite (COPSS) from the Midwest Integrated Center for Computational Materials (MICCoM); third, it should provide convenient interfaces for computational researchers who are not familiar with acceleration techniques or parallelizations to focus on the underlying physical problems, as opposed to software engineering. Our computational approaches open up numerous possibilities and will enable efficient modeling for a variety of large-scale many-body problems, such as dynamics of colloids and interactions of magnetic bodies, to explore new physics and functions of materials. Further improvements can be made on our computational approaches, such as using the parallelization strategy in ScalFMM with the concept of Morton ordering and compare its performance with partitioning only target/source points as in our current implementation.

CHAPTER 4

NUMERICAL APPROACH: AN ACCELERATED STOKES' SOLVER TOWARDS SCALABLE BROWNIAN DYNAMICS OF HYDRODYNAMICALLY INTERACTING OBJECTS IN GENERAL GEOMETRIES

4.1 Abstract

An efficient parallel Stokes's solver has been developed for complete description of hydrodynamic interactions between Brownian particles in bulk and confined geomteries. A Langevin description of the particle dynamics is adopted, where the long-range interactions are included using a Green's function formalism. A scalable parallel computational approach is presented, where the general geometry Stokeslet is calculated following a matrix-free algorithm using the General geometry Ewald-like method. Our approach employs a highly-efficient iterative finite-element Stokes' solver for the accurate treatment of long-range hydrodynamic interactions in arbitrary confined geometries. A combination of mid-point time integration of the Brownian stochastic differential equation, the parallel Stokes' solver, and a Chebyshev polynomial approximation for the fluctuation-dissipation theorem lead to an $O(N)$ parallel algorithm. We illustrate the new algorithm in the context of the dynamics of confined polymer solutions under equilibrium and non-equilibrium conditions. The method is then extended to treat suspended finite size particles of arbitrary shape in any geometry using an Immersed Boundary approach.

4.2 Introduction

The dynamics of suspended objects in confined geometries, such as colloidal particles or polymeric molecules, is important for a wide range of applications, including enhanced oil recovery, biology, materials design and medicine. For example, in modern genomic technolo-

gies, such as DNA sequencing or optical mapping, individual DNA molecules can be directly manipulated in microfluidic and nanofluidic devices, where hydrodynamic effects play a key role [66, 67, 68, 69, 70]. Another set of applications, involving lab-on-a-chip devices, aim to manipulate cell and particle suspensions through the precise design of flow conduits and accurate control of flow rates and hydrodynamic forces [71, 72]. From a physical point of view, many intriguing rheological behaviors in suspensions, including foam formation [73], shear thickening [74], solidification [75] and shear induced migration [76, 77, 78] have been traced back to hydrodynamic effects. Similarly, in the context of intracellular motion, the effects of crowding are of considerable interest and are believed to be caused by hydrodynamic interactions [79, 80, 81, 82, 83, 84, 85, 86]. The precise mechanisms that underpin such phenomena, however, remain poorly understood, particularly when they arise at high concentrations. Efficient methods and algorithms capable of accurately capturing hydrodynamic interactions and their influence on microstructure evolution are necessary in order to describe the dynamics of concentrated particle suspensions, and for design of fluidic devices.

Brownian Dynamics (BD) is generally used for problems that are characterized by a broad separation of length and time scales - on the order of several orders of magnitude, between the relaxation times of suspended particles or molecules and those of the solvent. The system is evolved through the integration of the Fokker-Planck equation for the probability distribution function, which incorporates a force balance for the suspended particles and the fluid, coupled through the fluctuation-dissipation theorem [87, 88]. A representative system is provided by a 21 μm DNA molecule suspended in an aqueous solution. The characteristic size of the molecule is 18×10^{-10} m), and it has a relaxation time of 0.1 seconds. In contrast, the fluid has a characteristic diffusion time, i.e., the time required for the fluid molecule to diffuse its own size, of 10^{-15} seconds. Simulations that include a solvent explicitly would be impractical. In BD, the fluid is represented as a continuum governed by the Stokes momentum equations [89, 90, 91, 88]. In such a system, the motion of each particle is influenced by that of all other particles, and it is mediated by hydrodynamic interactions

(HI), which are long-ranged. Explicit expressions to calculate HI are only available in free space and for simple geometries; for the general cases encountered in micro- or nano-fluidic devices, hydrodynamic forces must be obtained numerically.

BD simulations have been used extensively to study the dynamics of macromolecules and colloids [92, 93, 94, 95], the transport of DNA [96, 97, 98, 99, 100, 68], and the flow behavior of colloidal dispersions [101, 102, 103]. Such simulations are computationally demanding, and most simulations to date have been limited to small systems in unbounded domains or in simple geometries. Over the last two of decades, increasingly efficient methods and algorithms have been developed to evaluate HI. These include Stokes solvers [104, 105], Stokesian Dynamics (SD) [106, 107, 108], Lattice Boltzmann method (LBM) [109, 110, 111, 112], dissipative particle dynamics (DPD) [113, 114] and Green's functions based methods [104, 115, 116, 117, 95, 94, 118]. Fluid particle methods, DPD, and fluid mesh methods, LBM, are widely used and preferred by several authors. DPD can coarse grain the solvent molecules and greatly reduces the number of solvent particles and increased time intervals compared to classical molecular dynamics (MD). However, correct implementation of confining walls, i.e., no-slip boundary conditions, is not a trivial task in DPD. LBM only gives approximate solutions to incompressible Stokes flow since it requires a finite Reynold number Re. LBM also needs complementary methods to properly model complex geometries and eliminate viscosity-dependent errors [119, 120]; however, the implementation of these complementary methods are complicated. Another issue with LBM is that it become fluid element dependent as the concentration of suspended particles increases. In practice, as the concentration increases, the number of fluid elements has to increase consistently, thereby increasing the computational cost. The General geometry Ewald-like (GgEm) method [118] is of particular interest to our work because it directly solves Stokes equation ($Re = 0$) and is able to handle arbitrary geometries and no slip boundary conditions efficiently. GgEm uses the linear character of the momentum equations to split the contributions of long-range interactions into a local and a global calculation,

following the general philosophy of the Ewald split. It resolves short-range particle-particle interactions precisely, while far-field interactions are evaluated on a mesh using a Computational Fluid Dynamics approach. The GgEm method has been used for simulations of confined DNAs [68], of DNA pore translocation [95, 121], of charged dipoles [122] and polyelectrolytes [123], of suspensions of rigid and deformable particles [124, 125] and of active suspensions [126, 127, 128].

As helpful as the GgEm method has been, its implementation is challenging, particularly in highly parallel algorithms. The purpose of this chapter is to introduce an efficient and scalable computational implementation, and to publicly release the corresponding software. To do so, we rely on a finite element formulation for the far-field contributions, using distributed memory parallelization methods that include a direct LU analytic solver for systems with less than one million degrees of freedom, and a fast parallel iterative solver, with hybrid preconditioning, for larger systems. Our parallel Stokes' solver is combined with GgEm, a mid-point integration scheme, and a Chebyshev polynomial approximation for the fluctuation-dissipation theorem, to arrive at an efficient $O(N)$ and completely scalable parallel BD algorithm. In what follows we offer a detailed explanation of our proposed approach, including a discussion of important numerical issues and general aspects of the algorithm. We then illustrate its use in the context of confined polymer solutions and finite-size particle dynamics. More specifically, we calculate the diffusion of polymers in a slit geometry, and demonstrate that the correct Zimm scaling is obtained [91, 129]. We then simulate flowing polymers in a cross-channel geometry, and show how the method can be used in arbitrary domain shapes. We also show results for the dynamics of finite-sized particles using an Immersed Boundary-GgEm formulation.

4.3 Methods

4.3.1 The Fokker-Planck and the Brownian dynamics equations

The stochastic differential equation that governs the dynamics of N suspended beads in a viscous solvent is obtained from the force balance

$$\frac{\partial m\mathbf{U}}{\partial t} = \mathbf{f}_\nu^H + \mathbf{f}_\nu^B + \mathbf{f}_\nu^{EV} + \mathbf{f}_\nu^{\text{other}}, \tag{4.1}$$

for each bead $\nu = 1, ..., N$, where $\mathbf{f}_\nu^H$ is the hydrodynamic force, $\mathbf{f}_\nu^B$ is the Brownian force, $\mathbf{f}_\nu^{EV}$ are excluded volume forces (bead-bead and bead-wall), $\mathbf{f}_\nu^{\text{other}}$ are other external (non-Hydrodynamic and non-Brownian) forces that may apply (e.g. spring, electrostatic or magnetostatic forces), $\mathbf{U}$ is the translational velocity. Re is assumed to be zero and inertial effects are neglected, therefore the left hand size of Eqn. (4.1) is equal to zero.

In a Lagrangian frame of reference, the evolution equation for the probability distribution function, $\psi(\mathbf{x}, t)$, for the bead positions is a convection-diffusion equation of the Fokker-Planck type [87]:

$$\frac{\partial \psi}{\partial t} = -\frac{\partial}{\partial \mathbf{R}} \cdot \left[\left(\boldsymbol{\kappa} \cdot \mathbf{R} + \frac{1}{k_B T} \mathbf{D} \cdot \mathbf{F} \right) \psi \right] + \frac{\partial}{\partial \mathbf{R}} \cdot \mathbf{D} \cdot \frac{\partial}{\partial \mathbf{R}} \psi, \tag{4.2}$$

where $\mathbf{R} = (\mathbf{x}_1, \mathbf{x}_2, \ldots, \mathbf{x}_N)$ is a $3N$ vector containing the spatial coordinates of the beads, $\boldsymbol{\kappa}$ is a diagonal $3N \times 3N$ tensor with the diagonal components of the imposed velocity gradient $\nabla \mathbf{U}_0$, $\mathbf{D}$ is the $3N \times 3N$ diffusion tensor, $\mathbf{F}$ is a $3N$ vector with the non-Brownian and non-hydrodynamic components of the force, k_B is Boltzmann's constant and T the temperature.

The diffusion tensor is given by $\mathbf{D} = k_B T \mathbf{M}$, where $\mathbf{M}$ is the mobility tensor that includes the Stokes' drag and the pair-wise Stokeslets that account for the hydrodynamic interactions between beads. Note that the time evolution of ψ, according to the Fokker-Planck equation, is due to convection –first term on the right-hand side – and diffusion – second term on the right-hand side – of the probability density. This is particularly important, because once this

equation is transformed to produce an equivalent stochastic differential equation, convective and diffusive terms will be generated. Each of these terms imposes particular challenges for their efficient numerical integration.

Assuming a continuous probability density, using the Chapman-Kolmogorov equation together with the introduction of a Wiener process, an equivalent stochastic differential equation for the motion of the beads is obtained as follows [88],

$$d\mathbf{R} = \left[\mathbf{U_0} + \mathbf{M}\cdot\mathbf{F} + \frac{\partial}{\partial\mathbf{R}}\cdot\mathbf{D}\right]dt + \sqrt{2}\mathbf{B}\cdot d\mathbf{W}, \tag{4.3}$$

where $\mathbf{U_0}$ denotes a $3N$ vector with the unperturbed fluid velocity at the bead's position and $\mathbf{U} = \mathbf{M}\cdot\mathbf{F}$ contains the fluctuating velocities from the hydrodynamic interactions; this is a convective term. The divergence of the diffusion tensor $\frac{\partial}{\partial\mathbf{R}}\cdot\mathbf{D}$ is the drift resulting from the configuration-dependent mobility of the confined particles; this is the first diffusive term. Finally, $d\mathbf{W}$ is a random vector, the components of which are obtained from a real-valued Gaussian distribution with zero mean and variance dt. It is coupled to the diffusion tensor through the fluctuation-dissipation theorem: $\mathbf{D} = \mathbf{B}\cdot\mathbf{B}^T$. Consequently, the term $\sqrt{2}\mathbf{B}\cdot d\mathbf{W}$ – the second diffusive term – represents the Brownian displacement, which results from collisions between the beads and the surrounding molecules in the fluid.

Three issues must be addressed in order to arrive at an efficient numerical algorithm for Eqn. (4.3). First, the mobility/diffusion tensor cannot be constructed explicitly; this would result in a $O(N^2)$ algorithm. This implies that the fluctuating velocity, $\mathbf{U}$, the divergence of the diffusion tensor, $\nabla\cdot\mathbf{D}$, and the diffusion tensor decomposition, $\mathbf{B}$, must be implemented in a matrix-free scheme. In our proposed algorithm, we use (i) the General geometry Ewald-like method (GgEm) for a matrix-free product of the mobility tensor with any vector, $\mathbf{M}\cdot\mathbf{F}$; (ii) a mid-point algorithm, proposed by Fixman [130], that avoids the explicit calculation of $\nabla\cdot\mathbf{D}$; and (iii) a Chebyshev polynomial approximation for the $\mathbf{B}\cdot d\mathbf{W}$ product, also proposed by Fixman [131], that uses GgEm to avoid the explicit calculation of $\mathbf{D}$. The

entire algorithm scales as $O(N)$ and enables one to handle arbitrarily shaped systems by relying on GgEm [118]. In addition, we also rely on parallel finite element methods and parallel libraries to achieve the above tasks.

General geometry Ewald-like method (GgEm)

A velocity field, $\mathbf{U} = (\mathbf{u}_1, \mathbf{u}_2, ..., \mathbf{u}_N) = \mathbf{M} \cdot \mathbf{F}$, driven by a distribution of forces at the bead positions, $\mathbf{F} = (\mathbf{f}_1, \mathbf{f}_2, ..., \mathbf{f}_N)$, can be calculated directly by recognizing that, for zero Re, the force balance on the fluid is reduced to the Stokes's momentum equations:

$$-\nabla p + \mu \nabla^2 \mathbf{u} = -\boldsymbol{\rho}^f, \tag{4.4}$$

$$\nabla \cdot \mathbf{u} = \mathbf{0}, \tag{4.5}$$

where μ is the fluid viscosity, $\mathbf{u}(\mathbf{x})$ is the fluid velocity field generated by a force density $\boldsymbol{\rho}^f(\mathbf{x}) = \sum_{\nu=1}^{N} \mathbf{f}_\nu \delta(\mathbf{x} - \mathbf{x}_\nu)$ and p is the corresponding pressure. The inclusion of the Dirac delta function, $\delta(\mathbf{x})$, in the force density implies that we are assuming, for the moment being, that the forces exerted by the beads on the fluid are singular point-forces.

Similar to conventional particle-mesh Ewald methods [132], GgEm uses the linear character of Stokes' equation to re-define the force density in Eqn. (4.4):

$$\boldsymbol{\rho}^f(\mathbf{x}) = \boldsymbol{\rho}_l^f(\mathbf{x}) + \boldsymbol{\rho}_g^f(\mathbf{x}), \tag{4.6}$$

where the "local" density is

$$\boldsymbol{\rho}_l^f(\mathbf{x}) = \sum_{\nu}^{N} [\delta(\mathbf{x} - \mathbf{x}_\nu) - g(\mathbf{x} - \mathbf{x}_\nu)] \mathbf{f}_\nu(\mathbf{x}), \tag{4.7}$$

while the "global" density is given by

$$\boldsymbol{\rho}_g^f(\mathbf{x}) = \sum_\nu g(\mathbf{x} - \mathbf{x}_\nu)\mathbf{f}_\nu(\mathbf{x}). \tag{4.8}$$

The "screening" function, $g(\mathbf{x})$, must satisfy $\int_{\text{all space}} g(\mathbf{x}) = 1$ and it is chosen in a way that the local density contribution to the velocity field decays exponentially. We have found that [118] a modified Gaussian function of the type

$$g(\mathbf{r}) = \frac{\alpha^3}{\pi^{3/2}} e^{-\alpha^2 r^2} \left[\frac{5}{2} - \alpha^2 r^2\right], \tag{4.9}$$

results in an exponentially decaying "local" velocity field over a length scale α^{-1}.

Ignoring the confining walls, a Green's function calculation can be carried out to obtain the local contribution according to

$$\mathbf{u}_l(\mathbf{x}) = \sum_\nu \mathbf{G}_l(\mathbf{x} - \mathbf{x}_\nu) \cdot \mathbf{f}_\nu, \tag{4.10}$$

where $\mathbf{G}_l(\mathbf{x})$ is a screened Green's function given by

$$\begin{aligned} \mathbf{G}_l(\mathbf{x}) = &\frac{1}{8\pi\mu}\left[\boldsymbol{\delta} + \frac{\mathbf{x}\mathbf{x}}{r^2}\right]\left[\frac{\operatorname{erfc}(\alpha r)}{r}\right] \\ &- \frac{1}{8\pi\mu}\left[\boldsymbol{\delta} - \frac{\mathbf{x}\mathbf{x}}{r^2}\right]\left[\frac{2\alpha}{\pi^{1/2}} e^{-\alpha^2 r^2}\right], \end{aligned} \tag{4.11}$$

where $r = |\mathbf{x}|$.

Note that the aim here is to calculate the product of the mobility/diffusion tensor and a forcing vector. In doing so, the physical characteristics of such a tensor, its positive definiteness and self-adjoint form, must be preserved. As the concentration of beads is increased, using a point-force model does not ensure such limits. We can, however, introduce a point-force regularization using the same form of the modified Gaussian over a new length scale ξ^{-1}. For $\xi^{-1} = 3a/\pi^{1/2}$, the maximum fluid velocity is equal to that of a particle with

radius a and the pair mobility remains positive-definite. Introducing this regularization in the local contribution is trivial because it only modifies the screened Green's function as follows

$$\begin{aligned}\mathbf{G}_l^R(\mathbf{x}) = &\frac{1}{8\pi\mu}\left[\boldsymbol{\delta} + \frac{\mathbf{xx}}{r^2}\right]\left[\frac{\mathrm{erf}(\xi r)}{r} - \frac{\mathrm{erf}(\alpha r)}{r}\right] \\ &+ \frac{1}{8\pi\mu}\left[\boldsymbol{\delta} - \frac{\mathbf{xx}}{r^2}\right]\left[\frac{2\xi}{\pi^{1/2}}e^{-\xi^2 r^2} - \frac{2\alpha}{\pi^{1/2}}e^{-\alpha^2 r^2}\right].\end{aligned} \tag{4.12}$$

The functions $\mathbf{G}_l^R$ and $\mathbf{G}_l$ decay exponentially on the length scale α^{-1}. In practice, the local velocity field can be computed, as is done in Ewald-like methods, by only considering the neighbors of each particle. On the other hand, the "global" contribution to the velocity field, $\mathbf{u}_g(\mathbf{x})$, which is driven by the force density $\boldsymbol{\rho}_g^f(\mathbf{x})$, is obtained numerically by solving the Stokes equations:

$$-\nabla p_g + \mu\nabla^2\mathbf{u}_g = -\boldsymbol{\rho}_g^f, \tag{4.13}$$

$$\nabla\cdot\mathbf{u}_g = \mathbf{0}. \tag{4.14}$$

This requires that $\mathbf{u}_l + \mathbf{u}_g$ satisfy the appropriate boundary conditions at the domain walls and boundaries. For example, a Dirichlet boundary condition, where the wall velocity is given by $\overline{\mathbf{u}}(\mathbf{x_W})$, results in a boundary condition for the global contribution $\mathbf{u}_g(\mathbf{x}) = \overline{\mathbf{u}}(\mathbf{x_W}) - \mathbf{u}_l(\mathbf{x})$, for $\mathbf{x}\in\mathbf{x_W}$.

The global solution is obtained on a set of M discrete points on a mesh; in this regard, GgEm resembles a Particle-Particle-Particle-Mesh (PPPM) method, where the assignment function is replaced by the delta function. Several techniques (finite differences, finite elements, spectral methods) can be used to find the global contribution; after the mesh is resolved, interpolation is used to get the value of the global velocity at position $\mathbf{x}$. As mentioned earlier, in GgEm, $\mathbf{M}\cdot\mathbf{F}$ is determined implicitly, requiring $O(N)$ operations. For the point-force version, $\mathbf{M} = \mathbf{M}^T$, as required by the self-adjoint character of Stokes' equations. For the regularized version, $\mathbf{M} = \mathbf{M}^T$ if the boundary condition on $\mathbf{u}_g$ remains the same as for the point-force version, at the cost of violating the no-slip boundary condition for

points within $\sim \xi^{-1}$ from the wall (which would normally be prevented by excluded volume interactions).

Mid-point integration algorithm

To avoid the explicit calculation of $\nabla \cdot \mathbf{D}$, we adopt Fixman's mid-point algorithm [89], where the time evolution from time t to time $t + dt$ requires an intermediate step t^*:

$$\begin{aligned} \mathbf{R}^* = \mathbf{R}(t) + \frac{1}{2}\left[\mathbf{U}_0(\mathbf{R}) + \mathbf{M}(\mathbf{R}) \cdot \mathbf{F}(\mathbf{R})\right] \Delta t \\ + \frac{1}{2}\sqrt{2}\mathbf{D}(\mathbf{R})\mathbf{B}^{-1}(\mathbf{R}) \cdot d\mathbf{W}(t) \end{aligned} \tag{4.15}$$

$$\begin{aligned} \mathbf{R}(t + \Delta t) = \mathbf{R}(t) + \left[\mathbf{U}_0(\mathbf{R}^*) + \mathbf{M}(\mathbf{R}^*) \cdot \mathbf{F}(\mathbf{R}^*)\right] \Delta t \\ + \sqrt{2}\mathbf{D}(\mathbf{R}^*)\mathbf{B}^{-1}(\mathbf{R}) \cdot d\mathbf{W}(t) \end{aligned} \tag{4.16}$$

.

Chebyshev polynomial approximation

Finally, the diffusion tensor decomposition is carried out using a Chebyshev polynomial approximation as proposed by Fixman [130], which guarantees that the fluctuation-dissipation theorem is satisfied. When combined with the GgEm, it results in a matrix-free algorithm because it only requires matrix-vector products. This method has been widely implemented in previous studies with unbounded or periodic domains [92, 98, 76, 118, 68]. Here we only present a brief summary of the algorithm, and highlight some of the key issues that arise in our scalable numerical implementation.

An operation over a matrix, $f(\mathbf{M})$, can be approximated by a linear combination of Chebyshev polynomials as follows

$$f(\mathbf{M}) = \sum_{l=0}^{L} a_l \mathbf{C}_l \tag{4.17}$$

where a_l and L are the coefficients and order of the approximation, respectively, and

$$\begin{aligned} \mathbf{C}_0 &= \mathbf{I}, && (4.18) \\ \mathbf{C}_1 &= d_a\mathbf{M} + d_b\mathbf{I}, && (4.19) \\ \mathbf{C}_{1+1} &= 2(d_a\mathbf{M} + d_b\mathbf{I})\mathbf{C}_l - \mathbf{C}_{l-1}. && (4.20) \end{aligned}$$

The parameters d_a and d_b depend on the span of the approximation and are defined by

$$\begin{aligned} d_a &= \frac{2}{\lambda_{\max} - \lambda_{\min}} && (4.21) \\ d_b &= -\frac{\lambda_{\max} + \lambda_{\min}}{\lambda_{\max} - \lambda_{\min}}, && (4.22) \end{aligned}$$

where $[\lambda_{min}, \lambda_{max}]$ is the range of eigenvalues of $\mathbf{M}$ where the approximation takes effect.

For the mid-point algorithm, we require calculation of $\mathbf{y} = f(\mathbf{M}) \cdot d\mathbf{w}$. This can then be expressed in terms of a series of matrix-vector products given by

$$\mathbf{y} = f(\mathbf{M}) \cdot d\mathbf{w} = \sum_{l=0}^{L} a_l \hat{\mathbf{x}}_l \qquad (4.23)$$

where

$$\begin{aligned} \hat{\mathbf{x}}_0 &= d\mathbf{w}, && (4.24) \\ \hat{\mathbf{x}}_1 &= (d_a\mathbf{M} + d_b\mathbf{I}) \cdot d\mathbf{w}, && (4.25) \\ \hat{\mathbf{x}}_{1+1} &= 2(d_a\mathbf{M} + d_b\mathbf{I})\hat{\mathbf{x}}_l - \hat{\mathbf{x}}_{l-1}. && (4.26) \end{aligned}$$

The convergence rate of this polynomial approximation depends on both the condition number of the matrix and the accuracy of the evaluation of its eigenvalues. The well-conditioned character of the diffusion tensor is related to its positive-definite form, which is guaranteed by using GgEm and a point-force regularization. More important is the proper

calculation (or estimation) of the limiting eigenvalues. This procedure cannot rely on an explicit construction of the tensor, and it should be scalable and parallelizable. In our present numerical implementation, the eigenvalues, $\lambda_{\min}$ and $\lambda_{\max}$, are calculated by using the open-source software package SLEPc [133]. It is capable of rapidly solving upper and lower bounds of eigenvalues for large systems on parallel computers. SLEPc also provides a variety of solution methods in a matrix-free way. Therefore, combining pFE-GgEm with SLEPc results in a $O(N)$ scalable parallel algorithm.

4.3.2 Parallel FEM Stokes flow solver

To be able to accommodate complex confining geometries, we discretize the Stokes problem Eqn. (4.13) using the $P^2 - P^1$ Taylor-Hood mixed element for $\mathbf{u} - p$ [134]. This is a stable element that is a staple of Stokes discretizations. The discrete Stokes equation in this basis has the following form

$$\underbrace{\begin{pmatrix} \boldsymbol{A} & B^T \\ B & 0 \end{pmatrix}}_{Q} \begin{pmatrix} \hat{\mathbf{u}} \\ \hat{p} \end{pmatrix} = \begin{pmatrix} \hat{\boldsymbol{\rho}}_{\boldsymbol{g}}^{\boldsymbol{f}} \\ 0 \end{pmatrix}, \tag{4.27}$$

where $\hat{\mathbf{u}}$, $\hat{p}$ and $\hat{\boldsymbol{\rho}}_{\boldsymbol{g}}^{\boldsymbol{f}}$ are the vectors of FEM coefficients for the velocity, pressure and global forcing, respectively; A is the Laplacian operator and B is the divergence operator discretized using the FEM basis, both incorporating whichever boundary conditions are imposed on the velocity and pressure, respectively.

Once the bead positions are determined and $\hat{\boldsymbol{\rho}}_{\boldsymbol{g}}^{\boldsymbol{f}}$ is formed, the Stokes solver determines $\hat{\mathbf{u}}$ and evaluates it at the bead positions to obtain $\mathbf{U}$. This procedure implicitly defines the mobility tensor $\mathbf{M}$. Since $\mathbf{M}$ is applied repeatedly in the time-stepper and the Chebyshev approximation, it is crucial to have an efficient solver for Eqn. (4.27) that can handle sufficiently fine discretizations, necessary for resolving complicated confining geometries of large-size containers.

subDirect solver

For meshes with moderate numbers of degrees of freedom N_h, the best approach to solve Eqn. (4.27) is to use a direct solver, such as the LU factorization $Q = L\Lambda U$, where L and U are lower- and upper-triangular, respectively, and Λ is diagonal. The advantage of this approach is that the matrix has to be factored only once, and the factors can be reused repeatedly to compute the action of M, including inside the Chebyshev operator expansion, using back- and forward-solves U and L, respectively.

The main limitations of this approach is that the L, U factors have to be explicitly computed and stored, consuming $\mathcal{O}(N_h^3)$ time and $\mathcal{O}(N_h^2)$ storage, respectively. The solves with L and U can also consume $\mathcal{O}(N_h)$ time and can introduce substantial serialization among the processors in a parallel setting. While parallel direct solver packages, such as SuperLU_Dist [135] allow for moderately large systems to be solved in reasonable time by partitioning the factor matrices among processor memories, the direct approach is fundamentally unscalable: storage requirements with $N_h \approx 5.0 \times 10^5$ exceed $16GB$, a typical RAM size for many commodity machines.

Iterative solver

Modern scalable parallel solvers for sparse linear systems such as Eqn. (4.27) are usually implemented using Krylov subspace methods (KSP). These are a family of algorithms that rely solely on the availability of a subroutine implementing the matrix-vector product Qw to solve $Qw = h$ [136]. Because of this, KSP are highly parallelizable, provided an efficient *pre-conditioner* is available. Popular members of the KSP family are the conjugate-gradient method (CG), which is applicable to symmetric positive- (in)definite systems only, and the more flexible generalized minimal residual method (GMRES). It is useful, albeit not exactly accurate, to think of a pre-conditioner as an operator P that approximates the inverse to Q so that $PQ \approx I$ at least in the sense of a better clustering of the resulting spectrum. PETSc implements a wide variety of KSP methods as well as a number of general-purpose

pre-conditioners, or makes pre-conditioners from other packages available through a uniform API. This allows the user to quickly experiment with different combinations of solvers and fine-tune the solver parameters without changing the code.

Since Q in (4.27) is not positive definite, CG is inapplicable, but the more flexible GMRES can work well, given a good pre-conditioner for Q. Multigrid methods and other general-purpose pre-conditioners are not very effective for Q due to its indefinite nature and a zero diagonal pressure block. However, PETSc provides effective tools for building pre-conditioners out of block methods based on decompositions such as the natural velocity-pressure split.

Generally, the most effective pre-conditioners for the discrete Stokes system [137] exploit the *Schur complement* matrix $S = -BA^{-1}B^T$, obtained from a factorization of Q:

$$\begin{pmatrix} \boldsymbol{A} & B^T \\ B & \end{pmatrix} = \begin{pmatrix} \boldsymbol{A} & \\ B\boldsymbol{A}^{-1} & I \end{pmatrix} \begin{pmatrix} \boldsymbol{A} & \\ & S \end{pmatrix} \begin{pmatrix} I & \boldsymbol{A}^{-1}B^T \\ & I \end{pmatrix}$$

Indeed, inverting the block matrices left to right leads to an exact solution $\begin{pmatrix} x \\ y \end{pmatrix}$ to $Q \begin{pmatrix} \boldsymbol{x} \\ y \end{pmatrix} = \begin{pmatrix} \boldsymbol{f} \\ g \end{pmatrix}$ in terms of solutions to the subsystems:

$$\boldsymbol{A}\boldsymbol{z} = \boldsymbol{f}, \quad Sy = g - B\boldsymbol{z}, \quad \boldsymbol{A}\boldsymbol{x} = \boldsymbol{f} - B^T y, \tag{4.28}$$

defining the action of operator $\begin{pmatrix} \boldsymbol{x} \\ y \end{pmatrix} = P \begin{pmatrix} \boldsymbol{f} \\ g \end{pmatrix}$. The first and the last systems involve the solves with the discrete Laplacian, which can be effectively preconditioned by a multigrid method or, even more simply, using $ILU(0)$ – an incomplete LU factorization with zero fill applied locally on each processor [136]. The middle (negatively-definite) system also responds well to GMRES, provided that S can be applied efficiently without forming the

matrix, and that an effective pre-conditioner for S can be obtained.

Many common pre-conditioners for Stokes are approximate solution operators P obtained by solving the three systems above *inexactly* using Krylov solvers κ on the blocks of Q. This is done by replacing $\boldsymbol{A}^{-1}$ and S^{-1} in the three systems of Eqn. (4.28) by applications of $\kappa(\boldsymbol{A})$ and $\kappa(\hat{S})$, respectively. The Schur pre-conditioner itself is applied only approximately using $\kappa(\boldsymbol{A})$ to define

$$\hat{S}y = -B\kappa(\boldsymbol{A})B^T y.$$

Varying degrees of accuracy are required of the different κ, and frequently only a few iterations (or even one) are necessary for an effective pre-conditioner; in particular, each occurrence of $\kappa(\boldsymbol{A})$ potentially denotes a different solver.

The main difficulty is in preconditioning $\hat{S}$ in such a way that the overall solver performance does not degrade with mesh refinement. A classical approach to preconditioning S or $\hat{S}$ consists of using the *pressure mass matrix* M_p, which is simply the classical mass matrix for the pressure finite-element basis; in our case it is the mass matrix in the P^1 basis of piecewise linear continuous functions. Mass matrices have many desirable properties; in particular, they are symmetric, positive-definite, have positive entries. Many Stokes solvers use $-M_p$ to precondition $\hat{S}$ very successfully, since $-M_p^{-1}\hat{S}$ generally has very good spectral properties, making KSP converge rather well.

Since $-M_p$ is a good pre-conditioner for $\hat{S}$, it is spectrally similar to $\hat{S}$ and can in some sense replace $\hat{S}$. Using this observation we were able to devise a particularly effective pre-conditioner for Eqn. (4.27) that *replaces* $\hat{S}$ by $-M_p$. This solves the problem of preconditioning the middle system in Eqn. (4.28), since M_p is well pre-conditoned by the diagonal lumped mass matrix $\hat{M}_p$, which contains the row sums of M_p on its diagonal. At the same time, the use of M_p eliminates the need for the relatively expensive application of $\kappa(\boldsymbol{A})$ in the definition of the action of $\hat{S}$ on vectors.

Whenever pressure boundary conditions are used, it is important to observe that the lower-right block in Eqn. (4.27) is not actually zero, but contains rows of the negative

identity matrix corresponding to the mesh nodes where this boundary condition is applied. In that case, we add those rows to $-M_p$, which remains negative-definite. In fact, we use a penalty formulation of all Dirichlet boundary conditions, which adds large negative diagonal entries to $-M_p$ and, incidentally, preserves the symmetry of $\boldsymbol{A}$. In particular, we can use CG with ILU(0) or its Cholesky variant ICC(0) for both $\kappa(\boldsymbol{A})$ and κM_p. While ILU(0) is not guaranteed to preserve the symmetry or the definiteness of the preconditioned operator, in our experience this does not cause a problem. In case CG fails to converge, the more robust GMRES can be used.

An additional simplification of P can be obtained by dropping the last of the three factors and inverting the remaining two using κ in place of inverses. This is a rather common approximation (see [137]), which might increase the number of GMRES iterations needed for convergence, but makes each application of P considerably cheaper, since it omits the intermediate $\boldsymbol{z}$. Concretely, the action of our pre-conditioner P is defined as $\hat{P}\begin{pmatrix}\boldsymbol{f}\\ g\end{pmatrix} = \begin{pmatrix}\boldsymbol{x}\\ y\end{pmatrix}$, where $\boldsymbol{x}$ and y are computed as follows:

$$\boldsymbol{x} = \boldsymbol{z} - \kappa(\boldsymbol{A}), \quad y = -\kappa(M_p)(g - B\boldsymbol{x}).$$

The effectiveness of KSP methods depends on the particular right-hand side vector in the system being solved. For the specific case of $\begin{pmatrix}\hat{\boldsymbol{\rho}}_{\boldsymbol{g}}^{\boldsymbol{f}}\\ 0\end{pmatrix}$ GMRES preconditioned with the P described above proves to be extremely effective, outperforming all other iterative methods we are aware of.

Finally, we note that as defined above P is, in fact, a nonlinear operator, since it contains possibly under-converged KSP applications in it. This might cause GMRES to diverge, although this hasn't happened in our experience. In that case the more robust *flexible* GMRES or FGMRES should be used (see [136]).

Solver configuration and comparison

In our software, the selection of direct solver or iterative solver can be done by simply changing runtime parameters, depending on the specific demands of the problem – most commonly, the size of the computational mesh. Moreover, *all* of the iterative solver parameters can be controlled in this manner, allowing the user to fine-tune the solver to a specific problem. We provided defaults, however, that we found to be the most effective. These can be nonetheless overridden at runtime thanks to PETSc's flexible command-line options system. In particular, by default $\kappa(\boldsymbol{A})$ above is CG preconditioned with ILU(0) on each processor's local block, and solved to the relative tolerance 10^{-6} on the residual. CG is also used in $\kappa(M_p)$, likewise preconditioned with ILU(0) and to the same relative tolerance of 10^{-6}. These settings are used in all of the numerical experiments here whenever the iterative solver is employed. All of these settings can be easily overridden on the command line using the PETSc options database system.

We compared direct and iterative solvers using 128 CPU cores of Intel Xeon E5-2698v3 @ 2.3GHz on Blues at Argonne National Laboratory (ANL). We observe that, for problem sizes up to 1.2 million degrees of freedom, the direct solver performs better than iterative solvers. For systems with 0.32, 0.64, and 1.2 million degrees of freedom, the Stokes solution takes 0.083, 0.18, and 0.55 seconds, respectively, using a direct LU solver (in the preparation step, the LU decomposition takes 80, 225, and 1036 seconds, respectively). On the other hand, the iterative Stokes solution takes 6, 10, and 29 seconds, respectively, for the same system sizes. For a problem size with 2.4 million degrees of freedom, the direct solver was unable to provide a one-step Stokes solve and hung in the LU decomposition process for at least 6 hours. The iterative solver, for systems with 2.4, 9.7, and 16.1 million degrees of freedom, took during one step Stokes solve 57, 218, and 625 seconds, respectively.

4.3.3 pFE-GgEm routines and libraries

The parallel finite element GgEm (pFE-GgEm) routines are built using open source libraries, thereby facilitating usage of our routines. We list the required libraries and the repositories to download our pFE-GgEm routines:

- the finite element method is built using libMesh [44] and PETSc [138, 54, 139],
- for systems with less than one million fluid degrees of freedom, we recommend a direct solver such as the distributed-memory SuperLU_Dist [135, 140, 141],
- the scalable eigenvalue calculation uses SLEPc [133],
- the pFE-GgEm routines can be downloaded at http://ime-code.uchicago.edu as part of the Continuum-Particle Simulation Suite (COPSS) from the Midwest Integrated Center for Computational Materials (MICCoM).

4.4 Results

Multiple levels of validations of our parallel finite element GgEm solver (pFE-GgEM) are in order. We start from the Stokes's solver precision and scalability, and follow with the convergence and precision of the full BD code. We will include, however, two systems that illustrate the capability of these open-source and available routines.

4.4.1 Scalability and Stokes' flow validation

Accounting for the fact that GgEm is a proven and validated method, we wish to verify that the parallel FEM solver is correct and that the scalability of the system will allow its implementation to large systems (even though we already pointed out that the pFE-GgEm method permits the study of confined, non-equilibrium systems).

We start by locating three point particles in an infinite cubic domain, the boundary of which is unconstrained, so that an analytic solution, using the free space Green's function or

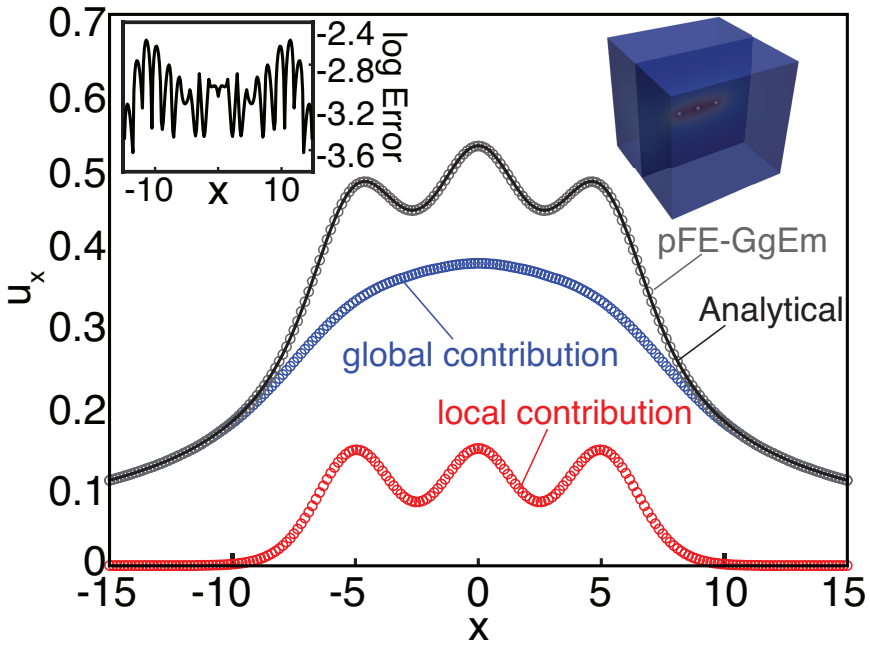

Figure 4.1: Velocity in the x–direction due to three point particles driven by point forces in a $30 \times 30 \times 30$ domain. The point-forces are located in $\mathbf{x}_1 = (-5, 0, 0)$, $\mathbf{x}_2 = (0, 0, 0)$ and $\mathbf{x}_1 = (+5, 0, 0)$, with a strength of $f_\nu = 1/3$ along the x–direction. The GgEm solution is obtained using $\alpha = 0.1$ and a global mesh of $15 \times 15 \times 15$.

Oseen tensor, is accessible. In order to make the solutions comparable, we set the exact values on the domain boundaries evaluated from the analytic method as the boundary conditions of the numerical method. It also helps to identify whether the boundary conditions for the GgEm solution are solved appropriately. The point-forces are located in $\mathbf{x}_1 = (-5, 0, 0)$, $\mathbf{x}_2 = (0, 0, 0)$ and $\mathbf{x}_1 = (+5, 0, 0)$ in a $30 \times 30 \times 30$ cube.

We used the bead hydrodynamic radius a as the characteristic length scale. The bead diffusion time $a^2\zeta/k_BT$ is the characteristic time ($\zeta = 6\pi\mu a$ is the Stokes drag coefficient); they result in a characteristic force k_BT/a and velocity $k_BT/a\zeta$. The point-forces have a strength of $f_\nu = 1/3$ along the x–direction. Figure 4.1 shows the velocity in the x–direction along centers of the beads calculated with GgEm and the analytical solution. The figure includes the GgEm local and global contributions for a solution with $\alpha = 0.1$, and a global mesh with a resolution of $1/\sqrt{2}\alpha$ ($15 \times 15 \times 15$ mesh). The inset shows the relative error between the solutions, where the maximum error is of order 10^{-2}.

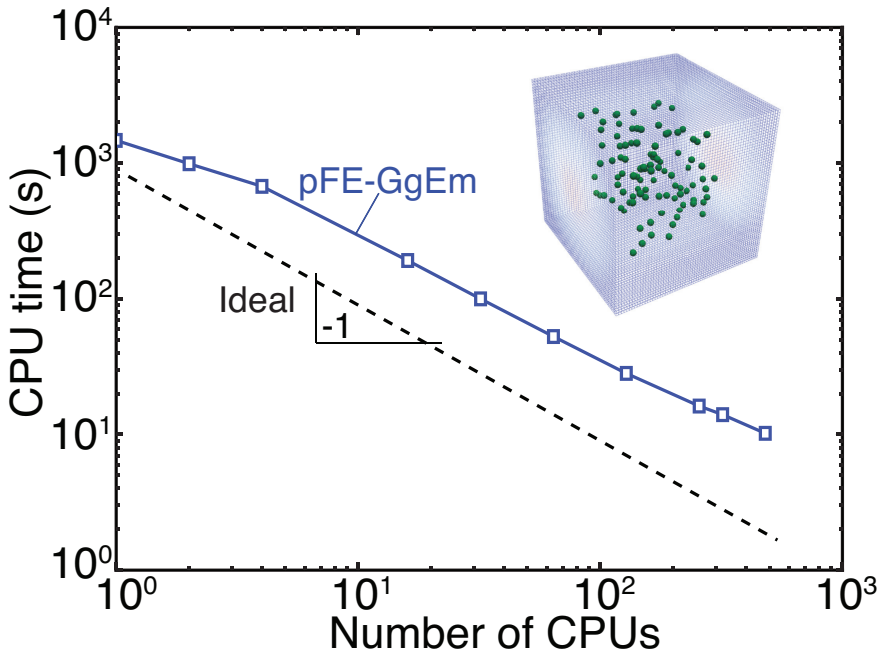

Figure 4.2: CPU scalability test on ANL's LCRC Blues supercomputer. The pFE-GgEm algorithm is used to calculate the velocity field due to 100 particles that are randomly distributed in a $30 \times 30 \times 30$ domain. For the GgEm, $\alpha = 0.1$ and the mesh is $60 \times 60 \times 60$ with HEX20 elements. The total number of degrees of freedom are approximately 2.9 million.

The parallel scalability of the pFE-GgEM algorithm is tested by placing 100 beads at random in a $30 \times 30 \times 30$ domain, using $\alpha = 0.1$ and a $1/\sqrt{2}\alpha$ mesh resolution, i.e. $60 \times 60 \times 60$ mesh. The FEM mesh results in approximately 2.9 million degrees of freedom from the $P^2 - P^1$ FEM formulation using hexahedron elements with 20 nodes (HEX20) [104]. An iterative solver described in Section 4.3.2 – (F)GMRES with a custom Schur complement-based pre-conditioner – is used to solve Stokes' equations. Simulations are carried out at ANL's LCRC Blues cluster, and the CPU time is measured as a function of the number of CPUs used for the calculation. Figure 4.2 shows the CPU time as a function of the number of CPUs for this system. As shown in the figure, the pFE-GgEm algorithm follows closely the ideal power law scaling of -1.

4.4.2 Confined DNA solutions

We now proceed to show how the pFE-GgEm algorithm translates into a full BD simulation. We start by calculating the diffusion coefficient of slit-confined DNA molecules. This simulation serves to validate the correct calculation of the diffusive terms in the stochastic differential equation. Both terms, the gradient of the diffusion tensor and the Chebyshev polynomial approximation, must be correct in order to obtain the proper diffusion coefficient and the Zimm scaling for the confined molecules.

The DNA model that we use was previously parametrized [76, 98, 142, 97]. A DNA molecule is described by a bead-spring chain composed of N_b beads, with hydrodynamic radius a, that are connected by $N_s = N_b - 1$ worm-like springs [143, 144]. The force between two connecting beads i and j is given by:

$$\mathbf{f}_{ij}^{\mathrm{wl}} = \frac{k_B T}{2b_k}\left[\left(1-\frac{r_{ij}}{q_0}\right)^{-2} - 1 + \frac{4r_{ij}}{q_0}\right]\frac{\mathbf{x}_{ij}}{r_{ij}}, \tag{4.29}$$

where $\mathbf{x}_{ij} = \mathbf{x}_j - \mathbf{x}_i$, $r_{ij} = |\mathbf{x}_{ij}|$, b_k is the Kuhn length and $q_0 = N_{k,s} b_k$ is the maximum spring length ($N_{k,s}$ is the number of Kuhn segments per spring). Consequently, the contour length of the DNA molecule is $L = N_s q_0$. A DNA chain behaves as an ideal Gaussian chain at short scales (over the Kuhn segment). Therefore, a Gaussian bead-to-bead excluded volume is used as follows [97, 142]

$$U_{ij}^{\mathrm{ev}} = \frac{1}{2}\upsilon k_B T N_{k,s}^2 \left(\frac{3}{4\pi S_s^2}\right)^{3/2} \exp\left[-\frac{3r_{ij}^2}{4S_s^2}\right] \tag{4.30}$$

where υ is the excluded volume parameter, related to the type of solvent, and $S_s^2 = N_{k,s} b_k^2/6$ is the radius of gyration of an ideal chain consisting of $N_{k,s}$ Kuhn segments.

The confining walls impose excluded volume interactions to the DNA beads. We use an

empirical bead-wall repulsive potential [76] of the type:

$$U_i^{\text{wall}} = \begin{cases} \frac{A_{\text{wall}}}{3b_k\delta_{\text{wall}}^2}\left(h-\delta_{\text{wall}}\right)^3 & \text{if } h < \delta_{\text{wall}} \\ 0 & \text{if } h \geq \delta_{\text{wall}} \end{cases} \tag{4.31}$$

where h represents the perpendicular distance between bead i and the wall, $A_{\text{wall}} = 25k_BT$ is the strength of this repulsion and $\delta_{\text{wall}} = N_{k,s}^{1/2}b_k/2$.

Following past studies [97], the model parameters used here are $a = 0.077$ μm, $b_k = 0.106$ μm, $v = 0.0012$ μm^3, and $N_{k,s} = 19.8$. Three different molecular weights are simulated, namely a 21 μm ($N_s = 10$), a 42 μm ($N_s = 20$) and a 84 μm ($N_s = 40$) long DNA molecule. The molecules are confined between two parallel walls with a separation of $H = 2$ μm between them. The domain is periodic in the non-confined directions with a 20 μm period. Ten chains were randomly distributed within the domain with a volume fraction of $\phi < 0.02\%$, to ensure that the system is in the dilute regime. The GgEm parameters are $\alpha = 0.1$ and a mesh resolution of $1/\sqrt{2}\alpha$, resulting in a $37 \times 37 \times 4$ HEX20 mesh and 89,913 degrees of freedom.

We measure the center-of-mass in–plane mean squared displacement (MSD) in order to obtain the chain diffusion coefficient, i.e. $\left\langle \Delta x_{1,\text{cm}}^2 \right\rangle + \left\langle \Delta x_{2,\text{cm}}^2 \right\rangle = 4Dt$ (see Figure 4.3). In the bulk, the diffusion coefficients of these DNA molecules are [145]: $D_{\text{bulk,21 }\mu\text{m}} = 0.53$ μm$^2/s$, $D_{\text{bulk,42 }\mu\text{m}} = 0.37$ μm$^2/s$ and $D_{\text{bulk,84 }\mu\text{m}} = 0.22$ μm$^2/s$; the radii of gyration are $R_{g,\text{bulk,21 }\mu\text{m}} = 0.594$ μm, $R_{g,\text{bulk,42 }\mu\text{m}} = 0.85$ μm and $R_{g,\text{bulk,84 }\mu\text{m}} = 1.43$ μm. Confinement and HI affect the value of the diffusion coefficient: it decreases due to the decrease of the chain mobility that is induced by the walls, and it follows a $(R_{g,\text{bulk}}/H)^{-2/3}$ [145] scaling. Figure 4.3(a) shows typical MSD curves for the different DNA chains; the corresponding diffusion coefficients are plotted as a function of the confinement in Fig. 4.3(b). The calculated diffusion coefficients are $D_{\text{slit,21 }\mu\text{m}} = 0.3395$ μm$^2/s$, $D_{\text{slit,42 }\mu\text{m}} = 0.2104$ μm$^2/s$ and $D_{\text{slit,84 }\mu\text{m}} = 0.0713$ μm$^2/s$, which are the same as those reported in previous reports [145, 97]. They follow the correct Zimm scaling [91, 129], ensuring that the "noise"

and the HI are correctly calculated.

We now proceed to illustrate how the pFE-GgEm algorithm is capable of handling a complex geometry under non-equilibrium conditions. To do this, we study the behavior of of 21 μm long DNA chains under an elongational flow within a cross-channel geometry. Figure 4.4 shows the geometry and contours of the magnitude of the imposed fluid velocity at a $z = 0$ plane. To impose the elongation, a Poiseuille flow is generated by applying a pressure gradient $\Delta P = P_{\text{in}} - P_{\text{out}}$ between the inlet and outlet boundaries. A fluid viscosity $\mu = 1$ cp is used; the strength of the flow field is characterized by a Weissenberg number $Wi = \lambda\gamma$, where λ is the longest relaxation time of the DNA chain and γ is the characteristic shear rate [95]. Three individual molecules were located near an inlet boundary, and their center of mass was then followed.

We measure the instantaneous molecular "stretch" of chain v along the y–direction, $S_{y,v}$, according to

$$S_{y,\nu} = \max(\mathbf{Y}_\nu) - \min(\mathbf{Y}_\nu), \tag{4.32}$$

where $\mathbf{Y}_\nu$ is a N_b vector with the y–Cartesian coordinates of the beads of chain $\nu = 1, ..., 3$. We plot the molecular stretch as a function of time and a reaction coordinate ϕ, defined as follows

$$\phi = \begin{cases} \frac{L_x}{2} + x_{\text{cm}} & \text{if} \quad x_{\text{cm}} \in \left[-\frac{L_x}{2}, -\frac{l_x}{2}\right] \\ \frac{L_x}{2} - x_{\text{cm}} & \text{if} \quad x_{\text{cm}} \in \left[\frac{l_x}{2}, \frac{L_x}{2}\right] \\ \frac{L_x}{2} - \frac{l_x}{2} + |y_{\text{cm}}| & \text{if} \quad x_{\text{cm}} \in \left[-\frac{l_x}{2}, \frac{l_x}{2}\right], \end{cases} \tag{4.33}$$

where $L_x = 50.82$ μm and $l_x = 5.39$ μm.

Figure 4.5 shows the instantaneous molecular stretch, along the y–direction, of the three DNA chains. Two main observations can be made from the figure. First, in the early stages ($t < 0.05$ s), the S_y values fluctuate around a value that corresponds to the initial configuration of the DNA chains. During this period, the chains are moving from the left inlet to the stagnation point under the elongational flow. Therefore, these chains are poorly

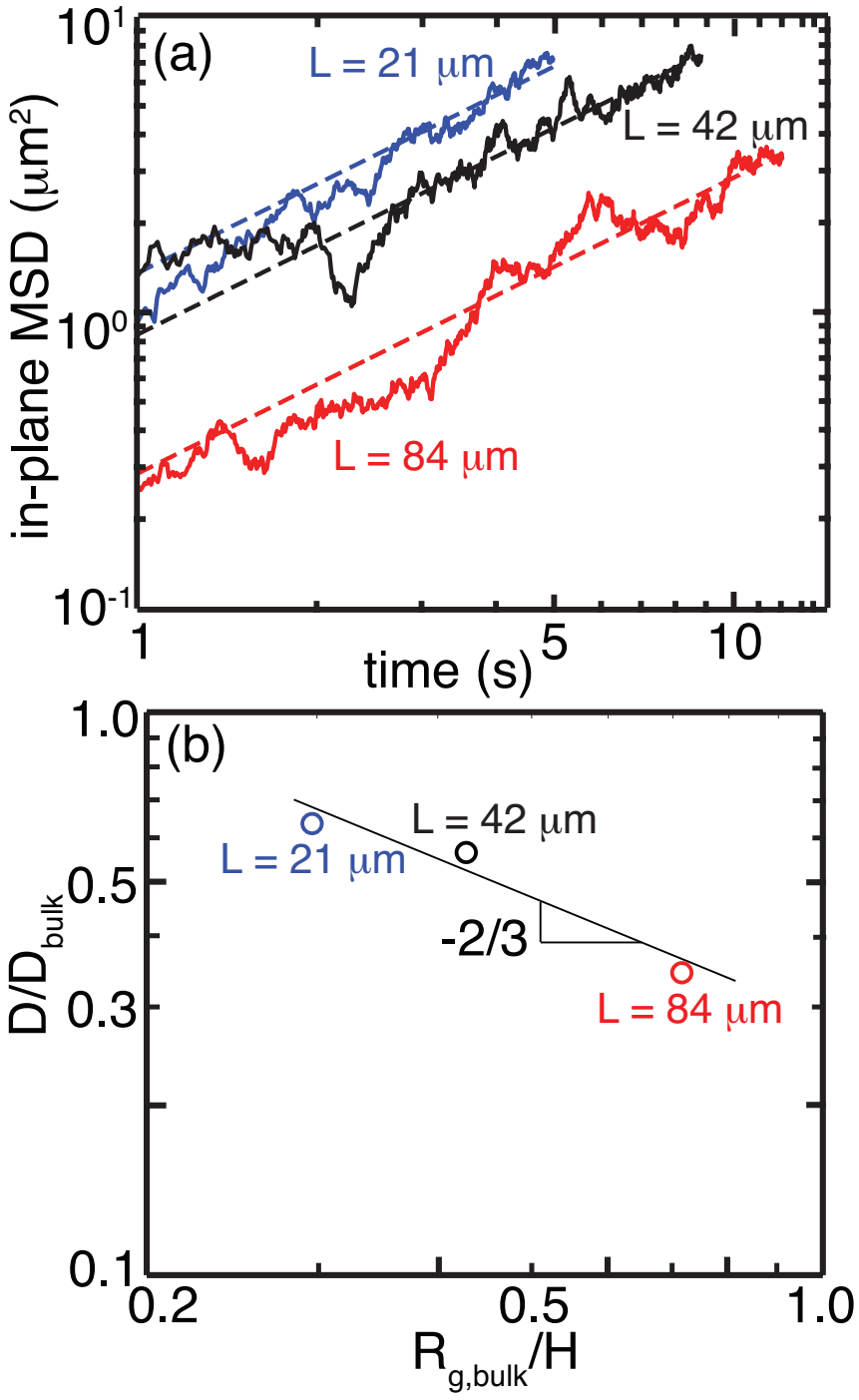

Figure 4.3: (a) Typical in-plane MSDs for DNA molecules with contour length of 21 μm, 42 μm and 84 μm confined in a slit, respectively. (b) Confined chain diffusion coefficient as a function of the confinement $R_{g,\mathrm{bulk}}/H$.

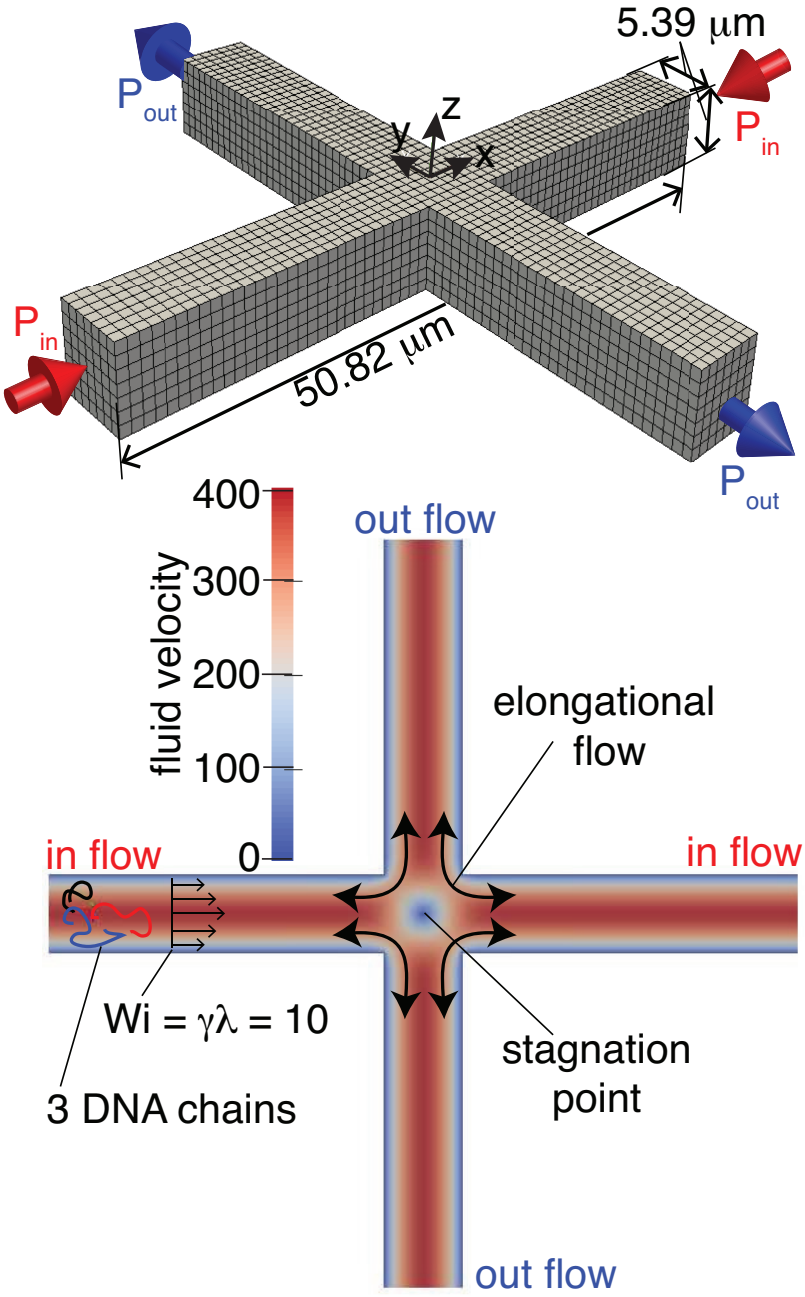

Figure 4.4: Cross-channel geometry, where a Poiseuille driven flow is generated by imposing a pressure gradient between the inlet and outlet boundaries. An elongational flow, with to $Wi = \gamma\lambda = 10$, is applied to three 21 μm long DNA chains. The fluid system for the pFE-GgEm has 180,317 degrees of freedom with $\alpha = 0.1$ and HEX20 elements under a $P^2 - P^1$ scheme. We also include the contour of the magnitude of the imposed solvent velocity, $\mathbf{u}_0$, in a $z = 0$ plane, highlighting the stagnation point.

stretched, and the fluctuations are mainly due to the Brownian motion and the HI. The stretch gradually increases to high values after a certain residency time. This maximum stretch, however, differs from chain to chain according to their positions along the flow lines. For instance, the chains represented by the black lines do not approach the stagnation point, and their elongation is low. On the other hand, blue and red chains manage to pass through the stagnation point, where the elongation is maximum, and their stretch is high. As a function of the reaction coordinate, the molecular stretch grows at approximately the same value of the reaction coordinate, namely $\phi = 23$ μm, which delimits the entrance of the "cross section". Within this section, these chains undergo a sharp velocity reduction and the transition from being elongated in the x–direction to being elongated in the y–direction.

4.4.3 Sedimentation of finite size particles: Immersed Boundary-pFE-GgEm

Our pFE-GgEm algorithm is generalizable to treat finite size particles through the Immersed Boundary (IB) method developed by Peskin [146, 66]. This generalization was applied previously by Pranay et al. [125] for a GgEm implementation that uses finite differences and fast Fourier transforms. Here, we use a IB-pFE-GgEm that can handle confined, large-scale suspensions of finite-size particles of arbitrary shape in an arbitrary geometry.

In the IB method, the force distributions at moving solids, interfaces or membranes are discretized as distributions of regularized point-forces, where the length scale for "smoothing" the delta function scales as the grid spacing used to represent the moving entities. That is, if h is a characteristic length for the node spacing or element size on the surface, then we relate this scale with the regularization scale of the GgEm, i.e. $\xi_{\text{IB}} \sim h^{-1}$. This ensures that the force density associated with each node, on the surface, is spread over the length scale of the associated elements, thereby preventing fluid from penetrating the membrane surface. Similar to conventional IB methods, in the IB-GgEm the simulation results are insensitive to the choice of the regularization parameter if $\xi h = O(1)$. Details of the IB-GgEM can be

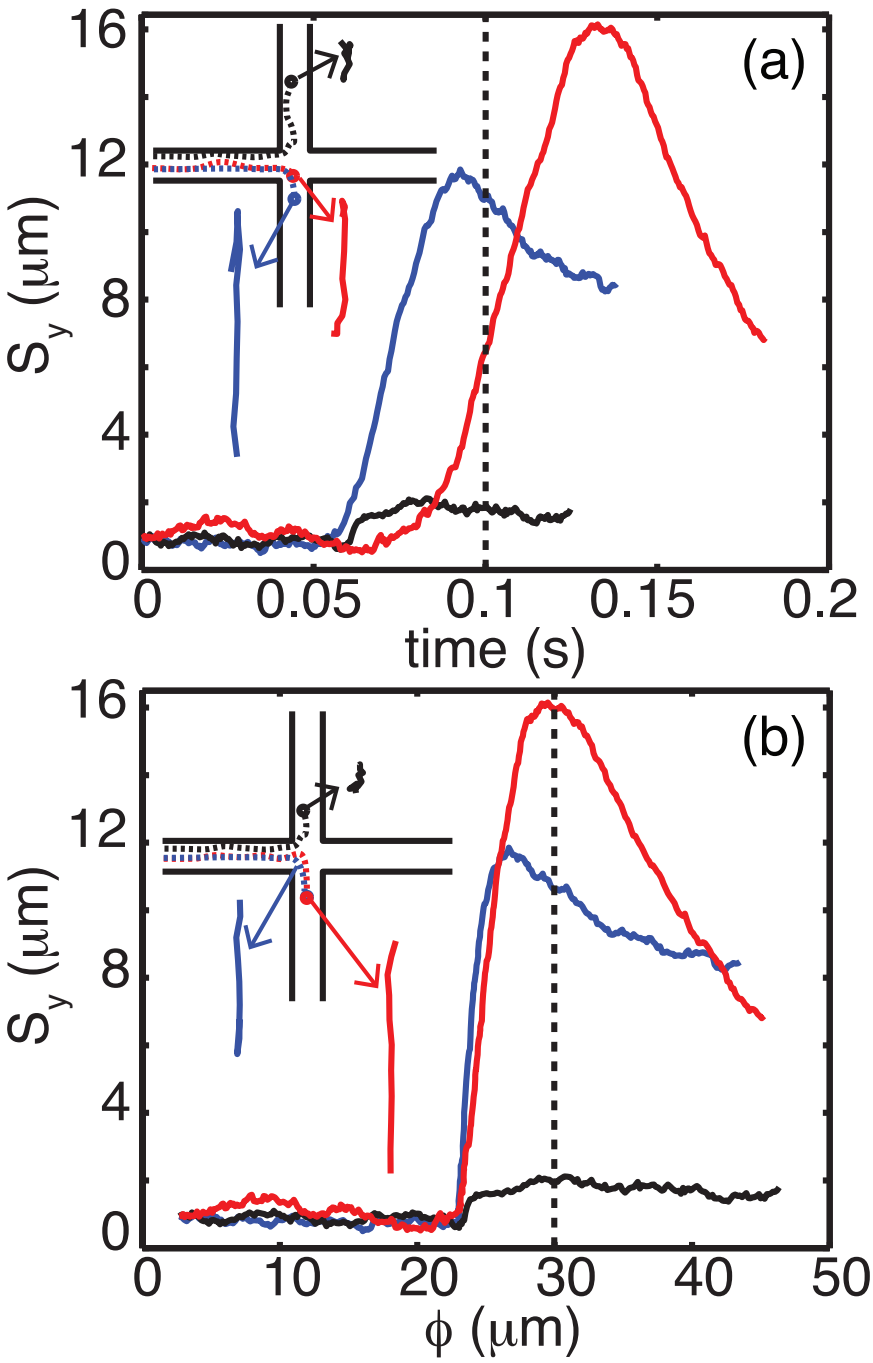

Figure 4.5: Molecular stretch in the y–direction for the three DNA chains as a function of the time and the reaction coordinate ϕ. Snapshots of typical molecular arrangements are included in the inset with their corresponding locations along the cross-channel domain.

found in the work of Pranay et. al [125]

As mentioned above, the forces exerted by a boundary immersed in a fluid are then modeled as a set of regularized point forces, just as is done in the regular GgEM. In particular:

$$\boldsymbol{\rho}^{f}_{\mathrm{IB}}(\mathbf{x}) = \sum_{\nu=1}^{N_{\mathrm{IB}}} \mathbf{f}^{\mathrm{C}}_{\nu} \delta_{\mathrm{IB}}(\mathbf{x} - \mathbf{x}_{\nu}), \tag{4.34}$$

where N_{IB} is the number of nodes (beads) that are used to represent the suspended solids, δ_{IB} is the regularization modified Gaussian that includes ξ_{IB} and $\mathbf{f}^{\mathrm{C}}_{\nu}$ is the constitutive force that is used to describe the particles. The fluid velocity field comes from the numerical solution of the Stokes' equation driven by this force density. We use the pFE-GgEm algorithm to efficiently calculate the dynamics of the particles. Recall that in traditional IB methods, the fluid mesh must be selected to resolve the ξ^{-1}_{IB} scale; using GgEm prevents this, because the fluid mesh resolves the α^{-1} scale [125], thereby increasing the performance of the algorithm.

We test the IB-pFE-GgEm approach by simulating the sedimentation of ten solid particles in a channel with rectangular symmetry. Seven cylinders and three spheres are initialized in a particular distribution, as shown in Fig. 4.6. The solids are modeled using 218 nodes for the spheres and 278 nodes for the cylinders, resulting in a total of 2,600 tracking points. The pFE-GgEm mesh, for the global contribution, has 145,696 degrees of freedom, for a $\alpha = 0.1$ and domain size of $300 \times 100 \times 100$. The node separation for the particles' surfaces are between $h_{\min} = 1.246247$ and $h_{\max} = 5.402710$; the smoothing parameter of the IB is $\xi_{\mathrm{IB}} = 1.0/0.75 h_{\min}$. We assume that the particles are "rigid", where each node point (tracking bead) on the particle is linked to its neighboring nodes by elastic springs with a prescribed large stiffness constant. In addition, all of the nodes are connected to its geometric center-of-mass point by an elastic spring. For simplicity, we assume that each link is a linear spring, and the force acting on the point i by the point j is given by

$$\mathbf{f}^{\mathrm{C}}_{ij} = k\left(r_{ij} - r_0\right)\frac{\mathbf{x}_{ij}}{r_{ij}}, \tag{4.35}$$

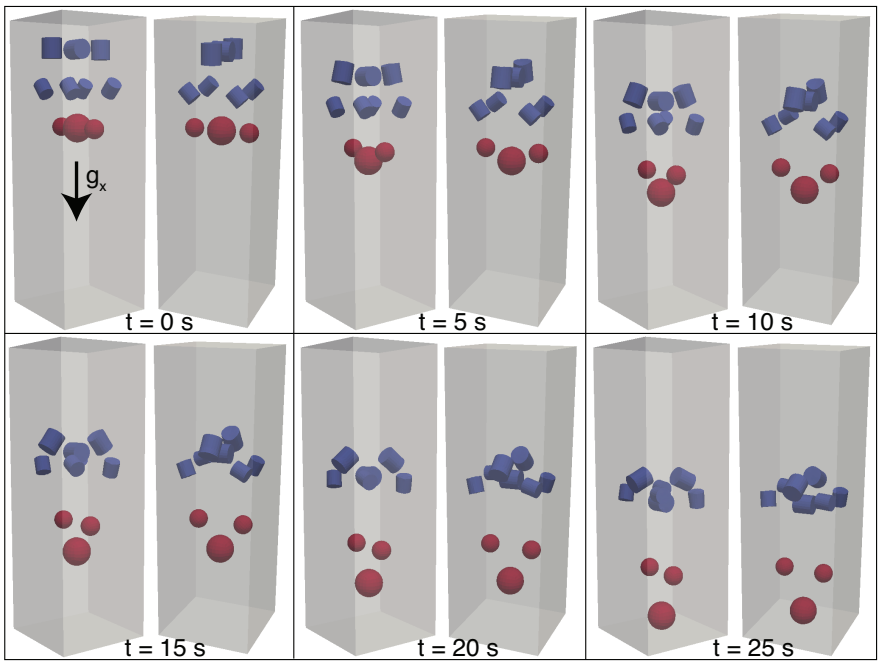

Figure 4.6: Time snapshots of ten suspended finite-size particles sedimenting in a squared channel. The simulation is done using a IB-pFE-GgEm formalism. The FEM mesh, for the global contribution, has a 145,696 degrees of freedom, for a $\alpha = 0.1$ and domain size of $300 \times 100 \times 100$. The IB particle discretization are 218 nodes for the spheres, while 278 nodes for the cylinders for a total of 2,600 tracking points. The node separation for the particles' surfaces are between $h_{\text{min}} = 1.246247$ and $h_{\text{max}} = 5.402710$; the smoothing parameter of the IB is $1.0/0.75 h_{\text{min}}$.

where k is the spring elastic constant and r_0 is the equilibrium spring size for each specific situation. For each particle, a spring network is formed, which generates the internal nodal force on each of the tracking beads to resist the deformation of the particles.

A time sequence of the particle's positions is shown in Fig. 4.6. Fluid velocity contours are also included in Fig. 4.7. One can appreciate that, as expected, particles located at the center of the channel sediment faster than those closer to the walls, due to the higher mobility, i.e. the fluid velocity is zero at the walls. The HI prevent the solids from sedimenting at the same rate, and change their relative orientation due to the different fluid resistances. The induced fluid velocity includes regions where the velocity goes against the sedimenting direction (negative values in Fig. 4.7), which is a typical characteristic of sedimenting systems [147].

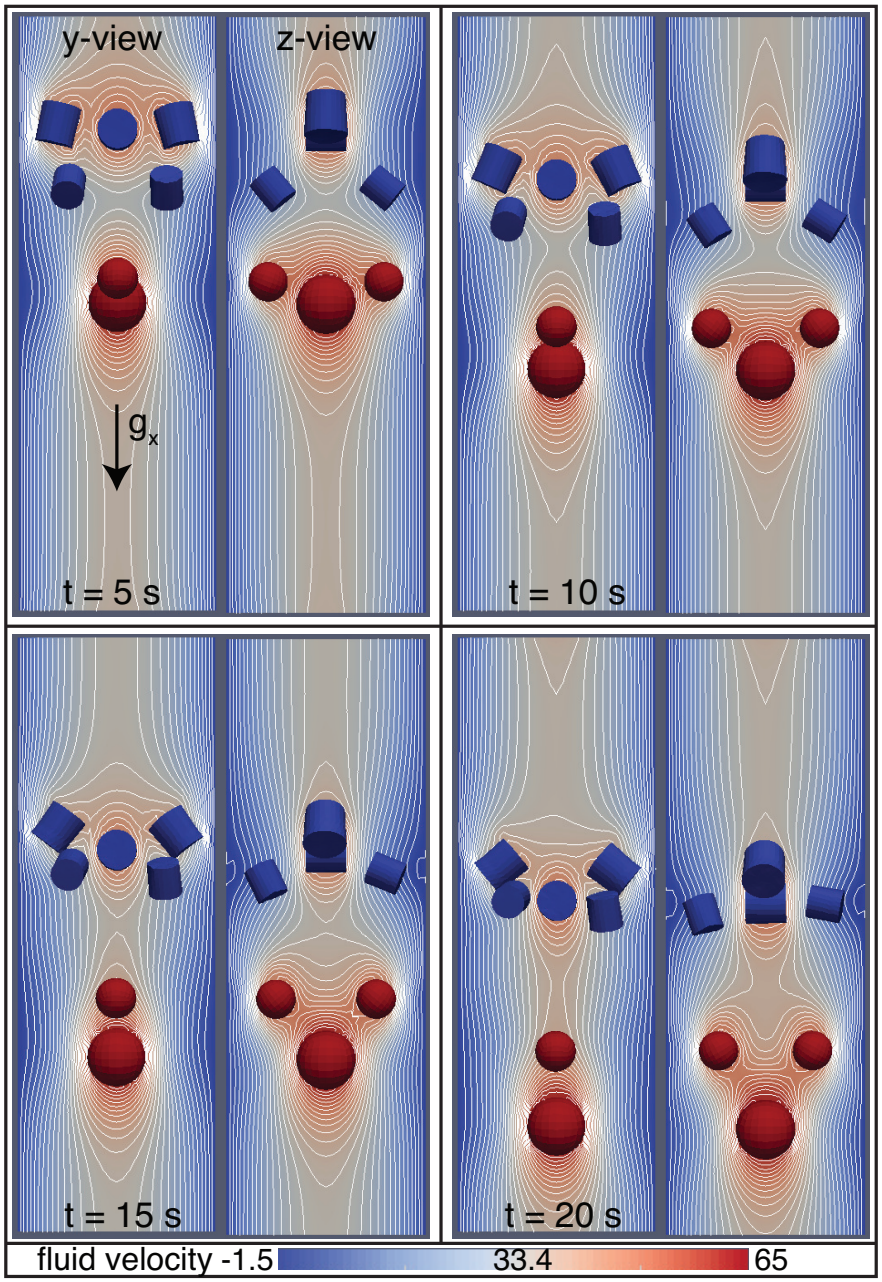

Figure 4.7: Fluid velocity contours during the sedimentation of the of ten suspended finite-size particles a squared channel. The contours represent the magnitude of the fluid velocity along the sedimentation direction. During the sedimentation, the hydrodynamic interactions induce fluid velocities in an opposite direction (dark blue colors). Solids near the center of the channel sediment at a faster rate than the solids near the walls.

4.5 Conclusions

We have developed an efficient $O(N)$ computational approach to model the dynamics of hydrodynamically interacting Brownian or micron-sized particles in arbitrary geometries. A parallel finite element Stokes' solver is the center of the algorithm. Once it is combined with the General geometry Ewald-like method (GgEm), a mid-point time integration scheme and a Chebyshev polynomial approximation, for the fluctuation-dissipation theorem, results in an scalable algorithm - the pFE-GgEm algorithm. The approximations within these methods reduce the precision on the fluctuation-dissipation theorem. However, the Chebyshev approximation has been used extensively in confined and unconfined systems and its performance is excellent. On the other hand, GgEm resolves Stokes equations with satisfactory precision. In particular, a 10% tolerance in the Chebyshev polynomial approximation and a proper selection of the GgEm alpha and mesh parameters result in the correct diffusion regime and diffusivities within a 5% error of the analytical or experimental values. In conclusion, it is always better to sacrifice the precision than the computational performance, i.e. N^3 [148] vs $NlogN$ or N. The finite element formulation in pFE-GgEm has a distributed memory parallelization, that may use a direct LU analytical solver or a fast parallel iterative solver with pre–conditioning.

The pFE-GgEm algorithm shows excellent parallel performance (linear) as a function of the number of CPUs. We validated the algorithm by comparing its solutions to theoretical solutions in a simple geometry (for the Stokes' solver), and by calculating the diffusion coefficients of slit-confined DNA molecules (for the mid-point scheme, eigenvalues of the diffusion tensor and the Chebyshev polynomial approximation).

It was also shown that the pFE-GgEm algorithm is capable of handling complex geometries under non-equilibrium conditions by studying the behavior of DNA chains under an elongational flow in a cross-channel geometry. Finally, the proposed algorithm was combined with the Immersed Boundary method, the IB-pFE-GgEm approach, to simulate finite-size particles of arbitrary shape in any geometry. To illustrate the use of IB-pFE-GgEm, we

presented results for the sedimentation of solid particles in a rectangular channel.

We stress that the proposed algorithms are built on top of open-source libraries, such as libMesh (a framework for parallel mesh management and FEM discretization of PDEs), PETSc (parallel linear and non-linear equation solvers) and SLEPc (eigenvalue calculations). We have provided convenient interfaces and building blocks for computational researchers that will facilitate implementations of our routines in available BD simulation codes.

CHAPTER 5

NUMERICAL APPROACH: A HYBRID FINITE-DIFFERENCE-FINITE-ELEMENT APPROACH TO THE POISSON-NERNST-PLANCK-STOKES EQUATION

5.1 Abstract

Classical Poisson-Boltzmann theory breaks down when the characteristic length of a confined system is comparable to the thickness of the diffusion layer, and thus fails to describe the complete electrostatic profiles of extremely confined systems. Relying on a hybrid Finite-Different-Finite-Element-method, we derive an efficient numerical approach to solve the electrostatic and hydrodynamic interactions for systems composed of discrete charged objects suspended in confined ionic solutions. The validity and accuracy of the method are then established by comparing its predictions to both analytic and other numerical solutions. The numerical framework will enable the study of electrokinetic phenomena in extremely confined systems.

5.2 Introduction

With the fast advancement of fabrication technology, nanofluidics have attracted growing interest in many applications, such as salinity gradient power generation [149, 150, 151, 152], single-molecule analysis and manipulation of DNA [153, 154], and nanoparticle detection [155], etc. Nanofluidics are usually referred to devices whose one or more dimensions are less than 100 nm [156] and thus fluids are confined to volumes smaller than their characteristic scaling lengths. Under such confinement, the electrokinetic motions of charged nanoparticles and the surrounding ionized liquids behave drastically different from those in microchannels and give rise to fascinating electrokinetic phenomena that remain poorly understood [157, 158, 159].

The common challenge to understand the electrokinetic phenomena computationally in nanofluidic devices is a proper theoretical approach that resolves the dynamics of both fluid and charged species over a wide range of time and length scales [123]. For example, typical ion radius is in the order of 1 $\mathring{A}$ while the length scale for nanoparticles of interest could be in the order of 10 nm. Conventionally, Poisson-Boltzmann equation is usually used to calculate the electric potential and Helmholtz-Smoluchowski theorem is commonly utilized to model the electroosmotic flow within microfluidics [160]. And these methods are based on assumptions of thin electric double layer (EDL) and equal number of co-ions and counterions in the bulk. However, these methods are no longer valid to describe the electrokinetic phenomena in nanofluidics because, in these systems, the thickness of EDL is comparable to the channel size in the confined dimension and leads to imbalanced co- and counter ions[161]. A few attempts have been taken to resolve these problems. Qian and Aluru proposed a modified Poisson-Boltzmann equation based on the electrochemical potential correction extracted from ion distributions in a smaller channel using molecular dynamics (MD) to account for ion-wall and ion-solvent interactions. Using this hybrid approach, they are able to predict ion distributions in larger channels with good accuracy [162, 163]. However, their method are not applicable to systems with nanoparticles and the MD approach may be too expensive to be practical for large systems. Movahed and Li proposed to directly solve the Poisson equation for electrostatic potential, the Navier-Stokes equations for fluid velocity and the Nernst-Planck equation for ion concentration [161, 164, 165]. However, their model neglected the Brownian motion of nanoparticles and their implementation were limited to small systems since they relied on the conventional finite-element solver supported by COMSOL. In this chapter, we propose a hybrid finite-difference-finite-element method (FD-FEM) as well as an efficient implementation to resolve these issues.

5.3 Models and methods

The system considered in this chapter consists of N_p discrete charged particles, with valence z_i and hydrodynamic radius a for the i-th particle, suspended in a solution that includes N_{ion} continuum ion species with diffusion coefficient D_j, valence z_j and concentration c_j for the j-th ion species. The proposed mathematical model resolves the dynamical coupling of discrete charged particles and continuum electrolytes.

Dynamics of the discrete charged particles follow the stochastic differential equation Eq. 4.3. As discussed in Section. 4.3, a mid-point integration scheme and the Chebyshev polynomial approximation can be used to avoid the explicit calculation of the mobility tensor $\mathbf{M}$ and its derivative $\frac{\partial \mathbf{M}}{\partial \mathbf{R}}$. The key to this procedure eventually collapses to resolving the velocity field, $\mathbf{U}$, from the Stokes equation (see Eq. 4.4) with the corresponding force density $\mathbf{F}$. Using the pFE-GgEm approach described in Section. 4.3.1, one can resolve the global and local velocity field from the global and local force density respectively. For the model considered here, the "local" force density is

$$\boldsymbol{\rho}_l^f(\mathbf{x}) = \sum_i^{N_p} [g_H(\xi_H, |\mathbf{x} - \mathbf{x}_i|) - g_H(\alpha_H, |\mathbf{x} - \mathbf{x}_i|)]\mathbf{f}_i, \tag{5.1}$$

while the "global" density is given by

$$\boldsymbol{\rho}_g^f(\mathbf{x}) = \sum_i^{N_p} g_H(\alpha_H, |\mathbf{x} - \mathbf{x}_i|)\mathbf{f}_i + eN_A \sum_j^{N_{\text{ion}}} z_j C_j(\mathbf{x})\mathbf{E}(\mathbf{x}), \tag{5.2}$$

where $\mathbf{f}_i$ is the total non-hydrodynamic and non-Brownian force exerts on the i-th discrete charged particle, $g_H(\alpha, \mathbf{x})$ is a modified Gaussian for the point-force (Hydrodynamics),

$$g_H(\alpha, r) = \frac{\alpha^3}{\pi^{(3/2)}} e^{(-\alpha^2 r^2)} [\frac{5}{2} - \alpha^2 r^2], \tag{5.3}$$

α_H is the GgEm parameter for the point-force, $\xi_H = \sqrt{\pi}/3a$ is the regularization param-

eter for the point-force and $\mathbf{E}(\mathbf{x})$ is the electric field induced by discrete charged particles, continuum ions and external electric field if existed (see Section 5.3.1).

The evolution of the continuum ions has to follow the momentum and mass balances, resulting in a convection-diffusion equation for the j-th ion species:

$$\frac{\partial C_j}{\partial t} = -\nabla \cdot \mathbf{j}_j \tag{5.4}$$

The total flux of the j-th ion species, $\mathbf{j}_j$, is defined as a sum of convection and diffusion fluxes. The latter are given by the Nernst-Planck diffusion, resulting in

$$\mathbf{j}_j = \mathbf{v}C_j - D_j[\nabla C_j + \frac{z_j e}{k_B T} C_j \nabla \Phi], \tag{5.5}$$

where $\mathbf{v}$ is the fluid velocity and Φ is the electrostatic potential induced by discrete charged particles, continuum ions and external electric field if existed (see Section 5.3.1). Combining Eq. 5.4 and Eq. 5.5, one can reach the Poisson-Nernst-Planck-Stokes (**PNP-Stokes**) equation (notice that $\nabla \cdot \mathbf{v} = 0$ for incompressible flow),

$$\frac{\partial C_j}{\partial t} = -\mathbf{v} \cdot \nabla C_j + D_j \nabla^2 C_j + D_j z_j e/(k_B T)[C_j \nabla^2 \Phi + \nabla C_j \cdot \nabla \Phi], \tag{5.6}$$

where k_B is Boltzmann's constant and T is the absolute temperature. In the rest of this Section, we will first discuss how to resolve the total electrostatic potential Φ (see Sec. 5.3.1) and then present a hybrid approach of finite-difference and finite-element method to evolve Equation. 5.6 (see Sec. 5.3.2).

5.3.1 Nernst-Planck-GgEm for continuum salt model

The electrostatic potential, $\Phi(\mathbf{x})$, is given by the poisson equation

$$\nabla^2 \Phi(\mathbf{x}) = -\frac{\rho(\mathbf{x})}{\epsilon_0 \epsilon}, \tag{5.7}$$

where ϵ_0 is the vacuum permmitivity, ϵ is the solvent relative permittivity, and $\rho(\mathbf{x})$ is the total charge density contributed by both continuum ions and discrete charged particles. The latter are considered as "regularized" point charges, where the charge density is distributed through a Gaussian function,

$$g_E(\xi_E, \mathbf{x}) = \frac{\xi_E^3}{\pi^{3/2}} \exp(-\xi_E^2 |\mathbf{x}|^2) \tag{5.8}$$

where $\xi_E = 3/a$ ensures the total charge of a particle is distributed throughout itself. The resulting total charge density is given by

$$\rho(\mathbf{x}) = \sum_{i=1}^{N_p} e z_i g_E(\xi_E, \mathbf{x} - \mathbf{x}_i) + \sum_{j=1}^{N_{\text{ion}}} e N_A z_j C_j(\mathbf{x}), \tag{5.9}$$

where N_A is Avogadro's number. Similar to the GgEm method applied to the Stokes problem (see Section 4.3.1), the total charge density is decomposed to a local (free-space) contribution and a global (bounded) contribution. The idea is that, given that Poisson's equation is linear, summation of the resulting local and global electrostatic potential is equivalent to the total electrostatic potential, i.e.,

$$\Phi(\mathbf{x}) = \Phi_l(\mathbf{x}) + \Phi_g(\mathbf{x}). \tag{5.10}$$

The local charge density is given by

$$\rho_l(\mathbf{x}) = \sum_{i=1}^{N_p} e z_i [g_E(\xi_E, \mathbf{x} - \mathbf{x}_i) - g_E(\alpha, \mathbf{x} - \mathbf{x}_i)], \tag{5.11}$$

where $g_E(\alpha, \mathbf{x})$ is a smoothing function that "screens" the local contribution over a distance of $1/\alpha$ and must satisfy the condition $\int_{\text{all space}} g_E(\alpha, \mathbf{x}) d\mathbf{x} = 1$. The most common selection for g_E is a Gaussian function

$$g_E(\alpha, \mathbf{x}) = \frac{\alpha^3}{\pi^{3/2}} \exp(-\alpha^2 |\mathbf{x}|^2). \tag{5.12}$$

The local electrostatic potential induced by this local charge density can be resolved analytically ignoring the walls,

$$\Phi_l(\mathbf{x}) = \sum_{i=1}^{N_p} e z_i G_l^R(\mathbf{x} - \mathbf{x}_i), \tag{5.13}$$

where $G_l^R(\mathbf{x})$ is the free-space Green's function for the Poisson's equation with the charge density defined as Eq. 5.11:

$$G_l^R(\mathbf{x}) = \frac{1}{4\pi\epsilon_0\epsilon}[\frac{\mathrm{erf}(\xi_E|\mathbf{x}|)}{|\mathbf{x}|} - \frac{\mathrm{erf}(\alpha|\mathbf{x}|)}{|\mathbf{x}|}]. \tag{5.14}$$

In practice, we only need to consider the neighboring discrete charged particles of local $\mathbf{x}$ to resolve the local electrostatic potential at $\mathbf{x}$. On the other hand, the global charge density is given by

$$\rho_g(\mathbf{x}) = \sum_{i=1}^{N_p} e z_i g_E(\alpha, \mathbf{x} - \mathbf{x}_i) + \sum_{j=1}^{N_{\mathrm{ion}}} e N_A z_j C_j(\mathbf{x}), \tag{5.15}$$

The global electrostatic potential is obtained numerically by Solving the Poisson's equation

$$\nabla^2 \Phi_g(\mathbf{x}) = -\frac{\rho_g(\mathbf{x})}{\epsilon_0\epsilon}. \tag{5.16}$$

This requires that $\Phi_l + \Phi_g$ satisfies the appropriate boundary conditions. For example, a Dirichlet boundary condition, where the electrostatic potential at a wall is given by $\Phi(\mathbf{x}_W)$, results in a boundary condition for the global contribution $\Phi_g(\mathbf{x}) = \Phi(\mathbf{x}_W) - \Phi_l(\mathbf{x})$ for $\mathbf{x} \in \mathbf{x}_W$. Several techniques (finite differences, finite elements, spectral methods) can be used to find the global contribution. In this work, finite element method is employed for its ability to handle complex geometries and boundary conditions. Once the global solution on mesh is resolved, interpolation is used to get the value of global electrostatic potential at any position $\mathbf{x}$.

5.3.2 A hybrid Finite-Difference-Finite-Element approach

For a system of interest, Eq. 5.6, Eq. 4.4 and Eq. 5.7 are coupled and need to be resolved together. The characteristic variables for the system can be set by the discrete charged particles: hydrodynamic radius, a for length, particle diffusion time, $6\pi\eta a^3/(k_BT)$, for time, $e/(4\pi\epsilon_0\epsilon a)$ for electrostatic potential, e/a^3, for volume charge density, velocity fluctuation, $k_BT/(6\pi\eta a^2)$ for velocity, M (molar) for ion concentration and $k_BT/(6\pi\eta a)$ for diffusion coefficient. With these characteristic variables, the governing equations are reduced to their non-dimensionless forms respectively,

$$-\nabla p + \frac{1}{6\pi}\nabla^2\mathbf{u} = -\boldsymbol{\rho}^f, \tag{5.17}$$

$$\nabla\cdot\mathbf{u} = \mathbf{0}, \tag{5.18}$$

$$\nabla^2\Phi(\mathbf{x}) = -4\pi\rho(\mathbf{x}), \tag{5.19}$$

$$\frac{\partial c_j}{\partial t} = D_j\nabla^2 c_j - \mathbf{v}\cdot\nabla c_j + D_j z_k\lambda_B/a[c_j\nabla^2\Phi + \nabla c_j\cdot\nabla\Phi], \tag{5.20}$$

where $\lambda_B = e^2/(4\pi\epsilon_0\epsilon k_BT)$ is the so-called Bjerrum length which defines the ratio between electrostatic force and thermal forces. A semi-implicit Euler time integration scheme is used to evolve the Nernst-Planck equation Eq. 5.20, where the Crank-Nicolson method is employed for the linear Laplacian operator and the nonlinear terms are considered explicitly

$$\frac{c_k^{t+\Delta t} - c_k^t}{\Delta t} = \frac{1}{2}D_k[(\nabla^2 c_k)^{t+\Delta t} + (\nabla^2 c_k)^t] + [-\mathbf{v}\cdot\nabla c_k]^t + \frac{\lambda_B D_k z_k}{a}[c_k\nabla^2\Phi + \nabla c_k\cdot\nabla\Phi]^t. \tag{5.21}$$

Rearrange the equation, one can get

$$[c_k - \frac{1}{2}D_k\Delta t\nabla^2 c_k]^{t+\Delta t} = [c_k + \frac{1}{2}D_k\Delta t\nabla^2 c_k - \Delta t\mathbf{v}\cdot\nabla c_k + \frac{\lambda_B D_k z_k\Delta t}{a}(c_k\nabla^2\Phi + \nabla c_k\cdot\nabla\Phi)]^t. \tag{5.22}$$

Then we follow a Finite-element method (FEM) to resolve ion concentration c_k at $t + \Delta t$ using Eq. 5.22 at given ion concentration c_k, electrostatic potential Φ and velocity field $\mathbf{u}$ at t. The weakform of such FEM scheme is given by

$$
\begin{aligned}
[\int_\Omega \{\mathbf{N}^T\mathbf{N}dv + \frac{1}{2}D\Delta t \int_\Omega \nabla\mathbf{N}^T \cdot \nabla\mathbf{N}\}dv]\mathbf{c}_{nn*1} = \int_\Omega \{ & c^t\mathbf{N}(\text{mass}) \\
& + \frac{1}{2}D\Delta t(-(\nabla c)^t \cdot \nabla\mathbf{N})(\text{diffusion}) \\
& - \Delta t(\mathbf{v}^t) \cdot \nabla\mathbf{N} \cdot \mathbf{N}(\text{convection}) \\
& + \frac{\lambda_B \cdot D \cdot z \cdot \Delta t}{a}((c^t \cdot \nabla^2\Phi)^t \\
& + (\nabla c)^t \cdot (\nabla\Phi)^t) \cdot \mathbf{N}\}dv(\text{electrostatics}).
\end{aligned}
$$

The solution, $c_k^{t+\Delta t}$, to Eq. 5.22 will then contribute to the global charge density (Eq. 5.15) and the global force density (Eq. 5.2) at time $t+\Delta t$, thus leading to impact on the electrostatic potential, $\Phi^{t+\Delta t}$ and the velocity field $\mathbf{u}^{t+\Delta t}$. The hybrid finite-difference-finite-element approach can be summarized as follows:

Algorithm 1: Hybrid Finite-Difference-Finite-Element Algorithm

initialization:

- $R_i^{t=0}(i = 1, ..., N_p)$: coordinates of all discrete charged particles
- $c_j^{t=0}(\mathbf{x})(j = 1, ..., N_{\text{ion}})$: ion concentration of all ion species at all mesh nodes
- $\Phi^{t=0}(\mathbf{x})$: electrostatic potential at all mesh nodes

(**Relaxation:**)

while $t < t_{relax}$ **do**

Solve Eq. 5.22 for all $j = 1, ..., N_{\text{ion}}$ with $\mathbf{v} = \mathbf{0}$: get $c_j^{t+\Delta t}$;

Solve Eq. 5.19: get $\Phi^{t+\Delta t}$;

$t = t + \Delta t$;

end

(**Time integration:**)

Reset $t = 0$;

while $t < t_{final}$ **do**

Solve Eq. 5.22 for all $j = 1, ..., N_{\text{ion}}$: get $c_j^{t+\Delta t}(j = 1, ..., N_{\text{ion}})$;

Solve Eq. 5.19: get $\Phi^{t+\Delta t}$, $\mathbf{E}^{t+\Delta t}$;

Solve Eq. 5.17: get $\mathbf{u}^{t+\Delta t}$;

Solve Eq. 4.3: get $R_i^{t+dt}(i = 1, ..., N_p)$;

$t = t + \Delta t$

end

5.4 Results

5.4.1 Accuracy and efficiency of the GgEm-accelerated Poisson's solver

Similar to the validation for the GgEm-accelerated Stokes' solver (see Sec. 4.4.1), we start by comparing the solution from the GgEm-accelerated Poisson's solver with analytic solutions. To do this, we locate three discrete charged particles in an infinite cubic domain with the

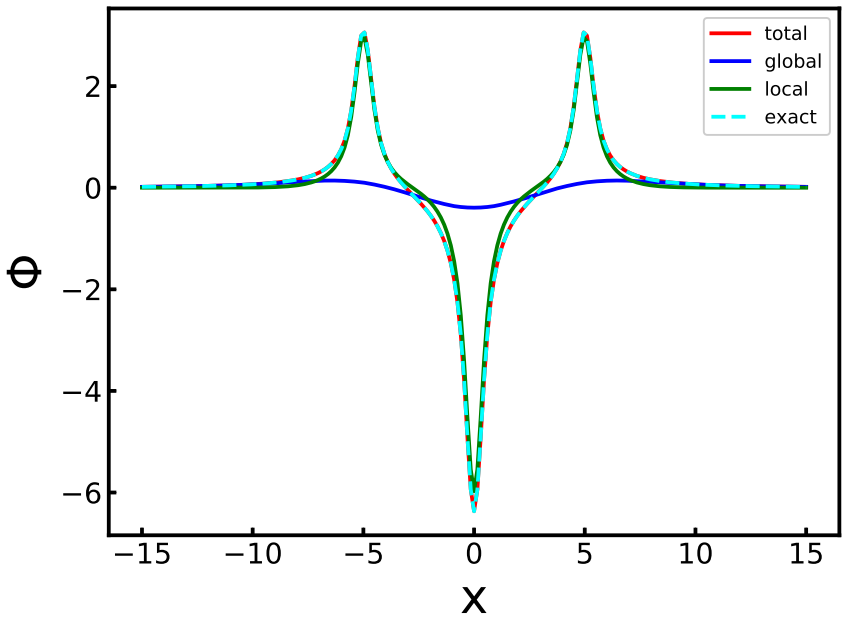

Figure 5.1: Electrostatic potential along centers of discrete point charges in a 30 x 30 x 30 domain. The point charges are located in $x_1 = (-5, 0, 0)$ $(Q_1 = +1)$, $x_2 = (0, 0, 0)$ $(Q_2 = -2)$ and $x_3 = (+5, 0, 0)$ $(Q_3 = +1)$. The GgEm solution is obtained using $\alpha = 0.35$ and a global mesh of 15 x 15 x 15.

absence of continuum ions. The boundaries of the domain are unconstrained so that the analytic solution, calculated using the free space Green's function, is accessible. In order to make the solutions comparable, we set the analytic solution on the boundaries as the boundary conditions of our numerical Poisson's solver. It also helps to identify whether the boundary conditions are satisfied appropriately in the numerical solver. In dimensionless unit defined in Sec. 5.3.2, the point-charges are located in $x_1 = (-5, 0, 0)$ $(Q_1 = +1)$, $x_2 = (0, 0, 0)$ $(Q_2 = -2)$ and $x_3 = (+5, 0, 0)$ $(Q_3 = +1)$ in a $30 \times 30 \times 30$ cube.

Figure 5.1 shows the electrostatic potential along centers of the discrete charges calculated by the GgEm-accelerated Poisson's solver and by the analytic solution. For the numerical solver, the total solution is the sum of the local solution calculated using $\alpha = 0.35$ and the global solution calculated using a mesh with the resolution of $15 \times 15 \times 15$. The result shows that the total solution overlaps with the analytic solution well. The first- and second-order spacial gradients of the electrostatic potential are required in the Nernst Planck equation,

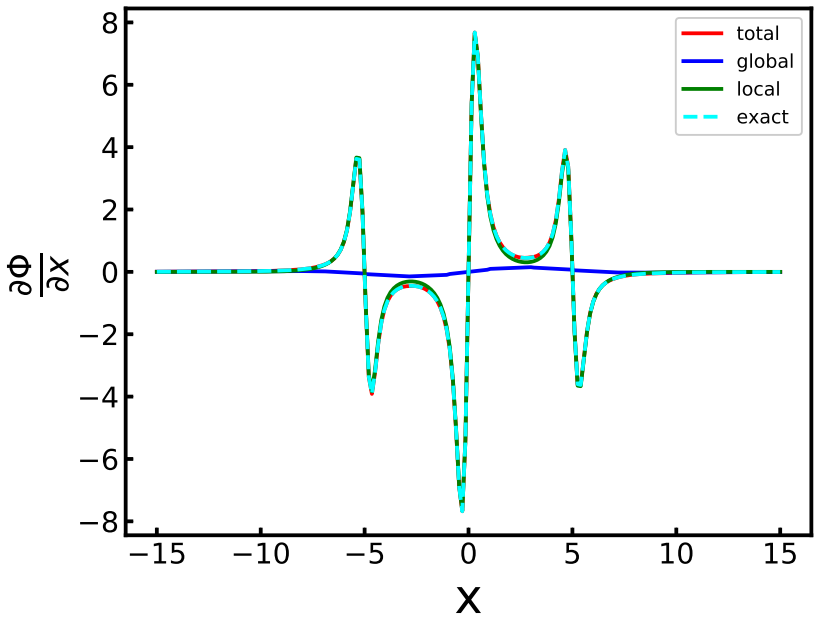

Figure 5.2: First–order gradient of the electrostatic potential in Fig. 5.1.

Eq. 5.20, and thus need to be validated as well. Figure 5.2 shows the x-direction gradient of the electrostatic potential, i.e., negative electric field in the x-direction, and Figure 5.3 shows the second order gradient, i.e., Laplacian of the electrostatic potential, along centers of the discrete charges. The results verify that both the first- and second-order gradients of the electrostatic potential are correctly recovered by the GgEm-accelerated Poisson's solver.

The efficiency of the Poisson's solver is examined by comparing its accuracy and speed with the commercial software, COMSOL [**?**], in solving the same benchmark system. The benchmark system has two discrete point charges in a cubit domain of size $20 \times 20 \times 10$. The electrostatic potential on domain boundaries are set to be zero and the point charges are placed in $x_1 = (-2, 0, 0)$ $(Q_1 = 1)$ and $x_2 = (2, 0, 0)$ $(Q_2 = -1)$. Figure 5.4 shows the electrostatic potential solved by COMSOL using meshes of different resolution. The most coarse mesh leads to a degree of freedom (DOF) of 18501 and the finest mesh used leads to a DOF of 85715. The result shows that the solution associated with a coarse mesh (low DOF) has nontrivial errors, especially near the point charges. This is as expected since traditional FEM requires fine space discretization near the charge source. Figure 5.5 shows

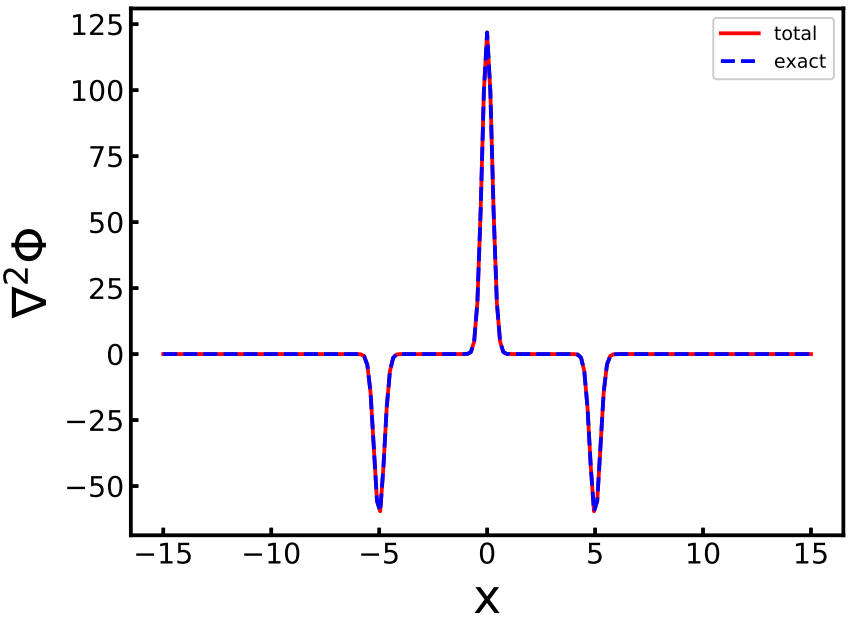

Figure 5.3: Second-order gradient of the electrostatic potential in Fig. 5.1.

the electrostatic potential solved by the GgEm-accelerated Poisson's solver using meshes of different resolution. The minimum mesh size, L_{min}, satisfies $L_{\text{min}} <= 1/\sqrt{2}\alpha$. The result shows that the numerical solver is insensitive to the global mesh as long as α is chosen appropriately. Consequently, the numerical Poisson's solver can resolve the electrostatic potential accurately, even near the point charges (see the inset figure in Figure 5.5), with significantly coarser mesh than COMSOL, and thus requires less computational power.

We continue our analysis by comparing the solving time of COMSOL and the GgEm-accelerated Poisson's solver for the benchmark system above. Figure 5.6 shows that, for both solvers, the solving time increases linearly with the DOF. However, the computation time of the GgEm-accelerated solver is two orders less than that of COMSOL for the same DOF. This, together with the observation that the GgEm-accelerated Poisson's solver requires much less DOF to resolve the Poisson system accurately, shows the remarkable efficiency of the GgEm-accelerated Poisson's solver.

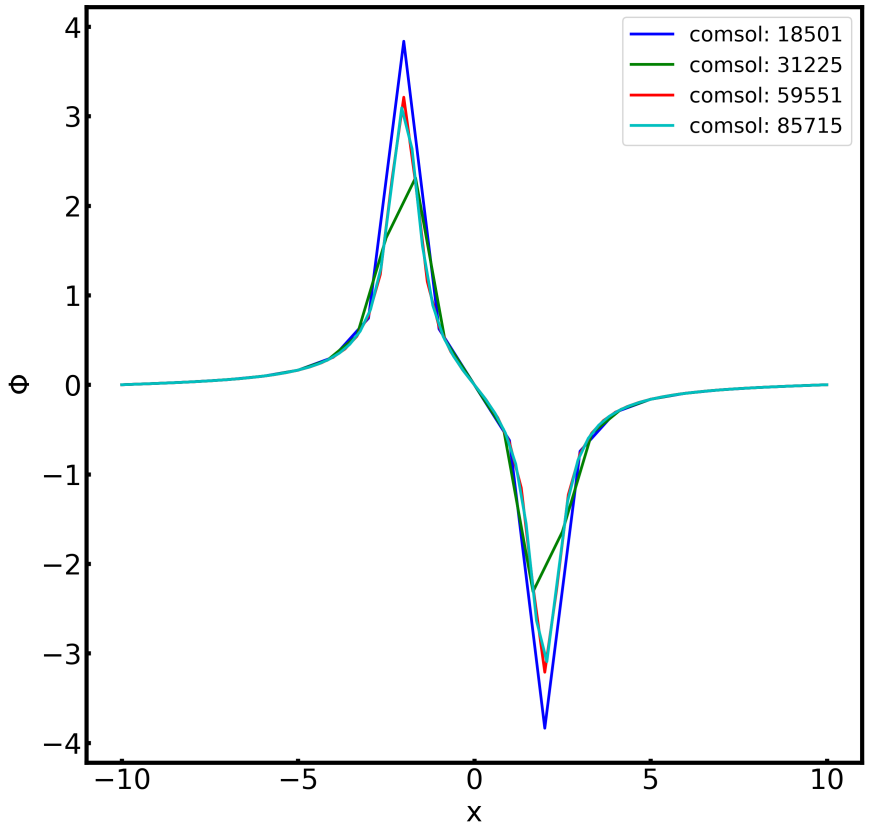

Figure 5.4: Electrostatic potential along centers of discrete point charges in a 20 x 20 x 10 domain with zero potential on boundaries solved by COMSOL using different meshes. The point charges are located in $x_1 = (-2, 0, 0)$ ($Q_1 = +1$) and $x_2 = (+2, 0, 0)$ ($Q_2 = -1$).

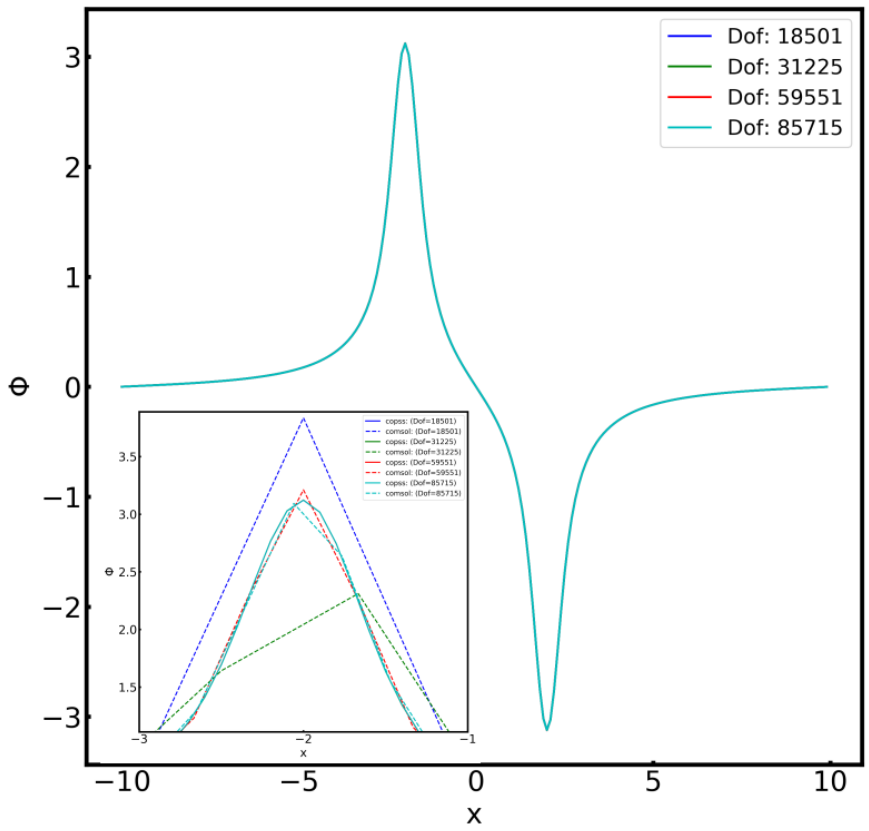

Figure 5.5: Electrostatic potential along centers of discrete point charges in a 20 x 20 x 10 domain with zero potential on boundaries solved by the NP-GgEm solver using different meshes for the global solution and corresponding α for the local solution. The point charges are located in $x_1 = (-2, 0, 0)$ ($Q_1 = +1$) and $x_2 = (+2, 0, 0)$ ($Q_2 = -1$). The inset figure compares the potential around the point charge at $x_1 = (-2, 0, 0)$ solved by COMSOL and NP-GgEm using different meshes.

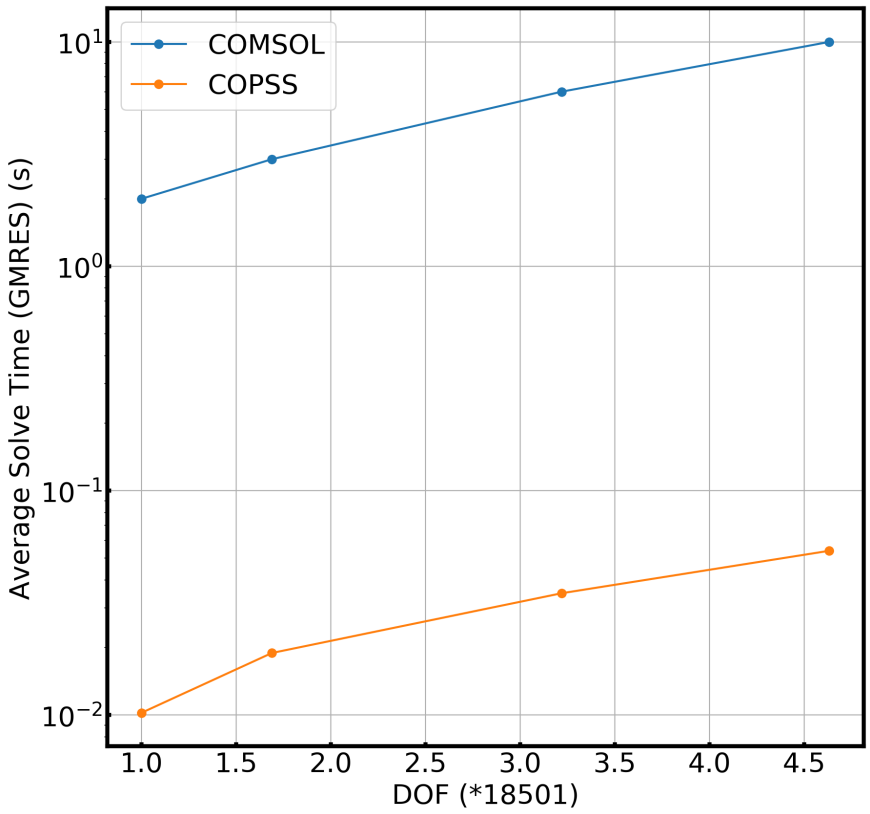

Figure 5.6: Average solving time of the Poisson system using COMSOL and NP-GgEM using different meshes. Tests are performed on Intel(R) Core(TM) i7-4790 CPU@3.60GHZ with 8 Cores and 16G Memory.

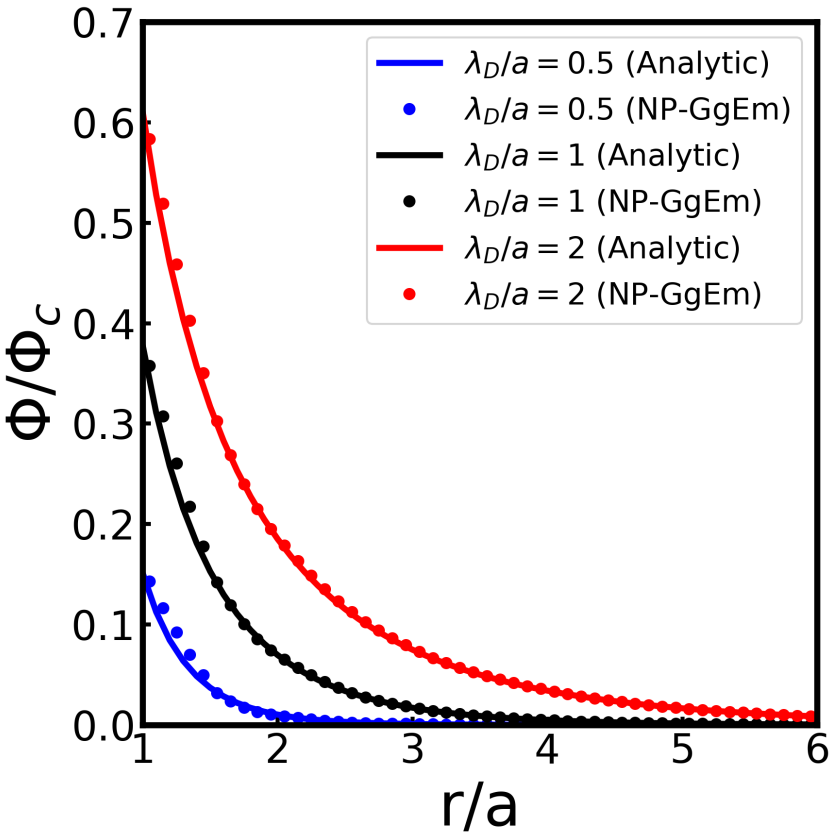

Figure 5.7: Electrostatic potential induced by an ion penetrable charged particle with charge density $\rho(r)$ as a function of the distance from the particle for different ionic strengths or Debye lengths. $\phi_c = 1$ (in characteristic electrostatic potential unit)

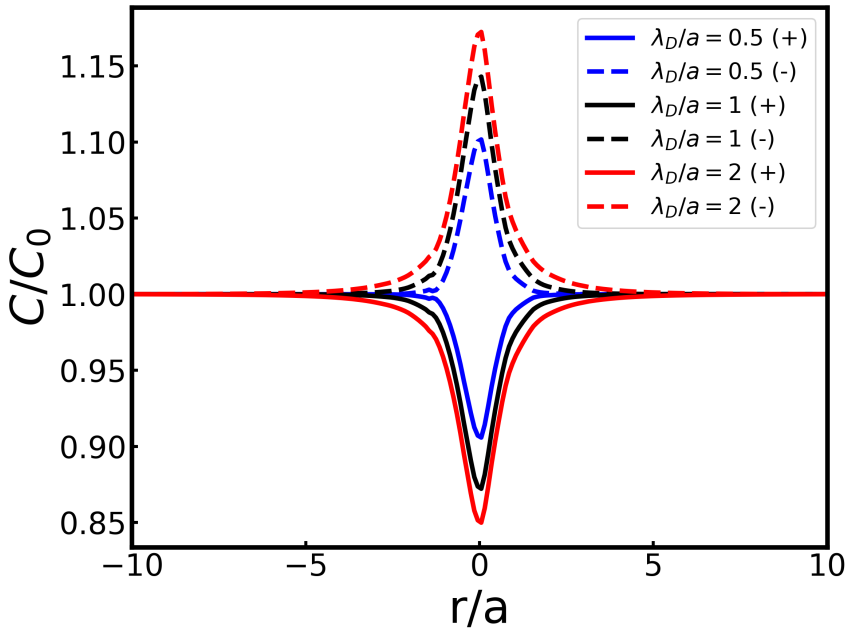

Figure 5.8: Cation and Anion concentration near an ion penetrable charged particle with charge density $\rho(r)$ as a function of the distance from the particle for different ionic strengths or Debye lengths. C_0 is the far-field ion concentration at a given Debye length.

5.4.2 Validation of Nernst-Planck-GgEm

We continue the validation of the Nernst-Planck-GgEm (NP-GgEm) solver by comparing its results to analytical solutions for a system composed of discrete charges suspended in a 1:1 electrolyte. More specifically, we aim to validate the electrostatic potential surrounding an ion-penetrable charged particle at equilibrium. The ion-penetrable charged particle has a radius of 1 (in characteristic length unit, a) and a volume charge density of $\rho(r) = \frac{3^3}{\pi^{3/2}}\exp(-3^2r^2)$ (in characteristic charge density unit, e/a^3), where r is the distance to the particle center in the characteristic length unit. Under this definition, the electrostatic potential on particle surface in a deionized solution is 1 (in characteristic electrostatic potential unit, $e/(4\pi\epsilon_0\epsilon a)$). The approximate analytic solution to this system has been derived by Ohshima et. al. [**?** **?**]:

$$\phi(r) = \phi_0 \frac{1}{r}\exp[-\kappa(r-1)], \tag{5.23}$$

where $\kappa^{-1} = \lambda_D$ (Debye length, in characteristic length unit) and ϕ_0 is the surface potential defined as:

$$\phi_0 = 4\pi \exp(-\kappa) \int_0^1 r\rho(r)\sinh(\kappa r)dr. \tag{5.24}$$

Figure 5.7 shows a comparison between the electrostatic potential induced by the ion penetrable charged particle with charge density $\rho(r)$ solved from Ohshima's analytic method and the NP-GgEm solver at different Debye lengths or ionic strengths. The good agreement between the solutions show that the NP-GgEm solver can recover the electrostatic profile at equilibrium accurately. Figure 5.8 shows the concentration distributions of both cations and anions in this validation system solved by the NP-GgEm solver. As expected, the concentration of cations is significantly lower than that of anions near the positively charged particle. And this difference shrinks as the distance to the particle center increases, leading to a neutral bulk solution in the bulk. The unneutral solution, i.e., diffusion layer, near the particle spans over a few Debye lengths, which match with predictions from classical electrical double layer theory [160].

5.5 Conclusions

We have presented a computational approach to study discrete charged particles suspended in confined ionic solutions. In this approach, the electrostatic and hydrodynamic coupling between continuum ion, charged particles and confined walls are fully considered. For the electrostatic and hydrodynamic interactions, an Ewald-like method is developed to solve the respective governing equations while satisfying arbitrary boundary conditions in complex geometries. For the continuum ions, the convection-diffusion equation is solved simutaneously considering the Nernst-Planck diffusion, thus enabling systems at or far from equilibrium. For the discrete charged objects, a stochastic partial differential equation is used to integrate their motions by coupling the hydrodynamic interactions with thermal fluctuations. With the method described here, it is possible to perform efficient simulations of discrete charged

objects embedded in charged solvents and find applications in a wide variety of situations involving the physics of polymeric and colloidal systems in micro- and nano- scales.

CHAPTER 6

APPLICATION: EVOLUTIONARY STRATEGY FOR INVERSE CHARGE MEASUREMENTS OF DIELECTRIC PARTICLES

6.1 Abstract

We report a computational strategy to obtain the charges of individual dielectric particles from experimental observation of their interactions as a function of time. This strategy uses evolutionary optimization to minimize the difference between trajectories extracted from experiment and simulated trajectories based on many-particle force fields. The force fields include both Coulombic interactions and dielectric polarization effects that arise due to particle-particle charge mismatch and particle-environment dielectric contrast. The strategy was applied to systems of free falling charged granular particles in vacuum, where electrostatic interactions are the only driving forces that influence the particles' motion. We show that when the particles' initial positions and velocities are known, the optimizer requires only an initial and final particle configuration of a short trajectory in order to accurately infer the particles' charges; when the initial velocities are unknown and only the initial positions are given, the optimizer can learn from multiple frames along the trajectory to determine the particles' initial velocities and charges. While the results presented here offer a proof-of-concept demonstration of the proposed ideas, the proposed strategy can be extended to more complex systems of electrostatically charged granular matter.

6.2 Introduction

Electrostatically charged granular particles are important in a wide variety of applications, ranging from particulate matter pollution to industrial handling of pharmaceutical products, food grains, and inks for printing and additive manufacturing, to name a

few[166, 167]. Granular dielectric particles often acquire charge through tribocharging or contact electrification[168, 169, 170, 171, 172, 173, 174, 175]; the charges they carry can significantly affect their dynamics and their interactions with the surrounding environment. In order to better understand how such charged, polarizable particles interact, it is therefore of fundamental importance to make detailed measurements of their actual charge[176]. Recently developed experimental techniques have made attempts to determine the charges of individual particles in a vacuum environment using free-fall videography[177, 178, 6]. In those experiments, particles falling under the influence of gravity were filmed as they interacted in a vacuum tube. In one experiment, by accelerating charged particles in a horizontal electrical field and analyzing approximately $\sim 10^4$ trajectories[178], the average particle charges were estimated by relying on the relationship between acceleration, mass, and charge. In another experiment, by identifying the relative positions of two particles and fitting Kepler-like orbits[7] to their motion, it was possible to determine their charges. The interactions that arise amongst polarizable particles are inherently many-body, and it is therefore essential that new approaches be developed that are capable of taking such effects into account. In this chapter, an approach is proposed that is capable of simultaneously measuring the charges of many individual particles from a *single* set of trajectories (i.e., the trajectories of the particles from a single experiment, as opposed to an ensemble of trajectories from many different experiments). The approach relies on two advances: (1) the availability of new numerical algorithms and new analytical expressions capable of describing polarizability effects on interacting particles [38, 39, 179, 40, 1, 180, 181, 182, 18, 59], and (2) the availability of modern evolutionary computation strategies [183, 184, 185, 186] that enable direct interpretation of experimental data from numerical computer experiments.

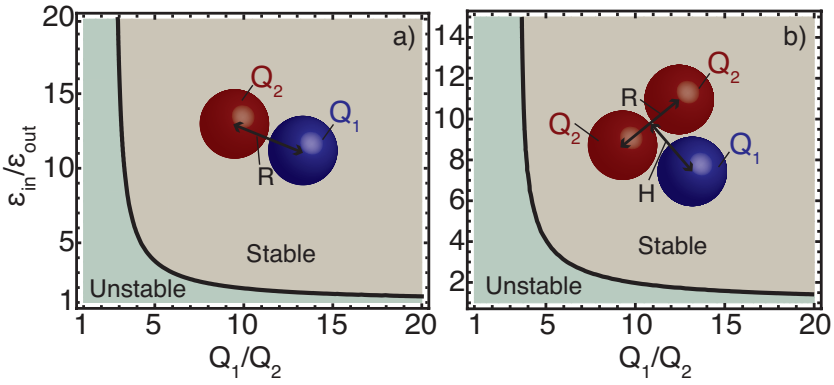

Figure 6.1: Stability diagram for dimer and trimers. Clusters of like-charged particles in close contacts are stabilized by surface charge polarization. The parameter regimes in which the close-contact particle aggregates are stabilized are highlighted with colored shades. The boundaries between different regimes are identified by computing the gradient of energy with respect to particle displacements. Notice that all particles here are positively charged and the different charge amount is labeled by red and blue color.

6.3 Models and methods

6.3.1 Inverse problem

To computationally determine charges on granular particles from a given single set of target trajectories assembled on a time-sequence of N_f frames, we adopt an evolutionary optimization technique that seeks to minimize a fitness function. Here that function f is defined as the deviation between trial trajectories generated in each optimization step and the target set of experimental or computational trajectories:

$$f = \frac{1}{N_f}\sum_{k=1}^{N_f}\left(\frac{1}{N_p}\sum_{i=1}^{N_p}|\boldsymbol{r}_{i,\mathrm{trial}}^{(k)} - \boldsymbol{r}_{i,\mathrm{target}}^{(k)}|\right), \tag{6.1}$$

where N_f excludes the initial configuration, N_p is the number of granular particles, $\boldsymbol{r}_{i,\mathrm{trial}}^{(k)}$ and $\boldsymbol{r}_{i,\mathrm{target}}^{(k)}$ are the positions of the i-th particle at k-th frame in the trial and the target trajectories, respectively. If the masses of the particles are known, the trial trajectories can be obtained using simulations with a suitable force field, i.e. in this case the electrostatic interactions, which include pair-wise Coulombic forces and many-body dielectric polarization

contributions. The bare Coulombic interaction can be attractive or repulsive, depending on the sign of the charges. Polarization effects, however, are purely attractive when the internal dielectric permittivity of materials is greater than that of the medium, and are purely repulsive in the opposite case [59]. This polarization-induced attraction is summarized in Fig. 6.1 for two and three particles of equal-sign charge. The figure shows the conditions, $\epsilon_{\text{in}}ß/\epsilon_{\text{out}}$ and Q_1/Q_2, under which two and three particles will form stable (attractive) aggregates. The boundary between the stable and unstable states is calculated using a recently developed analytical, perturbative theory [59](see Sec. 6.3.2 below). It is clear that dielectric polarization can strongly influence the nature of interactions between charged dielectric objects, particularly when sharp dielectric discontinuities are involved. In this chapter, we use the recently proposed analytical formalism (image method) to calculate electrostatic interactions between polarizable granular dielectric particles, and we have implemented the resulting electrostatic force field into LAMMPS (http://lammps.sandia.gov)[187] to simulate trajectories of the particles.

A Covariance Matrix Adaption Evolution Strategy (CMA-ES) is adopted, and we rely on the open source library libcmaes (https://github.com/beniz/libcmaes)[188] to extract the charges through an iterative optimization process. We address the inverse problem under two scenarios. In the first, the initial velocities of the particles are known, but their charges are not. The search variables are therefore the N_p charges. In the second scenario, both the initial velocities and charges of the particles are unknown, so there are in total $4N_p$ search variables (N_p charges and $3N_p$ velocities in 3-dimensional (3D) space). As our results demonstrate, the proposed strategy is able to determine the charges of the particles under both scenarios. It is difficult to know how many local optimum may be encountered in the fitness landscape. In our simulations, we find that the optimizer can be trapped in one of several optimum during a series of consecutive optimizations for the test cases in Sec. 6.4.2 and 6.4.3, which suggests that multiple optimum are generally accessible. To help the optimizer escape a local optimum, and move towards the global optimum, we restart the

optimization and rescale all search variables as shown in Sec. 6.4.2 and 6.4.3. Mathematically, the global optimum is found when the fitness function decays to zero; numerically, the global optimum is found when the fitness function is smaller than a tolerance. The value of the tolerance depends on the underlying errors in the experimental trajectories as well as on the numerical approximations involved in the particle simulations.

6.3.2 Image method

Image method is an analytical method capable of describing polarizability effects on interacting particles. We consider N spherical particles, with radius a and dielectric permittivity ϵ_{in}, embedded in a continuum with dielectric permittivity ϵ_{out}. In principle, our approach may be used for polydispersed particles with different ϵ_{in} and a, but we will limit the discussion in this chapter to monodispersed systems of equally sized spheres. The i–th particle carries a point charge $Q_i(\mathbf{x}_i) = z_i e$ at the center, where z_i is the valence and e is the elementary charge, which implies a homogeneous free surface charge density on the particle. Note, however, that in future work it should also be possible to pursue the proposed inverse calculations using numerical methods - such as those proposed in Chapter. 3 - that take inhomogeneous free charge distributions into account. In this chapter, we use the numerical method to calculate the induced surface charges on particles and found that the induced surface charges are inhomogeneous and their distribution changes as particles move along the trajectory as shown in Fig. 6.5.

The main interactions between the particles are the usual pairwise Coulombic interactions. However, when the particles are in close proximity, they induce surface charges, that give rise to additional interactions. We recently developed a systematic multiple-scattering formalism [18, 59] to describe this polarization interaction. In this formalism, the polarization energy is grouped in terms according to the number of interacting particles. The lowest-order of the polarization energy, i.e., the three-body terms E_3, is contributed to by 3 particles. The higher-order terms E_4, E_5 involve four-body, five-body interactions, etc.;

the two-body terms are reserved for the normal pairwise Coulombic interaction. Symbolically, the total electrostatic energy, E_E, for an ensemble of dielectric spheres may then be written as $E_E = E_2 + E_3 + E_4 + \cdots$, where each term in such an expansion involves a summation over all possible two-body, three-body, four-body, and so on, permutations. The key point to note about this multi-body expansion for E_E is that all interaction terms only depend on the particle positions. The references to surface charges are avoided by replacing the induced charges by the gradient of the electrostatic potential, therefore the degrees of freedom are greatly reduced. Furthermore, the forces on the particles can be computed via differentiation with respect to the particle positions, which enables N–body particle simulations. Three terms are preserved for the electrostatic multibody potential in the particle simulations, which have been shown to be essential in describing particle interactions in the presence of polarization[18, 59, 180].

6.3.3 CMA-ES

CMA-ES is one type of evolutionary optimization algorithm[189] that does not require derivative information of the fitness function, so it enables minimizing a broad range of fitness functions that have no analytical forms. In general, the idea of evolutionary optimization is to first generate a sample of random search variables every generation following a Gaussian distribution, then select the best search variables that produce the most optimized value of the fitness function. This process is then iterated until the fitness function is within a target convergence criterion. In CMA-ES, the mean and covariance matrix of the search variables as well as the step size are updated every generation to achieve fast and successful optimization. CMA-ES has found many applications in various materials design problems[190, 191, 192, 193, 194, 195].

6.3.4 Particle simulation

We consider spherical granular particles in a 3D vacuum environment, where only electrostatic interactions are the driving force for their motions. Recent experiments[7] in a similar setting have observed striking phenomena of aggregation and motion of charged granular particles, from which we adopt the particles' parameters for our simulations. Specifically, the particles are monodisperse and have relative dielectric constants of 15, diameters of 260 μm, and mass densities of 3800 kg/m^3. No thermal fluctuation or Brownian motion of the particles is included; the particles are in vacuum and have diameters of hundreds of microns. The system may become chaotic when it is evolved over time scales longer than those used in this chapter. However, a short-time trajectory without chaotic behavior (maximum of 25 ms in this work) is sufficient to successfully extract the charges of particles using our proposed strategy. We also neglect the particles' rotational motion and only account for their translational motion because particles studied in this work have spherical shapes. The charges on every particle are assumed to be uniformly distributed and the electrostatic interactions that include both Coulombic interaction and polarization effect are calculated using the aforementioned image charge method[182, 18, 59]. To simulate the trajectories of granular particles, Newton's equation of motion is integrated by the velocity-Verlet algorithm in LAMMPS with a time step of 1 μs. For the electrostatic interaction, the boundary condition is such that the electrical potential decays to zero at infinity. The particles are simulated in the *NVE* ensemble without periodic boundary conditions. In test problems, the initial positions of the particles are randomly generated while ensuring there are no overlaps between any two particles. For the test problems with 10 and 30 particles in this work, the target trajectories are generated by simulations with initial velocities all set to zero. For the problem with ten particles, the particles' charges are $\pm 1, \pm 2, \pm 3, \pm 4, and \pm 5$ pC (picoCoulomb), respectively. After $t = 0$, particles start to move under the influence of the electrostatic forces. For the problems with 10 and 30 particles, the dynamic simulations is run for 2000 steps (2 ms) and we sample and store the trajectories with a frequency of 1 frame per 10 steps (10 μs). There

are no collisions between any two particles in the trajectories, so tribocharging phenomena are avoided. The trajectories generated by these simulation are then imported as the target trajectories to the optimization program for inverse calculation of charges on the ten and 30 particles, respectively.

As alluded to earlier, in this work we assume that it is sufficient to assume a uniform charge distributions on the particles' surface, which is equivalent to placing a point charge in the center of the spherical particle according to Gauss' law[18, 59]. In reality, the free charges on particles' surface may be distributed inhomogeneously[196]. According to Ref. [196], immediately after the contact, the surface charge distributions are inhomogeneous in the contact areas; after 2.2 hours, they become uniform. In our experiments, the particles are placed and stabilized in the chamber for more than 3 hours before their free fall begins, such that the surface charge distributions are uniform. During free fall, there are collisions and contacts between particles, and charges are expected to be inhomogeneous in contact areas. Because the contact area is much smaller than the total surface area of each particle, however, the charges can be reasonably assumed to be mostly uniform on the particles' surfaces. As a result, the charge non-uniformity has a minor effect on the particles' trajectories. Ideally, we would include charge non-uniformity in our simulations and estimate charges on individual patches on all particles; this could be done by relying on numerical methods such as those introduced in Chapter. 3, but at greater computational expense. If there are many patches of charges, we conjecture that the number of solutions for the charges that can match experimental trajectories will still be one (with nonzero external electric field), or two (without external electric field, where the signs of the charges will be opposite in the two solutions). As the number of patches increases, the fitness function landscape becomes rougher, and the number of iterations to converge and the associated computational cost increases. Thus, using an efficient electrostatic solver (see Chapter 3) would help reduce the computational cost for this problem. However, in view of the lack of systematic experimental data on how the charges are really distributed on the particles during their free fall, we

find it difficult to assume a certain pattern of non-uniform surface charge distributions on the particles. By instead assuming a uniform distribution, we are still able to produce simulated trajectories that agree very well with experimental trajectories, serving to validate our assumptions. Although the free surface charges are assumed to be homogeneous, we find that the induced surface charges on particles are inhomogeneous by calculating induced charges using the numerical method, and the distribution of the induced surface charges changes as particles move as shown in Fig. 6.5.

6.4 Results and discussions

6.4.1 Known initial velocities

We first study the inverse problem when the charges of the particles are the only unknowns; the known particles' initial positions and velocities are used to start the simulation. In our test case, we first generate trajectories of ten charges with assigned charges, and we use a single final frame at $t = 2$ ms with the final positions of the particles, so N_f in Eq. (6.1) is 1. The true (assigned) charges of the particles are $\pm 1, \pm 2, \pm 3, \pm 4$, and ± 5 pC, respectively, and the aim of this first example is to demonstrate that the evolutionary optimization process can correctly recover those charges from knowledge of the particles' masses, initial positions and velocities. We use the following three parameters in the CMA-ES evolutionary optimization. The initial values for charges are set to zero; the initial search step is 2, and the number of offsprings is 10. Figure 6.2(top) shows the velocities of three representative particles as a function of time throughout the simulated trajectory. One can see that the trajectory generated by the simulation using inversely calculated charges (dotted line) agrees well with the target trajectory (solid line). Figures 6.2(middle) and 6.2(bottom) show the evolution of the fitness function and the estimated charges of ten particles as a function of the number of fitness function evaluations. The fitness function decreases as the number of evaluations increases, and it converges to about 2×10^{-2} after 110 generations ($\sim$ 1100 fitness function

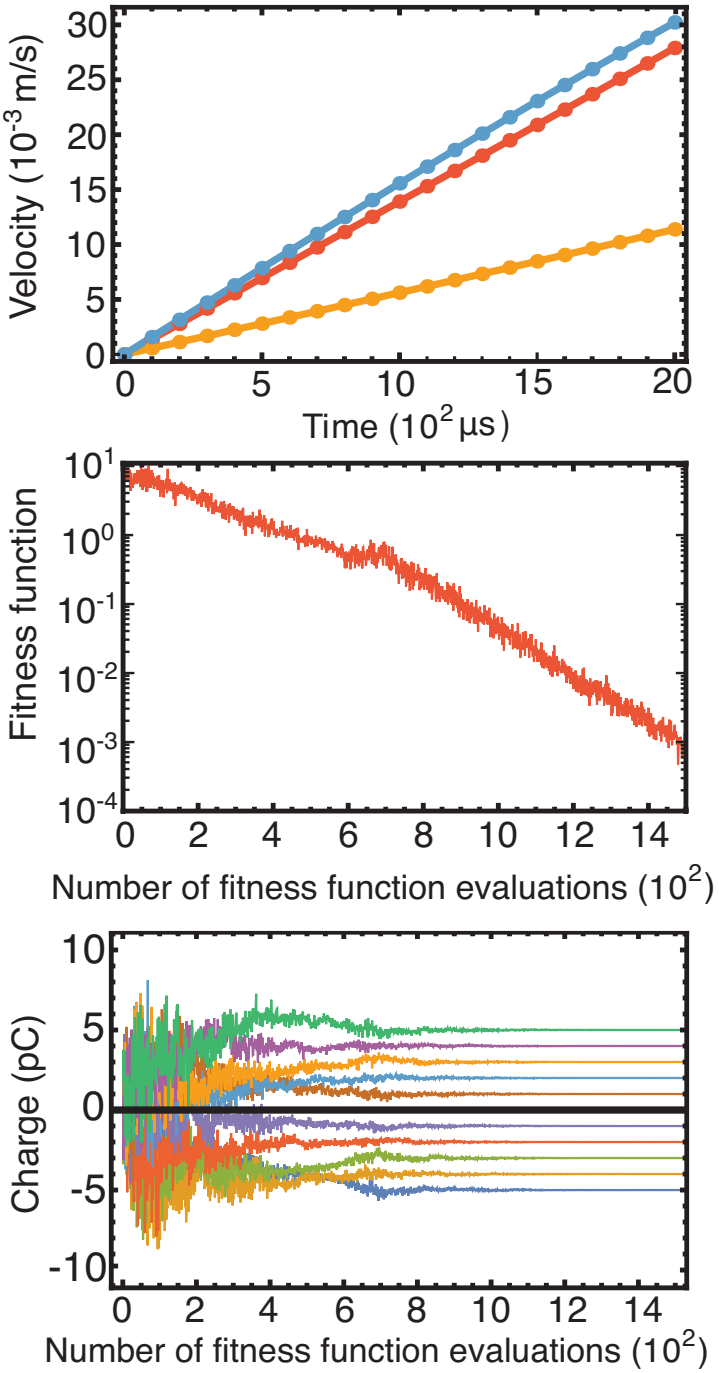

Figure 6.2: Top panel shows the evolution of velocities of three representative particles as a function of time in the target trajectory (solid line) and in the trajectory generated by the simulation using inversely calculated charges (dotted line). Middle and bottom panels show the evolution of the fitness function and charges of 10 individual particles, respectively, as a function of the number of fitness function evaluations. Every optimization step contains complete trajectories of ten electrostatically charged granular particles.

evaluations). The deviation between trial and target particle trajectories becomes smaller as the optimization proceeds, and the trial charges on the particles gradually evolve to their target values. When the fitness function reaches a plateau, the particles' charges stabilize at the correct values of $\pm 1, \pm 2, \pm 3, \pm 4$, and ± 5 pC, respectively.

To examine how the initial guess for the particle charges affects convergence, we chose four different starting values, i.e., 0 pC, 1 pC, 10 pC, and 100 pC, and examined the evolution of our optimization while keeping all other CMA-ES parameters constant. For an initial guess of 0 pC, 1 pC, and 10 pC, all three optimizations yielded correct estimates of the charges, but the number of generations to reach convergence increased as values of particle charges in the initial guess increased. When the initial guess is 100 pC, the optimizer cannot reach convergence in a single optimization, i.e., the estimated charges at the end of the first optimization are of a different order of magnitude. These findings serve to illustrate that it is critical to choose values for the initial particle's charges that are of the same order of magnitude as the target value, otherwise, rescaling the search variables multiple times is necessary to achieve convergence, as shown in Sec. 6.4.2.

In this test case, we also find that using only the Coulombic interactions (i.e. neglect polarization interactions) leads to 10% error in the inversely calculated charges. We note that the importance of polarization depends on i) the ratio between the dielectric constant of the particles and that of their surrounding environment, and ii) the charge ratio between interacting particles. The polarization effect becomes more important when the dielectric ratio or charge ratio increases. In the first problem considered here, the dielectric ratio is 15 and the maximum charge ratio is 5. According to Fig. 6.1, with this combination of parameters, the polarization effect is not too strong, which is consistent with the 10% error that is observed when polarization is neglected. However, for particles with dielectric ratios that are larger than 15 and charge ratios that are above 5, neglecting polarization effects leads to errors that are much larger than 10%; in those cases, polarization effects must be taken into account. Moreover, attractions and adhesions between like-charged particles were

observed in Ref. [7], where polarization was shown to play a central role.

6.4.2 Unknown initial velocities

Accurately recording both positions and velocities of granular particles using videography is challenging. In most experiments, only the particles' positions are recorded. It is of course possible to approximate velocities at every frame using a finite difference approximation, but that may lead to a loss of accuracy. It is therefore of interest to explore the use of *only* information about the positions of the particles for inverse determination of their charge. We find that, when the particles' initial velocities are unknown, using multiple frames from the particles' trajectories to evaluate the fitness function can enable such inverse charge calculation. Specifically, 20 consecutive frames are selected from the initial stage of the simulated trajectories for ten particles (having the same charges as above) at an interval of 10 μs; N_f in Eq. (6.1) is set to 20. The parameters for performing the CMA-ES evolutionary optimization are as follows: the charges and initial velocities are set to zero for all particles, the initial search step is 2, and the number of offsprings is 10. Figure 6.3 shows the evolution of the charges and initial velocities as a function of the number of fitness function evaluations. As the optimization progresses, the initial velocities are estimated to be close to their true values, as shown in Fig. 6.3(b). Unfortunately, however, there are significant deviations between the estimated charges and their true values, even when the charges stabilize at the end of the optimization process (about 200 generations), see Fig. 6.3(a). The converged value of the fitness function for Fig. 6.3(a) and (b) is 1.28 μm.

The estimated initial velocities at the end of the optimization process in Fig. 6.3(b) are on the order of 10^{-3} to 10^{-4} m/s, while the charges are on the order of 10^{0} pC. Thus there is a difference of about 3 to 4 orders of magnitude between the numerical values of the estimated charges and the initial velocities. This points to a numerical artifact of the optimization process as originally implemented; for successful optimization using CMA-ES, it is essential that variables be rescaled in order to ensure that all numerical values of the search parameters

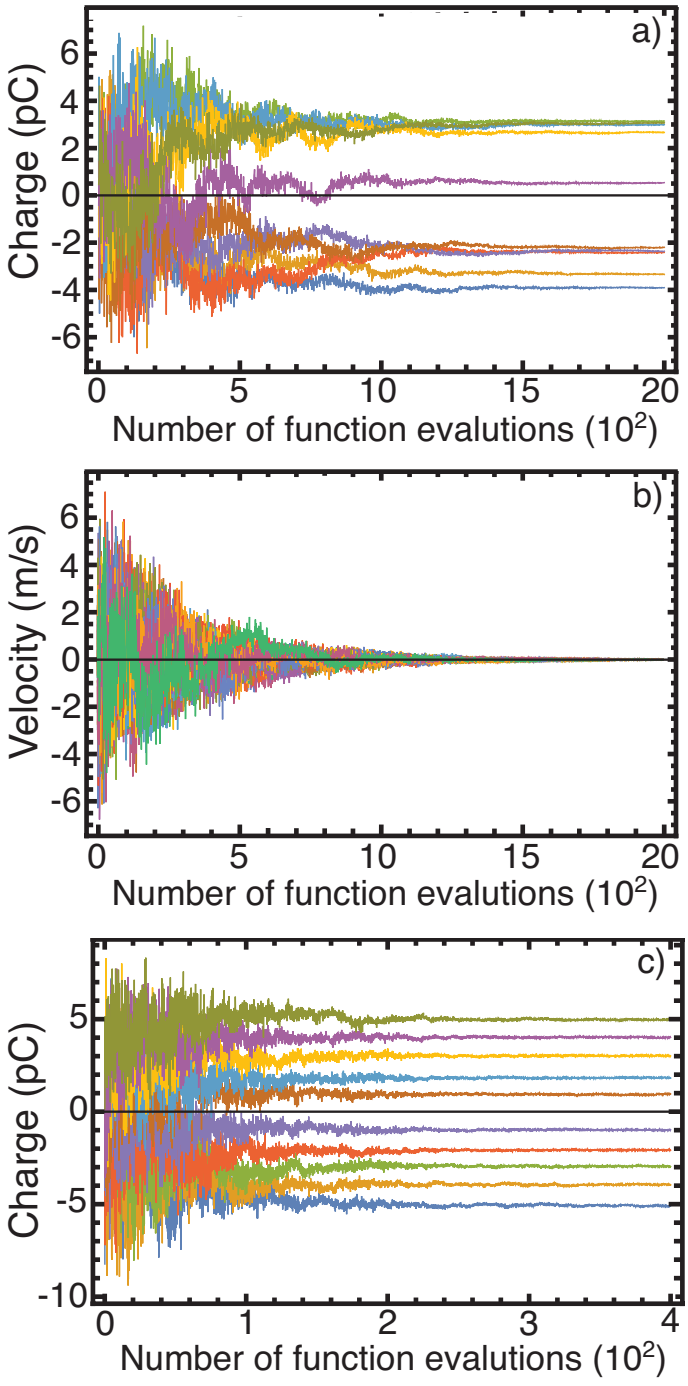

Figure 6.3: Evolution of charges and initial velocities for ten individual particles as a function of the number of fitness function evaluations when the initial velocities are unknown. (a) Evolution of charges in the first optimization; (b) Evolution of initial velocities in the first optimization; (c) Evolution of charges in the second optimization.

are of the same order of magnitude [197]. Then a second optimization simulation is started by setting initial values for the search parameters to those corresponding to the last step of the previous simulation; in the subsequent simulation, we re-scale the search variables for initial velocities by 10^{-4}, i.e., if one of the initial velocities in the optimizer is 1, then its value fed to the dynamical simulation is 10^{-4}. The results of this second optimization process are shown in Fig. 6.3(c). One can appreciate that the charges evolve rapidly towards their true values after about 30 generations (300 fitness function evaluations). At the end of the optimization process, the charges agree very well with their true values and the converged value of the fitness function for Fig. 6.3(c) is $3.69 \times 10^{-4} \mu m$, serving to demonstrate that the inverse calculation process can accurately estimate charges from known trajectories, even if the particles' initial velocities are unknown.

6.4.3 Random charges

To further test the robustness and applicability of our proposed strategy, a third test was performed on a system of 30 particles with randomly assigned charges, drawn from a Gaussian distribution with zero mean and a standard deviation of 5 pC. Their values are represented by red dots in Fig. 6.4. True trajectories were then generated from simulations using these random charges and zero initial velocities as inputs. We applied the evolutionary optimization strategy to this problem assuming unknown charges and unknown initial velocities. Multiple optimization simulations were performed consecutively to rescale the search variables properly. As can be seen in Fig. 6.4, upon convergence most of the estimated charges (blue dots) do not agree particularly well with their true values (red dots). In fact for the 13-th to 30-th particles, the signs of the estimated charges are just the opposite of their true values. On the other hand, the absolute values of the estimated charges agree well with the true values. This happens because of the symmetry of the system, i.e., a trajectory remains the same when the particles' charges all have reverse signs (the mass and shape for all particles are the same).

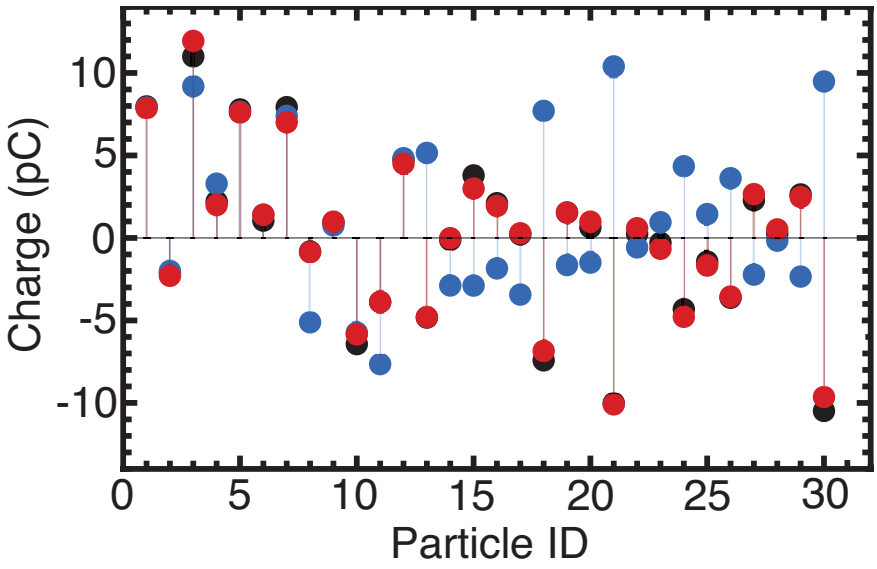

Figure 6.4: Particle charges as a function of particle number. Red, blue, and black dots represent true charges, calculated charges in the absence of the external electric field, and calculated charges in the presence of the external electric field, respectively.

To resolve the sign problem, an external electric field was applied to break the charge symmetry during the generation of model trajectories. The evolutionary optimization strategy was then used on these new trajectories. Fig. 6.4 shows that after optimization with applied field, the charges obtained through the optimization process (black dots) agree very well with the target values. This result shows that by breaking the charge symmetry by applying an electric field, the evolutionary optimization strategy can correctly recover the charges of the particles. We have also varied the magnitude of the applied field from 0.1 to 100 V/μm, and found that all values lead to the correct sign of the charges. The difference between various magnitudes of the applied field is that larger electric fields can generate a trajectory that is different from that without a field within a shorter amount of time. Since the only good of applying a field is to determine the sign of a charge (and not its magnitude), such differences have no influence on our results.

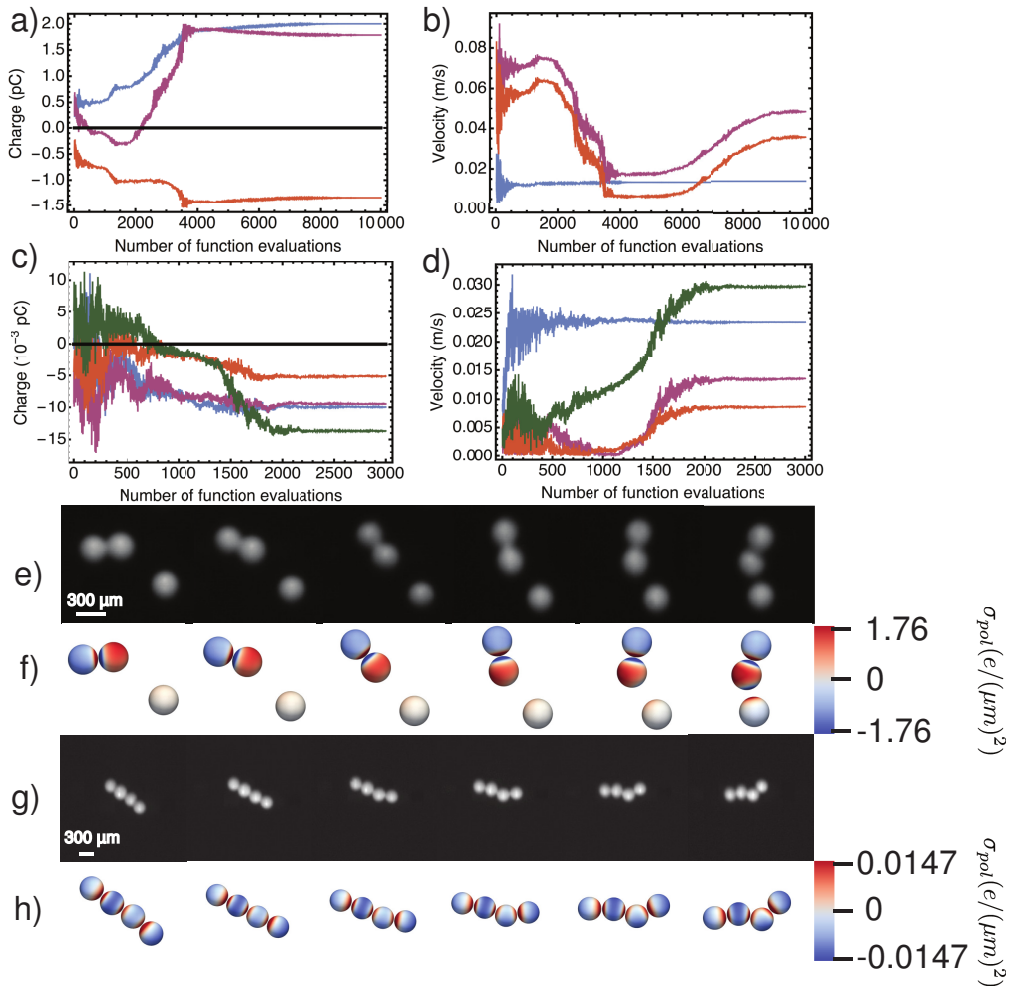

Figure 6.5: (a), (b) The evolution of charges and initial velocities of three individual particles as a function of the number of fitness function evaluations; (c), (d) The evolution of charges and initial velocities of four individual particles as a function of the number of fitness function evaluations; (e) and (f) show snapshots of three particles moving in vacuum environment from experiment (e) and simulations (f), and the time interval between two consecutive snapshots is 5 ms; (g) and (h) show snapshots of four particles moving in vacuum environment from experiment (g) and simulations (h), and the time interval between two consecutive snapshots is 4 ms.

6.4.4 Application to experimental trajectories

Lastly, we apply the evolutionary optimization strategy to experimental data to (i) calculate charges on granular particles in experiments, and (ii) reproduce the experimental trajectories using simulations. A set of trajectories for three granular particles and another set of trajectories for four granular particles are chosen from the experimental data. The data set, which consists of 25 frames, covers a span of 25 ms. Data were captured from videography; a particle tracking technique was applied to extract the coordinates of all particles. The time interval between consecutive frames is 1 ms. In the trajectory with three particles, two particles are always in contact with each other, while the third particle moves freely around the other two; in the trajectories with four particles, particles are always in contact with their neighbors. A bond is formed between the two sticking particles by short-range cohesive forces, including van der Waals forces or capillary forces due to absorbed molecular layers[177, 198, 199]. These short range interactions are strong enough to hold the two particles together without relative translational and rotational momentum between each other. To reproduce this behavior, a rigid bond is implemented in the simulations between the sticking particles. The length of the rigid bond is set to the diameter of one granular particle and is maintained in every simulation step using the SHAKE algorithm[200]. The charge on each particle is kept constant in particle simulations, because charge transfer between particles is negligible during the short trajectory time of 25 ms[7]. The coordinates of three and four particles extracted from experiments are then fed as the target trajectory into the optimizer, and the optimization strategy is applied. Note that in this case the signs of the particles' velocities can be inferred from experimental data, and we constrain the sign of the search variables for initial velocities in the optimization program to increase efficiency.

Figures 6.5(a), 6.5(b), 6.5(c), and 6.5(d) show the evolution of charges and initial velocities as the optimization proceeds, for three and four particles, respectively. The results presented here are from the last optimization simulation in a set of consecutive calculations. In the first few simulations, the fitness function decreases to a plateau at the end of each

simulation. However, the fitness function is still large and on the order of 10^2. Moreover, there is a difference of about three orders of magnitude between some of the search variables. These consecutive simulations are merely used to properly rescale all search variables; we then feed the final charges and initial velocities to the particle simulation to generate a simulated set of trajectories of three and four particles. Figures 6.5(e) and 6.5(f) show six snapshots of three particles from experiments and simulation, respectively. The induced surface charge density (σ_{pol}) on every particle is calculated using a parallel $O(N)$ numerical solver for electrostatic polarization (see Chapter 3). We obtain excellent agreement between the simulated and experimental trajectories of the particles. The charges on the three particles are obtained as 1.785, -1.338, and 2.0 pC, respectively (from left to right in the first snapshot in Fig. 6.5(f)). They could also be -1.785, 1.338, and -2.0 pC because of the symmetry of the system. The range of calculated charges is consistent with that inferred in previous experimental results[7]; the experimental charge distributions $P(q)$ have tails up to several million electron charges ($10^6 e \approx 0.16$ pC). It is also found that the two bound particles carry opposite charge, and the Coulombic attraction force helps bind them together. For the set of trajectories comprising four dielectric granular particles, Figs 6.5(g) and 6.5(h) show six snapshots from experiments and simulations, respectively. Excellent agreement is again found between both, serving to demonstrate the applicability of our proposed optimization strategy for inverse charge calculations. The charges on the four particles are obtained as -9.97×10^{-3}, -9.37×10^{-3}, -5.12×10^{-3}, and -1.37×10^{-2} pC, respectively (from right to left in the first snapshot in Fig. 6.5(h)). They could also be of positive sign because of the symmetry of the system. The range of calculated charges is consistent with that inferred from previous experimental measurements[7]. Note that the magnitudes of the charges for four particles are much smaller than those for three particles, and the signs of the four particles' charges are the same, indicating that polarizability is essential for describing the physics of the particles considered here. The converged values of the fitness function for Figs. 6.5(a) and 6.5(c) are 13.66 μm and 48.5 μm, respectively, which are larger than those for Fig. 6.3. The

converged values in Fig. 6.3 are relatively small, because i) the target trajectory is generated by simulation and the trajectory data are an exact representation of the simulated particles' motion; ii) there is no error from the numerical simulation results, since the models used in generating the trajectory and in optimizations are identical. The relatively large converged values in Fig. 6.5 when fitting the experimental data are likely due to errors from experimental measurements and approximations used in the numerical model. The experimental errors are from vibrations of the camera and the particles' position tracking process; note that the resulting errors in the particles' positions are on the order of 10 μm. The approximations in the numerical model include using rigid bonds to connect sticking particles, and assuming a homogeneous free surface charge density on each particle.

6.5 Conclusions

In summary, we have combined an evolutionary optimization strategy CMA-ES with a particle dynamics simulator to obtain the charges on granular polarizable particles based on a given set of experimental trajectories. The availability of a polarizable force field for electrostatically interacting charged granular particles is central to the particle dynamics simulator; electrostatic polarization and Coulombic interactions can in some cases have opposite signs, and lead to trajectories that are very different from those observed in the absence of polarizability effects. The proposed strategy was demonstrated in the context of several problems. In the first problem, the initial position and velocities of all particles were given, and the algorithms were used to infer the particles' charges. In the second and third problems, both the particles' charges and initial velocities were unknown, and it was shown that the evolutionary optimization can be used to successfully determine the particles' charges and their initial velocities. In the fourth problem, the evolutionary optimization strategy was applied to extract the charges from experimentally observed trajectories, and the charges were found to be within the ranges reported in previous experimental measurements from the literature.

The proposed strategy could be extended to more complex systems containing electro-

statically charged granular particles. For example, using a recently developed parallel $O(N)$ numerical solver for electrostatic polarization interactions among arbitrary-shaped particles (see Chapter 3), the evolutionary optimization strategy could be applied to determine charges not only of spherical particles, but also on arbitrarily-shaped particles with uniform or nonuniform surface charge distributions, and including rotational motion. The proposed strategy could also be used to determine the charges of particles in micro- or nano-fluid environments by coupling the strategy with a recently developed parallel $O(N)$ Stokes' solver for hydrodynamically interacting objects in general geometries[201]. We envision that our proposed strategy could find applications in material property measurements and material designs.

CHAPTER 7

APPLICATION: STRUCTURE AND DYNAMICS OF HYDRODYNAMICALLY INTERACTING FINITE-SIZE BROWNIAN PARTICLES IN A SPHERICAL CAVITY: SPHERES AND CYLINDERS

7.1 Abstract

The structure and dynamics of confined suspensions of particles of arbitrary shape is of interest in multiple disciplines, from biology to engineering. Theoretical studies are often limited by the complexity of long-range particle-particle and particle-wall forces, including many-body fluctuating hydrodynamic interactions. Here, we report a computational study on the diffusion of spherical and cylindrical particles confined in a spherical cavity. We rely on an Immersed-Boundary General geometry Ewald-like method to capture lubrication and long-range hydrodynamics, and include appropriate non-slip conditions at the confining walls. A Chebyshev polynomial approximation is used to satisfy the fluctuation-dissipation theorem for the Brownian suspension. We explore how lubrication, long-range hydrodynamics, particle volume fraction and shape affect the equilibrium structure and the diffusion of the particles. It is found that once the particle volume fraction is greater than 10%, the particles start to form layered aggregates that greatly influence particle dynamics. Hydrodynamic interactions strongly influence the particle diffusion by inducing spatially dependent short-time diffusion coefficients, stronger wall effects on the particle diffusion towards the walls, and a sub-diffusive regime –caused by crowding– in the long-time particle mobility. The level of asymmetry of the cylindrical particles considered here is enough to induce an orientational order in the layered structure, decreasing the diffusion rate and facilitating a transition to the crowded mobility regime at low particle concentrations. Our results offer fundamental insights into the diffusion and distribution of globular and fibrillar proteins

inside cells.

7.2 Introduction

Diffusion under confinement is central to multiple physical, chemical and biological systems, including colloidal and protein suspensions, devices for particle separation, and transport through membranes. A model system to study the diffusion and structure of highly concentrated particles under confinement could offer insights into the dynamics of crowded macromolecules, such as proteins, inside cells where they typically occupy 20 to 40% of the cytoplasm volume [202].

Previous studies have shown that crowding between macromolecules affects reaction rates of equilibrium reactions [202, 203, 204, 205, 206], and hinders the diffusion of intracellular particles [207]. *In vivo* experiments, using fluorescence recovery after photo-bleaching (FRAP) techniques, have reported that the apparent diffusion coefficient for green fluorescent proteins (GFP) in *E. Coli*'s cytoplasm is about 11 times lower than that in water [**?** **?** 208]. Even though a variety of intracellular activities, namely metabolism, cellular homeostasis, signaling, transcription, translation and locomotion, strongly depend on diffusion of the intracellular macromolecules, the mechanisms behind the hindered diffusion are not fully understood. A review by Skolnick, discussed several factors that could lead to hindrance, including the viscosity of cytoplasm, steric effects, hydrodynamic interactions (HI), and other short-range interactions between particles [209]. A significant effort that relied on Brownian simulations of 50 types of macromolecules modeled as spheres inside *E. Coli*'s cytoplasm was able to reproduce the translational diffusion coefficient of GFP [210, 83]. The authors demonstrated that steric repulsions cannot explain the hindered diffusion and suggested that electrostatic and other short-range interactions are essential variables to consider. However, short-range interactions modeled as Van der Waals potentials can always be tuned to match experimental results, and these authors were unable to provide conclusive remarks regarding the effects of short- and long-range HI. In other work, BD simulations considering fluctuating

HI have been performed in the bulk [79], confirming that HI plays a nontrivial role in the hindering of macromolecular diffusion. Unfortunately, the mobility variations induced by confinement was not considered in this work. Confinement, using a network of wall particles that are constrained by a predefined potential, was included in a subsequent study to represent a cell membrane [211]. In that work, the non-slip boundary condition was not strictly satisfied, allowing the flow to penetrate the membrane, and driving a tangential component of the particle average velocity. From the hydrodynamic interactions point of view, previous efforts were centered on the study of the dynamics of single or many particles immersed in an unconfined viscous fluid [? ? ? ? ? ? ? ? 222? ?] and of particles moving near a wall or confined in a slit and cylindrical geometries [? ? ? ? ? ? ? ? ?]. Recently, a theoretical study was performed by Zia et. al. to model the behavior of a concentrated colloidal dispersion confined in a spherical cavity [213]. Their framework relies on a set of hydrodynamic tensors that capture far- and near-field (lubrication) hydrodynamics between particles and walls. The authors studied the structure and diffusion of hydrodynamically interacting spherical particles confined in a spherical cavity following a Stokesian dynamics (SD) approach [212]. They found that the confinement, crowding and HI collectively lead to an anisotropic micro-structure, which then induce position-dependent and anisotropic short- and long-time dynamics. That study was, however, limited to spherical particles.

We have developed an efficient computational framework to perform BD simulations of arbitrarily shaped particles confined in any type of geometry. We use an Immersed-Boundary (IB) method to represent the suspended particles, a parallel Finite Element General geometry Ewald-like method (pFE-GgEm) [201] to calculate the confined Green's functions, and a Chebyshev polynomial approximation to satisfy the fluctuation-dissipation theorem. In this chapter, we use this methodology to study how steric repulsion, short- and long-range hydrodynamic interactions, confinement, particle volume fraction and particle shape affect the structure and the diffusion of spherical and cylindrical finite-size particles confined in a spherical cavity. The cylinders are selected to break the three-dimensional symmetry of the

particles, a feature that is common in protein structures.

The paper starts with a description of the particle model, the geometry, the methods and the dimensionless variables to characterize the system. The BD and the IB-pFE-GgEm methods are briefly summarized. We then proceed to present and discuss the results, including the spatial and orientational ordering of the particles and the short- and long-time diffusion behavior. We finish the paper with a summary of the most important findings.

7.3 Models and methods

Let's consider N mono-disperse and semi-rigid particles embedded in a viscous fluid of viscosity η, confined in an spherical cavity of radius R. Under a zero Reynolds number condition, the N-body force/torque balance on the particles is:

$$\mathbf{F}^H + \mathbf{F}^B + \mathbf{F}^C + \mathbf{F}^{EV} + \mathbf{F}^{ext} = 0, \tag{7.1}$$

where $\mathbf{F}^H$ is the $6N$ hydrodynamic force/torque vector, $\mathbf{F}^B$ is the Brownian force/torque vector, $\mathbf{F}^C$ is the force/torque vector containing configurational forces, $\mathbf{F}^{EV}$ represents the force/torque vector due to excluded volume interactions, and $\mathbf{F}^{ext}$ includes all external forces/torques.

The evolution of the suspended particles, from Eqn. (7.1), is carried out through the grand mobility or resistance tensors that relate the hydrodynamic forces/torques to the translational and rotational velocities of the particles [105, 214, 215]. SD [107, 108, 216] and boundary integral methods (BIM) [105, 104] have been used extensively to solve this "mobility problem". The regularized Stokeslets [116], the accelerated BIM [217], and the Immersed Boundary (IB) [146, 218] approaches all provide computational efficiency and simplicity, typically to improve (or avoid) the calculation of the single- and double-layer hydrodynamic potentials of the suspended particles. In particular, the IB method represents the surfaces of the suspended solids as a distribution of discrete force densities that, together

with a surface force description and Stokes equations, generate the temporal evolution of the suspended particles. This is the approach that we use in this chapter.

The surface of each suspended particle is discretized into a set of N_{IB} nodes that constitute a mesh, similarly to boundary element methods [104]. On the surface nodes, we define structural spring potentials that maintain particle shape, volume and surface. The force balance on each of the N particles is then translated into the N_{IB} surface nodes as follows,

$$\mathbf{f}_{\nu}^{H} + \mathbf{f}_{\nu}^{B} + \mathbf{f}_{\nu}^{C} + \mathbf{f}_{\nu}^{EV} = \mathbf{0}, \tag{7.2}$$

for every node $\nu = 1, ..., N_{\mathrm{IB}}$; where $\mathbf{f}_{\nu}^{H}$ is the hydrodynamic force, $\mathbf{f}_{\nu}^{B}$ is the Brownian force, $\mathbf{f}_{\nu}^{C}$ is the constitutive force and $\mathbf{f}_{\nu}^{EV}$ is the force from all the excluded volume interactions: particle-particle and particle–wall.

Assuming that the probability density for the nodal positions is a continuous density for the Fokker-Planck equation [87], an equivalent stochastic differential equation for the motion of the nodes is written as follows [88],

$$d\mathbf{R} = \left[\mathbf{M} \cdot \mathbf{F} + \frac{\partial}{\partial \mathbf{R}} \cdot \mathbf{D}\right] dt + \sqrt{2}\mathbf{B} \cdot \mathbf{dW}, \tag{7.3}$$

where $\mathbf{R} = (\mathbf{x}_1, \mathbf{x}_2, \ldots, \mathbf{x}_{N \times N_{\mathrm{IB}}})$ denotes a $3N \times N_{\mathrm{IB}}$ vector containing the spatial coordinates of the nodes, $\mathbf{D} = k_B T \mathbf{M}$ is the $3N \times 3N$ diffusion tensor, k_B is Boltzmann constant, T is the absolute temperature and $\mathbf{M}$ is the $(3N \times N_{\mathrm{IB}}) \times (3N \times N_{\mathrm{IB}})$ mobility tensor. In addition, $\mathbf{U} = \mathbf{M} \cdot \mathbf{F}$ contains the $3N$ fluctuating velocities from the hydrodynamic interactions and $\mathbf{F}$ is the $3N \times N_{\mathrm{IB}}$ vector that contains the non-HI and non-Brownian forces on the nodes. The divergence of the diffusion tensor $\frac{\partial}{\partial \mathbf{R}} \cdot \mathbf{D}$ is the drift resulting from the configuration-dependent mobility of the confined particles and $\mathbf{dW}$ is a random vector, the components of which are obtained from a real-valued Gaussian distribution with zero mean and variance dt; $\mathbf{dW}$ is coupled to the diffusion tensor through the fluctuation-dissipation theorem: $\mathbf{D} = \mathbf{B} \cdot \mathbf{B}^T$.

In IB methods, the force distributions at moving solids are discretized as distributions of regularized point-forces. The "smoothing" function for the the delta function scales as the distance between the surface nodes that are used to represent the moving particles. Consequently, the structural forces on the particles, $\mathbf{f}_{\nu}^{C}$, define a force density as follows

$$\boldsymbol{\rho}_{\mathrm{IB}}^{C}(\mathbf{x}) = \sum_{\nu=1}^{N_{\mathrm{IB}}} \mathbf{f}_{\nu}^{\mathrm{C}}(\mathbf{x}_{\nu}) \delta_{\mathrm{IB}}(a, \mathbf{x} - \mathbf{x}_{\nu}), \tag{7.4}$$

where $\delta_{\mathrm{IB}}(a, \mathbf{x})$ is a smoothing function that is a modified Gaussian (details available in [125]). The regularization parameter ξ_{IB} in δ_{IB} is related to the characteristic length h for the node spacing on the particle surface, i.e, $\xi_{\mathrm{IB}} \sim h^{-1} \sim a^{-1}$. The rational behind $\delta_{\mathrm{IB}}(a, \mathbf{x})$ is to ensure that the regularized force on each node is spread over the length scale of the associated surface elements, thereby preventing fluid from penetrating the particle surface.

In this work, we consider the particles as "semi-rigid", where each node on the particle is linked to its neighboring nodes by elastic springs with a prescribed large stiffness constant. The nodes are also connected to the particle center-of-mass by an elastic spring to conserve the desired shape. For simplicity, we assumed that each link is a linear spring, where the force acting on the point ν by the point μ is given by

$$\mathbf{f}_{\nu\mu}^{\mathrm{C}} = k \left(r_{\nu\mu} - q_0 \right) \frac{\mathbf{x}_{\nu\mu}}{r_{\nu\mu}}. \tag{7.5}$$

Here k is the spring elastic constant, q_0 is the equilibrium spring size for each specific situation, $\mathbf{x}_{\nu\mu} = \mathbf{x}_{\nu} - \mathbf{x}_{\mu}$ and $r_{\nu\mu} = |\mathbf{x}_{\nu\mu}|$. For each particle, a spring network is formed (see Fig. 7.1), resulting in an internal nodal force that resists the deformation of the particles. In addition, at each surface node of each particle a purely repulsive Lennard-Jones (LJ) force is added to account for particle-particle and particle-wall excluded volume interactions. This LJ force comes from two contributions: 1) interactions with nodes from a different particle; 2) interactions with the wall. And it is equivalent to the negative gradient of the LJ potential

which is defined by

$$V^{\mathrm{LJ}}(r) = 4k_BT\left[\left(\frac{\sigma}{r}\right)^{12} - \left(\frac{\sigma}{r}\right)^{6}\right] + k_BT, \tag{7.6}$$

for $r \leq 2^{1/6}\sigma$ and zero otherwise. Here, r is the Euclidean distance between nodes of two different particles or between the node and walls, and $\sigma = 2.2a$ is chosen empirically to guarantee that each surface node has an excluded volume of radius a. The translational and rotational velocity of particles are calculated by integrating the velocity over the surface mesh of each particle, thereby satisfying the force and torque balance. For completeness, we include a validation of our IB approach in the Appendix: (i) fulfillment of Stokes' law of particles under confinement, (ii) validation of the fluctuation-dissipation theorem (diffusion of particles), (iii) consistency of the particle shape as a function of the spring constants.

In what follows, we use dimensionless variables for all results and discussions. We use a as the characteristic length scale and the nodal spacing diffusion time, $a^2\zeta/k_BT$, as the characteristic time scale. We set k_BT as the scale for energy and k_BT/a for the force. The friction coefficient ζ is related to the fluid viscosity η and a through Stokes' law: $\zeta = 6\pi\eta a$, and the nodal diffusion coefficient is $D_0 = k_BT/\zeta$.

Our simulation method, denoted by **IB-pFE-GgEm**, is an $O(N)$ algorithm that includes hydrodynamic interactions for confined, large-scale suspensions of finite-size particles of arbitrary shape. Details can be found in our previous work [201]. Briefly, the $O(N)$ algorithm consists of three major components: (a) pFE-GgEm routines to calculate the Green's function (Stokeslet) for any geometry, (b) Fixman's mid-point algorithm for time integration and (c) the Chebyshev polynomial approximation for the fluctuation dissipation theorem. The parallel finite element GgEm (pFE-GgEm) routines are built using open source libraries, thereby facilitating usage of our software. The routines can be downloaded at http://miccomcodes.org as part of the Continuum-Particle Simulation Suite (COPSS) from the Mid-west Integrated Center for Computational Materials (MICCoM).

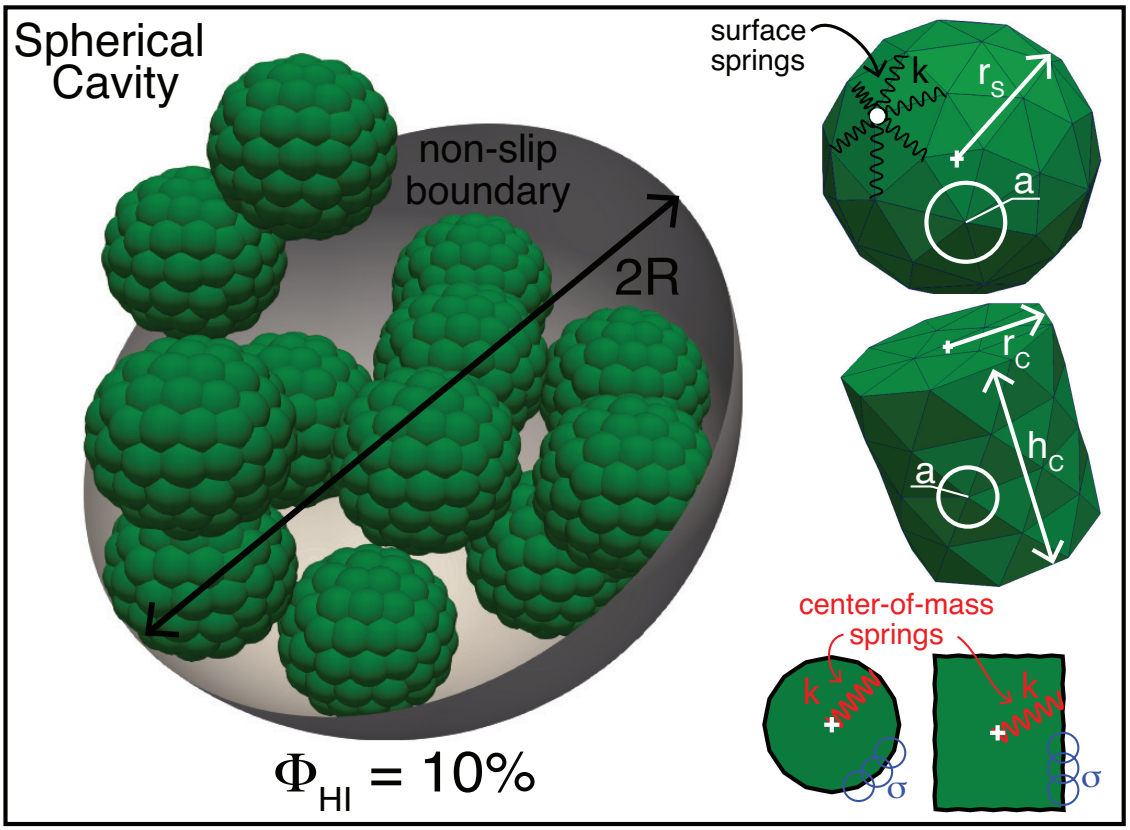

Figure 7.1: Snapshot of the spherical cavity of radius R containing spherical particles with $\Phi_{\mathrm{HI}} = 10\%$. The spherical particles radius is r_S, while the size of the cylindrical particles is determined by r_C and h_C. The surface of the particles is given by a collection of discrete nodes that are connected to six neighbors ("trimesh"), similar to boundary element discretizations, and with a characteristic node separation of $a \sim h \sim \xi_{\mathrm{IB}}^{-1}$. The neighboring nodes are connected with surface springs (black); each node is also connected to the particle center-of-mass (red spring). A repulsive Lennard-Jones excluded volume is included on each surface node, shown schematically in the particles' cross section by the blue circles. The characteristic size of the repulsion is given by $\sigma = 2.2a$.

7.4 Results

We consider spheres and cylinders, of equal volume, that are suspended in a spherical cavity of radius $R = 15$. The particles' radius is $r_S = 3$ (volume $V_{\rm HI} = 4/3\pi r_S^3$), while the cylinders' size is determined by $r_C = 2.62$ and $h_C = 2r_C$ (volume $V_{\rm HI} = \pi r_C^2 h_C$). Figure 7.1 shows the details of the system. According to our semi-rigid particle model, there are two ways to define the particle concentration in a cavity of volume V. One uses the hydrodynamic volume fraction, $\Phi_{\rm HI} = NV_{\rm HI}/V$, and a second one is based on the excluded volume effective size, $\Phi_{\rm EV} = NV_{\rm EV}/V$. Each surface node has an excluded volume of radius a, thus each spherical particle has an excluded volume of $V_{\rm EV} = 4/3\pi(r_S+a)^3$ and each cylindrical particle has an excluded volume of $V_{\rm EV} = \pi(r_C+a)^2(h_C+2a)$. We use the hydrodynamic volume fraction as the relevant scale for particle concentration. In this work, $\Phi_{\rm HI} = [5\%, 10\%, 15\%, 20\%]$ which is equivalent to $\Phi_{\rm EV} = [12\%, 24\%, 36\%, 48\%]$. The lower volume concentration selected in the work is 5%, which is the limiting volume fraction between dilution and finite concentration regimes. We found that all the results of dilute systems, starting from infinite dilution, is close to the limiting volume fraction of 5%. We start our analysis by exploring the structure of the particles using the particle number density as a function of radial position within the cavity. The number density (the probability that a particle is at a specific location) is calculated by discretizing the spherical cavity into m bins (spherical shells) with an even spacing in the radial direction. The shell radius of the i-th bin is $b_i = (i + 0.5)R/m$. The particle number density $n(r_i) =< N(r_i)/V_i >$, where $N(r_i)$ is the number of particles at shell that is located a distance r_i from the center of the cavity, V_i is the volume of the shell and <> represents an ensemble average over time. Figure 7.2 shows the number density of the particles within the cavity as a function of particle concentration. Figure 7.2(top) is for spherical particles, while Fig. 7.2(bottom) is for the cylindrical ones. At low concentrations, $\Phi_{\rm HI} = 5\%$, the number density is uniform throughout the cavity and goes to zero once the particles are in contact with the wall. Notice that the maximum density is at $r \sim 10.5$, which is smaller than wall contact. In our model, particles can never "touch" the wall

because of the strong repulsive Lennard-Jones potential. As the concentration increases, the probability of finding particles near the wall increases, forming a layered structure. At moderate concentrations, $\Phi_{\mathrm{HI}} = 10\%, 15\%$, particles start to form the first layer next to the wall, and inner particles prefer to stay near the center of the cavity where the steric effects with the particles in the first layer are the weakest. At higher concentrations, $\Phi_{\mathrm{HI}} = 20\%$, particles form a second layer, since there is not enough space at the center to accommodate them. Thus the layered structure becomes more pronounced, and the layer separation is determined by the particle size. In the figure, we include the number density of a "bead" system where particles are represented as spheres with an excluded volume with radius a. The spherical cavity has a radius of $R = 10a$. In this system, particles interact only through far-field hydrodynamics and steric repulsions. However the layered structure is also observed, becoming a characteristic of highly concentrated confined systems.

Cylindrical particles exhibits an orientational distribution within the cavity. Similar to liquid crystalline systems [219, 220], we define an orientational order parameter $\lambda = \frac{1}{2}\langle 3\cos^2\theta - 1\rangle$, where $\cos\theta = \frac{\mathbf{m}\cdot\mathbf{n}}{||\mathbf{m}||\cdot||\mathbf{n}||}$, $\mathbf{m}$ is the vector parallel to the cylinder's centerline and $\mathbf{n}$ is the vector pointing from the cavity center to the cylinder's center-of-mass. A random/disordered structure is characterized by $\lambda = 0$, whereas for ordered morphologies $\lambda = 1$, when all cylinders are aligned parallel to the radial direction of the spherical cavity (radial phase), and $\lambda = -1/2$ when all cylinders are aligned perpendicular to the radial direction of the spherical cavity (concentric phase). Figure 7.3 shows the orientational order parameter of cylindrical particles within the cavity as a function of particle concentration. A major result is that for all concentrations the cylinders are in a disordered state at the center of the cavity and oriented concentrically near the wall. For $\Phi_{\mathrm{HI}} = 5\%$, the disordered morphology spans all locations in the cavity, whereas for $\Phi_{\mathrm{HI}} = 15\%$ two concentric regions are observed, separated by a layer where the cylinders are oriented following a $< \theta >= 35^o$ or 145^o. Interestingly, the radial–centripetal ordering, $\lambda = 1$, is never observed; we believe this is due to small aspect ratio of the cylindrical particles.

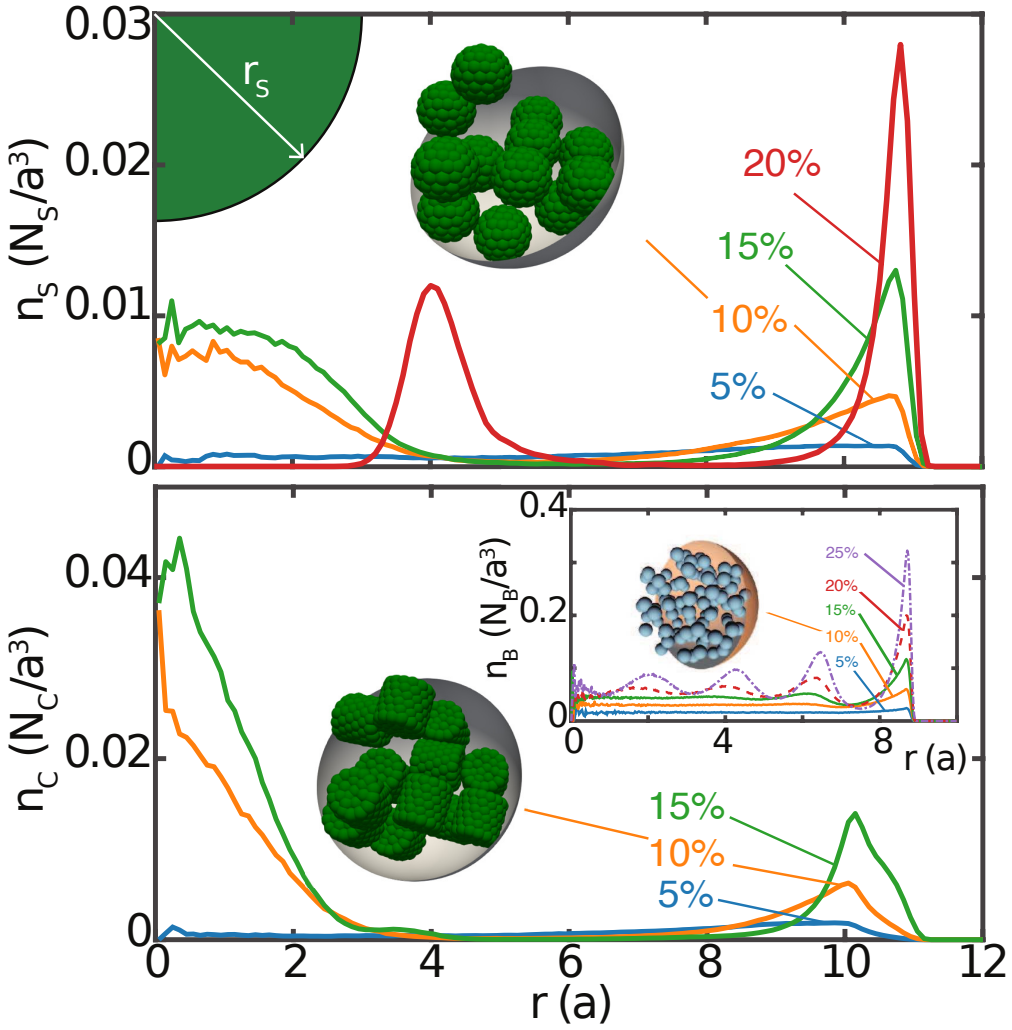

Figure 7.2: Number density of the particles within a spherical cavity of radius $R = 15$ as a function of the particle concentration. (top) spheres with $r_S = 3$; and (bottom) cylinders with $r_C = 2.62$ and $h_C = 2r_C$. Snapshots for $\Phi_{\text{HI}} = 10\%$ are shown for both systems, while the number density of HI "beads" is included in the inset.

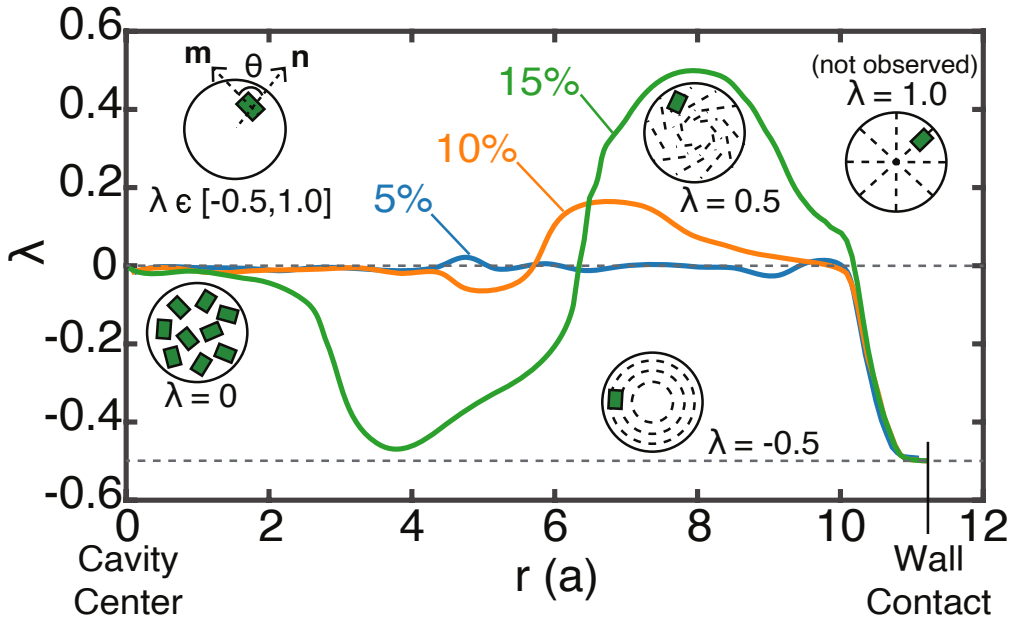

Figure 7.3: Orientational order parameter λ of cylindrical particles within a spherical cavity of $R = 15$. The radius of cylinders is $r_C = 2.62$ and the height $h_C = 2r_C = 5.24$.

We now proceed to analyze the short- and long-scale diffusive behavior in an attempt to delineate the consequences of long- and short-range HI on the dynamics of the particles. The short-time diffusion coefficient and the mean squared displacement (MSD) of the particles are used to quantify these effects. The particles are suspended in a viscous fluid under zero Reynolds number conditions; they interact with other particles and walls through the HI. Recall that under these conditions, momentum transport is infinitely fast [78, 94, 126, 68]. Previous studies of confined suspensions have shown that there are multiple factors that originate from HI that should affect the diffusion (mobility) of the particles: (i) the reduction of the particle mobility due to confinement – particles in the bulk diffuse faster than in confined geometries –, (ii) the space dependent mobility due to the non-slip conditions at the walls – particle diffusion is zero at the walls –, and (iii) the decrease of particle mobility as the concentration increases – there is an interplay between lubrication and long-range HI that becomes important as the average inter-particle distance decreases [**?** **?** **?** 213]. We seek to quantify and determine the consequences of such factors in a cavity enclosure using our model.

We start by measuring the particles' radial and tangential short-time diffusivities within the cavity as a function of particle concentration. These transport coefficients are calculated from the relation between MSD and time from Stokes–Einstein following a directional decomposition [221], i.e.

$$\langle \Delta \mathbf{x}_{\mathrm{R}}^2 \rangle(r_i) = 2D_{\mathrm{R}}(r_i)dt, \tag{7.7}$$

$$\langle \Delta \mathbf{x}_{\mathrm{T}}^2 \rangle(r_i) = 4D_{\mathrm{T}}(r_i)dt, \tag{7.8}$$

for $t \to 0$ and where $\Delta\mathbf{x} = \mathbf{x}(\mathbf{t} + \mathbf{dt}) - \mathbf{x}(\mathbf{t})$, the radial displacement $\Delta\mathbf{x}_{\mathrm{R}} = \Delta\mathbf{x} \cdot \mathbf{x}/|\mathbf{x}|$, the tangential displacement $\Delta\mathbf{x}_{\mathrm{T}} = \Delta\mathbf{x} - \Delta\mathbf{x}_{\mathrm{R}}$, $D_{\mathrm{R}}(r_i)$ and $D_{\mathrm{T}}(r_i)$ are the instantaneous radial and tangential short-time diffusivities at a distance r_i from the center of the cavity, and dt is an infinitesimal time interval. $D_{\mathrm{R}}(r_i)$ and $D_{\mathrm{T}}(r_i)$ are blocked averaged during a typical simulation at each shell, and then averaged over independent simulations. Figure 7.4 summarizes the diffusion coefficients within the cavity for spherical particles as a function of concentration. In the figure, the diffusivities are normalized by the bulk value, which is defined as single particle diffusivity at infinite dilution.

We find that the confinement hinders the particle diffusion in both directions. The highest value for the particle diffusivity at $\Phi_{\mathrm{HI}} = 5\%$ is around 60% of the bulk value. The lower particle mobility is directly related to the long-range character of the HI and the non-slip conditions at the walls. As the particle concentration increases, lubrication forces begin to dominate and particle diffusion decreases monotonically. In addition, the short-time coefficients are not constant within the cavity, showing sudden decrease as the particles approach the wall. For $\Phi_{\mathrm{HI}} = 10\%$, we calculated the averaged "inner" coefficients, which are represented by the orange dashed lines in Fig. 7.4. Importantly, the decrease in particle mobility at the walls has a stronger effect on the radial diffusion coefficient, indicated by i) the radial particle mobility decreases at $r = 7$, when compared with the tangential diffusivity that "feels" the presence of the walls at $r = 9$, ii) the radial diffusivity decreases by 0.2 from

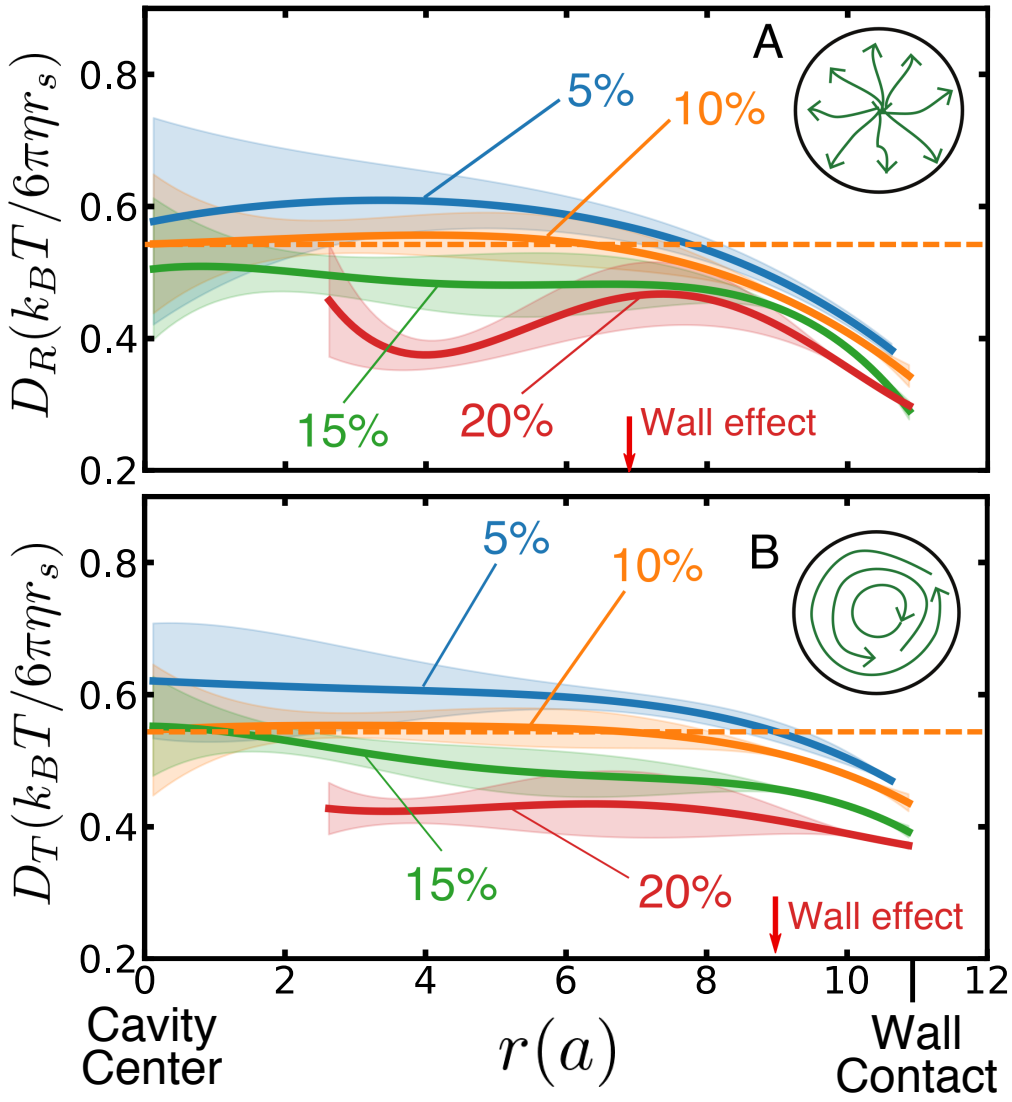

Figure 7.4: Short-time diffusion coefficients for sphere particles ($r_S = 3$) that are confined in a spherical cavity with $R = 15$: (top) Radial diffusivity and (bottom) Tangential diffusivity. The coefficients are normalized by the diffusivity of spherical particles in bulk at infinite dilution, $k_BT/(6\pi\eta r_S)$. The orange dashed line represents the averaged "inner" diffusivities for $\Phi_{\mathrm{HI}} = 10\%$. The filled shadow area around each curve represents their respective statistical error. The diffusion coefficients for $r/a < 2.3$ at $\Phi_{\mathrm{HI}} = 20\%$ are missing because there are not enough particles appearing in this zone for the diffusivity measurement due to the layered structure.

$r(a) = 7$ to the wall contact, whereas the tangential diffusivity only decreases by about 0.12. For a spherical particle near the walls, it is easier to diffuse concentrically than radially. Finally, note that for $\Phi_{\mathrm{HI}} = 20\%$ the coefficients adopt a non monotonic character, which is correlated with the layered structure of particle density in the cavity. The diffusivity data for $r(a) < 2.3$ is missing for the case of $\phi_{\mathrm{HI}} = 20\%$ because the short-time diffusion coefficient at a given location is measured on particles that appear at the location; in other words, the diffusion coefficients are measured conditionally on particle density, which is close to zero in this region (see Fig. 7.2(top)). Similar observations have also been reported by Zia et. al. using a Stokesian dynamics (SD) approach [213].

In Fig. 7.5 we include the short-time diffusion coefficients of spheres with an excluded volume confined to a spherical cavity, with and without long-range HI (no lubrication forces). Our intention is to change the level of the particle description to isolate the HI contributions. Free draining point-particles do not undergo a space dependent diffusion and the concentration perturbs the diffusion rate only weakly. For HI point particles, the mobility decreases monotonically as the particles approach the walls and the diffusion rate has a stronger dependence on concentration. Consequently, long-range HI and the zero mobility at the walls are responsible for the non-uniform particle diffusion inside the cavity. Lubrication, on the other hand, imposes a directionality on the short-time mobility – radial diffusion is different than concentric diffusion near the walls – and correlates the particle diffusion with the layered density at high volume fractions. The observed behavior is consistent with the experimental findings [**?** **?**].

It is of interest to compare the short-time diffusion coefficient between spherical and cylindrical particles and to validate the effects of the level of confinement. Figure 7.6 includes the short-time diffusion coefficients for cylindrical particles (left) in a cavity with $R = 15$ and for spherical particles (right) in a cavity with $R = 30$. In the figure, $\Phi_{\mathrm{HI}} = 5\%$ and the results for spherical particles in a cavity with $R = 15$ are included for reference. Similar to the spherical particles, the cylinders exhibit position-dependent diffusion coefficients, and

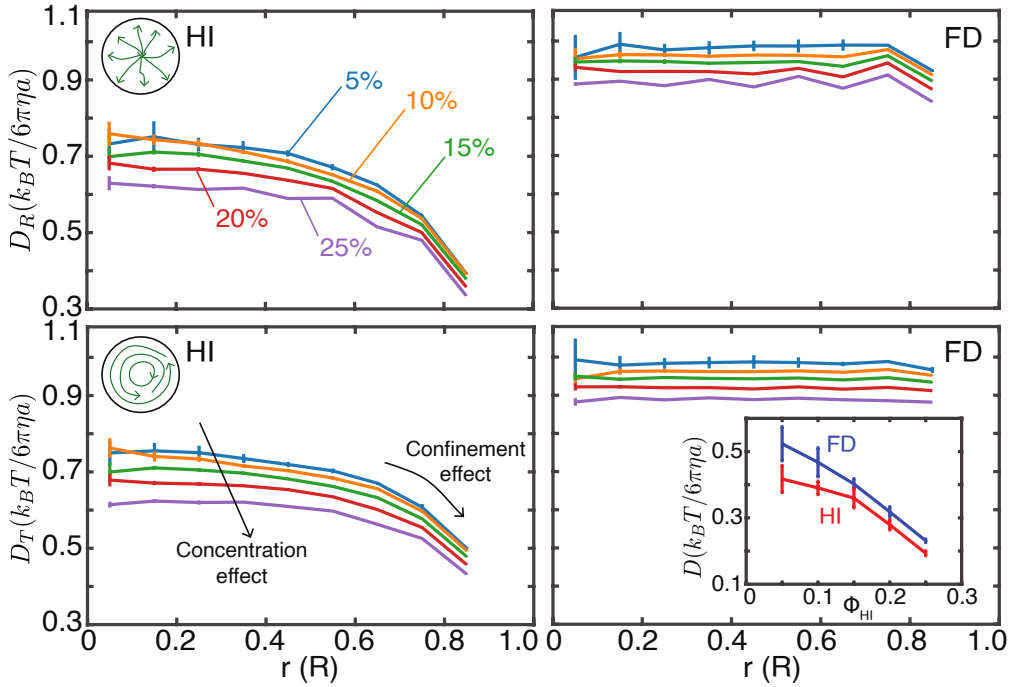

Figure 7.5: Short-time diffusion coefficients for point-particles ("beads", $r_B = 1$) that are confined in a spherical cavity with $R = 10$: Radial and tangential diffusivities for HI (left) and free-draining (right) particles. The inset shows the long-time diffusion coefficient as a function of the particle concentration.

radial diffusion is affected strongly by the presence of the walls when compared to tangential diffusion. Interestingly, the shape of the cylindrical particles has an important effect on the rate of diffusion. Recall that the cylinders and spheres have the same volume, and that the diffusion coefficients are normalized by the bulk diffusivity of spherical particles. Consequently, the short-time diffusion of particles of equal volume is decreased when the geometrical symmetry is broken. Finally, decreasing the level of confinement does not change the qualitative behavior of the short-time mobility but, as the confinement decreases, the inner diffusion coefficients approach the bulk value.

Finally, we examine the long time diffusive behavior. We use a generalized Stokes-Einstein relation where the MSD is linearly correlated with a mobility coefficient following a power law by:

$$\left\langle \left(\mathbf{R}(t) - \mathbf{R}(0)\right)^2 \right\rangle = Mt^{\alpha}, \tag{7.9}$$

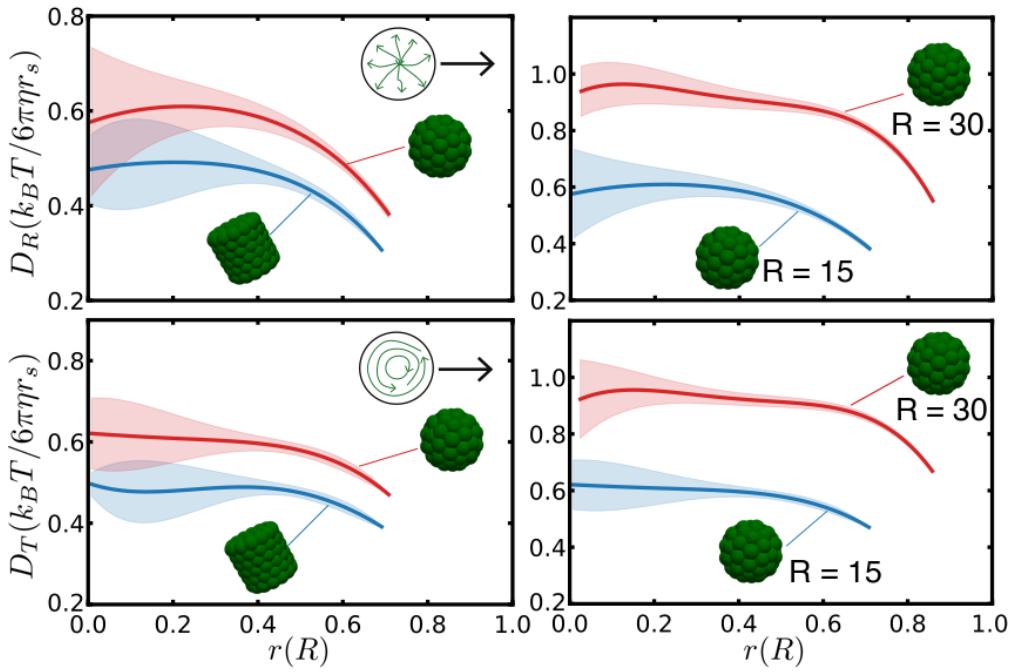

Figure 7.6: Short-time diffusion coefficients for: (left) cylindrical particles with $r_C = 2.62$ and $h_C = 2r_C = 5.24$ confined in a spherical cavity with $R = 15$ and (right) spherical particles with $r_S = 3$ confined in a spherical cavity with $R = 30$. The particle concentration is $\Phi_{\mathrm{HI}} = 5\%$ and the results for spherical particles with $r_S = 3$ confined in a spherical cavity with $R = 15$ are included for comparative purposes. The filled shadow area on each curve represents their respective statistical error.

where $\mathbf{R}$ is the $3N$ particle coordinate vector, M is the particle mobility coefficient and α is the power law exponent that characterizes the type of particle transport. For isotropic diffusion, if $\alpha = 1$ the particles are diffusive and $M = 6D$, where D is the particle long-time diffusion coefficient. If $\alpha \neq 1$, the transport of Brownian particles is said to be in the anomalous diffusion regime: $\alpha < 1$ is sub-diffusive, while $\alpha > 1$ is super-diffusive. For confined systems, as $t \to \infty$, the walls impose long-time restrictions on the mobility along the confined direction. Therefore, for particles confined in a spherical cavity, the MSD should reach a plateau on a time scale corresponding to the particle diffusion time over the cavity size.

Figure 7.7 shows the MSD of spherical (top) and cylindrical (bottom) particles in a cavity of $R = 15$ as a function of particle concentration. The time scale in Fig. 7.7 is in a diffusion time unit, $a^2\zeta/k_BT$, where $\zeta = 6\pi\eta a$. In the figures, we include the results for $\Phi_{\rm HI} = 15\%$ of the other particle shape for comparison purposes. The MSDs are collected from ten independent simulations with different random seeds; the particles were able to diffuse more than 300 a diffusion times. As expected, the MSD exhibits diffusive behavior as $t \to 0$ and a plateau when MSD$\sim 200 \sim R^2$ at τ_R, where τ_R is characteristic particle diffusion time over the cavity. At low concentrations, the diffusive behavior, for spheres and cylinders, spans from $t = 0$ to $t = \tau_R$ (for 5% spheres, $\tau_R \sim 300$ in $a^2\zeta/k_BT$ units). As the particle concentration is increased, the diffusion rate decreases; it is correlated with the short-time behavior, as indicated by the monotonic shift of the MSDs in Fig. 7.7. For spherical particles at $\Phi_{\rm HI} \geq 15\%$, there is clear sub-diffusive regime over more than two decades that increases as the concentration is increased. Interestingly, the sub-diffusive regime for cylindrical particles starts at $\Phi_{\rm HI} = 10\%$. Note that the MSD for cylindrical particles at $\Phi_{\rm HI} = 15\%$ is almost equal to the MSD for spherical particles at $\Phi_{\rm HI} = 20\%$. In the inset, we have included the MSD of spheres with excluded volume but no lubrication, to show how the sub-diffusive regime is never observed when only long-range HI is included, thereby suggesting that the sub-diffusive regime is a lubrication effect. It is then natural

to attribute this anomalous diffusion to crowding, driven by short-range HI. This regime is then characterized by the diffusion-to-crowding transition τ_{DtC} time, and by the power law exponent α. In this regime, there are two major features: τ_{DtC} and α decrease as the particle concentration increases. In particular, $\tau_{\mathrm{DtC}} = 20$ and $\alpha = 0.85$ for cylinders at $\Phi_{\mathrm{HI}} = 10\%$, while $\tau_{\mathrm{DtC}} = 5$ and $\alpha = 0.65$ for cylinders at $\Phi_{\mathrm{HI}} = 15\%$. After the highly concentrated systems enter the crowding regime, and given the fact that there are three dimensional restrictions in their mobility as t approaches τ_R, the particles transition from the slow rate sub-diffusive behavior to the plateau. In Appendix 7.6.3, we show that our mean square displacements for spheres agree with the isotropic mean square displacement analysis reported in literature [213, 212], both qualitatively and quantitatively. Ref.[213] reported both sub-diffusive and super-diffusive regimes at intermediate time scales, where the latter was only observed for high-concentration systems.

7.5 Conclusions

We have used an Immersed Boundary approach to study the structure and dynamics of suspended spherical and cylinderical particles confined in a spherical cavity.

At low concentrations, the particle number density distribution is uniform in the interior of the cavity. As the concentration increases, a layered structure appears. Cylindrical particles exhibit a random orientation at low concentrations, and at the center of the cavity, for all concentrations. Excluded volume interactions at the wall force the cylinders to orient concentrically. Interestingly, at high concentrations the layered morphology of the cylinders is correlated with concentric layers that are separated by a layer of cylinders oriented at an average angle of 35^o with respect to the radial direction. Cylinders are never found forming radial morphologies within the spherical cavity.

We used a multiple hydrodynamical description of the suspended particles to determine the specific influence of hydrodynamic interactions during the dynamic of the particles (diffusion/mobility): (i) free draining point-particles, (ii) long-range hydrodynamic "beads" and

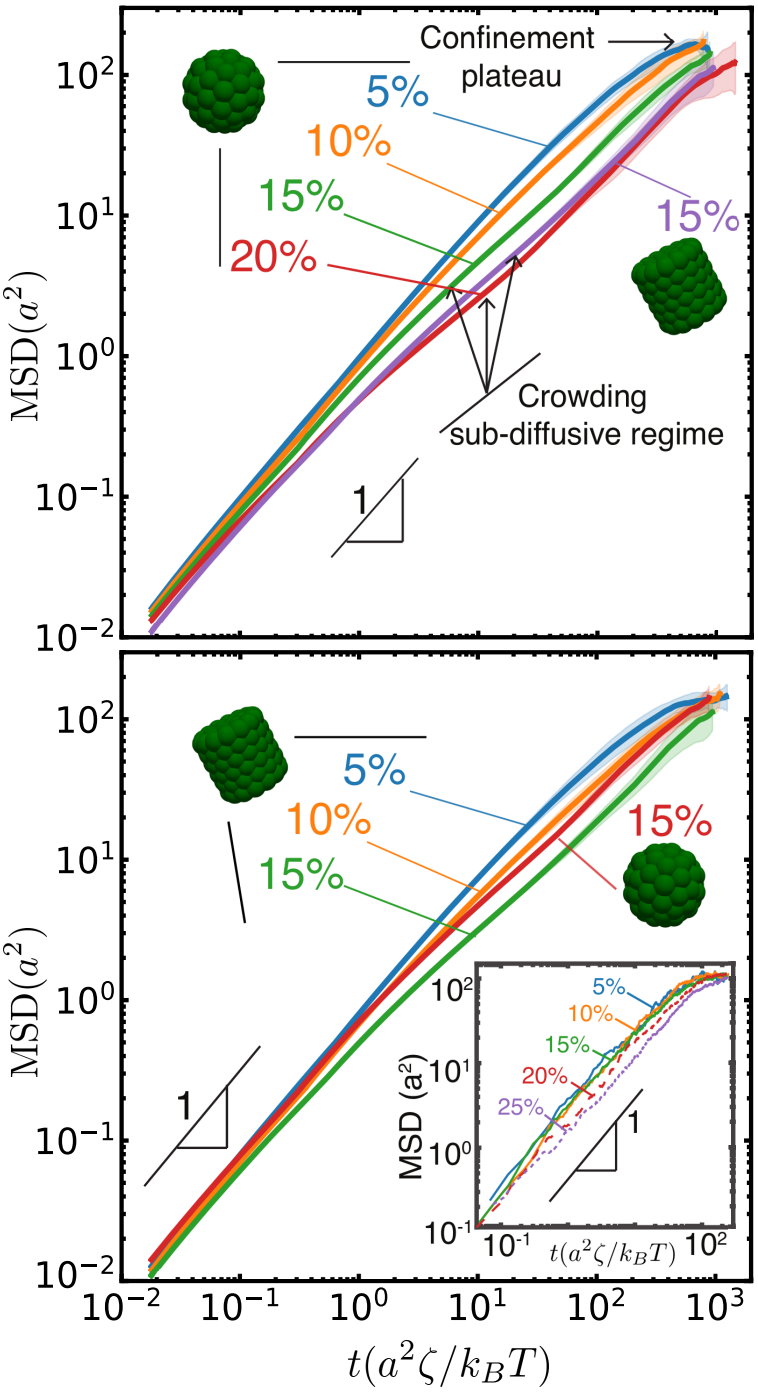

Figure 7.7: Mean square displacement as a function of time for finite-size particles suspended in a spherical particle of size $R = 15$. (top) spheres with a radius $r_S = 3$ and (bottom) cylinders with $r_C = 2.62$ and $h_C = 2r_C$. In the inset is the evolution of the mean square displacement for point-particles ("beads") suspended in a spherical cavity of radius $R = 10$. In each figure, the MSDs for $\Phi_{\text{HI}} = 15\%$ of the other particle shape are included for comparison purposes. The filled shadow area around each curve represents their respective statistical error.

(iii) finite size particles considering lubrication and long-range HI. We found that long-range HI leads to a position-dependent diffusion of the particles inside the cavity; the particles diffuse faster near the center of the cavity and slower near the walls. The HI also decrease the global mobility of the suspended particles, when compared with their diffusion in the bulk. The increase in particle concentration also results in a decrease of the particles' diffusion coefficients; this effect is observed for free-draining and HI particles. However, the concentration decrease of the diffusion rate is stronger when HI are considered. Lubrication forces, or short-range HI, influence the dynamics of highly concentrated suspensions; they generate a direction dependent diffusion, where particles diffuse at a lower rate when moving towards the walls than when moving parallel to the walls. The non-slip conditions at the walls, i.e. zero particle mobility, work synergistically with lubrication forces, resulting in an stronger wall dependence of the diffusion coefficients in the radial direction.

Regarding the long–time dynamics, lubrication gives rise to a sub-diffusive regime at high particle concentrations. The sub-diffusive regime, characterized by the diffusion-to-crowding transition time and the mobility power law exponent, becomes more prominent as the concentration increases.

Introducing cylindrical particles has two major consequences: (i) cylindrical particles have lower short-time diffusion coefficients and (ii) the crowding regime is observed at lower concentrations compared with spheres of equal volume. These observations suggest that the shape of bio-molecules, particles and polymers could determine their mobility and diffusion inside cells and tissues.

7.6 Appendix

7.6.1 Suspended Brownian spheres with the IB-pFE-GgEm

There are three important validations that are in order to verify the Immersed Boundary approach that we used in this work. We start by verifying the fulfillment of Stokes' law by

measuring the sedimentation velocity of a spherical particle that is confined between two parallel walls. Analytical values for this velocity are extracted from previous works [222**?** **?** , 225, 226, 227, 216]. For the specific IB-pFE-GgEm calculation, the particle radius $r_S = 5$ and the wall distance is $H = 15$. Periodic boundary condition (PBC) is enforced in the unconfined directions, which are set to a length of 200 ($\gg H$) to avoid the influence of the particle periodic images. The surface of the spherical particle is discretized using 119 surface nodes, resulting in a nodal separation between $h_{\min} = 1.33408$ and $h_{\max} = 1.90539$ and a smoothing parameter $\xi_{\text{IB}} = 1/0.76h_{\min}$. For the calculation we used a GgEm parameter $\alpha_{\text{GgEm}} = 0.2$ and a mesh resolution with a spacing of $1/\sqrt{2}\alpha$. The resulting mesh was $60 \times 60 \times 6$ HEX20 elements with 324,886 degrees of freedom. The particle is initially located at (0, 0, d) between the two parallel walls and it moves parallel to the walls under a sedimenting force with a body force density of (0, 0, 1). The particle's sedimenting velocity ($U_{||}$) is calculated by averaging particle's velocities over 100 time steps. Figure 7.8(top) shows the sedimenting velocity, normalized by Stokes' velocity $U_{||}/U_0$, as a function of normalized location ($(d - R)/H$). According to the results, the IB-pFE-GgEm provides an excellent agreement with analytical values.

In addition to Stokes' law, it is important to verify that our combined approach, between the IB-pFE-GgEm, Fixman's mid-point algorithm and the Chebyshev polynomial approximation, is satisfying the Fluctuation-Dissipation Theorem. A sphere that is confined in a spherical cavity and between parallel walls offers a scenario to validate the connection between the diffusion and the fluctuating tensors and the proper calculation of the mobility gradients inside the confined geometries. First, we used three different particle discretizations, using 20, 40 and 60 nodes, for the sphere of size $r_S = 3$ that is confined in a spherical cavity of size $R = 15$. Figure 7.8(center) shows the comparison between the short-time diffusion coefficient of the sphere computed through our IB-pFE-GgEm algorithm and SD algorithm previously reported in literature [213]. These results suggest that even with poor surface descriptions, as long as the IB parameter is appropriately chosen, the IB-pFE-GgEm follows

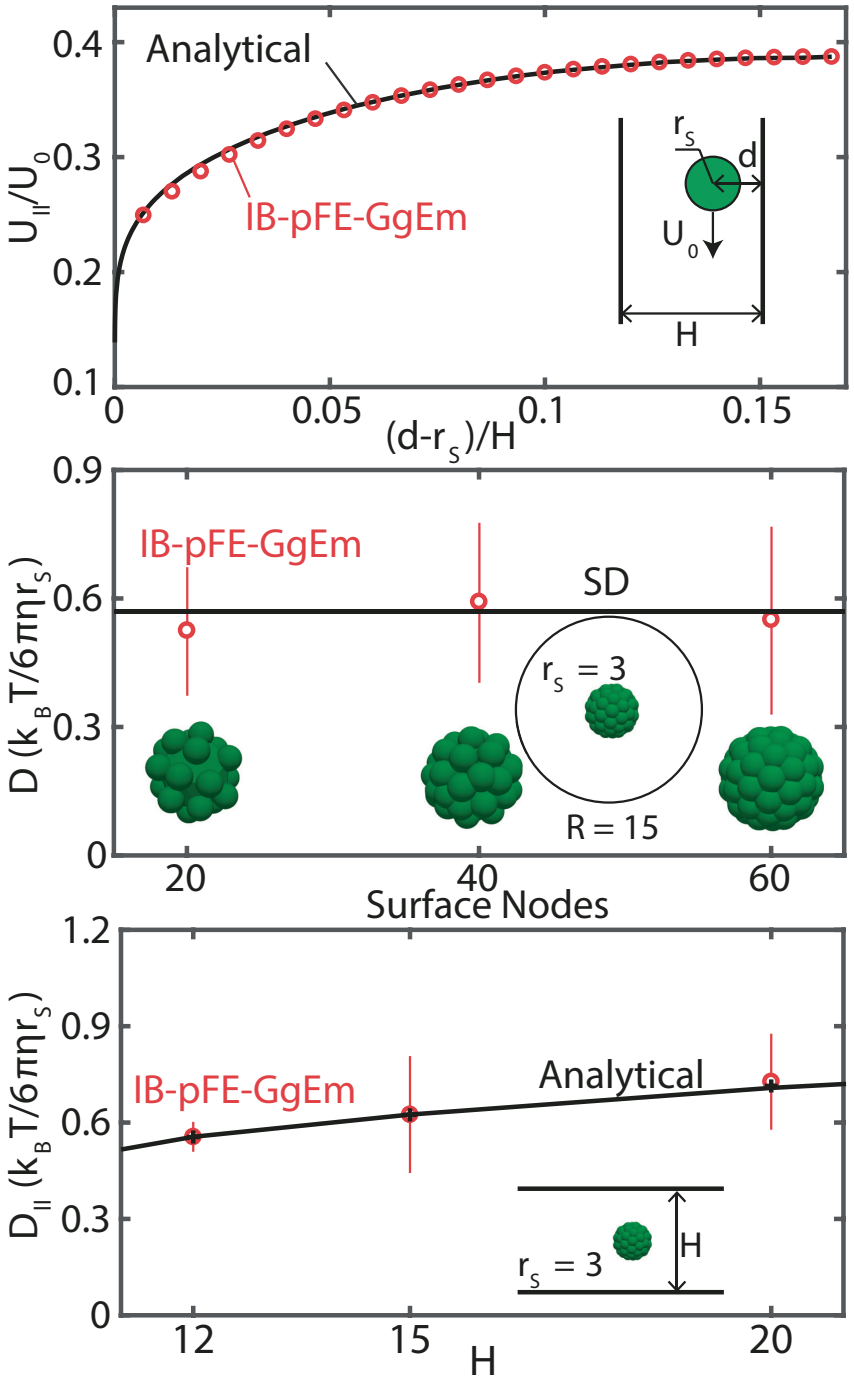

Figure 7.8: Sphere representation with the Immersed Boundary method: (top) Normalized sedimenting velocity of a spherical particle between two parallel walls as a function of the distance between the particle and the nearest wall. Analytical data are taken from Ref. [216]. (center) Diffusion coefficient of a spherical particle with $r_S = 3$ that is confined in a spherical cavity of size $R = 15$. SD data are taken from Ref. [213]. (bottom) $xy-$plane diffusion coefficient for a spherical particle with radius $r_S = 3$ in the center of a slit with heights $H = 12$, 15, and 20. Analytical data are taken from Ref. [228].

the correct fluctuating short-time behavior. Finally, the long-time diffusion for a sphere confined in a slit as a function of the separation between the walls is shown in Fig. 7.8(bottom). Analytical and numerical solutions for this coefficient had been well assessed in the literature [228, 229, 230, 231]. For the IB-pFE-GgEm, the particle is initially located at the mid-plane between two parallel walls. During the particle's Brownian movement, its motion is restricted to the plane of symmetry. The surface of the spherical particle is discretized using 20 surface nodes ($h_{\min} = 2.19826$, $h_{\max} = 2.52608$ and $\xi_{\mathrm{IB}} = 1/0.35h_{\min}$). The slit mesh resulted in $60 \times 60 \times 4$ HEX20 elements with 228,872 degrees of freedom. To calculate the error bars of the MSD, five independent simulations for each confinement ratio are performed with a constant time step of 0.002 [232]. The diffusion coefficients from the IB-pFE-GgEm shows an excellent agreement with analytical and numerical results.

7.6.2 Rigidity of the suspended particle

In our Immersed Boundary description of the finite-size particles, each surface node is linked to its neighboring nodes and the center-of-mass through linear springs with a prescribed stiffness constant k. This parameter controls the stiffness (shape) of particles. If the springs are too weak, particles are deformable and special care must be done to forbid fluid penetration. On the other hand, if the springs are too stiff, the forces acting on surface nodes will be too large, requiring very small time steps to ensure numerical stability. We performed simulations of spherical particles that are confined in a spherical cavity at high concentrations varying the particle stiffness. We measured the particles' moment of inertia for each particle ν as follows:

$$I_\nu(t) = \sum_{j=1}^{N_{\mathrm{S}}} r_j(t)^2, \tag{7.10}$$

where $I_\nu(t)$ is the moment of inertia of particle ν at time t and $r_j(t)$ is the distance between node j on surface and the particle center-of-mass. Rigid spheres will have an equal and constant moment of inertia. On the other hand, our semi-rigid particles will show a variation

in $I_\nu(t)$. Figure 7.9 shows the averaged standard deviation of moment of inertia as a function of time for particles with different k for $\Phi_{\mathrm{HI}} = 20\%$. The standard deviation is calculated by

$$\sigma_{\mathrm{MI}}(t) = \sqrt{\frac{\sum_{\nu=1}^{N} \left(I_\nu(t) - I_\nu(0)\right)^2}{N}}, \tag{7.11}$$

where $I_\nu(0)$ is the moment of inertia of particle ν at time 0, which corresponds to a perfect sphere. As one can observe from the figure, in the case that $k = 10$, the moment of inertia jumps from 0.05 to 0.06 at $t \approx 10$, indicating $k = 10$ is not stiff enough to maintain particle shape. As the stiffness is increased the shape variations decrease. In this work, we used a $k = 200$ for all simulations.

7.6.3 Comparison of MSD with literature results

The equilibrium structure and diffusion in concentrated hydrodynamically interacting spherical particles confined in a spherical cavity was studied using SD by Aponte-Rivera *et al.*[213]. There are differences between methods in our and their work such as particles models, HI models, etc. However, one can draw both quantitative and qualitative agreements between results from two methods. Here we present the comparison of isotropic MSD at different volume fractions (Fig.15a in Ref. [213] and the top panel in Fig.7.7 in this work). Qualitatively, a short-time diffusive regime and a long-time plateau for systems at all concentrations are observed in both works. At intermediate times, a sub-diffusive region emerges for highly concentrated systems only. To make a semi-quantitative comparison, we convert the MSD data in Ref. [213] to those with the units used in our work at the same level of excluded volume crowding. Specifically, the length and time reported by Aponte-Rivera *et al.* is normalized by the radius of a sphere with radius r_s and the characteristic diffusion time t_0 of a sphere with radius r_s, respectively ($t_0 = r_s^2/D_0$, where $D_0 = k_B T/6\pi\eta r_s$). By multiplying the time, MSD, and volume fraction in the their work by r_s^3, r_s^2, and $(r_s/r_s + a)^3$ ($r_s = 3a$), respectively, we can compare the isotropic MSD directly. For example, for the system with

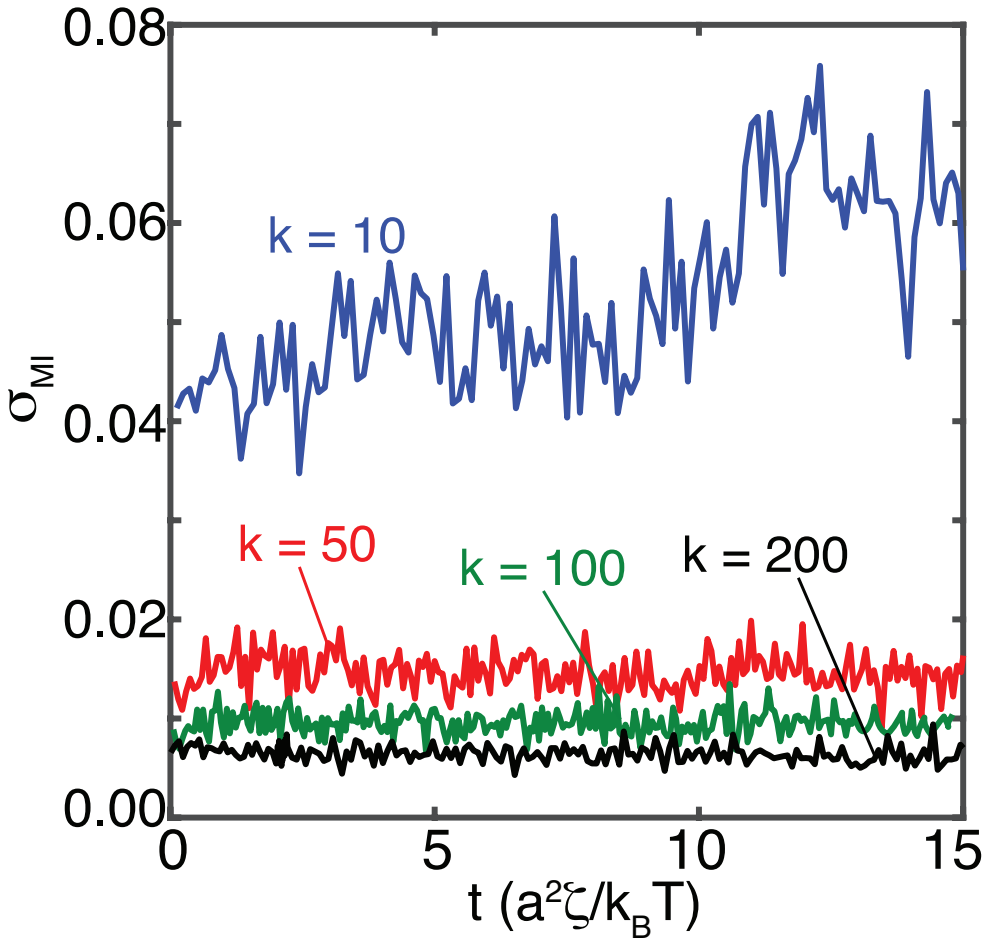

Figure 7.9: Time evolution of the standard deviation of the sphere moment of inertia as a function of the spring stiffness. The particle volume fraction is $\Phi_{\mathrm{HI}} = 20\%$, the particle radius is $r_S = 3$ and the number of surface nodes on each particle is 20.

the highest concentration in Ref. [213] (40% in their work and 17% after conversion to our unit; the converted value will be reported in round brackets in the following), the short-time diffusive regime lasts from t $\approx 10^{-3}$ (10^{-2}) to $\approx 10^{-1}$ (10^{0}) while the MSD increases from 10^{-3} (10^{-2}) to 10^{-1} (10^{0}); the intermediate sub-diffusive regime lasts from t $\approx 10^{-1}$ (10^{0}) to t $\approx 10^{1}$ (10^{2}) while the MSD increases from 10^{-1} (10^{0}) to 10^{0} (10^{1}); the MSD reaches the plateau 10^{1} (10^{2}) at t $\approx 10^{2}$ (10^{3}). Good agreement is found between our MSD data and those reported in Ref. [213].

CHAPTER 8

APPLICATION: SHAPE INDUCED SEGREGATION AND ANOMALOUS PARTICLE TRANSPORT UNDER SPHERICAL CONFINEMENT

8.1 Abstract

Colloid or nanoparticle mobility under confinement is of central importance to a wide range of physical and biological processes. Here, we introduce a minimal model of particles in a hydrodynamic continuum to examine how particle shape and concentration affect the transport of particles in spherical confinement. Specifically, an immersed boundary–General geometry Ewald-like approach is adopted to simulate the dynamics of spheres and cylinders under the influence of short- and long-range fluctuating hydrodynamic interactions with appropriate non-slip conditions at the confining walls. An efficient $O(N)$ parallel finite element algorithm is used, thereby allowing simulations at high concentrations, while a Chebyshev polynomial approximation is implemented in order to satisfy the fluctuation–dissipation theorem. A concentration–dependent anomalous diffusion is observed for suspended particles. It is found that introducing cylinders in a background of spheres, i.e. particles with a simple degree of anisotropy, has a pronounced influence on the structure and dynamics of the particles. First, increasing the fraction of cylinders induces a particle segregation effect, where spheres are pushed towards the wall and cylinders remain near the center of the cavity. This segregation leads to a lower mobility for the spheres relative to that encountered in a system of pure spheres at the same volume fraction. Second, the diffusive-to-anomalous transition and the degree of anomaly – quantified by the power law exponent in the mean square displacement vs. time relation – both increase as the fraction of cylinders becomes larger. These findings are of relevance for studies of diffusion in the cytoplasm, where proteins exhibit a distribution of size and shapes that could lead to some of the effects identified

in the simulations reported here.

8.2 Introduction

) Colloidal and nanoparticle diffusion in confined environments arises in a wide range of scientific and engineering systems, including living cells, mesoporous materials, or microfluidic devices [222, 233, 234, 235, 236]. It is also of interest for energy generation processes that rely on salinity or electrostatic gradients in pores [149, 150, 152, 237]. In the particular case of the cytoplasm, the diffusion of biomolecules underpins a variety of intracellular metabolic, translational and locomotion processes, to name a few. [238, 239, 208, 202, 202]. Interestingly, particle diffusion in these confined systems is often found to be severely hindered and anomalous [240, 241, 81]. The mechanisms behind those observations, however, remain poorly understood.

Several literature studies have examined particle mobility in living cells [242, 83] by relying on Brownian dynamics (BD) simulations. In such studies, biological macromolecules have been represented as spheres, and numerical simulations have found evidence of hindered diffusion, in agreement with experimental results. Majority of previous studies, however, have failed to consider hydrodynamic interactions between particles or between particles and the confining walls. Some exceptions are provided by the work of Ando et al. [79] and Chow et al. [211], who included hydrodynamic interactions between particles, but did not enforce the no-slip boundary condition at the walls. More recently, Stokesian dynamics (SD) simulations of spheres by Aponte-Rivera et al. [212, 213] considered both far– and near–field (lubrication) hydrodynamic interactions (HI) between particles and walls. The authors demonstrated that HI have a pronounced influence on the local structure and the short–time and long–time diffusive behavior of particle suspensions. The framework employed by these authors relied on SD, and was restricted to a homogeneous system of spherical particles [213].

Recently, we have introduced an efficient computational approach in order to overcome some of the limitations of other available numerical approaches for hydrodynamic interac-

tions. In particular, this approach can be easily extended to particles of arbitrary shape dispersed in a confined geometry also of arbitrary shape [201**?**]. An Immersed–Boundary (IB) method is used to represent the suspended finite–sized particles. A parallel Finite Element General geometry Ewald-like method (pFE-GgEm) [201] is used to calculate the confined Green's functions, which relies on a Chebyshev polynomial approximation to satisfy the fluctuation-dissipation theorem. In Chapter 7, we relied on this approach to compare the structure of pure spherical and pure cylindrical particles confined in a spherical cavity. It was found that cylindrical particles diffuse slower as compared to spherical particles of the same volume and at the same volume fraction, and that for cylinders the transition from the diffusive to the sub-diffusive regime occurs at a lower volume fraction.

The studies mentioned above focused on pure spheres or cylinders confined in a spherical cavity. The more relevant case of mixtures of spheres and cylinders was not considered. Indeed, in applications (e.g. cytoplasm or colloidal suspensions) one rarely deals with systems of pure mono-disperse spheres, and it is therefore of interest to consider how mixtures behave relative to their pure counterparts. Note that limited experimental evidence with mixtures of particles of different sizes and shapes indicates that cells exhibit preferential accumulation of some particles near the nucleus [244, 245]. In those cases, size based segregation was explained on the basis of a "sieving effect" that has been advanced in the dry granular segregation literature [246, 247]. An explanation for shape-based segregation was not proposed in that work. Other experimental work, including a study of centrifugation of colloidal rods and spheres [248], and a study in which milli–meter sized glass beads and rods were subject to strong vibration [249], have also reported segregation effects based on particle shape, and proposed that hydrodynamic forces based on the different shapes contribute to that segregation.

Our particular goal here is to provide a standard against which past and future observations of segregation and diffusion can be compared by simulating mixtures of particles of equal volume but having a spherical or a cylindrical aspect ratio $h_c/r_c = 2$. By doing so,

we seek to rationalize past reports with new evidence for size-based segregation and mobility gradients in systems where dimensions and interactions are perfectly controlled, thereby eliminating or avoiding some of the complexity that arises in laboratory experiments. The outline of this chapter is as follows: in Section 8.3 we describe our numerical setup and methodology. Our results on the structure and dynamics of mixtures of spheres and cylinders are presented in Section 8.4. We conclude the manuscript with a discussion of our findings in Section 8.5, along with a possible outlook for future studies.

8.3 Models and methods

The system considered here consists of N semi–rigid particles embedded in a viscous fluid of viscosity η that are enclosed in a spherical cavity of radius R. The equations of motion under the condition of zero Reynolds number and zero Stokes number are given by

$$\mathbf{F}^H + \mathbf{F}^B + \mathbf{F}^C + \mathbf{F}^{EV} + \mathbf{F}^{ext} = 0 \ , \tag{8.1}$$

where $\mathbf{F}^H$ is the $6N$ vector containing the hydrodynamic force/torque, $\mathbf{F}^B$ is the Brownian force/torque, $\mathbf{F}^C$ is the force/torque containing configuration terms, $\mathbf{F}^{EV}$ represents force/torque excluded volume contributions and $\mathbf{F}^{ext}$ includes any external force/torque.

Evolution of the suspended particles, using Eqn. (8.1), is achieved using the grand mobility or resistance tensors that relate the hydrodynamic force/torque with the translational and rotational velocities of the particles [105, 214, 215]. Approaches like SD [107, 108, 216] and boundary integral methods (BIM) [105, 104] are used extensively to solve the "mobility problem". The regularized Stokeslets [116], the accelerated BIM [217] and the Immersed Boundary (IB) [146, 218, 250, 251, 252] provide examples of numerical methods developed to improve computational efficiency by simplifying or avoiding the calculation of the single- and double-layer hydrodynamic potentials of suspended particles. On the case of the Immersed Boundary (IB) approach, the surfaces of the suspended solids are represented by a

distribution of discrete force densities on a surface mesh (N_{IB} immersed boundary nodes) that, together with a surface force description and Stokes equations, leads to the evolution of the suspended particles. This is the approach that we use in this chapter.

The probability distribution function for the surface mesh positions in a Lagrangian frame of reference evolves according to a convection-diffusion equation of the Fokker-Planck type [87]. We assume a continuous probability density and use the Chapman-Kolmogorov equation white noise to obtain an equivalent stochastic differential equation for the motion of the mesh points [88]

$$d\mathbf{R} = \left[\mathbf{U_0} + \mathbf{M}\cdot\mathbf{F} + \frac{\partial}{\partial\mathbf{R}}\cdot\mathbf{D}\right]dt + \sqrt{2}\mathbf{B}\cdot d\mathbf{W}, \tag{8.2}$$

where $\mathbf{U_0}$ denotes a $3(N \times N_{\mathrm{IB}})$ vector of the unperturbed fluid velocity generated by external pressure differences or shear at the mesh point positions; $\mathbf{M}$ is the mobility tensor that includes the Stokes' drag and the pair-wise Stokeslets accounting for the hydrodynamic interactions between mesh points; $\mathbf{D} = k_B T\mathbf{M}$ is the $(3N \times N_{\mathrm{IB}}) \times (3N \times N_{\mathrm{IB}})$ diffusion tensor; $\mathbf{F}$ is a $3(N \times N_{\mathrm{IB}})$ vector of the non-Brownian and non-hydrodynamic forces; k_B is the Boltzmann constant; T is the temperature; $\mathbf{M}\cdot\mathbf{F}$ is a convection term that represents the bead velocities arising from hydrodynamic interactions; the divergence of the diffusion tensor, $\partial/\partial\mathbf{R}\cdot\mathbf{D}$, is the first diffusive term resulting from the configuration-dependent mobility of the confined mesh points; $d\mathbf{W}$ is a random vector, the components of which are obtained from a real-valued Gaussian distribution with zero mean and variance dt, and it is coupled to the diffusion tensor through the fluctuation-dissipation theorem, $\mathbf{D} = \mathbf{B}\cdot\mathbf{B}^T$; and finally, the second diffusive term, $\sqrt{2}\mathbf{B}\cdot d\mathbf{W}$, represents the Brownian displacement that results from collisions between mesh points and the surrounding (implicit) solvent.

The main challenge in simulating a stochastic process using Eqn. (8.2) is the fact that the mobility tensor, $\mathbf{M}$, cannot be constructed explicitly under confinement for arbitrary geometries. This implies that the fluctuating velocity, $\mathbf{U}$, the divergence of the diffusion

tensor, $\nabla \cdot \mathbf{D}$, and the diffusion tensor decomposition, $\mathbf{B}$, must be implemented in a way such that the scheme is matrix-free. To address this issue, we have developed an efficient $O(N)$ numerical algorithm, parallel Finite Element - General Geometry Ewald-like Method (pFE-GgEm)[201]. The algorithm uses (i) the General geometry Ewald-like method (GgEm)[118] for a matrix-free product of the mobility tensor with any vector, $\mathbf{M} \cdot \mathbf{F}$; (ii) a mid-point algorithm, proposed by Fixman[130], that avoids the explicit calculation of $\nabla \cdot \mathbf{D}$; and (iii) a Chebyshev polynomial approximation for the $\mathbf{B} \cdot d\mathbf{W}$ product that uses GgEm to avoid the explicit calculation of $\mathbf{D}$. The algorithm is able to handle arbitrarily shaped confining walls.

Each particle is represented by a discretized surface, whose details are available in Chapter 7. Using the Immersed Boundary (IB) method [125], the force distributions at these particles are discretized as distributions of regularized point-forces. In particular,

$$\boldsymbol{\rho}^{f}_{\mathrm{IB}}(\mathbf{x}) = \sum_{\nu=1}^{N_{\mathrm{IB}}} \mathbf{f}^{\mathrm{C}}_{\nu} \delta_{\mathrm{IB}}(\mathbf{x} - \mathbf{x}_{\nu}), \tag{8.3}$$

where $\mathbf{f}^{\mathrm{C}}_{\nu}$ represents the constitutive force acting on ν-th surface node (point force with an excluded volume of radius a), N_{IB} represents the number of surface nodes that are used to represent the suspended finite-size particles, δ_{IB} is the modified Gaussian regularization function. The regularization parameter ξ_{IB} in δ_{IB} is related to the characteristic length h for the node spacing on the particle surface, i.e. $\xi_{\mathrm{IB}} \sim h^{-1} \sim a^{-1}$. By doing this, we ensure that the regularized force on each node is spread over the length scale of the associated surface elements to prevent fluid from "penetrating" the particles.

The volume of spheres and cylinders is the same. Each surface node is linked to the neighboring node as well as to the center-of-mass point of the particle using an elastic spring with stiffness k. A spring network is formed for every particle, which results in an internal nodal force that resists deformation and maintains its shape. At the same time, a repulsive Lennard-Jones (LJ) potential is used for particle-particle and particle-wall excluded volume interactions. The ratio between mesh and particle size controls the number of surface nodes

on each particle. Increasing the number of nodes improves accuracy but also increases the computational cost. In Chapter 7, we showed that a spring stiffness $k = 200$ is sufficient to simulate "semi-rigid" particles, where despite the high concentration of particles, excluded volume interactions do not alter the particle shape. In addition, we found that particle discretization at the level of $N_{IB} = 20$ is enough to avoid fluid penetration, satisfy Stokes' law and provide the correct diffusional behavior. In this chapter, however, we use spheres and cylinders discretized with $N_{IB} = 88$ to ensure extremely high accuracy.

In what follows, the characteristic units are: a for length, $a^2\zeta/k_BT$ for time, k_BT for the energy and k_BT/a for the force. ζ, the node friction coefficient is related to the fluid viscosity η and a through Stokes' law, i.e., $\zeta = 6\pi\eta a$, and the unit diffusivity, D_0, is defined as the diffusivity of a sphere in an infinite fluid with viscosity η, i.e., $D_0 = k_BT/6\pi\eta a$.

8.4 Results

We consider different particle mixtures of spheres and cylinders suspended in a Newtonian viscous fluid within a spherical cavity of radius $R = 15$. The spherical particle has a radius $r_s = 3$, leading to a hydrodynamic volume of $V_{\mathrm{HI}} = 4/3\pi r_s^3$. The cylinders have an aspect ratio of 2, i.e., $h_c = 2r_c$, where $r_c = 2.62$ is the radius and h_c is the height. Figure 8.1 shows several details of our simulations and representative snapshots for $\phi = 0.2$ with different cylinder fractions.

In our semi-rigid particle model, there are two ways to define the particle concentration in a cavity of volume V. A hydrodynamic volume fraction can be defined as $\phi_{\mathrm{HI}} = N_T V_{\mathrm{HI}}/V$; a second one is based on the excluded volume, $\phi_{\mathrm{EV}} = N_T V_{\mathrm{EV}}/V$, where for spheres and cylinders we have $V_{\mathrm{EV}} = 4/3\pi(r_S + a)^3$ and $V_{\mathrm{EV}} = \pi(r_C + a)^2(h_C + 2a)$, respectively. In the remainder of the article, we will use the hydrodynamic volume fraction ϕ_{HI} (referred to as ϕ in the rest of the paper) to denote the concentration of the particles. In this work, we explore $\phi = [5\%, 10\%, 15\%, 20\%]$; this would correspond to $\phi_{\mathrm{EV}} = [12\%, 24\%, 36\%, 48\%]$.

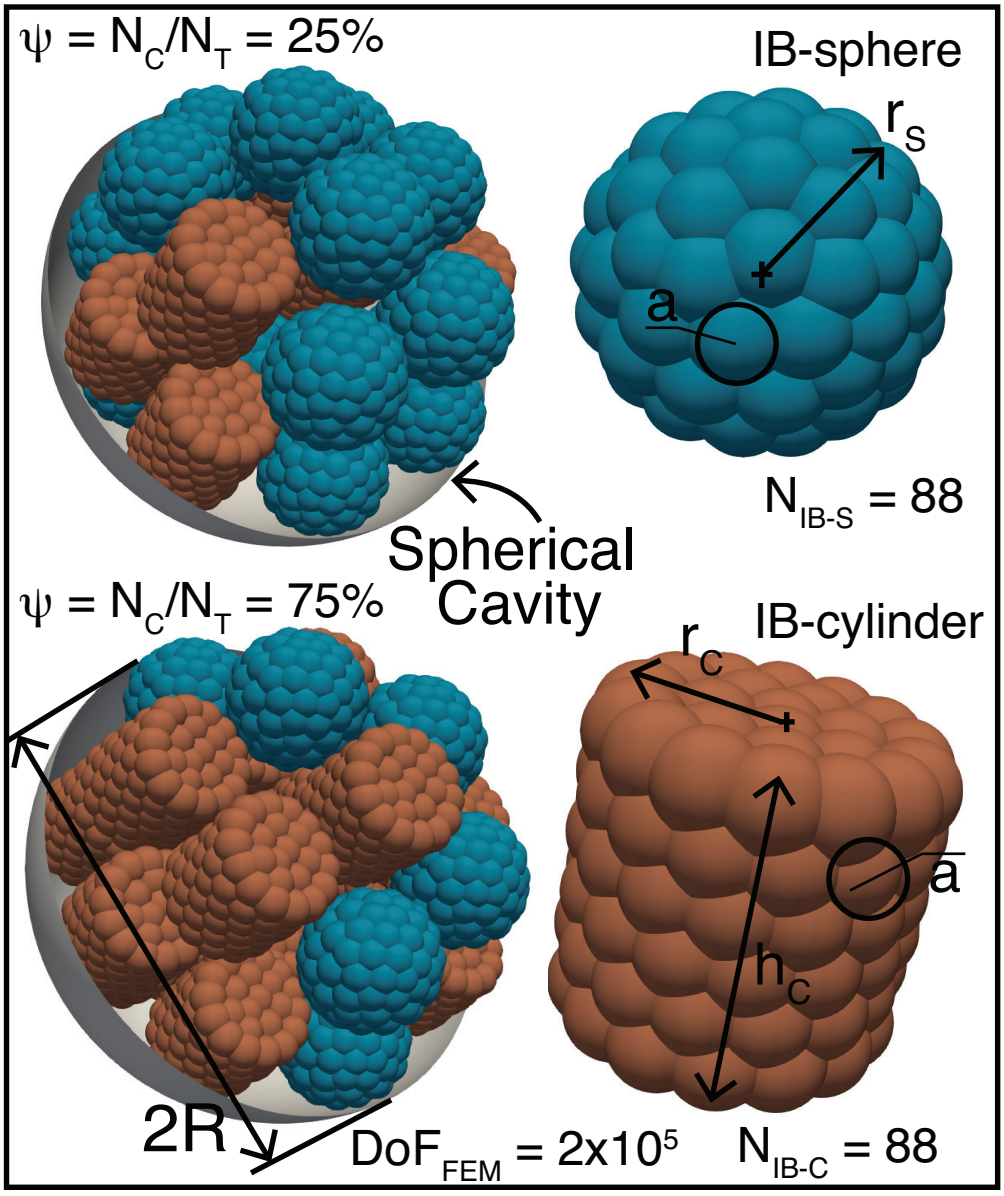

Figure 8.1: Snapshots of the spherical cavity of radius R containing spherical and cylindrical particles with $\phi_{\mathrm{HI}} = 0.2$ for fraction of cylinders $\psi = \mathrm{N_C/N_T}$ being 0.25 and 0.75. The spherical particles radius is r_S, while the size of the cylindrical particles is determined by r_C and h_C. The surface of the particles is given by a collection of discrete nodes that are connected to six neighbors, similar to boundary element discretizations, and with a characteristic node separation of $a \sim h \sim \xi_{\mathrm{IB}}^{-1}$. A repulsive Lennard-Jones excluded volume is included on each surface node, shown schematically in the particles' cross section by the black circles. The characteristic size of the repulsion is given by $\sigma = 2.2a$.

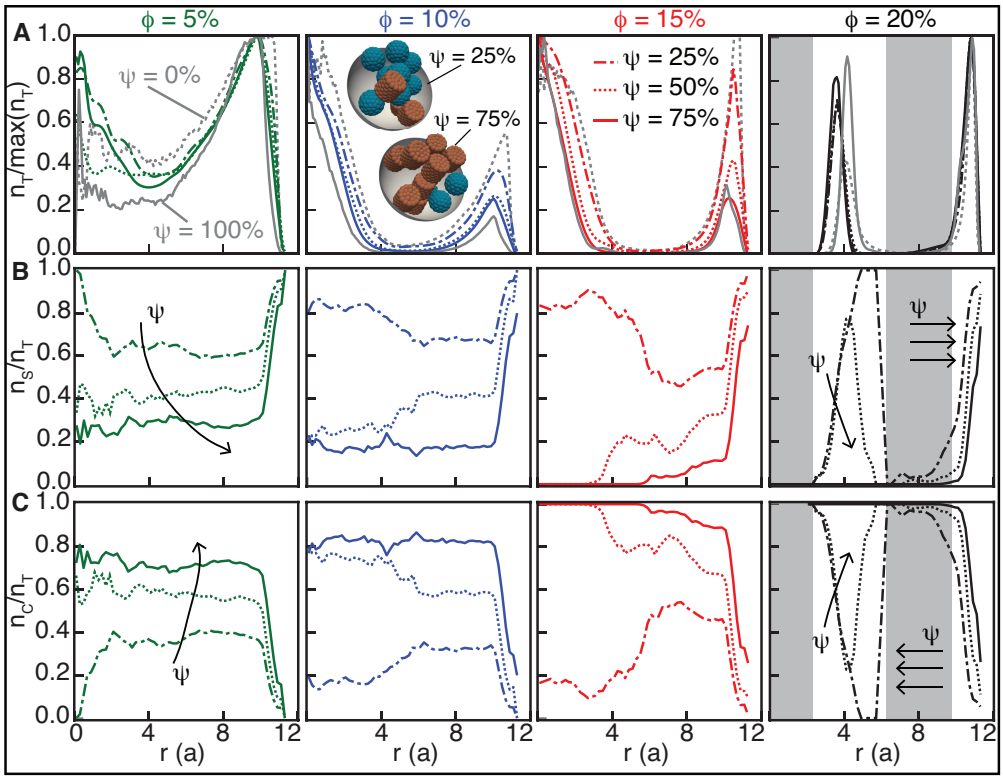

Figure 8.2: Particle number density in the mixture of spherical and cylindrical particles within a spherical cavity of radius $R = 15$ as a function of radial distance. The radii of spheres and cylinders are $r_S = 3$ and $r_C = 2.62$, respectively. The cylinder has an aspect ratio of 2, i.e., $h_C = 2r_C = 5.24$. (A): Number density of all particles scaled with the maximum density $\mathrm{n_T/max(n_T)}$ for particle concentrations $\phi = 5\%$, 10%, 15%, and 20% (from left to right). For each particle concentration, different fractions of cylinders ψ are displayed along with the pure sphere (0%) and pure cylinder (100%) cases. (B): Relative number density of only spherical particles scaled with the total density $\mathrm{n_S/n_T}$ for various particle concentrations $\phi = 5\%$, 10%, 15%, and 20% (from left to right). (C): Relative number density of only cylindrical particles scaled with the total density $\mathrm{n_C/n_T}$ for various particle concentrations $\phi = 5\%$, 10%, 15%, and 20% (from left to right).

8.4.1 Structure of sphere and cylinder mixture.

We begin by analyzing the structure of mixtures through the local particle number density. To calculate it, the spherical cavity is discretized into m evenly-spaced spherical shells along the radial direction, leading to a shell radius of the i-th shell that is given by $b_i = (i + 0.5)R/m$. The particle number density is then given by $n(r_i) = \langle N(r_i)/V_i \rangle$, where $N(r_i)$ is the number of particles in the $i - th$ shell with volume V_i, and is at a distance r_i from the center of the cavity; $\langle\rangle$ represents the ensemble average over time. We calculate the number

density for all particles, only spheres, and only cylinders, and denote them by n_T, n_S, and n_C, respectively.

Figure 8.2 displays the number density for particles within the cavity for various particle concentrations ϕ and different fractions of cylinders for each ϕ. Figure 8.2A shows the number density for all particles $n_T(r)$ within the cavity for various particle concentrations ϕ and different fractions of cylinders ψ. Cases with $\psi = 0\%$ and 100% cylinders refer to packings with pure spheres and cylinders, respectively. The density of particles is scaled with the maximum number density for each case. A common observation is that the scaled density profiles exihibit a peak close to the wall, decreases in the bulk and then increases at the center of the cavity. For low concentration, $\phi = 5\%$, the peak in scaled number density near the wall is independent of ψ, while it decreases with ψ in the bulk. At particle concentration $\phi = 10\%$, the scaled density shows a peak at the center, decreasing with increasing r and increasing again near the wall. A similar observation can also be drawn for the case of $\phi = 15\%$. Note that for the two cases ($\phi = 10, 15\%$) the scaled density at the center is higher than that near the wall. Another common feature of these two cases is that the difference between the two scaled densities decreases with increasing ψ, implying that the addition of cylinders enhances the heterogeneity in the local density. At the highest concentration considered here $\phi = 20\%$, we observe a layered structure with two distinct peaks at $r = 3$ and 10, along with a depletion zone in the regions $r < 2$ and $5 < r < 7$. The peak position of the layered structure for the pure cylinder case is slightly different compared to other fractions, and the difference between the two peaks decreases with increasing ψ.

To further understand the local particle density, we analyze the relative density of spheres and cylinders. Figure 8.2 (middle row) displays the number density of spheres relative to the total density as a function of r for various values of ϕ and $\psi = 25$, 50, and 75% for each case. We observe that the scaled sphere density relative to the total number density n_S/n_T is highest close to the wall and decreases with increasing fraction of cylinders. n_S/n_T decreases with increasing fraction of cylinders in the bulk and is always greater than zero

for low particle concentrations $\phi = 5\%$ and 10%. n_S/n_T becomes zero for higher particle concentrations $\phi = 15\%$ and 20% at large cylinder fraction (75%); only cylinders are found in this range of r, as confirmed by n_C/n_T being equal to 1, as shown in Fig. 8.2 (bottom row). These two observations demonstrate that only cylinders are present in the interior of the cavity and that spheres are close to the wall. Another point to note is that the numerical values of the scaled densities for $\psi = 25\%$ and 50% in the bulk are more "separated" compared to the differences between $\psi = 50\%$ and 75%.

These results serve to establish the equilibrium segregation of spheres to the walls induced by a subtle difference in particle shape but for the same particle volume. As a side note, we mention here that the difference in particle volume may not be the only reason for the observed segregation in experiments [245].

Next, we analyze the orientational order parameter for different particle concentrations and cylinder fractions. The orientational order parameter is defined as $\lambda = \frac{1}{2}\langle 3\cos^2\theta - 1\rangle$, where $\cos\theta = \mathbf{m}\cdot\mathbf{n}/(||\mathbf{m}||\cdot||\mathbf{n}||)$, $\mathbf{m}$ is the vector parallel to the centerline of the cylinder and $\mathbf{n}$ is the vector connecting the cavity center and the cylinder's center-of-mass. A parameter λ is often used in liquid crystalline systems to quantify the nematic ordering [253, 220]; $\lambda = 0$ corresponds to a random/disordered configuration, whereas λ is unity for ordered morphologies, with the cylinder axis being coaxial with the radial direction of the spherical cavity (radial phase), and $\lambda = -1/2$ when all cylinders are aligned transversal to the radial direction (concentric phase). Figure 8.3 displays λ for various particle concentrations with different fractions of cylinders. A common observation is that, very close to the wall, the order parameter is $\lambda = -1/2$ irrespective of the volume fraction, indicating a concentric phase close to the wall. We also find that λ fluctuates around zero in the bulk for low volume fractions, i.e, $\phi = 5\%, 10\%$, indicating a disordered configuration of cylinders. For moderate concentrations, $\phi = 15\%$, λ is zero close to center and is negative with increasing r, reaching a minimum and increasing further with r to reach a maximum value of 0.5; λ then decreases with r reaching -0.5 close to the wall. For the highest concentration, we find

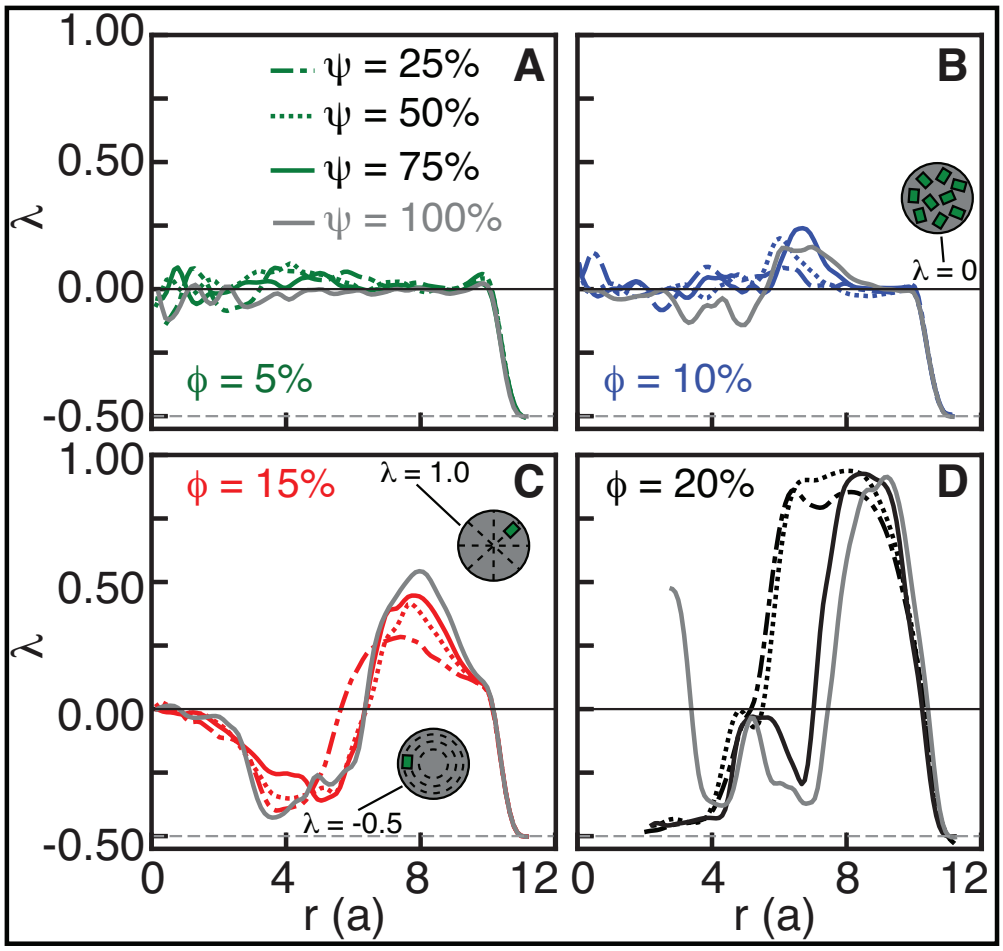

Figure 8.3: Orientational order parameter λ of cylindrical particles within a spherical cavity of $R = 15$ as a function of radial distance for particle concentration $\phi =$ (A) 5%, (B) 10%, (C) 15%, and (D) 20%. The radius of cylinders are $r_C = 2.62$ and the height $h_C = 2r_C = 5.24$.

that $\lambda = -1/2$ at both the center and close to the wall, and we also find a depletion zone with no particles for $r < 2$. For this concentration, we find another ordered state with $\lambda \sim 1$ in the region $7 < r < 10$. The ordered morphology arises from segregation in the cavity. At the highest volume fraction $\phi = 20\%$, the cylinders display ordered morphologies, i.e., perpendicular to the radial direction very close to the wall and parallel to the radial direction for $7 < r < 10$. With increasing ψ, the cylinders push the spheres to the wall in order to minimize free volume and gain orientational order.

Excluded volume potential calculations yield $10.88k_BT$ for a single sphere, $2.3k_BT$ for a cylinder oriented perpendicular to the cavity wall, and $1.01k_BT$ for a cylinder oriented

parallel to the cavity wall. These numbers imply that the cylinder oriented parallel to the cavity wall ($\lambda = -0.5$) would be the most preferable configuration, which explains $\lambda = -0.5$ irrespective of the volume fraction ϕ and fraction of cylinders ψ. At low volume fractions, both the spheres and cylinders are found in the bulk with cylinders oriented parallel to the cavity wall. However, as the volume fraction increases, cooperative effects related to the ordering of cylinders in the bulk lead the spheres to segregate to the cavity wall. Also note that, even though we demonstrate the layering of particles in the density profiles and structure in the orientational order parameter, the system is not crystalline; instead, it is still fluid-like, and particles diffuse throughout the system, as discussed in the following section.

8.4.2 Local mobility of the particles in the cavity.

As mentioned earlier, recent experiments [**?** **?** 221, 254] and simulations [212, 213] suggest that confinement can lead to anisotropic self–diffusion, which is not the case for unconfined suspensions. To examine this, mobilities (short-time diffusivity) in both the radial and tangential directions are calculated using the Einstein–Stokes relation [221]

$$\langle \Delta \mathbf{x}_{\mathrm{R}}^2(t) \rangle (r_i) = 2M_{\mathrm{R}}(r_i)t, \tag{8.4}$$

$$\langle \Delta \mathbf{x}_{\mathrm{T}}^2(t) \rangle (r_i) = 4M_{\mathrm{T}}(r_i)t, \tag{8.5}$$

for short–time $t \to 0$; $\Delta \mathbf{x} = \mathbf{x}(t + dt) - \mathbf{x}(\mathrm{t})$, $\Delta \mathbf{x}_{\mathrm{R}} = \Delta \mathbf{x} \cdot \mathbf{x}/|\mathbf{x}|$, $\Delta \mathbf{x}_{\mathrm{T}} = \Delta \mathbf{x} - \Delta \mathbf{x}_{\mathrm{R}}$ denote the radial and tangential displacements, respectively. $M_{\mathrm{R}}(r_i)$ and $M_{\mathrm{T}}(r_i)$ correspond to the instantaneous radial and tangential mobilities at radial location r_i in an infinitesimal time interval dt. Instantaneous radial and tangential mobilities are averaged in each shell during a simulation, and then over 10 independent realizations.

Figure 8.4 displays both the radial M_{R} and tangential M_{T} components of mobility within the cavity for mixtures of spherical and cylindrical particles as a function of radial distance for various particle concentrations. Note that the two components are normalized by the

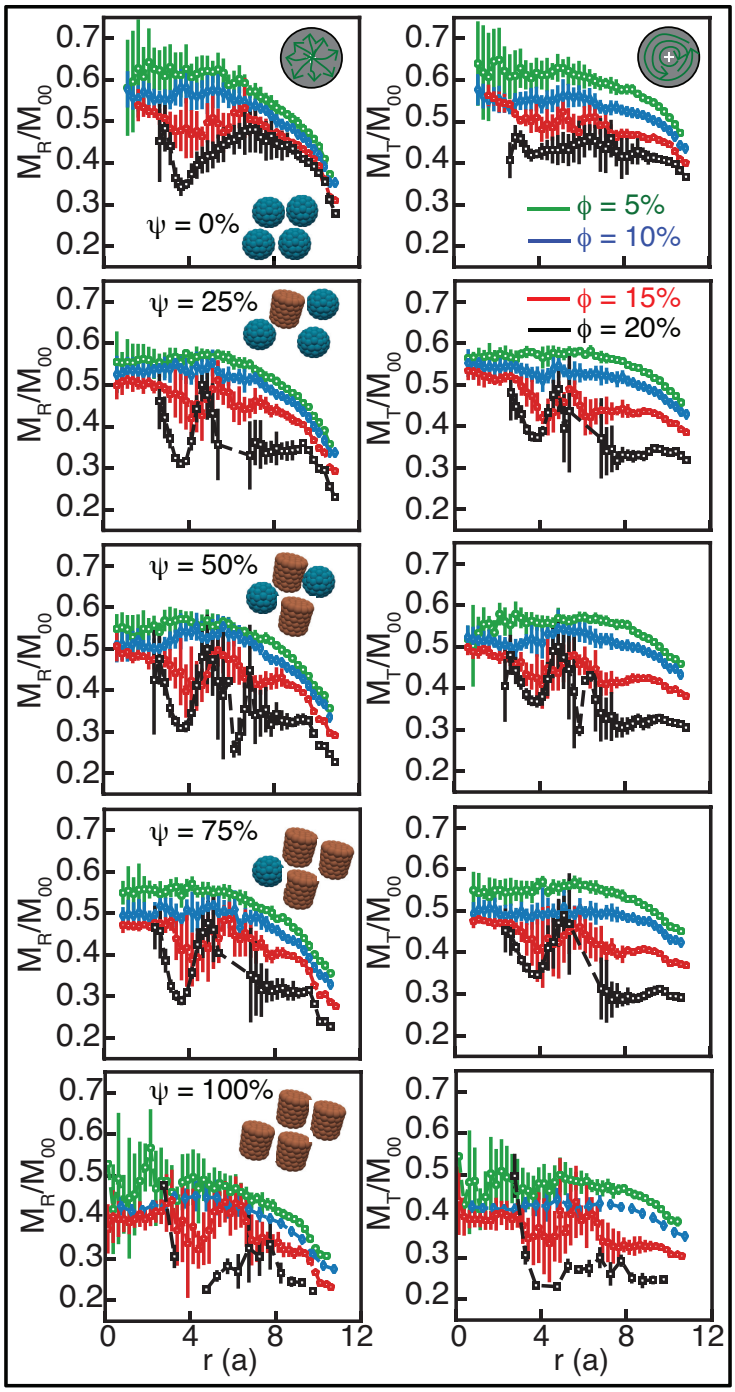

Figure 8.4: Radial mobility M_R (left) and tangential mobility M_T (right) for mixture of cylindrical particles with $r_C = 2.62$ and $h_C = 2r_C = 5.24$, and spherical with $r_S = 3$ confined in a spherical cavity of $R = 15$ for various particle concentrations, ϕ, and different fraction of cylinders ψ. Both components of mobility are normalized by the mobility of spherical particles in the bulk at infinite dilution M_{00} for $t \to 0$. The error bars represent the statistical error.

mobility of a spherical particle at infinite dilution M_{00}. A few observations can be drawn: mobilities along both directions are not constant along the radial direction; instead, the particles diffuse fastest at the cavity center and slowest at the cavity wall. Second, both M_{R} and M_{T} decrease with increasing particle concentration due to enhanced many–body hydrodynamic interactions with ϕ. Next, the peaks and trough in mobility appear at the same radial position, corresponding to the local particle density as shown in Fig. 8.2, thereby revealing a correlation between structure and dynamics. This becomes particularly apparent for the case of $\phi = 20\%$, where a layered structure for both M_{R} and M_{T} corresponds to a similar density profile as observed in Fig. 8.2, e.g., the dip in mobility at $2 < r < 7$ corresponds to the peak in ρ in the same radial range. Both M_{R} and M_{T} display the expected decrease with increasing ϕ close to the wall for all cylinder fractions. For $\phi = 5$ and 10%, we observe an expected decrease in mobility with ϕ in the bulk as well. In contrast, for higher particle concentrations (ϕ= 15%), the mobility does not exhibit a decrease with ϕ in the bulk, and mobility for $\phi = 20\%$ at radial location $r \sim 5$ becomes equal or even larger than that for $\phi = 15\%$. Taken together, these observations reveal that a structural inhomogeneity leads to unexpected inhomogeneities in the corresponding mobility.

8.4.3 Long time mobility of the particles.

The displacement of a Brownian particle in a confined system is hindered, and thus the mean square displacement (MSD) over time is lower than that observed in a bulk system [211, 213]. Chapter 7 showed that a change in shape from spherical to cylindrical at constant volume fraction leads to slower particle diffusion. The question that arises here is: how does the fraction of cylinders in a mixture affect long-time dynamics?

Fig. 8.5A shows the average MSDs for mixtures at different particle concentrations. The MSD of each system is calculated from ten independent simulations in which the particles diffuse for more than 300 particle diffusion times within the cavity. A couple of observations can be drawn. First, the MSDs grow linearly as short times, $t \to 0$, and reach a plateau

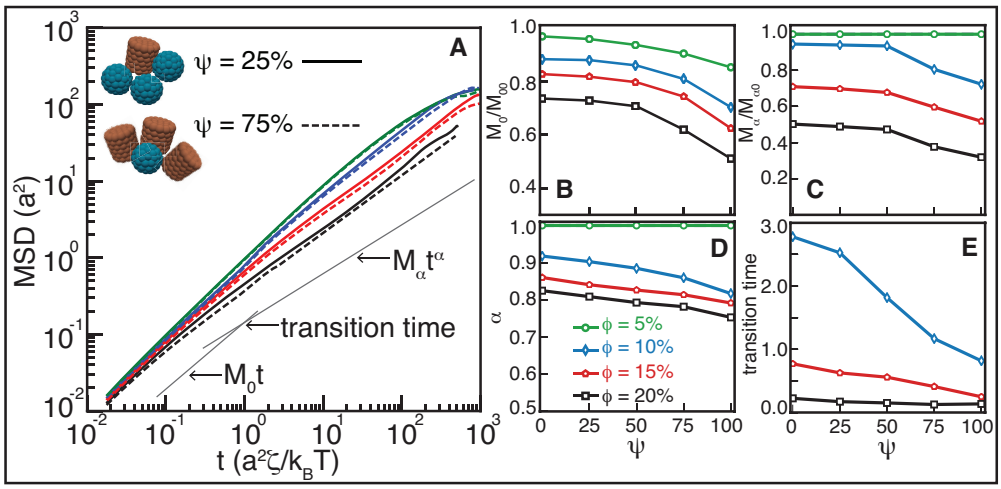

Figure 8.5: (A) Mean square displacement as a function of time for mixture of spherical and cylindrical particles that are confined in a spherical cavity with $R = 15$ for various particle concentrations ϕ with varying fraction of cylinders. Solid and dashed lines are the results for $\psi = 25$, and 75 % fraction of cylinders. (B) short time mobility scaled with the mobility of spherical particles in bulk at infinite dilution M_{00} plotted against ψ, (C) sub-diffusive (at intermediate time) mobility scaled with the mobility of spherical particles in bulk at infinite dilution M_{00} plotted against ψ, (D) sub-diffusive exponent α plotted against ψ, and (E) time scale to make transition between diffusive to sub–diffusive behavior plotted as a function of fraction of cylinders for various values of ϕ.

in the long time limit, $t \to \infty$. Second, at intermediate times, particle motion becomes sub–diffusive for systems with $\phi \geq 10\%$.

To analyze the diffusion behavior in detail we express the MSD as the generalized Stokes-Einstein relation

$$\left\langle \left(\mathbf{R}(t) - \mathbf{R}(0)\right)^2 \right\rangle = M_i t^i, \tag{8.6}$$

where $\mathbf{R}$ is the $3N_p$ particle coordinate vector, M_i is the generalized particle mobility coefficient and i is the power law exponent that characterizes whether the particle motion is sub–diffusive ($\alpha < 1$), diffusive ($\alpha = 1$) or super-diffusive ($\alpha > 1$). For the case of ($\alpha = 1$), the mobility M_0 is the diffusion coefficient.

Figure 8.5B–E displays our findings for the mean square displacement. Short time mobility (Fig. 8.5B) and sub–diffusive mobility (Fig. 8.5C) decrease with increasing cylinder fraction ψ and particle concentration ϕ. The dependence of M_0/M_{00} and M_α/M_{00} on par-

ticle concentration ϕ is monotonic; however, the dependence on cylinder fraction is weak at smaller cylinder fraction ψ and becomes strong beyond 50%, showing a smooth to "rigid" transition at $\psi = 50\%$. Note that for the case of $\phi = 5\%$, sub–diffusion is not observed at any cylinder fraction ψ. On the other hand, the sub–diffusive–exponent α (Fig. 8.5D) that characterizes the strength of sub–diffusive behavior decreases with both ϕ and ψ. In the case of short–time and sub–diffusive mobilities M_0/M_{00} and M_α/M_{00}, the dependence on ψ is monotonic; however, the correlation gets less pronounced with increasing particle concentration. Finally, the transition time, defined as the time at which the system transitions from the short–time diffusive to the intermediate time sub–diffusive regime, is displayed in Fig. 8.5E. We observe that for $\phi = 0.1$ the transition time decreases strongly with the cylinder fraction and becomes nearly independent of cylinder fraction for higher particle concentrations.

To explain the smooth to rigid transition as observed in both M_0/M_{00} and M_α/M_{00}, we refer to the scaled density profiles with increasing ψ. We observe that the scaled densities $n_T/\max(n_T)$ for $\psi = 0$ and 25% are similar but then drop drastically for $\psi \geq 50\%$, which affects the mobility in both the diffusive and sub–diffusive cases. On the other hand, for the transition time between the diffusive to the sub–diffusive regime (i.e. roughly the time needed for particles to diffuse a distance nearly equal to the radius), collisions between particles slow down their motion, leading to sub–diffusive behavior. It follows that the transition time would decrease with increasing particle concentration ϕ. Further, at low ϕ, changing shape from spheres ($\psi = 0$) to ($\psi = 100\%$) to cylinders, due their larger aspect ratio the latter should feel each other at shorter–time scales, compared to what is seen for spheres, and hence yield a transition time that decreases with ψ. At larger ϕ, the system is so dense that even for different packings, i.e., sphere–sphere, sphere–cylinder and cylinder–cylinder cases, the particle interaction time scales become similar.

8.5 Conclusions

We have studied the structure and dynamics of mixtures of finite size in mixtures of spherical and cylindrical particles confined in a spherical cavity. An Immersed Boundary-General geometry Ewald-like Method (IB-GgEm) approach was used in the corresponding calculations, thereby taking into account hydrodynamic interactions between particles and between particles and confining walls. By systematically varying the cylinder fraction at different particle concentrations, it was found that particle shape has a pronounced effect on both the structure and dynamics of confined Brownian suspensions. Our results suggest that introducing non–spherical particles affects the local structure and local dynamics and global dynamics in different ways. At a local level, particles are found to segregate based on shape, with cylinders adopting conformations with high orientational order. At a global level, cylinders give rise to pronounced differences in the short-time mobility, the sub–diffusive behavior at intermediate timescales, and the transition time from diffusive to sub-diffusive behavior. Particle concentration has a strong effect on such transitions. To start with, the mobility shows a smooth to stiff transition at 50% cylinder fraction for all particle concentrations and the sharpness of this transition increases with particle concentration. Secondly, the sub-diffusive slope and sub–diffusive exponent show mixed features as a function of cylinder fraction. The slope shows a smooth to stiff transition similar to that of the short time mobility. The exponent decreases smoothly with increasing cylinder fraction. In both cases, the dependence on the cylinder fraction is insensitive to particle concentration. Lastly, the transition time from the diffusive to sub–diffusive regime depends strongly on the cylinder fraction for low particle concentrations ($\phi = 0.1$); that dependence weakens with increasing particle concentration.

As an outlook, the role of aspect ratio and electrostatic interaction on particle mobility in confined mixtures will be considered in future that arise in a realistic cell environment.

CHAPTER 9

APPLICATION: ON THE HYDRODYNAMICS OF POLARIZABLE PARTICLES

9.1 Abstract

Electrokinetic forces are central to the dynamics of far-from-equilibrium charged colloidal systems, dominating biological homeostasis and offering engineering routes for control in biotechnology. Dissipative and conservative forces sway the structure and interaction of particles, thereby mediating active and passive physical-chemical reactions at the molecular level. Here, we report a theoretical study on the sedimentation of charged particles including contributions from the Coulombic forces, the surface charge polarization, and hydrodynamic interactions. This model serves to illustrate how the directional motion of particulate clusters, moving in a low Reynolds fluid flow, is strongly correlated with the interactions between the constituent particles. We found the equilibrium conditions for homopolar particles to aggregate, forming clusters that are stabilized by surface charge polarization. These are determined by the charge ratio between particles and by the difference between dielectric constants of the fluid and the particles. Interestingly, far-from-equilibrium sedimenting particles inherit the conditions to form agglomerates, resulting in accelerated sedimentation rates. In a confined suspension, the dielectric contrast between the fluid and the confining walls significantly affects the sedimentation dynamics and the directional migration of the particles toward or away from the surfaces. The results presented in this work ordain the central role of surface charge polarization during the dynamics of charged entities at molecular and colloidal scales.

9.2 Introduction

Having charged and polarizable particles, with different amounts of charges and dielectric permittivities, immersed in a Stokes fluid, with its own dielectric permittivity, is a common scenario in biological systems, including blood flows, protein suspensions, cytoplasm, and lymph, and during water filtration/purification in macropores of the soil. The associated problem is non-trivial to attack for the reason that interactions between particles include both electrostatic (conservative) and hydrodynamic (dissipative) interactions. The dielectric permittivity of charged particles are usually different from that of the fluid, giving rise to electrostatic polarization and induced surface charges on particles. If one further considers particles moving under confinement, it becomes extremely challenging to study hydrodynamic interactions (HI), in general confined geometries, together with the induced surface charges on particles and arbitrarily-shaped walls. Dynamics of particles with regular shapes considering HI in unconfined and confined domains are well assessed in the literature[255, 256, 257, 258, 216, 212]; however, how electrostatic effects and polarizability affect the dynamics of hydrodynamically interacting charged dielectric particles, in both unconfined and confined domains, remains poorly understood.

Electrostatic interactions are ubiquitous in both natural and industrial settings [4, 5]. Free charges respond to applied electric fields by generating a net current, whereas dielectric materials become polarized and generate bound surface charges. These, in turn, give rise to additional electric fields, the magnitude and effects of which on the surrounding charged objects are largely determined by the relative dielectric permittivity of the materials and its surroundings. At the interface between two regions with different dielectric properties, surface charges will accumulate in response to an applied external electric field. Charge accumulation can influence the interactions between dielectric objects in profound ways. Examples include the aggregation or dispersion of colloids [5], charged granular materials [6, 7], and nano-particles [8]. Charge accumulation also plays a central role in understanding colloidal dispersion stability, crystallization by secondary bonding, and the clustering of

dust involved in the early stages of planet formation [9, 259, 11]. The majority of previous works on charged particles (equilibrium and far from equilibrium) limited considerations of electrostatic forces and energies to the direct Coulombic interactions, for which charges with equal signs repel, while charges with opposite signs attract [261, 262, 123, 122]. We present an extension of the electrostatic interaction that includes electrostatic polarizability, where charged particles (or any entities such as molecules, fibers, etc.) embedded in a media with a different dielectric permittivity induce additional electrostatic forces between them.

Recent theoretical and numerical works have sought to explain the nature of interactions between polarizable particles [59, 18, 263, 180, 14, 40, 1]. Among a number of intriguing findings, it has been shown that under certain circumstances, particles having the same charge can in fact experience attractive forces, which eventually may lead to the clustering phenomena [7]. Past efforts in studying many-body interactions between polarizable particles have been limited to the case of particles moving in vacuum [6, 7]. The effects of HI arise when particles are suspended in a solvent. In the rheological community, previous efforts have been directed at studying the electrodynamical response of charged particle suspensions [264, 265, 266, 267, 268, 269, 270]. In the present work, we examine how coupled hydrodynamics and electrostatic polariziability affect the interactions between particles in many-body systems. Specifically, we explore these effects during sedimentation of positively charged particles in a solvent under a zero Reynolds number condition.

9.3 Models and methods

We consider N spherical particles, with hydrodynamic radius a and dielectric permittivity ϵ_{in}, embedded in a Stokes fluid with viscosity μ and dielectric permittivity ϵ_{out}. In principle, our approach may be used for poly-dispersed particles with different ϵ_{in} or a, but we limit the discussion in this work to mono-dispersed systems of spheres with the same properties. Each i-th particle carries a point charge $Q_i(\mathbf{x}_i) = z_i e$ at the center, where z_i is the valence and e is the elementary charge. This implies that the free surface charge density on each

particle's surface is uniform according to Gauss law.

The main interactions between particles are the usual pairwise Coulombic interactions. However, when the particles are in close proximity, they induce surface charges, giving rise to the polarization interaction. In Chapter 2 we show a systematic multiple-scattering formalism [17, 59, 18] to describe the polarization interactions. In this formalism, the polarization energy is grouped according to the number of interacting particles. The lowest order polarization energy, the three-body terms E_3, are participated by three particles. The higher order terms involve E_4, E_5 for four-body, five-body interactions, etc. The two-body terms are reserved for the normal pairwise Coulombic interaction. Symbolically, the total electrostatic energy, E_E, for an ensemble of dielectric spheres may be written as $E_E = E_2 + E_3 + E_4 + \cdots$, where each term in such an expansion involves a summation over all possible two-body, three-body, four-body, and so on, permutations. The key point to note about the multibody expansion for E_E is that all interaction terms only depend on particles' positions. The references to surface charges are avoided by replacing the induced charges by the gradient of the electrostatic potential, therefore the degrees of freedom are greatly reduced. Furthermore, forces on particles can be computed via differentiation with respect to the particles' positions, which enables N-body simulations with molecular dynamic or hydrodynamic evolution schemes. A second point to note is that an image charge method, based on consecutive construction of image lines, can be introduced for an efficient and fast evaluation of contributions from surface charges [59, 18]. It transforms the two-dimensional surface charge integral to a one-dimensional line integral. This allows us to show that each single N-body term is smaller than a typical $(N-1)$-body term by a factor proportional to $\hat{\epsilon}\,(a/R)^3$, where $\hat{\epsilon} = (\epsilon_{\text{in}} - \epsilon_{\text{out}}) / (\epsilon_{\text{in}} + \epsilon_{\text{out}})$ and R is the average particle separation. As a consequence, the expansion for E_E represents a series that converges sufficiently fast as number of terms increases.

The focus of this chapter is to understand the collective dynamics of charged dielectric particles embedded in a Stokes fluid with a different dielectric permittivity from that of the

particles and the effects of hydrodynamic and electrostatic interactions on particle dynamics. As a proof of concept, we impose a constant sedimenting force on the particles. Given the fact that the particle size ranges from hundreds of nanometers to few microns, the relevant regime for fluid flow is inertialess, i.e. nearly zero Reynolds number flow. Therefore, the force/torque balance for all particles reduces to $\mathbf{F}^{\mathrm{H}}+\mathbf{F}^{\mathrm{S}}+\mathbf{F}^{\mathrm{C}}+\mathbf{F}^{\mathrm{P}}+\mathbf{F}^{\mathrm{EV}}=0$, where $\mathbf{F}^{\mathrm{H}}$ are the hydrodynamic forces/torques acting on the particles due to the motion of the particles relative to the fluid, $\mathbf{F}^{\mathrm{S}}$ are the sedimenting forces, $\mathbf{F}^{\mathrm{C}}$ and $\mathbf{F}^{\mathrm{P}}$ are the electrostatic forces that arise from the Coulombic interaction and electrostatic polarization, and $\mathbf{F}^{\mathrm{EV}}$ are the excluded volume forces/torques. Note that each $\mathbf{F}=(\mathbf{f}_1,\mathbf{T}_1,...,\mathbf{f}_N,\mathbf{T}_N)^T$ is a $6N$ vector that includes forces $\mathbf{f}_i$ and torques $\mathbf{T}_i$ on each particle $i=1,...,N$.

In the Stokes limit, the hydrodynamic forces/torques acting on the particles are given by $\mathbf{F}^{\mathrm{H}}=-\mathbf{R}_{\mathrm{FU}}\cdot\mathbf{U}$, where $\mathbf{U}=(\mathbf{U}_1,\boldsymbol{\Omega}_1,\cdots,\mathbf{U}_N,\boldsymbol{\Omega}_N)^T$ is the $6N$ particle translational and rotational velocity vector and $\mathbf{R}_{\mathrm{FU}}$ is the $6N\times 6N$ configuration-dependent multi-body hydrodynamic resistance tensor.[255, 215, 256] Particle dynamics is obtained from the particle translational and rotational velocity, which is a solution of the following the mobility problem,

$$\mathbf{R}_{\mathrm{FU}}\cdot\mathbf{U}=\mathbf{b}=\mathbf{F}^{\mathrm{S}}+\mathbf{F}^{\mathrm{C}}+\mathbf{F}^{\mathrm{P}}+\mathbf{F}^{\mathrm{EV}}, \tag{9.1}$$

that results in a $6N\times 6N$ linear system of equations where the coefficient matrix $\mathbf{R}_{\mathrm{FU}}$ and the known vector $\mathbf{b}$ depend only on particle locations.

We use two different approaches to solve the mobility problem in the unconfined space. For the case of two sedimenting particles ($N=2$), approximate expressions for the resistance tensor [257, 258] are used; for $N>2$, a Stokesian dynamics [107] approach accelerated by the General geometry Ewald-like method (GgEm) [95, 118, 126, 127, 68] is used. Details of the SD-GgEm for a periodic domain are included in Appendix 9.6.1. Both solutions were verified and validated with direct integral formulations resolved through the boundary element method [104]. For particle dynamics in the confined space, GgEm with the immersed boundary method [201] coupled with the electrostatic polarization solver [180] is used.

9.4 Results and discussions

We use a few examples to illustrate how electrostatic polarization and HI collectively affect the dynamics of sedimenting particles. We expect that because of the electrostatic polarizability, particle agglomerates will form; therefore, it is important to know the energy landscape and phase diagram for the formation of dimers, trimers, tetramers, etc. In other words, there is a set of equilibrium states resulting from the electrostatic forces. These states should be a function of $\epsilon_{\text{in}}/\epsilon_{\text{out}}$ (ϵ_{in} and ϵ_{out} are the dielectric permittivities of particles and background continuous medium, respectively) and the charge ratio between particles. The relevant questions are: how do HI perturb these equilibrium states and vice versa? Are the clustering conditions, at equilibrium states, applicable to the dynamical system at non-equilibrium states? And, how confining walls introduce another level of control to the dynamics of sedimenting particles? We start to answer these questions by analyzing the stability diagram for lower order clusters with electrostatic polarization, and continuing with their implications on the dynamics of sedimenting particles.

9.4.1 Electrostatic polarization

We start with the qualitative effects of electrostatic polarization. The normal Coulomb interaction can be attractive or repulsive, depending on the signs of particle charges. The electrostatic interactions with polarization effects among particles with equal signs, however, can be attractive when the dielectric permittivities of particles are larger than that of the embedding medium, and can be repulsive in the opposite case. According to the Image Method in Chapter 2, at the scaling level, we may write the energy of a two particle system with the same radius, a, and the same dielectric constant, ϵ_{in}, as

$$E_2 + E_3 \simeq \frac{Q_1 Q_2}{4\pi\epsilon_{\text{out}} R_{12}} + \frac{1}{4\pi\epsilon_{\text{out}} R_{12}} \hat{\epsilon} \left(Q_1^2 + Q_2^2 \right) f(a/R_{12}), \tag{9.2}$$

where $\hat{\epsilon} = 1 - \epsilon_{\text{in}}/\epsilon_{\text{out}}$, R_{12} is the center-to-center separation between particles, and $f(a/R_{12})$ is a function that captures the shape of the surface charge distribution, which is generally a small quantity of order $(a/R)^3$. For a two particle system, the ratio between the lowest order polarization energy E_3 and the Coulomb energy E_2 can be written as $E_3/E_2 = \hat{\epsilon}\,(Q_1/Q_2 + Q_2/Q_1)\,f(a/R_{12})$. Therefore, if $\epsilon_{\text{in}}/\epsilon_{\text{out}} \gg 1$ or $Q_1/Q_2 \gg 1$, the contribution from polarization may exceed that from the Coulombic term. As a result, for those cases, the homopolar particles (charges with equal signs) may actually attract each other at sufficiently small separations.

This polarization-induced attraction is summarized in Fig. 9.1 for two and three homopolar particles. The figure shows the conditions, $\epsilon_{\text{in}}/\epsilon_{\text{out}}$ and Q_1/Q_2, for two and three particles to form agglomerates. The boundary between the stable and unstable states are calculated using the image method with up to the fourth order polarization contribution. Whereas dimers occur naturally as a function of the distance between the particles for specific values of $\epsilon_{\text{in}}/\epsilon_{\text{out}}$ and Q_1/Q_2, trimer formation includes two additional degrees of freedom: the geometrical arrangement and the particle type. Note that the phase diagram in Fig. 9.1 for three particles is calculated for two species (Q_1 and Q_2) only, where $Q_1 \geq Q_2$. The condition, $Q_1 \geq Q_2$, is not arbitrary as we find that the triangular trimer is the only possible configuration for two species if and only if the magnitudes of charges on two particles with the same charge are smaller than that on the third particle. Recall that the conditions for attractive electrostatic interaction with polarization effect are $\epsilon_{\text{in}}/\epsilon_{\text{out}} \gg 1$ or $Q_1/Q_2 \gg 1$, therefore in a three particle system with three different species, a trimer will form only if the magnitude of charge on one of the particles is larger than that on the other two particles and this trimer will always form a triangular shape.

For tetramers, we present the energy landscape for two species with $Q_1 \geq Q_2$ and $\epsilon_{\text{in}}/\epsilon_{\text{out}} = 15$ as shown in Fig. 9.2. These conditions are set to achieve significant polarization effects. Similar to the trimer, there are specific conditions for the charge ratio and the geometrical distribution of particles with smaller amount of charge (low-charged particles)

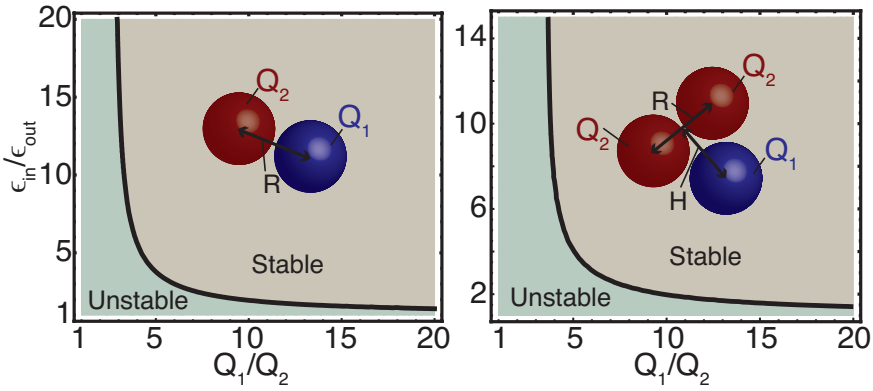

Figure 9.1: Stability diagrams for dimers (left) and trimers (right). Clusters of homopolar particles in close contacts are stabilized by surface charge polarization. The parameter regimes for stabilized close-contact aggregates are highlighted with colored shades. The boundaries between different regimes are identified by computing the gradient of energy with respect to particle displacements. Note that all particles here are positively charged and the different charge amount is labeled by red and blue color.[3]

around the particle with larger amount of charge (high-charged particle) to form stable tetramers. In Fig. 9.2, the energy is normalized by the in-plane configuration ($H = 0$) where the low-charged particles surround the high-charged particle and form a triangular shape on the same plane. This configuration shows a local minimum in the energy landscape. Once $H \neq 0$, the geometrical arrangement that results in the global energy minimum is that of a tetrahedron ($H = \pm 1$). And the energy landscape is symmetric about $H = 0$. The above analysis shows the importance of the geometrical arrangements to form stable agglomerates. Symmetric geometrical distributions, like lines or lattices, are unstable configurations for many particle systems. In addition, there are particular sequences between high- and low-charged particles to form stable clusters.

9.4.2 Sedimentation in an unconfined domain

We next discuss the dynamics of sedimenting particles. The force balance for a single spherical particle in a gravitational field suspended in a Stokes fluid reduces to $F^{\mathrm{H}} + F^{\mathrm{S}} = 0$ along the direction of the gravity. The hydrodynamic force on the particle is defined by $F^{\mathrm{H}} = \zeta U_0$ from Stokes's law, where $\zeta = 6\pi a\mu$ is the drag coefficient, a is the radius of the sphere, μ is

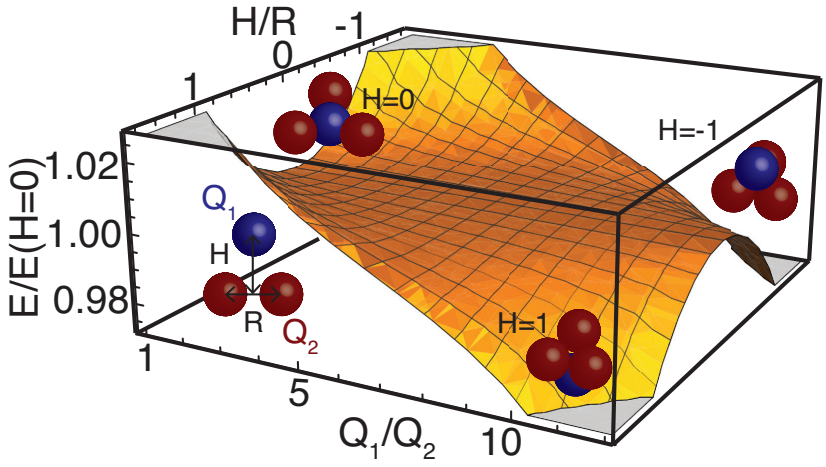

Figure 9.2: Energy landscape for a four particle aggregate with two species (Q_1 and Q_2) and $Q_1 \geq Q_2$. The ratio between dielectric permittivities of particles and the embedding medium is $\epsilon_{\text{in}}/\epsilon_{\text{out}} = 15$, while particles' geometrical distribution and charges are varied smoothly. Note that all particles here are positively charged and the different charge amount is labeled by red and blue color. In this figure, R is the distance between centers of any two of the three particles with the same charge Q_2, and H is the distance between the particle with charge Q_1 and the plane formed by other three particles.

the viscosity of the fluid, and U_0 is the sedimenting velocity of the isolated particle. For two sedimenting particles, Stokes' law is usually generalized in terms of a resistance coefficient λ defined from the force balance as $\mathbf{F}^{\text{H}} = \zeta\lambda\mathbf{U}_0$. It is known that $\lambda \approx 0.64659$ for equally sized spheres sedimenting along to the line of centers when they are touching ($R = 2a$), while $\lambda \approx 0.71581$ for spheres sedimenting perpendicular to the line of centers (with an additional torque that prevents the particles to rotate) with $R = 2a$ [255, 256]. In both situations, $\lambda \to 1$ as $R \to \infty$. According to these values, sedimenting particles with an equal velocity will exert a lower hydrodynamic drag on the fluid than that in the case of single particle. Conversely, sedimenting particles in a constant gravitational field will sediment faster as their separation becomes smaller; the sedimenting velocity $U \to U_0$ as the separation between particles goes to infinity. Figure 9.3 shows the value of the resistance coefficient λ for non-electrostatically interacting particles as a function of the separation R for two particles sedimenting along (blue) and perpendicular (black) to the line of centers. These coefficients

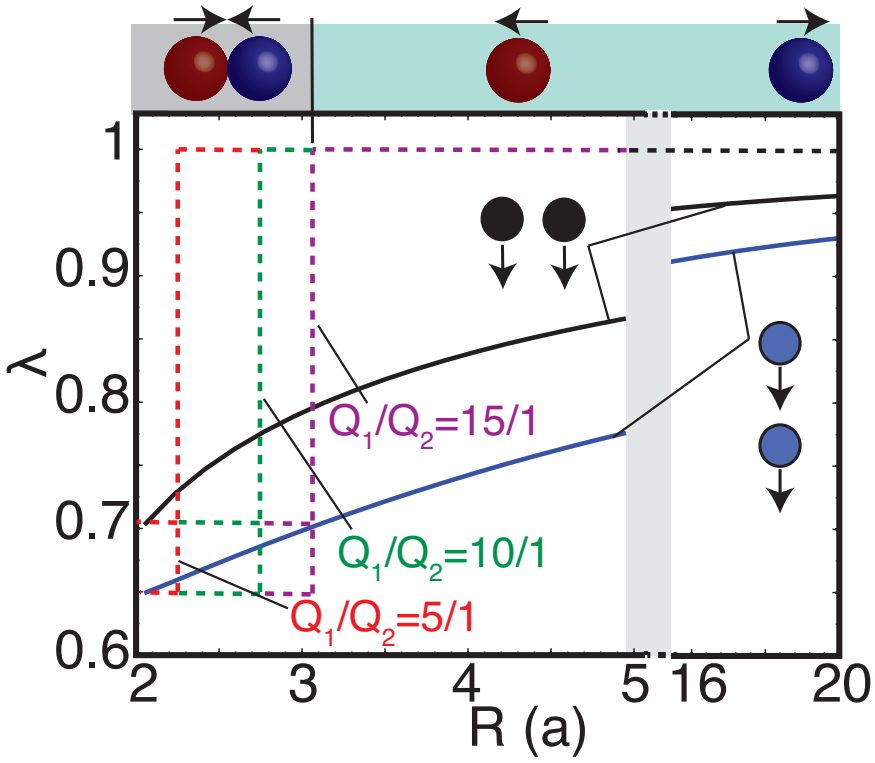

Figure 9.3: Resistance coefficient λ for two particles sedimenting along (blue line) and perpendicular (black line) to their line of centers. Without electrostatic interactions, λ increases as particles' center-to-center separation R increases (solid lines). Coulombic interaction forces charged particles with equal signs to repel and eventually sediment far from each other, resulting in $\lambda = 1$ at steady state. Electrostatic polarizability could agglomerate charged particles with equal signs depending on specific values of $\epsilon_{\text{in}}/\epsilon_{\text{out}}$ and Q_1/Q_2 and the phase diagram for dimers, resulting in $\lambda(R = 2a)$ at steady state. This figure includes three scenarios (dotted lines) with $\epsilon_{\text{in}}/\epsilon_{\text{out}} = 15$ and $Q_1/Q_2 = [5/1, 10/1, 15/1]$ for electrostatic polarizability.

are calculated using the approximate solution of the resistance tensor [257, 258].

For charged particles with equal signs, the inclusion of Coulombic interactions implies that the particles will repel each other and eventually they will sediment independently with $U = U_0$ as their separation goes to infinity. On the other hand, electrostatic polarizability will affect the sedimenting velocity according to $\epsilon_{\text{in}}/\epsilon_{\text{out}}$ and Q_1/Q_2. Once the conditions for stable dimers are satisfied, inheriting from the phase diagram in Fig. 9.1, effect of electrostatic polarizability will force the particles to sediment together and faster than that in the pure Coulombic case. As a consequence, for two polarizable particles, the resistance coefficient as

a function of the separation between particles will be a step function from $\lambda(R = 2a)$ to $\lambda = 1$ at a stepping distance R_S. In Fig. 9.3, we include the resistance coefficient for particles with $\epsilon_{\text{in}}/\epsilon_{\text{out}} = 15$ and three different charge ratios $Q_1/Q_2 = [5/1, 10/1, 15/1]$. The charge ratio, at a constant $\epsilon_{\text{in}}/\epsilon_{\text{out}}$, determines whether particles attract or repel each other. It is therefore not surprising that the stepping distance R_S, which is a function of Q_1/Q_2, corresponds to the location where the electrostatic energy reaches maximum, i.e., where electrostatic force is zero. From our calculations, $R_S(Q_1/Q_2 = 10) = 2.74a$, $R_S(Q_1/Q_2 = 5) = 2.27a$ and $R_S(Q_1/Q_2 = 15) = 3.09a$.

Now we turn to the situation where N polarizable particles are sedimenting in a constant gravitational field in an unconfined fluid domain. In what follows, we will use the particle hydrodynamic radius a as the characteristic length scale, $\tau_s = a/U_0$ as the characteristic time scale, $e^2/(4\pi\epsilon_{\text{out}}a^2)$ as the characteristic electrostatic force, and $6\pi\mu a U_0$ as the characteristic hydrodynamic force. For completeness, $8\pi\mu a^2 U_0$ is the characteristic hydrodynamic torque and $20/3\pi\mu a^2 U_0$ is the characteristic particle Stresslet. Let's consider a system of N sedimenting particles with a dielectric permittivity that satisfies $\epsilon_{\text{in}}/\epsilon_{\text{out}} = 15$. Two different species both of positive charge are considered, and half of the particles carry $Q_1 = +10$ and the other half carry $Q_2 = +1$. The particles are sedimenting in an infinite fluid and are initially distributed at $z = 0$ in a 40×40 plane. According to the stability conditions from the polarizability phase diagrams in Fig. 9.1, $\epsilon_{\text{in}}/\epsilon_{\text{out}} = 15$ and $Q_1/Q_2 = 10$ satisfy the "stability" conditions for cluster formation. Recall that for $N > 2$, there are additional geometrical constrains for this agglomerates to form. We perform simulations using a Stokesian dynamics-GgEm algorithm (details are included in Appendix 9.6.1), and let the particles sediment one hundred characteristic time. Statistics are collected over 20 independent simulations for each system.

Our first focus is to investigate the effects of HI on the dynamics of cluster formation and particle arrangement. Non-hydrodynamically interacting particles will serve as the scenario for comparison, and we call these sedimenting particles as free-draining (FD) particles. There

is no point in comparing Coulombic-only to polarizable particles because it is a trivial extension of the two particle case, as all particles will simply repel each other with pure Coulombic interaction. Figure 9.4 shows the initial and final histograms of particle arrangement during the sedimentation of $N = 200$ particles. In the histogram, "one" denotes particles sedimenting independently, "two" denotes dimers, so on and so forth. At $t = 0$, the random positioning of particles in the 40×40 plane results in the presence of some dimers and trimers. These are counted as $Q_1 - Q_2$ dimers and $Q_2 - Q_1 - Q_2$ trimers. As particles sediment, the number of dimers gets reduced considerably, while the number of agglomerates with $N > 2$ increases for both HI and FD particles. Note that the number of HI particles that sediment individually is higher than that for the FD particles. On the other hand, for FD particles the number of individual particles is conserved, while the number of clusters with $N > 2$ increases, including a higher percentage of trimers, tetramers and agglomerates with $N > 5$ than that for HI particles; HI particles form trimers and tetramers in a much lower fraction than that for FD particles. Before we expand the reasons behind these differences between HI and FD particles, Fig. 9.4 also includes the time required to reach a steady state cluster distribution as a function of N. The time is quantified in terms of the characteristic time τ_S. We observe that FD particles reach their steady state distribution faster than that for HI particles. Both types of system show an asymptotic behavior as $N \to \infty$.

To understand these observations, we analyze the equilibrated particle configurations after twenty characteristic times in Fig. 9.5 for HI and FD particles. Both HI and FD particles start from the same initial random distribution at the $z = 0$ plane. The first point to notice is that all FD particles sediment in a constant z-plane, as there are no HI between particles. Therefore, they interact only electrostatically in a two-dimensional (2D) plane, and because we ignore their Brownian motions, there are no forces that make the particles to escape that z-plane. As a consequence, FD particles form only 2D clusters and follow a concentric-like distribution as shown in the xy-view in Fig. 9.5-FD. In this distribution, individual high-charge particles located at the periphery form clear concentric rings and there

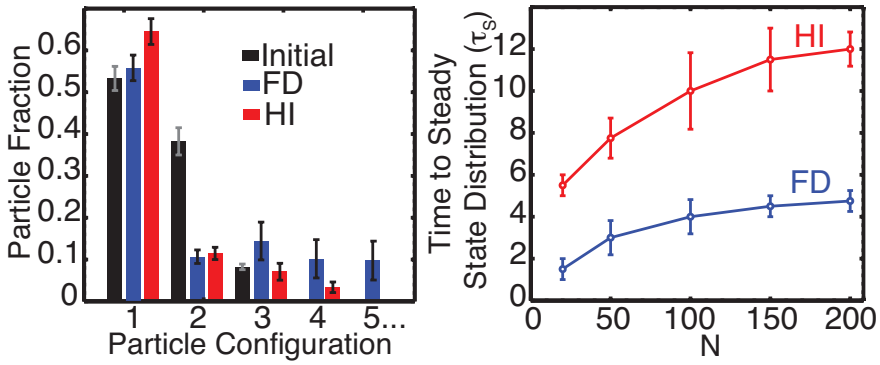

Figure 9.4: Fraction for monomer, dimer, trimer, tetramer, and pentamer for initial and steady state configurations (left) and time to reach steady state configuration (right). Blue bar and line are results for free-draining particles, while red bar and line are for hydrodynamically interactive particles. Two species are considered with $Q_1 = +10$, $Q_2 = +1$, and $\epsilon_{\text{in}}/\epsilon_{\text{out}} = 15$.

is a sharp transition from the high-charge particles to the clusters and individual low-charge particles that are located at the center. As the FD particles have a lower dimensionality, the conditions for cluster formation are easily satisfied, which explains why $N > 2$ agglomerates are observed with a higher probability (see Fig. 9.4). We include some of the in-plane agglomerates of FD particles in Fig. 9.5. Similar to the stability conditions for trimers and tetramers, the in-plane particles must satisfy a "low-charge particles surrounding a high-charge particle" rule. A notable observation is that the distribution of FD particles shows a self-similar behavior with respect to time. The time to reach steady state distribution, where the number of clusters, i.e., monomer, dimer, trimer, etc., remains nearly unchanged, is between two and four characteristic time. After this time regime, the only thing that changes is the separation distances between clusters due to electrostatic interactions.

Dynamics of hydrodynamically interacting particles is completely different, as every moving particle generates fluid flows that is transported by momentum diffusion and instantly affects dynamics of other particles. The dynamics of N particles is now coupled together by HI in a collective way. The resulting flow fields will disrupt the in-plane configuration, as it is shown in the xy-plane in Fig. 9.5-HI. After twenty particle sedimenting time, the particles are dispersed along the sedimenting direction over a distance about 100 times their sizes.

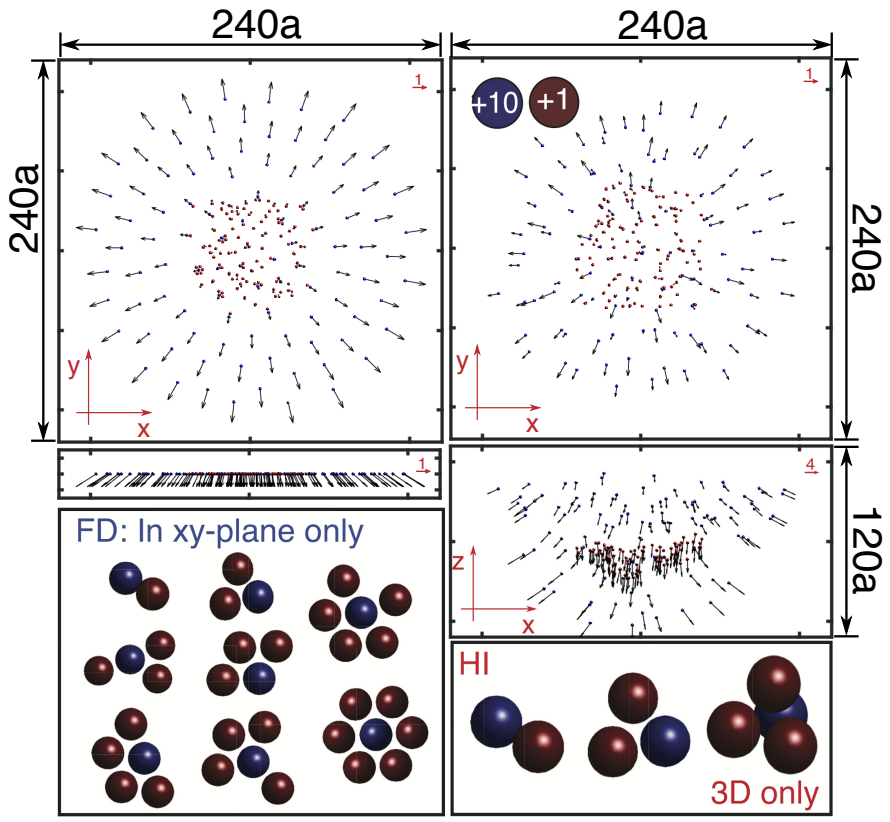

Figure 9.5: Position and momentum configuration of sedimenting particles after twenty particle sedimenting time for $N = 200$. The arrow vectors represent the instantaneous velocities of the particles. A scale bar is plotted at the upper-right corner in each panel to show the scale of velocity vectors. The figure includes results for free-draining particles (left column) and hydrodynamically interacting particles (right column), where top and side views of the particles are shown with the corresponding observed agglomerates. Two species are considered with $Q_1 = +10$, $Q_2 = +1$, and $\epsilon_{\text{in}}/\epsilon_{\text{out}} = 15$.

In the xy-plane, the particle configuration is also different compared to the FD case. The concentric distribution with clear ring structures at the periphery no longer persists. High-charge particles sedimenting individually are still "on average" found in the periphery, but the transition between them and the clusters in the center is no longer sharp and it resembles a diffusive pattern. Particles sedimenting individually at the periphery of the distribution are left behind along the sedimenting direction, and clusters near the center sediment faster according to Fig. 9.3. This is also evidenced by the larger z-component velocities of particles in the clusters compared to those individual particles at periphery shown in Fig. 9.5-HI. Another difference between HI and FD cases is that the HI particles only form dimers, trimers, and tetramers, with decreasing cluster fraction as N increases. Contrary to the FD case, the tetramer follows the global minimum in the energy landscape in Fig. 9.2 by forming a tetrahedron. Three-dimensional (3D) clustering have higher degrees of freedom and is harder to form than that for 2D clusters, which explains why the number of clusters is smaller and why it takes more time to reach the steady-state distribution for HI particles than that for FD particles.

So far we have discussed the differences in cluster formation and particle arrangement between FD and HI systems after sedimenting from an initial 2D configuration. Next we show the differences between FD and HI systems after sedimenting from a 3D configuration, to further emphasize the effect of hydrodynamic interaction on the collective motion of sedimenting particles. To do this, we restart the simulation with and without HI from the very instant shown in Fig. 9.5-HI, i.e., the particle configuration after sedimenting from a 2D configuration for twenty particle sedimenting time. During the simulation, we remove the motion of the center of mass (CoM) of all 200 particles at every time step to obtain particle trajectories relative to the CoM of the system. In Fig. 9.6, we plot the trajectories of FD and HI particles in the xy and xz plane during twenty particle sedimenting time since restarting from the 3D configuration. By our definition in this case, the CoM of particles stays at the origin all the time. In the xy-plane, high-charge individual particles at the periphery are

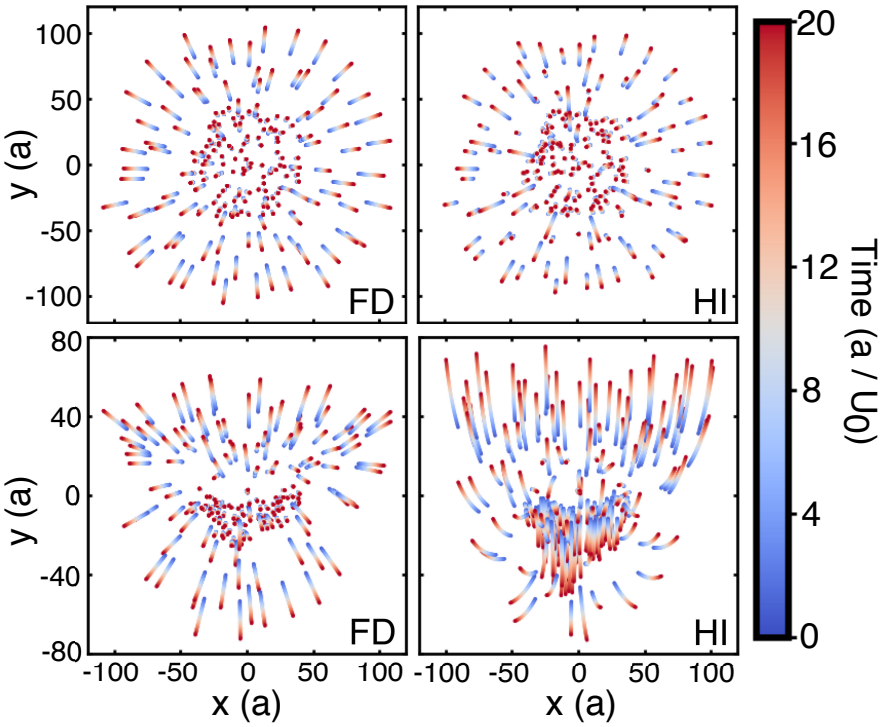

Figure 9.6: Particle trajectories after restarting from the configuration of HI system in Fig. 9.5 for another twenty particle sedimentating time with HI(right column) and without HI (left column). The simulation time from zero to twenty is shown as a continuous color gradient from blue to red. For lower panels, the yaxis lable should be z(a)

pushed further away from the center, while clusters and individual low-charge particles at the center show marginal movement in both FD and HI systems. However, most particles at the periphery in the FD case move faster and further away from the center compared to those in the HI case, due to the absence of viscous effects in the FD system. In the xz-plane, the trajectories of the FD and HI particles show completely different patterns. In the FD system, individual high-charge particles at the periphery move against the center along straight trajectories, while the particles near the center mostly remain still. In the HI system, clusters and low-charge particles near the center sediment faster than individual high-charge particles at the periphery. Consequently, both particles near and away from the center move against the but in opposite directions to the CoM. These observations confirm the significant effect of HI on the collective motion of sedimenting particles.

9.4.3 Sedimentation in a confined domain

We now proceed to study the sedimentation of polarizable particles in a quiescent fluid confined in a cylindrical cavity. Two polarizable particles are placed in a cylinder, where the particles' movement is driven by gravity and electrostatic interactions (see Fig. 9.7). The radius of cylinder in 3 and its length is 40. Periodic boundary conditions are enforced in the longitudinal direction. The origin (0, 0, 0) is located at the center of cylinder axis; the initial positions of the particles are (-1.2, 0, -18.8) and (1.2, 0, 18.8). The dielectric permittivity of the fluid $\epsilon_{\text{fluid}} = 2$ to represent an oil solvent and $\epsilon_{\text{wall}} \in [2, 80]$ to model various materials. The dielectric permittivity of particles $\epsilon_{\text{in}} = 30$, similar to an oxide and defining $\epsilon_{\text{in}}/\epsilon_{\text{fluid}} = 15$. The charges on particles are $Q_1 = Q_2 = +50$. We use $Q_1/Q_2 = 1$ to make the system symmetric with respect to the cylinder axis. As the particles sediment, they can migrate towards the center of the cylinder or towards the walls – changing their radial distance. When $\epsilon_{\text{wall}} = 2$, there is no electrostatic polarization on the interface between the wall and the fluid, i.e. the dielectric ratio between the wall and the fluid is one. Therefore, the particles repel each other and sediment slowly towards the walls as shown in Fig. 9.7(top). As ϵ_{wall} increases, the electrostatic polarization at the wall–fluid interfaces increases, inducing negative charges at the surfaces, thereby driving a faster migration of the particles towards the walls. Therefore, as $\epsilon_{\text{wall}} \to \infty$, the particle migration towards the walls becomes stronger (see Fig. 9.7). We also use a stable condition from Fig. 9.1, for instance $Q_1/Q_2 = 50$ and $\epsilon_{\text{in}}/\epsilon_{\text{out}} = 15$, where the polarization between the particles will now compete with the polarization effects at the wall–fluid interface. In Fig. 9.7(top) we included the case with a weak wall polarization, $\epsilon_{wall} = 3$. In this situation, the inter-particle attraction is strong enough to overcome the attraction from the wall, and particles sediment forming a cluster at the center of the cylinder. The sedimentation is two-fold faster due to (i) the dimmer formation and (ii) the mobility at the center of the cylinder is higher than the mobility near the walls.

We finish the discussion simulating three particles in the cylindrical cavity. Firstly, a

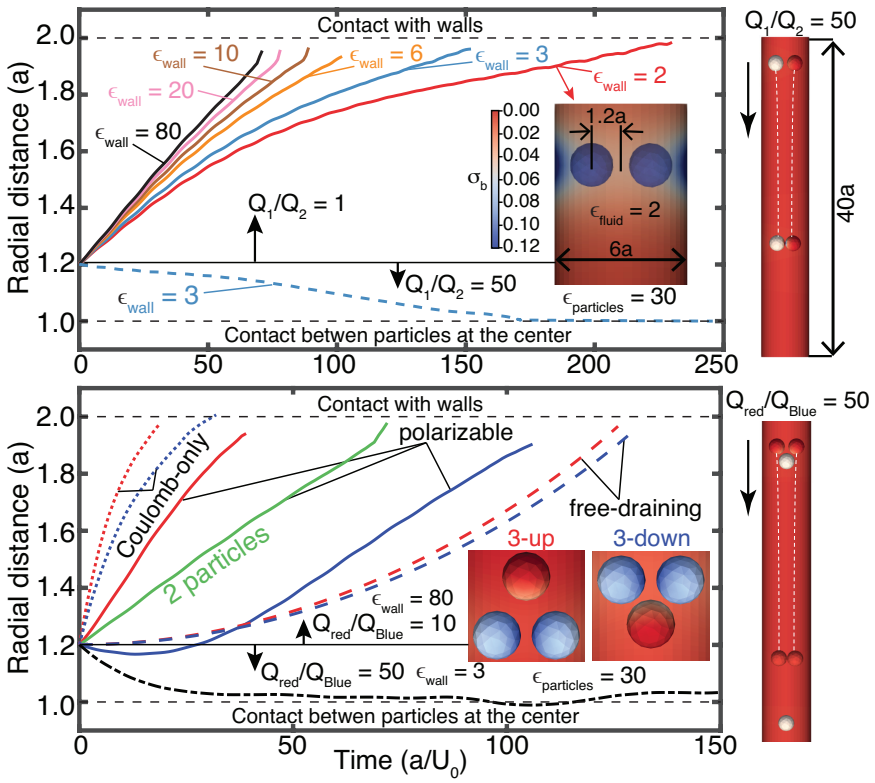

Figure 9.7: Sedimentation of polarizable particles in a Stokes fluid confined in a cylindrical cavity. (upper panel) Radial distance between the center of the particles and the cylinder axis as a function of time, for the case of two particles; solid lines are for $Q_1/Q_2 = 1$, and dashed line is for $Q_1/Q_2 = 50$ and $\epsilon_{\text{wall}} = 3$. (lower panel) Radial distance between the center of mass of blue particles shown in the insets and the cylinder axis as a function of time, and the red lines are for the "up" configuration (3-up), while the blue ones are for the "down" initial arrangement (3-down); for $Q_{\text{red}}/Q_{\text{blue}} = 10$, solid lines are for polarizable particles, dotted lines are for charged particles without polarization, and dashed lines correspond free-draining particles; for $Q_{\text{red}}/Q_{\text{blue}} = 50$, dash-dot black line is for charged particles with HI and polarization. In the insets, color contours representing the surface charge are included. On the right hand side of the plots, the systems' snapshots show the paths of particles during sedimentation and clustering.

third particle is placed above and bellow two particles, as shown in Fig. 9.7(bottom). The radius and dielectric permittivity of the particles are equal, $\epsilon_{\text{wall}} = 80$, and $Q_{\text{red}}/Q_{\text{blue}} = 10$. Similar to the two particles case, the polarization effects at the wall–fluid interface dominate during the sedimentation and the particles migrate towards the walls. However, the rates of sedimentation and migration depends strongly on the configuration and inter-particle interactions. In the Fig. 9.7(bottom), we compare the two particle migration with the three particle cases: "3-up" and "3-down". We observe that when the 3rd particle is above the other two, the time it takes for the 1st and 2nd particles to approach the wall is less than that when the 3rd particle is absent. This originates from the fact that the 3rd particle moves along the cylinder axis and sediments faster than the other two [255]; therefore, as the 3rd particle approaches the other two, it pushes them towards the wall. On the other hand, when the 3rd particle is below the other two, the 1st and 2nd particles will first approach each other at $0 < t < 15$ and then approach the wall at $t > 15$. The initial attraction between the 1st and 2nd particles is caused by the back-flow behind the 3rd particle. The attractive motions between the 1st and 2nd particles then slows down and they repel each other as their repulsive electrostatic interaction dominates. At $t > 30$, they gradually approach the wall at a rate that is nearly the same as that when the 3rd particle is absent, because the axial distance between the 3rd particle and the other two increases as time increases (the 1st and 2nd particles sediments at a lower rate as they approach cylinder wall [255]) and the HI from the 3rd particle to the other two becomes less important. The dotted red and blue lines in Fig. 9.7(bottom) correspond to situations without polarization effects. The particles migrate towards the wall faster because the repulsive forces between the 1st and 2nd particles are larger. The different migration between polarizable and non-polarizable particles highlights the importance of surface charge polarization during dynamics. For completness, The dashed red and blue lines correspond to cases without HI (free draining). The particles undergo free-falling in the cylindrical cavity with only electrostatic interaction and their motions are independent; the mobility is also independent of the radial direction. Without HI, the 1st

and 2nd particles approach the wall at an increasing rate. This is because the hydrodynamic drag on particles when they approach the wall is absent for FD particles. We also performed a simulation with the "3-down' configuration and $Q_{\text{red}}/Q_{\text{blue}} = 50$ with $\epsilon_{wall} = 3$ to study particle clustering. The results are included in Fig. 9.7(bottom) and are represented by the black dash-dot line; particle trajectories are included for completeness. In this case, the two particles form a dimer while the 3rd particle is repeled and sediments faster along the cylinder axis. What we intent to demonstrate is that heterogeneous dielectric properties of materials (particle, fluid, and confining wall), the electrostatic polarization effect, and the HI cooperatively affect particle dynamics in the confined geometry; they not only open serious degrees of freedom for particle mobility and migration, but also novel routes for engineering control and optimization of particulate transport.

9.5 Conclusions

We studied the effect of electrostatic polarization on the dynamics of hydrodynamically interacting particles during sedimentation in unconfined and confined Stokes fluids. This particular problem serves as a fundamental build up to understand the effect of hydrodynamic and electrostatic interactions on a wide range of applications including dynamics of biological entities in vascular environments and particle dynamics during water filtration and purification. We found that charged particles with equal signs will form stable clusters depending on their charge ratio and the difference between dielectric permittivities of the particle and the fluid. Stability conditions for this cluster formation are inherited during the dynamical evolution of the sedimenting particles. As particles agglomerate because of the electrostatic interaction and polarization effect, their collective motions are concomitantly modified by HI and fluid flows. Without HI, sedimenting particles will remain the xy-plane only configuration; with HI, agglomerates with $N > 2$ sediment faster than individual particles, and particles no longer remain the xy-plane only configuration and their positions along the sedimenting direction are different. Moreover, it takes longer time to form stable

agglomerates in HI case than that in FD case, and the number of agglomerates with $N > 2$ is smaller in HI case when particles reach steady state distribution. For the confined geometry, we studied sedimenting particles confined in a cylindrical cavity and demonstrated that dynamics of charged polarizable particles is strongly affected by the dielectric permittivities of the particle, fluid, and the confining geometry.

9.6 Appendix

9.6.1 Stokesian-Dynamics GgEm

Consider N rigid particles of hydrodynamic radius a suspended in an incompressible Newtonian fluid of viscosity η and density ρ. The motion of the fluid is governed by the Navier-Stokes equations, while the motion of the particles is described by the N-body Langevin equation [90]:

$$\mathbf{m} \cdot \frac{d\mathbf{U}_p}{dt} = \mathbf{F}^h + \mathbf{F}^c + \mathbf{F}^B, \tag{9.3}$$

where $\mathbf{m}$ is the mass/moment of inertia tensor, of dimension $6N \times 6N$, $\mathbf{U}_p$ is the particle translational/rotational velocity vector, $\mathbf{F}^h$, $\mathbf{F}^c$, and $\mathbf{F}^B$ are the hydrodynamic, conservative, and Brownian force/torque vectors of dimension $6N$. For one particle these vectors will be

$$\mathbf{U}_P = \begin{pmatrix} U_{p,1} \\ U_{p,2} \\ U_{p,3} \\ \Omega_{p,1} \\ \Omega_{p,2} \\ \Omega_{p,3} \end{pmatrix} \quad \text{and} \quad \mathbf{F}^h = \begin{pmatrix} F_1^h \\ F_2^h \\ F_3^h \\ T_1^h \\ T_2^h \\ T_3^h \end{pmatrix}, \tag{9.4}$$

where $U_{p,i}$ is the translational velocity, $\Omega_{p,i}$ is the angular velocity, F_i^h is the hydrodynamic force and T_i^h is the hydrodynamic torque.

In the absence of particle inertia and ignoring Brownian forces, (9.3) reduces to

$$\mathbf{F}^h + \mathbf{F}^c = 0. \tag{9.5}$$

At low particle Reynolds numbers, the hydrodynamic forces and torques acting on the particles in a suspension undergoing a bulk linear flow that can be written as [see for example 215, 105]

$$\mathbf{F}^h = -\mathbf{R}_{\mathrm{FU}} \cdot \left(\mathbf{U}_p - \mathbf{u}^\infty\right) - \mathbf{R}_{\mathrm{FE}} : \left(-\mathbf{E}^\infty\right), \tag{9.6}$$

where $\mathbf{u}^\infty$ is the fluid bulk linear translational/rotational velocity at the particle center, $\mathbf{E}^\infty$ is the externally imposed rate-of-strain tensor, and $\mathbf{R}_{FU}$ and $\mathbf{R}_{FE}$ are the configuration-dependent components of the multi-body hydrodynamic resistance tensor. For one particle the fluid velocity vector will be

$$\mathbf{u}^\infty = \begin{pmatrix} u_1^\infty \\ u_2^\infty \\ u_3^\infty \\ \omega_1^\infty \\ \omega_2^\infty \\ \omega_3^\infty \end{pmatrix}, \tag{9.7}$$

where u_i^∞ is the translational fluid velocity and ω_i^∞ is the fluid angular velocity.

We proceed to describe the methodology for solving what is known as the mobility problem [255, 215], which is calculating the particle translational and rotational velocities, given the conservative (non-hydrodynamic) forces/torques acting on the particles. As in Stokesian Dynamics (SD) simulations, the hydrodynamic force/torque vector is split into far-field and near-field parts as [272, 273, 107, 274, 275, 276, 277]

$$\begin{aligned} \mathbf{F}^h &= \mathbf{F}^h_{\mathrm{ff}} + \mathbf{F}^h_{\mathrm{nf}} \\ &= \mathbf{F}^h_{\mathrm{ff}} - \mathbf{R}_{\mathrm{FU,nf}} \cdot \left(\mathbf{U}_p - \mathbf{u}^\infty\right) - \mathbf{R}_{\mathrm{FE,nf}} : \left(-\mathbf{E}^\infty\right). \end{aligned} \tag{9.8}$$

The near-field or lubrication forces are added in a pair-wise additive manner, whenever two particles, or a particle and a wall are within a specified cutoff separation. The lubrication interactions are added via the near-field resistance tensors. The addition of the lubrication corrections is described in detail in a latter section, but for the purpose of describing the overall formalism, it is suffice to mention that there are analytical expressions for the near-field resistance tensors. The only unknowns in the problem are the far-field hydrodynamic forces/torques and the particle velocities.

Far-field hydrodynamic interactions

In conventional SD, the far-field component of the hydrodynamic force/torque vector is calculated by explicitly calculating the hydrodynamic resistance tensor. This involves an $O(N^2)$ calculation of the N-particle mobility tensor, and an $O(N^3)$ inversion. To avoid this, we use the methodology of Accelerated Stokesian Dynamics (ASD) [108], and directly compute the far-field force/torque vector, as a product of the resistance tensor and a known velocity. The different steps involved in calculating the far-field force/torque vector are outlined below.

The far-field hydrodynamic forces/torques are solved in an iterative manner. We begin by assuming values for the far-field hydrodynamic forces, torques, and stresslets for all particles. In Stokes flow, the velocity at any point in the fluid can be expressed using Green's functions in a very general form as

$$\mathbf{u}(\mathbf{x}) = \mathbf{u}^{\infty}(\mathbf{x}) + \sum_{\nu=1}^{N} \boldsymbol{\xi}(\mathbf{x} - \mathbf{x}_{\nu}) \cdot \mathbf{F}_{\nu}, \tag{9.9}$$

where $\mathbf{x}$ represents the cartesian coordinates, $\mathbf{u}$ is the disturbance velocity at any point $\mathbf{x}$, and $\mathbf{F}_{\nu}$ is the hydrodynamic force/torque/stresslet exerted by particle ν on the fluid. $\boldsymbol{\xi}(\mathbf{x})$ is a Green's tensor which relates the hydrodynamic force and its moments to the disturbance velocity. It should be noted that (9.9) is just a schematic representation, and the actual

calculation of the disturbance velocity will be described in detail later.

The motion of a particle immersed in a flow field described by (9.9) can be calculated using Faxen's relations that relate the hydrodynamic forces and higher moments on a particle ν to the particle velocity and the disturbance velocity [255], i.e.

$$\mathbf{F}_\nu = -6\pi\eta a \left(\mathbf{U}_{p,\nu} - \mathbf{u}^\infty(\mathbf{x}_\nu)\right) + 6\pi\eta a H\left(\mathbf{u}(\mathbf{x}) - \mathbf{u}^\infty(\mathbf{x})\right), \tag{9.10}$$

where H is a known functional operator acting on the disturbance velocity. In conventional Stokesian Dynamics, (9.9) and (9.10) are used to eliminate the fluid velocity and thus relate the particle velocity $\mathbf{U}$ directly to the forces $\mathbf{F}$. However, this involves the expensive $O(N^2)$ calculation. Equations (9.9) and (9.10) are iteratively solved using a method such as GMRES [See for example 278, 279] to get a converged value for the far-field forces/torques/stresslets. Fast convergence is achieved by using the forces calculated in the previous time step as the initial guess.

Once the far-field hydrodynamic forces/toques are calculated, (9.8) can be used to solve for the particle velocities, $\mathbf{U}_p$. Note that while solving for the far-field forces, (9.10), we have assumed that the particle velocities are known. The particle velocities from the previous time step can be used to calculate the hydrodynamic forces in (9.10). Alternatively, the particle velocities can also be calculated iteratively. This would begin with a guess for the particle velocities and far-field hydrodynamic forces, and for the value of the particle velocities chosen, the far-field force is calculated, which is then used in the force balance to get an improved estimate of the particle velocities. However, it has been shown that the former method yields satisfactory results [108].

In describing the general methodology for calculating the particle velocities, we have glossed over the details on the calculation of the disturbance velocity (9.9) and implementing the operator in Faxen's formulae (9.10). We shall now describe these two steps in more detail.

Disturbance velocity and its derivatives

Consider the Stokes equations for the disturbance created by N point forces,

$$-\nabla p + \eta \nabla^2 \mathbf{u}(\mathbf{x}) = -\boldsymbol{\rho}(\mathbf{x}), \tag{9.11}$$

$$\nabla \mathbf{u}(\mathbf{x}) \cdot = 0, \tag{9.12}$$

where the force density is defined by

$$\boldsymbol{\rho}(\mathbf{x}) = \sum_{\nu=1}^{N} \delta(\mathbf{x} - \mathbf{x}_\nu) \mathbf{F}_\nu, \tag{9.13}$$

where $\mathbf{F}_\nu$ is the force exerted by the particle on the fluid at $\mathbf{x}_\nu$. For an unbounded domain, the disturbance velocity field is given by

$$\mathbf{u}(\mathbf{x}) = \sum_{\nu=1}^{N} \mathbf{G}(\mathbf{x} - \mathbf{x}_\nu) \cdot \mathbf{F}_\nu, \tag{9.14}$$

where $\mathbf{G}(\mathbf{x})$ is the free-space Green's function of Stokes equations, also known as the stokeslet, and it is given by

$$\mathbf{G}(\mathbf{x}) = \frac{1}{8\pi\eta r} \left(\boldsymbol{\delta} + \frac{\mathbf{x}\mathbf{x}}{r^2} \right), \tag{9.15}$$

where $\boldsymbol{\delta}$ is the 3×3 identity matrix and $r = |\mathbf{x}|$.

To treat bounded domains, we use the General geometry Ewald-like method (GgEm) [118]. The GgEm starts with the restatement of the force-density expression in (9.13):

$$\boldsymbol{\rho}(\mathbf{x}) = \boldsymbol{\rho}_l(\mathbf{x}) + \boldsymbol{\rho}_g(\mathbf{x}), \tag{9.16}$$

similar to conventional $\mathrm{P^3M}$ methods. Here the "local" density is

$$\boldsymbol{\rho}_l(\mathbf{x}) = \sum_{\nu=1}^{N} \mathbf{f}_\nu \left[\delta(\mathbf{x} - \mathbf{x}_\nu) - g(\mathbf{x} - \mathbf{x}_\nu) \right], \tag{9.17}$$

which drives the local contribution of the velocity field, $\mathbf{u}_l(\mathbf{x})$; and, the "global" density is

$$\boldsymbol{\rho}_g(\mathbf{x}) = \sum_{\nu=1}^{N} \mathbf{f}_\nu \left[g(\mathbf{x} - \mathbf{x}_\nu) \right], \tag{9.18}$$

responsible for the global contribution of the velocity field, $\mathbf{u}_g(\mathbf{x})$. By linearity $\mathbf{u}(\mathbf{x}) = \mathbf{u}_l(\mathbf{x}) + \mathbf{u}_g(\mathbf{x})$.

The local velocity, $\mathbf{u}_l(\mathbf{x})$, is calculated assuming an unbounded domain:

$$\mathbf{u}_l(\mathbf{x}) = \sum_{\nu}^{N} \mathbf{G}_l(\mathbf{x} - \mathbf{x}_\nu) \cdot \mathbf{f}_\nu, \tag{9.19}$$

where $\mathbf{G}_l(\mathbf{x})$ is composed of a free-space Stokeslet minus a smoothed Stokeslet obtained from the solution of Stokes equations with the forcing term given by the function $\boldsymbol{\rho}_g(\mathbf{x})$. For the Stokes equations we found that a modified Gaussian

$$g(r) = \frac{\alpha^3}{\pi^{3/2}} \mathrm{e}^{(-\alpha^2 r^2)} \left[5/2 - \alpha^2 r^2 \right], \tag{9.20}$$

yields a simple expression for $\mathbf{G}_l(\mathbf{x})$:

$$\mathbf{G}_l(\mathbf{x}) = \frac{1}{8\pi\eta} \left[\boldsymbol{\delta} + \frac{\mathbf{x}\mathbf{x}}{r^2} \right] \frac{\mathrm{erfc}(\alpha r)}{r} - \frac{1}{8\pi\eta} \left[\boldsymbol{\delta} - \frac{\mathbf{x}\mathbf{x}}{r^2} \right] \frac{2\alpha}{\sqrt{\pi}} \mathrm{e}^{(-\alpha^2 r^2)}. \tag{9.21}$$

Because $\mathbf{G}_l(\mathbf{x})$ decays exponentially on the length scale α^{-1}, in practice the local velocity can be computed, as in normal Ewald methods, by only considering near-neighbors to each particle ν [132].

The global velocity is due to the force distribution $\boldsymbol{\rho}_g(\mathbf{x})$. In Ewald formulations this solution is given in Fourier space. For a general domain, on the other hand, we find the solution to Stokes' equation numerically, requiring that $\mathbf{u}_l + \mathbf{u}_g$ satisfy appropriate boundary conditions. At a no-slip boundary we would require $\mathbf{u}_g(\mathbf{x}) = -\mathbf{u}_l(\mathbf{x})$. For problems with periodic boundary conditions, Fourier techniques can be used to guarantee the periodicity

of the global velocity $\mathbf{u}_g$. The periodicity on the local velocity, $\mathbf{u}_l$, is obtained using the minimum image convention. The solution is obtained on a set of M discrete points on a mesh; in this regard, GGEM resembles a P^3M method where the assignment function is replaced by the delta function [280, 132]. Many techniques (finite differences, finite elements, spectral methods) can be used to find the global contribution; after the mesh is resolved, interpolation can be used to get the value of the global velocity at the location $\mathbf{x}_\nu$ of each point [132].

The above description was assuming point forces, and is suitable for studying polymeric systems, where the force can be assumed to act at the center of a bead. For simulating particle suspensions, this assumption is only valid in the dilute regime, where inter-particle separation is considerably larger than the particle size. For concentrated dispersions, it is necessary to include the fact that the point forces are not concentrated at the center of the particle, but rather distributed on the surface of each particle. So, the disturbance velocity (9.14) changes to [215, 105]

$$\mathbf{u}(\mathbf{x}) = \sum_{\nu=1}^{N} \int_{S_\nu} \mathbf{G}(\mathbf{x} - \mathbf{x}_\nu) \cdot \mathbf{F}_\nu(\mathbf{y}) dS_\nu(\mathbf{y}), \tag{9.22}$$

where integral is over S_ν, the surface of the particle. Expanding the Green's function inside the integral in (9.22) in moments about the center of the particle, $\mathbf{x}_\nu$ [275]

$$\begin{aligned} \mathbf{u}(\mathbf{x}) = \sum_{\nu=1}^{N} \quad & \left[\int_{S_\nu} \mathbf{G}(\mathbf{x} - \mathbf{x}_\nu) \cdot \mathbf{F}_\nu(\mathbf{y}) dS_\nu(\mathbf{y}) + \right. \\ & \left. \int_{S_\nu} \frac{\partial}{\partial \mathbf{x}_\nu} \cdot \mathbf{G}(\mathbf{x} - \mathbf{y})|_{\mathbf{y}=\mathbf{x}_\nu} (\mathbf{y} - \mathbf{x}_\nu) \cdot \mathbf{F}_\nu(\mathbf{y}) dS_\nu(\mathbf{y}) \right], \end{aligned} \tag{9.23}$$

where the monopole or zeroth moment is the total force acting on the particle ν, the first moment or dipole can be split into symmetric and anti-symmetric parts corresponding to the Stresslet and Rotlet respectively, and so on [See for example 215, 105, 256]. The disturbance

velocity can thus be written as a sum of force moments as [275, 107]

$$\mathbf{u}(\mathbf{x}) = \sum_{\nu=1}^{N} \left[\left(1 + \frac{a^2}{6}\nabla^2 \right) \mathbf{G} \cdot \mathbf{F}_\nu + \mathbf{R} \cdot \mathbf{T}_\nu + \left(1 + \frac{a^2}{10}\nabla^2 \right) \mathbf{K} \cdot \mathbf{S}_\nu \right], \tag{9.24}$$

where the $\mathbf{F}$ and $\mathbf{T}$ are the force and torque (vectors) exerted by the particle on the fluid and $\mathbf{S}$ is the stress (tensor) exerted by the particle on the fluid. The tensors $\mathbf{R}$ and $\mathbf{K}$ are the anti-symmetric (Rotlet) and symmetric (Stresslet) derivatives of the Stokeslet or Green's function of Stokes equations, they are given by

$$R_{ij}(\mathbf{x}) = \epsilon_{ijk} \frac{1}{2} \left(\nabla_k G_{ij}(\mathbf{x}) - \nabla_j G_{ik}(\mathbf{x}) \right), \tag{9.25}$$

$$K_{ijk}(\mathbf{x}) = \frac{1}{2} \left(\nabla_k G_{ij}(\mathbf{x}) + \nabla_j G_{ik}(\mathbf{x}) \right). \tag{9.26}$$

With (9.24) the local contribution to the velocity, $\mathbf{u}_l$, according to the GGEM methodology will be

$$\mathbf{u}_l(\mathbf{x}) = \sum_{\nu=1}^{N} \left[\left(1 + \frac{a^2}{6}\nabla^2 \right) \mathbf{G}_l \cdot \mathbf{F}_\nu + \mathbf{R}_l \cdot \mathbf{T}_\nu + \left(1 + \frac{a^2}{10}\nabla^2 \right) \mathbf{K}_l \cdot \mathbf{S}_\nu \right], \tag{9.27}$$

Green's function, $\mathbf{R}_l$ and $\mathbf{K}_l$, are calculated from (9.21), they are listed below. The global contribution for the velocity, $\mathbf{u}_g$, is calculated numerically by solving Stokes equations (9.12) with the following force density

$$\boldsymbol{\rho}_g(\mathbf{x}) = \sum_{\nu=1}^{N} \left[\left(1 + \frac{a^2}{6}\nabla^2 \right) g(r)\mathbf{F}_\nu + \nabla g(r) \times \mathbf{T}_\nu + \left(1 + \frac{a^2}{10}\nabla^2 \right) \nabla g(r) \cdot \mathbf{S}_\nu \right], \tag{9.28}$$

where $r = |\mathbf{x} - \mathbf{x}_\nu|$ and the derivatives account for the distribution of point forces on the surface of the particle. For example, to calculate the disturbance velocity at the center of particle ν, a force density given by (9.28) is distributed at the centre of all particles and their periodic neighbors, including particle ν. Next, the force density on the particles is interpolated on to mesh points within a certain cut-off distance, which is identical to the

cut-off distance taken in the local calculations. Now that the force density is distributed on to regular mesh points, we solve Stokes equations (9.12) numerically to obtain the disturbance velocity on the mesh points due to all particles and their periodic neighbors. In the presence of any bounding surfaces, boundary conditions are enforced while solving Stokes equations. For example, to enforce no-slip we required $\mathbf{u}(\mathbf{x}) = \mathbf{u}_l(\mathbf{x}) + \mathbf{u}_g(\mathbf{x}) = 0$.

The solution is obtained on M discrete points on a mesh, and interpolated on to the center of each particle to find the disturbance velocity at the particle center. The criteria for selection of α are reported elsewhere [118, 127, 281]. It should be noted that while calculating the global part of the disturbance velocity on particle ν, we included the forcing due to the particle itself, along with its periodic neighbors. However, we only want the disturbance velocity due to its periodic neighbors and other particles. To correct for this, we subtract the global contribution of the velocity distribution due to particle ν. This is done by calculating the product of the global Green's function and its derivatives, calculated at the limit of zero separation, and the respective force moments. This self-correction is given by

$$\mathbf{u}_{\text{self}}(\mathbf{x}) = \lim_{r\to 0}\left[\left(1+\frac{a^2}{6}\nabla^2\right)\mathbf{G}_g\cdot\mathbf{F}_\nu + \mathbf{R}_g\cdot\mathbf{T}_\nu + \left(1+\frac{a^2}{10}\nabla^2\right)\mathbf{K}_g\cdot\mathbf{S}_\nu\right], \tag{9.29}$$

where

$$\mathbf{G}_g(\mathbf{x}) = \frac{1}{8\pi\eta}\left[\boldsymbol{\delta}+\frac{\mathbf{xx}}{r^2}\right]\frac{\text{erf}(\alpha r)}{r} + \frac{1}{8\pi\eta}\left[\boldsymbol{\delta}-\frac{\mathbf{xx}}{r^2}\right]\frac{2\alpha}{\sqrt{\pi}}\text{e}^{(-\alpha^2 r^2)}. \tag{9.30}$$

To complete the iterative scheme described earlier, we require a new estimate for the forces and torques to be calculated using Faxen's relations. These are explicitly written as

$$\mathbf{F}(\mathbf{x}_\nu) = -6\pi\eta a\left(\mathbf{U}_p-\mathbf{u}^\infty\right) + 6\pi\eta a\left(1+\frac{a^2}{6}\nabla^2\right)\left[\mathbf{u}_l(\mathbf{x}_\nu)+\mathbf{u}_g(\mathbf{x}_\nu)\right], \tag{9.31}$$

$$\mathbf{T}(\mathbf{x}_\nu) = -8\pi\eta a^3\left(\boldsymbol{\Omega}_p-\boldsymbol{\omega}^\infty\right) + 4\pi\eta a^3\nabla\times\left[\mathbf{u}_l(\mathbf{x}_\nu)+\mathbf{u}_g(\mathbf{x}_\nu)\right], \tag{9.32}$$

$$\mathbf{S}(\mathbf{x}_\nu) = \frac{20}{3}\pi\eta a\mathbf{E}^\infty + \frac{20}{3}\pi\eta a^3\left(1+\frac{a^2}{10}\nabla^2\right)\left[\mathbf{e}_l(\mathbf{x}_\nu)+\mathbf{e}_g(\mathbf{x}_\nu)\right], \tag{9.33}$$

where $\mathbf{e}$ is the rate-of-strain tensor. The local velocity and its gradients are calculated analytically, combining (9.27) and (9.33).

Solving Stokes equations yields the global velocity on M mesh points. We first compute the Laplacian of the global velocity on all mesh points by taking finite differences around 5 neighboring mesh points in each direction. Thus, both the global velocity, $\mathbf{u}_g$, and its Laplacian, $\nabla^2\mathbf{u}_g$, are known at every mesh point. These two quantities are sufficient to calculate all derivatives in at the centre of each particle. The coarse global mesh is sufficiently accurate for the calculation of the derivatives since the global velocity decays slowly on the length scale of α^{-1}.

Near-field (lubrication) interactions

The near-field or lubrication corrections are calculated as in traditional Stokesian Dynamics [107]. Lubrication corrections are added for every pair of particles (particle-particle (pp)), which are within a certain cut-off separation. Lubrication corrections are included by adding exact two-body resistance tensors to the far-field many-body resistance tensor. Since the far-field part of the exact resistance tensor is already accounted for by the many-body resistance tensor, a two-body far-field resistance tensor must be subtracted in order to avoid double counting [275, 107]. This far-field two-body resistance tensor is calculated by inverting a two-body mobility tensor, constructed to the same order (in multipole expansion) as the far-field many-body resistance tensor, i.e.,

$$\mathbf{R}_{\mathrm{nf}} = \left(\mathbf{R}_{\mathrm{pp}} - \mathbf{R}^{\infty}_{\mathrm{pp}}\right) \tag{9.34}$$

The exact solutions ($\mathbf{R}_{\mathrm{pp}}$) are reported in literature as series solutions or tabulated data [**?** 283, 284, 284, 258, 257]. For the case of equal-sized spheres, the data is fit with simple rational expressions, accurate ($R^2 > 0.999$) to a surface-surface separation of $0.01a$.

The second part of the lubrication correction is to subtract the far-field two body compo-

nent already included in the many-body resistance tensor. To do this, a two-body mobility tensor is constructed and inverted, to the same order of approximation as in (9.24). To describe how this tensor is constructed, consider the grand mobility tensor, $\mathbf{M}$, defined by [257]

$$\begin{pmatrix} \mathbf{U} \\ \mathbf{\Omega} \\ -\mathbf{E} \end{pmatrix} = \begin{bmatrix} \mathbf{M}_{\mathrm{UF}} & \mathbf{M}_{\mathrm{UT}} & \mathbf{M}_{\mathrm{US}} \\ \mathbf{M}_{\Omega\mathrm{F}} & \mathbf{M}_{\Omega\mathrm{T}} & \mathbf{M}_{\Omega\mathrm{S}} \\ \mathbf{M}_{\mathrm{EF}} & \mathbf{M}_{\mathrm{ET}} & \mathbf{M}_{\mathrm{ES}} \end{bmatrix} \cdot \begin{pmatrix} \mathbf{F} \\ \mathbf{T} \\ -\mathbf{S} \end{pmatrix}. \tag{9.35}$$

For sphere-sphere far-field interactions, the different components of (9.35) are calculated as functions of the Green's function or Stokeslet [215, 105], for two given spheres ν and μ are defined by

$$\mathbf{M}_{\mathrm{UF}}^{\nu\mu} = \left(1+\frac{a^2}{6}\nabla_\nu^2\right)\left(1+\frac{a^2}{6}\nabla_\mu^2\right)\mathbf{G}(\mathbf{x}_\nu,\mathbf{x}_\mu), \tag{9.36}$$

$$\mathbf{M}_{\mathrm{UT}}^{\nu\mu} = \left(1+\frac{a^2}{6}\nabla_\nu^2\right)\mathbf{R}(\mathbf{x}_\nu,\mathbf{x}_\mu), \tag{9.37}$$

$$\mathbf{M}_{\mathrm{US}}^{\nu\mu} = \left(1+\frac{a^2}{6}\nabla_\nu^2\right)\left(1+\frac{a^2}{10}\nabla_\mu^2\right)\mathbf{K}(\mathbf{x}_\nu,\mathbf{x}_\mu), \tag{9.38}$$

$$\mathbf{M}_{\Omega\mathrm{T}}^{\nu\mu} = \nabla_\nu \times \mathbf{R}(\mathbf{x}_\nu,\mathbf{x}_\mu), \tag{9.39}$$

$$\mathbf{M}_{\Omega\mathrm{S}}^{\nu\mu} = \nabla_\nu \times \left(1+\frac{a^2}{10}\nabla_\mu^2\right)\mathbf{K}(\mathbf{x}_\nu,\mathbf{x}_\mu), \tag{9.40}$$

$$\mathbf{M}_{\mathrm{ES}}^{\nu\mu} = \left(1+\frac{a^2}{10}\nabla_\nu^2\right)\left[\nabla_\nu\left(1+\frac{a^2}{10}\nabla_\mu^2\right)\mathbf{K}(\mathbf{x}_\nu,\mathbf{x}_\mu)\right] + \tag{9.41}$$

$$\left(1+\frac{a^2}{10}\nabla_\nu^2\right)\left[\nabla_\nu\left(1+\frac{a^2}{10}\nabla_\mu^2\right)\mathbf{K}(\mathbf{x}_\nu,\mathbf{x}_\mu)\right]^T, \tag{9.42}$$

with the remaining terms calculated using symmetry property of the grand mobility tensor.

Inverting the far-field tensor, gives a far-field two-body (2B) resistance tensor, expressed as

$$\begin{aligned}\begin{pmatrix}\mathbf{F}\\ \mathbf{T}\\ \mathbf{S}\end{pmatrix} &= \left[\mathbf{M}^{\infty}_{\mathrm{2B}}\right]^{-1}\cdot\begin{pmatrix}\mathbf{U}\\ \boldsymbol{\Omega}\\ -\mathbf{E}\end{pmatrix} = \left[\mathbf{R}^{\infty}_{\mathrm{2B}}\right]\cdot\begin{pmatrix}\mathbf{U}\\ \boldsymbol{\Omega}\\ -\mathbf{E}\end{pmatrix}\\ &= \begin{bmatrix}\mathbf{R}^{\infty}_{\mathrm{2B,FU}} & \mathbf{R}^{\infty}_{\mathrm{2B,F\Omega}} & \mathbf{R}^{\infty}_{\mathrm{2B,FE}}\\ \mathbf{R}^{\infty}_{\mathrm{2B,TU}} & \mathbf{R}^{\infty}_{\mathrm{2B,T\Omega}} & \mathbf{R}^{\infty}_{\mathrm{2B,TE}}\\ \mathbf{R}^{\infty}_{\mathrm{2B,SU}} & \mathbf{R}^{\infty}_{\mathrm{2B,S\Omega}} & \mathbf{R}^{\infty}_{\mathrm{2B,SE}}\end{bmatrix}\cdot\begin{pmatrix}\mathbf{U}\\ \boldsymbol{\Omega}\\ -\mathbf{E}\end{pmatrix}. \end{aligned} \tag{9.43}$$

Note that in general, $\mathbf{R}^{\infty}_{\mathrm{FU}} \neq \left[\mathbf{M}_{\mathrm{FU}}\right]^{-1}$ and so on. The sub-scripts are merely used to denote the appropriate parts of the two-body resistance tensor. Extracting the relevant components from the particle-particle and particle-wall resistance tensors, and subtracting it from the exact solutions as in (9.34), yields the lubrication corrections $\mathbf{R}_{\mathrm{FU,nf}}$ and $\mathbf{R}_{\mathrm{FE,nf}}$.

Smoothed Green's function moments

In order to obtain the local-contribution from (9.27) and (9.33) the moments from the smoothed Green's function are needed. These functions come from the use of

$$g(r) = \frac{\alpha^3}{\pi^{3/2}}\mathrm{e}^{(-\alpha^2 r^2)}\left[5/2 - \alpha^2 r^2\right], \tag{9.44}$$

as the smearing function, which yields

$$G_{l,ij}(\mathbf{x}) = \frac{1}{8\pi\eta}\left\{\left[\delta_{ij} + \frac{x_i x_j}{r^2}\right]\frac{\mathrm{erfc}(\alpha r)}{r} - \left[\delta_{ij} - \frac{x_i x_j}{r^2}\right]\frac{2\alpha}{\sqrt{\pi}}\mathrm{e}^{(-\alpha^2 r^2)}\right\}. \tag{9.45}$$

From the definitions (9.26), the smoothed local-moments are given by

$$R_{l,ijk}(\mathbf{x}) = \frac{1}{16\pi\eta} \quad \left\{ \left[\delta_{ik}x_j - \delta_{ij}x_k\right] \frac{2\mathrm{erfc}(\alpha r)}{r^3} + \left[\delta_{ik}x_j - \delta_{ij}x_k\right] \frac{4\alpha}{\sqrt{\pi}} \frac{\mathrm{e}^{(-\alpha^2 r^2)}}{r^2} \right.$$
$$\left. \left[\delta_{ij}x_k - \delta_{ik}x_j\right] \frac{4\alpha^3}{\sqrt{\pi}} \mathrm{e}^{(-\alpha^2 r^2)} \right\}, \tag{9.46}$$

$$K_{l,ijk}(\mathbf{x}) = \frac{1}{16\pi\eta} \quad \left\{ \left[\delta_{kj}x_i - 3\frac{x_i x_j x_k}{r^2}\right] \frac{2\mathrm{erfc}(\alpha r)}{r^3} + \left[\delta_{kj}x_i - 3\frac{x_i x_j x_k}{r^2}\right] \frac{4\alpha}{\sqrt{\pi}} \frac{\mathrm{e}^{(-\alpha^2 r^2)}}{r^2} \right.$$
$$\left. \left[\delta_{ij}x_k + \delta_{ik}x_j - 2\frac{x_i x_j x_k}{r^2}\right] \frac{4\alpha^3}{\sqrt{\pi}} \mathrm{e}^{(-\alpha^2 r^2)} \right\}. \tag{9.47}$$

The local-Laplacians by

$$\nabla^2 G_{l,ij}(\mathbf{x}) = \frac{1}{8\pi\eta} \left\{ \left[\delta_{ij} - 3\frac{x_i x_j}{r^2}\right] \frac{2\mathrm{erfc}(\alpha r)}{r^3} + \left[\delta_{ij} - 3\frac{x_i x_j}{r^2}\right] \frac{4\alpha}{\sqrt{\pi}} \frac{\mathrm{e}^{(-\alpha^2 r^2)}}{r^2} \right.$$
$$\left. \left[2\delta_{ij} - \frac{x_i x_j}{r^2}\right] \frac{8\alpha^3}{\sqrt{\pi}} \mathrm{e}^{(-\alpha^2 r^2)} - \left[r^2\delta_{ij} - x_i x_j\right] \frac{8\alpha^5}{\sqrt{\pi}} \mathrm{e}^{(-\alpha^2 r^2)} \right\}, \tag{9.48}$$

$$\nabla^2 K_{l,ijk}(\mathbf{x}) = \frac{1}{16\pi\eta} \left\{ \left[5\frac{x_i x_j x_k}{r^2} - \delta_{ij}x_k - \delta_{ik}x_j - \delta_{kj}x_i\right] \frac{12\mathrm{erfc}(\alpha r)}{r^5} + \left[5\frac{x_i x_j x_k}{r^2} - \right.\right.$$
$$\delta_{ij}x_k - \delta_{ik}x_j - \delta_{kj}x_i \left] \frac{16\alpha^3}{\sqrt{\pi}} \frac{\mathrm{e}^{(-\alpha^2 r^2)}}{r^2} + \left[4\frac{x_i x_j x_k}{r^2} - \delta_{ij}x_k - \right.\right.$$
$$\delta_{ik}x_j - \delta_{kj}x_i \left] \frac{24\alpha}{\sqrt{\pi}} \frac{\mathrm{e}^{(-\alpha^2 r^2)}}{r^4} - \left[-4\frac{x_i x_j x_k}{r^2} + 5\delta_{ij}x_k + 5\delta_{ik}x_j - \right.\right.$$
$$2\delta_{kj}x_i \left] \frac{8\alpha^5}{\sqrt{\pi}} \mathrm{e}^{(-\alpha^2 r^2)} + \left[\delta_{ij}x_k r^2 + \delta_{ik}x_j r^2 - \right.\right.$$
$$\left. \left. 2x_i x_j x_k \right] \frac{16\alpha^7}{\sqrt{\pi}} \mathrm{e}^{(-\alpha^2 r^2)} \right\}. \tag{9.49}$$

The local-curls by

$$\begin{aligned}\nabla\times G_{l,ijk}(\mathbf{x}) &= \epsilon_{ijk}\frac{1}{8\pi\eta}\left\{\left[-3\frac{x_kx_mx_j}{r^2}-\delta_{km}x_j+\delta_{kj}x_m+\delta_{jm}x_k\right]\frac{\mathrm{erfc}(\alpha r)}{r^3}+\right.\\ &\left[-3\frac{x_kx_mx_j}{r^2}-\delta_{km}x_j+\delta_{kj}x_m+\delta_{jm}x_k\right]\frac{2\alpha}{\sqrt{\pi}}\frac{\mathrm{e}^{(-\alpha^2r^2)}}{r^2}+\\ &\left.\left[-\frac{x_kx_mx_j}{r^2}+\delta_{km}x_j\right]\frac{4\alpha^3}{\sqrt{\pi}}\mathrm{e}^{(-\alpha^2r^2)}\right\},\end{aligned}\tag{9.50}$$

$$\begin{aligned}\nabla\times R_{l,ijk}(\mathbf{x}) &= \epsilon_{ijk}\frac{1}{32\pi\eta}\left\{\left[\delta_{km}\delta_{jn}-\delta_{kn}\delta_{jm}-3\frac{\delta_{km}x_nx_j}{r^2}+3\frac{\delta_{kn}x_mx_j}{r^2}\right]\frac{2\mathrm{erfc}(\alpha r)}{r^3}+\right.\\ &\left[\delta_{km}\delta_{jn}-\delta_{kn}\delta_{jm}-3\frac{\delta_{km}x_nx_j}{r^2}+3\frac{\delta_{kn}x_mx_j}{r^2}\right]\frac{4\alpha}{\sqrt{\pi}}\frac{\mathrm{e}^{(-\alpha^2r^2)}}{r^2}+\\ &\left[\delta_{km}\delta_{jn}-\delta_{kn}\delta_{jm}-2\frac{\delta_{km}x_nx_j}{r^2}+2\frac{\delta_{kn}x_mx_j}{r^2}\right]\frac{4\alpha^3}{\sqrt{\pi}}\mathrm{e}^{(-\alpha^2r^2)}-\\ &\left.\left[\delta_{km}x_nx_j-\delta_{kn}x_mx_j\right]\frac{8\alpha^5}{\sqrt{\pi}}\mathrm{e}^{(-\alpha^2r^2)}\right\},\end{aligned}\tag{9.51}$$

$$\begin{aligned}\nabla\times K_{l,ijkm}(\mathbf{x}) &= \epsilon_{ijk}\frac{1}{16\pi\eta}\left\{\left[15\frac{x_kx_nx_mx_j}{r^4}+\delta_{mn}\delta_{kj}-3\delta_{mn}x_kx_j-3\delta_{kj}x_nx_m-\right.\right.\\ &\left.3\delta_{jn}x_kx_m-3\delta_{mj}x_kx_n\right]\frac{2\mathrm{erfc}(\alpha r)}{r^3}+\left[15\frac{x_kx_nx_mx_j}{r^4}+\delta_{mn}\delta_{kj}-\right.\\ &\left.3\delta_{mn}x_kx_j-3\delta_{kj}x_nx_m-3\delta_{jn}x_kx_m-3\delta_{mj}x_kx_n\right]\frac{4\alpha}{\sqrt{\pi}}\frac{\mathrm{e}^{(-\alpha^2r^2)}}{r^2}+\\ &\left[10\frac{x_kx_nx_mx_j}{r^4}+\delta_{kn}\delta_{mj}+\delta_{km}\delta_{nl}-2\frac{\delta_{mn}x_kx_j}{r^2}-2\frac{\delta_{kj}x_nx_m}{r^2}-\right.\\ &\left.2\frac{\delta_{nj}x_kx_m}{r^2}-2\frac{\delta_{mj}x_kx_n}{r^2}\right]\frac{4\alpha^3}{\sqrt{\pi}}\mathrm{e}^{(-\alpha^2r^2)}-\left[\delta_{kn}x_mx_j+\delta_{km}x_nx_j-\right.\\ &\left.\left.2\frac{x_kx_nx_mx_j}{r^2}\right]\frac{8\alpha^5}{\sqrt{\pi}}\mathrm{e}^{(-\alpha^2r^2)}\right\}.\end{aligned}\tag{9.52}$$

The local-Laplacians of the Curl by

$$\begin{aligned}\nabla\times\left(\nabla^2\mathbf{G}_l\right)_{ijk}(\mathbf{x}) &= \epsilon_{ijk}\frac{1}{8\pi\eta}\left\{\left[5\frac{x_kx_mx_j}{r^2}-\delta_{km}x_j-\delta_{kj}x_m-\delta_{jm}x_k\right]\frac{6\mathrm{erfc}(\alpha r)}{r^5}+\right.\\ &\left[5\frac{x_kx_mx_j}{r^2}-\delta_{km}x_j-\delta_{kj}x_m-\delta_{jm}x_k\right]\frac{12\alpha}{\sqrt{\pi}}\frac{\mathrm{e}^{(-\alpha^2r^2)}}{r^4}+\left[5\frac{x_kx_mx_j}{r^2}-\right.\\ &\left.\delta_{km}x_j-\delta_{kj}x_m-\delta_{jm}x_k\right]\frac{8\alpha^3}{\sqrt{\pi}}\frac{\mathrm{e}^{(-\alpha^2r^2)}}{r^2}-\left[-2\frac{x_kx_mx_j}{r^2}-\delta_{jm}x_k-\right.\\ &\left.\delta_{kj}x_m+6\delta_{km}x_j\right]\frac{8\alpha^5}{\sqrt{\pi}}\mathrm{e}^{(-\alpha^2r^2)}+\left[\delta_{km}x_jr^2-\right.\\ &\left.\left.x_jx_kx_m\right]\frac{16\alpha^7}{\sqrt{\pi}}\mathrm{e}^{(-\alpha^2r^2)}\right\},\end{aligned}\tag{9.53}$$

$$
\begin{aligned}
\nabla \times \left(\nabla^2 \mathbf{K}_l\right)_{ijkm}(\mathbf{x}) &= \epsilon_{ijk}\frac{1}{16\pi\eta}\left\{\left[\delta_{kn}\delta_{mj}-\delta_{nm}\delta_{jk}-\delta_{km}\delta_{nj}+5\frac{\delta_{kn}x_m x_j}{r^2}+\right.\right.\\
&5\frac{\delta_{nm}x_k x_j}{r^2}+5\frac{\delta_{km}x_n x_j}{r^2}+5\frac{\delta_{jk}x_n x_m}{r^2}+5\frac{\delta_{mj}x_k x_n}{r^2}-\\
&\left.35\frac{x_k x_n x_m x_j}{r^4}\right]\frac{12\mathrm{erfc}(\alpha r)}{r^5}+\left[\delta_{kn}\delta_{mj}-\delta_{nm}\delta_{jk}-\delta_{km}\delta_{nj}+\right.\\
&5\frac{\delta_{kn}x_m x_j}{r^2}+5\frac{\delta_{nm}x_k x_j}{r^2}+5\frac{\delta_{km}x_n x_j}{r^2}+5\frac{\delta_{jk}x_n x_m}{r^2}+\\
&\left.5\frac{\delta_{mj}x_k x_n}{r^2}-35\frac{x_k x_n x_m x_j}{r^4}\right]\frac{24\alpha}{\sqrt{\pi}}\frac{\mathrm{e}^{(-\alpha^2 r^2)}}{r^4}+\left[2\delta_{kn}\delta_{mj}-\right.\\
&2\delta_{nm}\delta_{jk}-2\delta_{km}\delta_{nj}+7\frac{\delta_{kn}x_m x_j}{r^2}-7\frac{\delta_{nm}x_k x_j}{r^2}+7\frac{\delta_{km}x_n x_j}{r^2}+\\
&\left.10\frac{\delta_{jn}x_k x_m}{r^2}+10\frac{\delta_{mj}x_k x_n}{r^2}-55\frac{x_k x_n x_m x_j}{r^4}\right]\frac{8\alpha^3}{\sqrt{\pi}}\frac{\mathrm{e}^{(-\alpha^2 r^2)}}{r^2}-\\
&\left[5\delta_{kn}\delta_{mj}-2\delta_{nm}\delta_{jk}+5\delta_{km}\delta_{nj}-4\frac{\delta_{kn}x_m x_j}{r^2}-4\frac{\delta_{nm}x_k x_j}{r^2}-\right.\\
&4\frac{\delta_{km}x_n x_j}{r^2}-4\frac{\delta_{kj}x_n x_m}{r^2}-4\frac{\delta_{jn}x_k x_m}{r^2}-4\frac{\delta_{mj}x_k x_n}{r^2}+\\
&\left.28\frac{x_k x_n x_m x_j}{r^4}\right]\frac{8\alpha^5}{\sqrt{\pi}}\mathrm{e}^{(-\alpha^2 r^2)}+\left[\delta_{kn}\delta_{mj}r^2+\delta_{km}\delta_{jn}r^2+\right.\\
&7\delta_{kn}x_m x_j-2\delta_{nm}x_k x_j+2\delta_{km}x_n x_j-2\delta_{kj}x_n x_m-\\
&\left.2\delta_{jn}x_k x_m-2\delta_{mj}x_k x_n-4\frac{x_k x_n x_m x_j}{r^4}\right]\frac{16\alpha^7}{\sqrt{\pi}}\mathrm{e}^{(-\alpha^2 r^2)}-\\
&\left.\left[\delta_{kn}x_m x_j r^2+\delta_{km}x_n x_j r^2-2x_k x_n x_m x_j\right]\frac{32\alpha^9}{\sqrt{\pi}}\mathrm{e}^{(-\alpha^2 r^2)}\right\}. \qquad (9.54)
\end{aligned}
$$

For the global contribution we need the following functions for the force density (9.28)

$$
\begin{aligned}
(\nabla g(r))_i &= -\frac{2\alpha^5}{\pi^{3/2}}\mathrm{e}^{(-\alpha^2 r^2)}\left[\frac{7}{2}-\alpha^2 r^2\right]x_i \qquad (9.55)\\
\nabla^2 g(r) &= -\frac{2\alpha^5}{\pi^{3/2}}\mathrm{e}^{(-\alpha^2 r^2)}\left[\frac{21}{2}-12\alpha^2 r^2+2\alpha^4 r^4\right] \qquad (9.56)\\
\nabla\left(\nabla^2 g(r)\right)_i &= \frac{4\alpha^7}{\pi^{3/2}}\mathrm{e}^{(-\alpha^2 r^2)}\left[13-4\alpha^2 r^2\right]x_i, \qquad (9.57)
\end{aligned}
$$

where $r = |\mathbf{x}|$.

CHAPTER 10

CONCLUSIONS

In conclusion, this dissertation has shown various numerical approaches developed to resolve the long-range and many-body electrostatic and hydrodynamic interactions in the continuum scale. Specifically, we have developed models to describe dielectric polarization, hydrodynamic interactions and their coupling with thermal fluctuations, and electrokinetic phenomena in extremely confined systems. We have also build some applications based on these approaches and derived new perspectives for the respective systems.

In Chapter 2, we derived an analytical method to describe the electrostatic interactions and polarization effects for dielectric spheres embedded in an unconfined continuum. The model was used to demonstrate the importance of polarizability for clusters of dielectric spheres, as well as periodic crystal of charged dielectric spheres arranged into a NaCl-type lattice. In Chapter 3, we developed an $O(N)$ numerical solver based on the Induced Charge Computation (ICC) method, the Boundary Element Method (BEM) and the Fast Multipole Method (FMM) to solve the electrostatic and polarization effects for arbitrarily-shaped particles embedded in a confined or unconfined continuum. In Chapter 4, we developed an efficient $O(N)$ computational approach, parallel-Finite-Element-General-geometry-Eward like-method (pFE-GgEm), to resolve hydrodynamic interactions in confined systems and their coupling with thermal fluctuations. We then illustrated its use in the context of confined polymer solutions and finite-size particle dynamics. More specifically, we calculated the diffusion of polymers in a slit geometry, and demonstrated that the correct Zimm scaling is obtained. We then simulated flowing polymers in a cross-channel geometry, and show how the method can be used in arbitrary domain shapes. We also showed results for the dynamics of finite-sized particles using an Immersed Boundary-GgEm formulation. In Chapter 5, we developed a numerical approach to solve the electrostatic and hydrodynamic interactions with the consideration of ionic screening. The proposed approach was then validated for several systems with analytical solutions and also compared with COMSOL in terms

of accuracy and CPU speed. It was found that the approach can successfully recover the diffusion and convection process of continuum ionic field, as well as its interactions with the electrostatic field. In Chapter 6, we proposed a new strategy that coupled the evolutionary optimization algorithm (optimizer), CMA-ES, with a particle dynamics simulator based on the electrostatic force field developed in Chapter 2 and Chapter 3 to measure charges carried by granular particles from experimental trajectories directly. We found that the strategy could successfully measure charges on multiple polarizable dielectric particles using particle' trajectories from experiments. In Chapter 7, we studied the structure and dynamics of suspended finite size particles confined in a spherical cavity relying on the IB-pFE-GgEm approach developed in Chapter 4. We found that particles started to form a layered structure in the cavity in the high-concentration conditions. We also found that particle shape, concentration, confinement, short- and long-range HI contributed to the hindered and anomalous diffusion of confined Brownian particles collectively. This study was extended in Chapter 8 to the case of mixtures of spherical and cylinderical particles to mimic more realistic biological systems. We found that increasing the fraction of cylinders induced a particle segregation effect, where spheres were pushed towards the wall and cylinders remain near the center of the cavity. We also found that the diffusive-to-anomalous transition and the degree of anomaly both increased as the fraction of cylinders becomes larger. Finally, in Chapter 9, we examined the collective effect of hydrodynamic and electrostatic interactions on the clustering and sedimentation dynamics of charged polarizable particles. We found that charged particles with equal signs would form stable clusters depending on their charge ratio and the difference between dielectric permittivities of the particle and the fluid. We also found that as particles agglomerate because of the electrostatic interaction and polarization effect, their collective motions were concomitantly modified by HI and fluid flows.

REFERENCES

[1] Kipton Barros, Daniel Sinkovits, and Erik Luijten. Efficient and accurate simulation of dynamic dielectric objects. *Journal of Chemical Physics*, 140(6), 2014.

[2] James W. Swan and John F. Brady. Particle motion between parallel walls: Hydrodynamics and simulation. *Phys. Fluids*, 22(10):103301, 2010.

[3] Christian Aponte-Rivera, Yu Su, and Roseanna N. Zia. Equilibrium structure and diffusion in concentrated hydrodynamically interacting suspensions confined by a spherical cavity. *J. Fluid Mech.*, 836:413–450, 2018.

[4] M. De Corato, J.J.M. Slot, M. Hütter, G. D'Avino, P.L. Maffettone, and M.A. Hulsen. Finite element formulation of fluctuating hydrodynamics for fluids filled with rigid particles using boundary fitted meshes. *J. Comput. Phys.*, 316:632 – 651, 2016.

[5] Xikai Jiang, Jiyuan Li, Victor Lee, Heinrich M Jaeger, Olle G Heinonen, and Juan J de Pablo. Evolutionary strategy for inverse charge measurements of dielectric particles. *The Journal of chemical physics*, 148(23):234302, 2018.

[6] Jacob N Israelachvili. *Intermolecular and surface forces*. Academic press, 2015.

[7] Jason W Merrill, Sunil K Sainis, and Eric R Dufresne. Many-body electrostatic forces between colloidal particles at vanishing ionic strength. *Physical review letters*, 103(13):138301, 2009.

[8] Scott R. Waitukaitis, Victor Lee, James M. Pierson, Steven L. Forman, and Heinrich M. Jaeger. Size-dependent same-material tribocharging in insulating grains. *Phys. Rev. Lett.*, 112:218001, May 2014.

[9] Victor Lee, Scott R Waitukaitis, Marc Z Miskin, and Heinrich M Jaeger. Direct observation of particle interactions and clustering in charged granular streams. *Nature Physics*, 11(9):733–737, 2015.

[10] D. V. Talapin, E. V. Shevchenko, M. I. Bodnarchuk, X. Ye, J. Chen, and C. B. Murray. Quasicrystalline order in self-assembled binary nanoparticle superlattices. *Nature*, 461:964–967, 2009.

[11] Jürgen Blum and Gerhard Wurm. The growth mechanisms of macroscopic bodies in protoplanetary disks. *Annu. Rev. Astron. Astrophys.*, 46:21–56, 2008.

[12] A. Zsom, C. W. Ormel, C. Güttler, J. Blum, and C. P. Dullemond. The outcome of protoplanetary dust growth: pebbles, boulders, or planetesimals? *Astronomy and Astrophysics*, 513:A57, apr 2010.

[13] Akimasa Kataoka, Hidekazu Tanaka, Satoshi Okuzumi, and Koji Wada. Fluffy dust forms icy planetesimals by static compression. *Astronomy & Astrophysics*, 557:L4, sep 2013.

[14] Rosalind Allen, Jean Pierre Hansen, and Simone Melchionna. Electrostatic potential inside ionic solutions confined by dielectrics: A variational approach. *Physical Chemistry Chemical Physics*, 3(19):4177–4186, 2001.

[15] Rosalind Allen and Jean Pierre Hansen. Density functional approach to the effective interaction between charges within dielectric cavities. *Journal of Physics Condensed Matter*, 14(46):11981–11997, nov 2002.

[16] Jaydeep P. Bardhan, Robert S. Eisenberg, and Dirk Gillespie. Discretization of the induced-charge boundary integral equation. *Physical Review E*, 80(1):011906, jul 2009.

[17] E. Cancès, B. Mennucci, and J. Tomasi. A new integral equation formalism for the polarizable continuum model: Theoretical background and applications to Isotropic and anisotropic dielectrics. *Journal of Chemical Physics*, 107(8):3032–3041, aug 1997.

[18] S. Miertuš, E. Scrocco, and J. Tomasi. Electrostatic interaction of a solute with a continuum. A direct utilizaion of AB initio molecular potentials for the prevision of solvent effects. *Chemical Physics*, 55(1):117–129, feb 1981.

[19] Karl F. Freed. Perturbative many-body expansion for electrostatic energy and field for system of polarizable charged spherical ions in a dielectric medium. *Journal of Chemical Physics*, 141(3), jul 2014.

[20] Jian Qin, Juan J. De Pablo, and Karl F. Freed. Image method for induced surface charge from many-body system of dielectric spheres. *Journal of Chemical Physics*, 145(12), sep 2016.

[21] J D Jackson and Ronald F Fox. Classical Electrodynamics, 3rd ed. *Citation: American Journal of Physics*, 67:841, 1999.

[22] Carl Neumann. *Hydrodynamische untersuchungen: nebst einem Anhange über die Probleme der Elektrostatik und der magnetischen Induction*. BG Teubner, 1883.

[23] Ismo V. Lindell. Electrostatic image theory for the dielectric sphere. *Radio Science*, 27(1):1–8, 1992.

[24] René Messina. Image charges in spherical geometry: Application to colloidal systems. *Journal of Chemical Physics*, 117(24):11062–11074, dec 2002.

[25] Wei Cai, Shaozhong Deng, and Donald Jacobs. Extending the fast multipole method to charges inside or outside a dielectric sphere. *Journal of Computational Physics*, 223(2):846–864, may 2007.

[26] Sangtae Kim. A new approach to hydrodynamic interactions in polydisperse suspensions. *Particulate Science and Technology*, 6(1):69–80, 1988.

[27] Charles Kittel, Paul McEuen, and Paul McEuen. *Introduction to solid state physics*, volume 8. Wiley New York, 1996.

[28] Carlos Alberto Brebbia, José Claudio Faria Telles, and Luiz Wrobel. *Boundary element techniques: theory and applications in engineering*. Springer Science & Business Media, 1984.

[29] Marc Bonnet. Boundary integral equation methods for solids and fluids. *Meccanica*, 34(4):301–302, 1999.

[30] T.Y. Hou, J.S. Lowengrub, and M.J. Shelley. Boundary integral methods for multicomponent fluids and multiphase materials. *Journal of Computational Physics*, 169(2):302 – 362, 2001.

[31] Leslie Greengard and Patrick Lin. Spectral approximation of the free-space heat kernel. *Applied and Computational Harmonic Analysis*, 9(1):83 – 97, 2000.

[32] A.M. Zhang and B.Y. Ni. Three-dimensional boundary integral simulations of motion and deformation of bubbles with viscous effects. *Computers & Fluids*, 92:22 – 33, 2014.

[33] I. Charpentier and N. Jakse. Phase diagram of complex fluids using an efficient integral equation method. *The Journal of Chemical Physics*, 123(20), 2005.

[34] Yuhong Fu, Kenneth J. Klimkowski, Gregory J. Rodin, Emery Berger, James C. Browne, Jürgen K. Singer, Robert A. Van De Geijn, and Kumar S. Vemaganti. A fast solution method for three-dimensional many-particle problems of linear elasticity. *International Journal for Numerical Methods in Engineering*, 42(7):1215–1229, 1998.

[35] N Nishimura and S Kobayashi. A regularized boundary integral equation method for elastodynamic crack problems. *Computational mechanics*, 4(4):319–328, 1989.

[36] Dezsö Boda, Dirk Gillespie, Wolfgang Nonner, Douglas Henderson, and Bob Eisenberg. Computing induced charges in inhomogeneous dielectric media: Application in a monte carlo simulation of complex ionic systems. *Phys. Rev. E*, 69:046702, Apr 2004.

[37] Sandeep Tyagi, Mehmet Süzen, Marcello Sega, Marcia Barbosa, Sofia S. Kantorovich, and Christian Holm. An iterative, fast, linear-scaling method for computing induced charges on arbitrary dielectric boundaries. *The Journal of Chemical Physics*, 132(15):154112, 2010.

[38] Claudio Berti, Dirk Gillespie, Jaydeep P. Bardhan, Robert S. Eisenberg, and Claudio Fiegna. Comparison of three-dimensional poisson solution methods for particle-based simulation and inhomogeneous dielectrics. *Phys. Rev. E*, 86:011912, Jul 2012.

[39] Kipton Barros and Erik Luijten. Dielectric Effects in the Self-Assembly of Binary Colloidal Aggregates. *Physical Review Letters*, 113(1):017801, jul 2014.

[40] Youcef Saad and Martin H. Schultz. Gmres: A generalized minimal residual algorithm for solving nonsymmetric linear systems. *SIAM Journal on Scientific and Statistical Computing*, 7(3):856–869, 1986.

[41] Zecheng Gan, Huanxin Wu, Kipton Barros, Zhenli Xu, and Erik Luijten. Comparison of efficient techniques for the simulation of dielectric objects in electrolytes. *Journal of Computational Physics*, 291:317 – 333, 2015.

[42] R.W. Hockney, S.P. Goel, and J.W. Eastwood. A 10000 particle molecular dynamics model with long range forces. *Chemical Physics Letters*, 21(3):589 – 591, 1973.

[43] Benjamin S. Kirk, John W. Peterson, Roy H. Stogner, and Graham F. Carey. libmesh: A c++ library for parallel adaptive mesh refinement/coarsening simulations. *Eng. with Comput.*, 22(3):237–254, December 2006.

[44] Pierre Blanchard, Bérenger Bramas, Olivier Coulaud, Eric Darve, Laurent Dupuy, Arnaud Etcheverry, and Guillaume SYLVAND. ScalFMM: A Generic Parallel Fast Multipole Library. In *Computational Science and Engineering (CSE)*, Salt Lake City, United States, March 2015. SIAM.

[45] William Fong and Eric Darve. The black-box fast multipole method. *Journal of Computational Physics*, 228(23):8712 – 8725, 2009.

[46] Matthias Messner, Martin Schanz, and Eric Darve. Fast directional multilevel summation for oscillatory kernels based on chebyshev interpolation. *Journal of Computational Physics*, 231(4):1175 – 1196, 2012.

[47] George Karypis and Vipin Kumar. A fast and high quality multilevel scheme for partitioning irregular graphs. *SIAM Journal on Scientific Computing*, 20(1):359–392, 1998.

[48] Berenger Bramas. *Optimization and Parallelization of the Boundary Element Method for the Wave Equation in Time Domain*. PhD thesis, University of Bordeaux, Bordeaux, France, 2016.

[49] Emmanuel Agullo, Bérenger Bramas, Olivier Coulaud, Eric Darve, Matthias Messner, and Toru Takahashi. Task-based fmm for multicore architectures. *SIAM Journal on Scientific Computing*, 36(1):C66–C93, 2014.

[50] Jian Qin, Jiyuan Li, Victor Lee, Heinrich Jaeger, Juan J. de Pablo, and Karl F. Freed. A theory of interactions between polarizable dielectric spheres. *Journal of Colloid and Interface Science*, 469:237—-241, 2016.

[51] Tom Darden, Darrin York, and Lee Pedersen. Particle mesh ewald: An nlog(n) method for ewald sums in large systems. *The Journal of Chemical Physics*, 98(12):10089–10092, 1993.

[52] Axel Arnold, Florian Fahrenberger, Christian Holm, Olaf Lenz, Matthias Bolten, Holger Dachsel, Rene Halver, Ivo Kabadshow, Franz Gähler, Frederik Heber, Julian Iseringhausen, Michael Hofmann, Michael Pippig, Daniel Potts, and Godehard Sutmann. Comparison of scalable fast methods for long-range interactions. *Phys. Rev. E*, 88:063308, Dec 2013.

[53] Ranganathan Bharadwaj, Andreas Windemuth, S. Sridharan, Barry Honig, and Anthony Nicholls. The fast multipole boundary element method for molecular electrostatics: An optimal approach for large systems. *Journal of Computational Chemistry*, 16(7):898–913, 1995.

[54] Y.J. Liu and N. Nishimura. The fast multipole boundary element method for potential problems: A tutorial. *Engineering Analysis with Boundary Elements*, 30(5):371 – 381, 2006.

[55] Rio Yokota, Jaydeep P. Bardhan, Matthew G. Knepley, L.A. Barba, and Tsuyoshi Hamada. Biomolecular electrostatics using a fast multipole {BEM} on up to 512 gpus and a billion unknowns. *Computer Physics Communications*, 182(6):1272 – 1283, 2011.

[56] Benzhuo Lu, Xiaolin Cheng, Jingfang Huang, and J. Andrew McCammon. Order n algorithm for computation of electrostatic interactions in biomolecular systems. *Proceedings of the National Academy of Sciences*, 103(51):19314–19319, 2006.

[57] T T Perkins, D E Smith, and S Chu. Single polymer dynamics in an elongational flow. *Science*, 276(5321):2016–2021, 1997.

[58] D E Smith, H P Babcock, and S Chu. Single-polymer dynamics in steady shear flow. *Science*, 283:1724–1727, 1999.

[59] Kristy L. Kounovsky-Shafer, Juan P. Hernandez-Ortiz, Kyubong Jo, Theo Odijk, Juan J. de Pablo, and David C. Schwartz. Presentation of large DNA molecules for analysis as nanoconfined dumbbells. *Macromolecules*, 46(20):8356–8368, 2013.

[60] C. Gupta, W. C. Liao, D. Gallego-Perez, C. E. Castro, and L. J. Lee. Dna translocation through short nanofluidic channels under asymmetric pulsed electric field. *Biomicrofluidics*, 8(2):024114, 2014.

[61] Chao Wang, Robert L. Bruce, Elizabeth A. Duch, Jyotica V. Patel, Joshua T. Smith, Yann Astier, Benjamin H. Wunsch, Siddharth Meshram, Armand Galan, Chris Scerbo, Michael A. Pereira, Deqiang Wang, Evan G. Colgan, Qinghuang Lin, and Gustavo Stolovitzky. Hydrodynamics of diamond-shaped gradient nanopillar arrays for effective dna translocation into nanochannels. *ACS Nano*, 9(2):1206–1218, 2015.

[62] Todd M. Squires and Stephen R. Quake. Microfluidics: Fluid physics at the nanoliter scale. *Rev. Mod. Phys.*, 77(3):977–1026, 2005.

[63] Andreas Lenshof and Thomas Laurell. Continuous separation of cells and particles in microfluidic systems. *Chem. Soc. Rev.*, 39(3):1203–1217, 2010.

[64] S. K. Bindal, G. Sethumadhavan, A. D. Nikolov, and D. T. Wasan. Foaming mechanisms in surfactant free particle suspensions. *AIChE Journal*, 48(10):2307–2314, 2002.

[65] B. M. Guy, M. Hermes, and W. C. K. Poon. Towards a unified description of the rheology of hard-particle suspensions. *Phys. Rev. Lett.*, 115:088304, Aug 2015.

[66] Rahul Pandey and Jacinta C. Conrad. Dynamics of confined depletion mixtures of polymers and bidispersed colloids. *Soft Matter*, 9:10617–10626, 2013.

[67] Richard M Jendrejack, David C Schwartz, Juan J de Pablo, and Michael D Graham. Shear-induced migration in flowing polymer solutions: simulation of long-chain dna in microchannels. *J. Chem. Phys.*, 120(5):2513–29, feb 2004.

[68] H. Ma and M. D. Graham. Theory of shear-induced migration in dilute polymer solutions near solid boundaries. *Phys. Fluids*, 17:083103, 2005.

[69] J. P. Hernandez-Ortiz, H. Ma, J. J. de Pablo, and M. D. Graham. Cross stream-line migration on confined flowing polymer solutions: theory and simulation. *Phys. Fluids*, 18(12):123101, December 2006.

[70] T Ando and J Skolnick. Crowding and hydrodynamic interactions likely dominate in vivo macromolecular motion. *Proceedings of the National Academy of Sciences*, 107(43):18457–18462, 2010.

[71] R J Ellis. Macromolecular crowding: obvious but underappreciated. *Trends Biochem. Sci.*, 26(10):597–604, 2001.

[72] Felix Höfling and Thomas Franosch. Anomalous transport in the crowded world of biological cells. *Reports on Progress in Physics*, 76(4):046602, 2013.

[73] Hiroaki Matsuda, Gregory Garbès Putzel, Vadim Backman, and Igal Szleifer. Macromolecular crowding as a regulator of gene transcription. *Biophys. J.*, 106(8):1801–1810, 2014.

[74] Sean R McGuffee and Adrian H Elcock. Diffusion, crowding & protein stability in a dynamic molecular model of the bacterial cytoplasm. *PLoS Comput. Biol.*, 6(3):1–18, 03 2010.

[75] Marco J Morelli, Rosalind J Allen, and Pieter Rein ten Wolde. Effects of macromolecular crowding on genetic networks. *Biophys. J.*, 101(12):2882–2891, 2011.

[76] Piotr Polanowski and Andrzej Sikorski. Simulation of diffusion in a crowded environment. *Soft Matter*, 10(20):3597–3607, May 2014.

[77] Qian Wang, Kao Chen Liang, Arkadiusz Czader, M. Neal Waxham, and Margaret S. Cheung. The effect of macromolecular crowding, ionic strength and calcium binding on calmodulin dynamics. *PLoS Comput. Biol.*, 7(7):1–16, 07 2011.

[78] H. Risken. *The Fokker-Planck Equation*, volume 18. Springer, Berlin, Heidelberg, 2nd edition, 1989.

[79] Hans Christian Öttinger. *Stochastic processes in polymeric fluids*. Springer-Verlag, Berlin, Heidelberg, 1996.

[80] Marshall Fixman. Simulation of polymer dynamics. i. general theory. *J. Chem. Phys.*, 69(4):1527, 1978.

[81] Donald L Ermak and J A McCammon. Brownian dynamics with hydrodynamic interactions. *J. Chem. Phys.*, 69(4):1352–1360, 1978.

[82] R. Byron Bird, Charles F. Curtiss, Robert C. Armstrong, and Ole Hassager. *Dynamics of Polymeric Liquids, Kinetic Theory*, volume 2. John Wiley & Sons, Inc.,, New York, 2nd edition, 1987.

[83] Richard M. Jendrejack, Michael D. Graham, and Juan J. de Pablo. Hydrodynamic interactions in long chain polymers: Application of the chebyshev polynomial approximation in stochastic simulations. *J. Chem. Phys.*, 113(7):2894–2900, 2000.

[84] Madan Somasi, Bamin Khomami, Nathanael J. Woo, Joe S. Hur, and Eric S G Shaqfeh. Brownian dynamics simulations of bead-rod and bead-spring chains: Numerical algorithms and coarse-graining issues. *J. Non-Newtonian Fluid Mech.*, 108(1-3):227–255, 2002.

[85] Juan P Hernández-Ortiz, Juan J de Pablo, and Michael D Graham. N log n method for hydrodynamic interactions of confined polymer systems: Brownian dynamics. *The Journal of chemical physics*, 125(16):164906, 2006.

[86] Juan P. Hernandez-Ortiz, Manan Chopra, Stephanie Geier, and Juan J. de Pablo. Hydrodynamic effects on the translocation rate of a polymer through a pore. *J. Chem. Phys.*, 131(4):044904, 2009.

[87] Joe S. Hur, Eric S. G. Shaqfeh, and Ronald G. Larson. Brownian dynamics simulations of single dna molecules in shear flow. *J. Rheol.*, 44(4):713, jul 2000.

[88] Richard M. Jendrejack, Juan J. de Pablo, and Michael D. Graham. Stochastic simulations of dna in flow: Dynamics and the effects of hydrodynamic interactions. *J. Chem. Phys.*, 116(17):7752, may 2002.

[89] Richard M. Jendrejack, Eileen T. Dimalanta, David C. Schwartz, Michael D. Graham, and Juan J. de Pablo. Dna dynamics in a microchannel. *Phys. Rev. Lett.*, 91(3):038102, jul 2003.

[90] Chih Chen Hsieh, Lei Li, and Ronald G. Larson. Modeling hydrodynamic interaction in brownian dynamics: Simulations of extensional flows of dilute solutions of dna and polystyrene. *J. Non-Newtonian Fluid Mech.*, 113(2-3):147–191, 2003.

[91] Aslin Izmitli, David C. Schwartz, Michael D. Graham, and Juan J. de Pablo. The effect of hydrodynamic interactions on the dynamics of dna translocation through pores. *J. Chem. Phys.*, 128(8):085102, 2008.

[92] D. M. Heyes and J. R. Melrose. Brownian dynamics simulations of model hard-sphere suspensions. *J. Non-Newtonian Fluid Mech.*, 46(1):1–28, 1993.

[93] M. Miyahara, S. Watanabe, and K. Higashitani. Modeling adsorption and order formation by colloidal particles on a solid surface: A brownian dynamics study. *Chem. Eng. Sci.*, 61(7):2142–2149, 2006.

[94] Matthias Schmidt, C. Patrick Royall, Alfons van Blaaderen, and Joachim Dzubiella. Non-equilibrium sedimentation of colloids: confocal microscopy and brownian dynamics simulations. *J. Phys. Condens. Matter*, 20:494222, 2008.

[95] T. A. Osswald and J. P. Hernandez-Ortiz. *Polymer Processing: Modeling and Simulation*. Carl Hanser-Verlag, Munich, 2006.

[96] C. Pozrikidis. *Boundary Integral and Singularity Methods for Linearized Viscous Flow*. Cambridge University Press, Cambridge, 1992.

[97] Adolfo J. Banchio and John F. Brady. Accelerated stokesian dynamics: Brownian motion. *J. Chem. Phys.*, 118(22):10323–10332, 2003.

[98] John F. Brady and G. Bossis. Stokesian dynamics. *Annu. Rev. Fluid Mech.*, 20(1):111–157, 1988.

[99] Asimina Sierou and John F. Brady. Accelerated stokesian dynamics simulations. *J. Fluid Mech.*, 448:115–146, 2001.

[100] S. Succi. *The Lattice Boltzmann Equation for Fluid Dynamics and Beyond*. Oxford University Press, Oxford, 2001.

[101] Simone Melchionna and Sauro Succi. Electrorheology in nanopores via lattice boltzmann simulation. *J. Chem. Phys.*, 120(9):4492–4497, 2004.

[102] Rahul Kekre, Jason E. Butler, and Anthony J C Ladd. Comparison of lattice-boltzmann and brownian-dynamics simulations of polymer migration in confined flows. *Phys. Rev. E*, 82(1):011802, 2010.

[103] P. Ahlrichs and B. Dünweg. Simulation of a single polymer chain in solution by combining lattice boltzmann and molecular dynamics. *J. Chem. Phys.*, 111:8225, 1999.

[104] M Serrano, P Espanol, and Ignacio Zúñiga. Collective effects in dissipative particle dynamics. *Comput. Phys. Commun.*, 121:306–308, 1999.

[105] M Ripoll, M H Ernst, and P Espanol. Large scale and mesoscopic hydrodynamics for dissipative particle dynamics. *J. Chem. Phys.*, 115(15):7271–7284, October 2001.

[106] M. R. Maxey and B. K. Patel. Localized force representations for particles sedimenting in stokes flow. *Int. J. Multiph. Flow*, 27:1603, 2001.

[107] R. Cortez. The method of regularized stokeslets. *SIAM J. Sci. Comput.*, 23:1204–1225, 2001.

[108] R. Cortez, L. Fauci, and A. Medovikov. The method of regularized stokeslets in three dimensions: analysis, validation, and application to helical swimming. *Phys. Fluids*, 17:031504, 2005.

[109] J. P. Hernández-Ortiz, J.J. de Pablo, and M. D. Graham. Fast computation of many-particle hydrodynamic and electrostatic interactions in a confined geometry. *Phys. Rev. Lett.*, 98(14):140602, April 2007.

[110] Irina Ginzburg, Frederik Verhaeghe, and Dominique d'Humieres. Two-relaxation-time lattice boltzmann scheme: About parametrization, velocity, pressure and mixed boundary conditions. *Commun. Comput. Phys.*, 3(2):427–478, 2008.

[111] Yang Hu, Decai Li, Shi Shu, and Xiaodong Niu. An efficient smoothed profile-lattice boltzmann method for the simulation of forced and natural convection flows in complex geometries. *Int. Commun. Heat Mass Trans.*, 68:188–199, 2015.

[112] Stephanie Geier, Juan Pablo Hernandez-Ortiz, and Juan Jose de Pablo. Numerical determination of the translocation rate of particles through a pore. *Chem. Ing. Tech.*, 83(6):900–906, Jan 2011.

[113] C. A. Miller, J. P. Hernandez-Ortiz, N. L. Abbott, S. H. Gellman, and J. J de Pablo. Dipole-induced self-assembly of helical β-peptides. *J. Chem. Phys.*, 129:015102, 2008.

[114] J. P. Hernandez-Ortiz and J. J. de Pablo. Self-consistent description of electrokinetic phenomena in particle-based simulations. *J. Chem. Phys.*, 143:014108, 2015.

[115] Amit Kumar and Michael D. Graham. Mechanism of margination in confined flows of blood and other multicomponent suspensions. *Phys. Rev. Lett.*, 109(10):108102, September 2012.

[116] P Pranay, S G Anekal, J P Hernandez-Ortiz, and M D Graham. Pair collisions of fluid-filled elastic capsules in shear flow: Effects of membrane properties and polymer additives. *Phys. Fluids*, 22(12):123103, 2010.

[117] J. P. Hernandez-Ortiz, C. G. Stoltz, and M. D. Graham. Transport and collective dynamics in suspensions of confined swimming particles. *Phys. Rev. Lett.*, 95(20):204501, 2005.

[118] Juan P. Hernandez-Ortiz, Patrick T. Underhill, and Michael D. Graham. Dynamics of confined suspensions of swimming particles. *J. Phys. Condens. Matter*, 21:204107, 2009.

[119] P. T. Underhill, J. P. Hernandez-Ortiz, and M. D. Graham. Diffusion and spatial correlations in suspensions of swimming particles. *Phys. Rev. Lett.*, 100(24):248101, 2008.

[120] Anthony Balducci, Pan Mao, Jongyoon Han, and Patrick S. Doyle. Double-stranded dna diffusion in slitlike nanochannels. *Macromolecules*, 39(18):6273–6281, 2006.

[121] Marshall Fixman. Implicit algorithm for brownian dynamics of polymers. *Macromolecules*, 19(4):1195–1204, 1986.

[122] Marshall Fixman. Construction of langevin forces in the simulation of hydrodynamic interaction. *Macromolecules*, 19(4):1204–1207, jul 1986.

[123] R. W. Hockney and J. W. Eastwood. *Computer Simulation Using Particles*. Taylor & Francis Group, New York, 1988.

[124] Vicente Hernandez, Jose E Roman, and Vicente Vidal. {SLEPc}: A scalable and flexible toolkit for the solution of eigenvalue problems. *ACM Trans. Math. Softw.*, 31(3):351–362, 2005.

[125] Franco Brezzi and Michel Fortin. *Mixed and Hybrid Finite Element Methods*. Springer, New York, 1991.

[126] Xiaoye S Li and James W Demmel. Superlu_dist: A scalable distributed-memory sparse direct solver for unsymmetric linear systems. *ACM Transactions on Mathematical Software (TOMS)*, 29(2):110–140, 2003.

[127] Y. Saad. *Iterative Methods for Sparse Linear Systems*. Society for Industrial and Applied Mathematics, second edition, 2003.

[128] H. C. Elman, D. Loghin, and A. J. Wathen. Preconditioning techniques for newton's method for the incompressible navier–stokes equations. *BIT Numer. Math.*, 43:961–974, 2003.

[129] Satish Balay, Shrirang Abhyankar, Mark F. Adams, Jed Brown, Peter Brune, Kris Buschelman, Lisandro Dalcin, Victor Eijkhout, William D. Gropp, Dinesh Kaushik, Matthew G. Knepley, Lois Curfman McInnes, Karl Rupp, Barry F. Smith, Stefano Zampini, Hong Zhang, and Hong Zhang. PETSc Web page. http://www.mcs.anl.gov/petsc, 2016.

[130] Satish Balay, Shrirang Abhyankar, Mark F. Adams, Jed Brown, Peter Brune, Kris Buschelman, Lisandro Dalcin, Victor Eijkhout, William D. Gropp, Dinesh Kaushik, Matthew G. Knepley, Lois Curfman McInnes, Karl Rupp, Barry F. Smith, Stefano Zampini, and Hong Zhang. PETSc users manual. Technical Report ANL-95/11 - Revision 3.6, Argonne National Laboratory, 2015.

[131] Satish Balay, William D. Gropp, Lois Curfman McInnes, and Barry F. Smith. Efficient management of parallelism in object oriented numerical software libraries. In E. Arge, A. M. Bruaset, and H. P. Langtangen, editors, *Modern Software Tools in Scientific Computing*, pages 163–202. Birkhäuser Boston, 1997.

[132] James W. Demmel, Stanley C. Eisenstat, John R. Gilbert, Xiaoye S. Li, and Joseph W. H. Liu. A supernodal approach to sparse partial pivoting. *SIAM J. Matrix Anal. Appl.*, 20(3):720–755, 1999.

[133] James W. Demmel, John R. Gilbert, and Xiaoye S. Li. An asynchronous parallel supernodal algorithm for sparse gaussian elimination. *SIAM J. Matrix Anal. Appl.*, 20(4):915–952, 1999.

[134] Richard M. Jendrejack, David C. Schwartz, Michael D. Graham, and Juan J. de Pablo. Effect of confinement on dna dynamics in microfluidic devices. *J. Chem. Phys.*, 119(2):1165, jul 2003.

[135] J. F. Marko and E. D. Siggia. Bending and twisting elasticity of dna. *Macromolecules*, 27(4):981–988, jul 1994.

[136] John F. Marko and Eric D. Siggia. Stretching DNA. *Macromolecules*, 28(26):8759–8770, dec 1995.

[137] Y. L. Chen, M D Graham, J J de Pablo, G C Randall, M Gupta, and P S Doyle. Conformation and dynamics of single dna molecules in parallel-plate slit microchannels. *Phys. Rev. E*, 70:060901, 2004.

[138] Charles S. Peskin. The immersed boundary method. *Acta Numer.*, 11(January 2002):479–517, 2002.

[139] P. J. Mucha, S. Y. Tee, D. A. Weitz, B. I. Shraiman, and M. P. Brenner. A model for velocity fluctuations in sedimentation. *J. Fluid Mech.*, 501:71–104, 2004.

[140] Alexey V. Lyulin, David B. Adolf, and Geoffrey R. Davies. Brownian dynamics simulations of linear polymers under shear flow. *J. Chem. Phys.*, 111(2):758–771, 1999.

[141] Jun Gao, Wei Guo, Dan Feng, Huanting Wang, Dongyuan Zhao, and Lei Jiang. High-performance ionic diode membrane for salinity gradient power generation. *Journal of the American Chemical Society*, 136(35):12265–12272, 2014.

[142] Zhen Zhang, Xin Sui, Pei Li, Ganhua Xie, Xiang-Yu Kong, Kai Xiao, Longcheng Gao, Liping Wen, and Lei Jiang. Ultrathin and ion-selective janus membranes for high-performance osmotic energy conversion. *Journal of the American Chemical Society*, 139(26):8905–8914, 2017.

[143] Hao-Cheng Yang, Yunsong Xie, Jingwei Hou, Anthony K Cheetham, Vicki Chen, and Seth B Darling. Janus membranes: creating asymmetry for energy efficiency. *Advanced materials*, 30(43):1801495, 2018.

[144] Seth B Darling. Perspective: Interfacial materials at the interface of energy and water. *Journal of Applied Physics*, 124(3):030901, 2018.

[145] Douwe Jan Bonthuis, Christine Meyer, Derek Stein, and Cees Dekker. Conformation and dynamics of dna confined in slitlike nanofluidic channels. *Physical review letters*, 101(10):108303, 2008.

[146] Walter Reisner, Niels B Larsen, Asli Silahtaroglu, Anders Kristensen, Niels Tommerup, Jonas O Tegenfeldt, and Henrik Flyvbjerg. Single-molecule denaturation mapping of dna in nanofluidic channels. *Proceedings of the National Academy of Sciences*, 107(30):13294–13299, 2010.

[147] Joachim Fritzsche, David Albinsson, Michael Fritzsche, Tomasz J Antosiewicz, Fredrik Westerlund, and Christoph Langhammer. Single particle nanoplasmonic sensing in individual nanofluidic channels. *Nano letters*, 16(12):7857–7864, 2016.

[148] David Andrews, Thomas Nann, and Robert H Lipson. *Comprehensive Nanoscience and Nanotechnology*. Academic Press, 2019.

[149] Derek Stein, Maarten Kruithof, and Cees Dekker. Surface-charge-governed ion transport in nanofluidic channels. *Physical Review Letters*, 93(3):035901, 2004.

[150] Takehiko Tsukahara, Kazuma Mawatari, Akihide Hibara, and Takehiko Kitamori. Development of a pressure-driven nanofluidic control system and its application to an enzymatic reaction. *Analytical and bioanalytical chemistry*, 391(8):2745–2752, 2008.

[151] Junfang Zhang, BD Todd, and Karl P Travis. Viscosity of confined inhomogeneous nonequilibrium fluids. *The Journal of chemical physics*, 121(21):10778–10786, 2004.

[152] Dongqing Li. *Electrokinetics in microfluidics*, volume 2. Elsevier, 2004.

[153] Saeid Movahed and Dongqing Li. Electrokinetic transport through nanochannels. *Electrophoresis*, 32(11):1259–1267, 2011.

[154] R Qiao and Narayana R Aluru. Ion concentrations and velocity profiles in nanochannel electroosmotic flows. *The Journal of chemical physics*, 118(10):4692–4701, 2003.

[155] R Qiao and Narayana R Aluru. Transient analysis of electroosmotic flow in nanodiameter channels. *Model. Simul. Microsyst*, pages 28–31, 2002.

[156] Saeid Movahed and Dongqing Li. Electrokinetic motion of a rectangular nanoparticle in a nanochannel. *Journal of Nanoparticle Research*, 14(8):1032, 2012.

[157] Saeid Movahed. Electrokinetic motion of particles in nanochannels. *Encyclopedia of Microfluidics and Nanofluidics*, pages 823–828, 2015.

[158] Roger W Pryor. *Multiphysics modeling using COMSOL®: a first principles approach*. Jones & Bartlett Publishers, 2009.

[159] Hiroyuki Ohshima. *Electrical phenomena at interfaces and biointerfaces: fundamentals and applications in nano-, bio-, and environmental sciences*. John Wiley & Sons, 2012.

[160] Hiroyuki Ohshima and Kimiko Makino. Electrophoretic mobility of a particle covered with a partially ion-penetrable polyelectrolyte layer. *Colloids and Surfaces A: Physicochemical and Engineering Aspects*, 109:71–75, 1996.

[161] Stephan M Dammer, Jochen Werth, and Haye Hinrichsen. Electrostatically charged granular matter. *The Physics of Granular Media*, pages 253–280, 2004.

[162] Martin Z. Bazant and Todd M. Squires. Induced-charge electrokinetic phenomena. *Current Opinion in Colloid & Interface Science*, 15(3):203 – 213, 2010.

[163] Torsten Poppe, Jürgen Blum, and Thomas Henning. Experiments on collisional grain charging of micron-sized preplanetary dust. *The Astrophysical Journal*, 533(1):472, 2000.

[164] Bartosz A Grzybowski, Adam Winkleman, Jason A Wiles, Yisroel Brumer, and George M Whitesides. Electrostatic self-assembly of macroscopic crystals using contact electrification. *Nature materials*, 2(4):241–245, 2003.

[165] L. B. Schein. Recent progress and continuing puzzles in electrostatics. *Science*, 316(5831):1572–1573, 2007.

[166] Daniel J. Lacks, Nathan Duff, and Sanat K. Kumar. Nonequilibrium accumulation of surface species and triboelectric charging in single component particulate systems. *Phys. Rev. Lett.*, 100:188305, May 2008.

[167] Keith M. Forward, Daniel J. Lacks, and R. Mohan Sankaran. Charge segregation depends on particle size in triboelectrically charged granular materials. *Phys. Rev. Lett.*, 102:028001, Jan 2009.

[168] Thomas Pähtz, Hans J Herrmann, and Troy Shinbrot. Why do particle clouds generate electric charges? *Nature Physics*, 6(5):364–368, 2010.

[169] Deepak Kumar, A Sane, Smita Gohil, PR Bandaru, S Bhattacharya, and Shankar Ghosh. Spreading of triboelectrically charged granular matter. *Scientific reports*, 4, 2014.

[170] Yanzhen Zhang, Thomas Pähtz, Yonghong Liu, Xiaolong Wang, Rui Zhang, Yang Shen, Renjie Ji, and Baoping Cai. Electric field and humidity trigger contact electrification. *Phys. Rev. X*, 5:011002, Jan 2015.

[171] Razieh Yousefi, Allen B. Davis, Jorge Carmona-Reyes, Lorin S. Matthews, and Truell W. Hyde. Measurement of net electric charge and dipole moment of dust aggregates in a complex plasma. *Phys. Rev. E*, 90:033101, Sep 2014.

[172] John R Royer, Daniel J Evans, Loreto Oyarte, Qiti Guo, Eliot Kapit, Matthias E Möbius, Scott R Waitukaitis, and Heinrich M Jaeger. High-speed tracking of rupture and clustering in freely falling granular streams. *Nature*, 459(7250):1110–1113, 2009.

[173] S. R. Waitukaitis and H. M. Jaeger. In situ granular charge measurement by free-fall videography. *Review of Scientific Instruments*, 84(2):025104, 2013.

[174] Vikram Jadhao, Francisco J. Solis, and Monica Olvera de la Cruz. Simulation of charged systems in heterogeneous dielectric media via a true energy functional. *Phys. Rev. Lett.*, 109:223905, Nov 2012.

[175] Xikai Jiang, Jiyuan Li, Xujun Zhao, Jian Qin, Dmitry Karpeev, Juan Hernandez-Ortiz, Juan J. de Pablo, and Olle Heinonen. An o(n) and parallel approach to integral problems by a kernel-independent fast multipole method: Application to polarization and magnetization of interacting particles. *The Journal of Chemical Physics*, 145(6):064307, August 2016.

[176] Zhenli Xu. Electrostatic interaction in the presence of dielectric interfaces and polarization-induced like-charge attraction. *Phys. Rev. E*, 87:013307, Jan 2013.

[177] Karl F Freed. Perturbative many-body expansion for electrostatic energy and field for system of polarizable charged spherical ions in a dielectric medium. *The Journal of Chemical Physics*, 141(3):034115, July 2014.

[178] L. J. Fogel, A. J. Owens, and M. J. Walsh. *Artificial Intelligence through Simulated Evolution*. John Wiley, New York, USA, 1966.

[179] Nikolaus Hansen and Andreas Ostermeier. Completely derandomized self-adaptation in evolution strategies. *Evolutionary Computation*, 9(2):159–195, 2001.

[180] Yaochu Jin and J. Branke. Evolutionary optimization in uncertain environments-a survey. *IEEE Transactions on Evolutionary Computation*, 9(3):303–317, June 2005.

[181] Zhenyu Yang, Ke Tang, and Xin Yao. Large scale evolutionary optimization using cooperative coevolution. *Information Sciences*, 178(15):2985 – 2999, 2008. Nature Inspired Problem-Solving.

[182] Steve Plimpton. Fast parallel algorithms for short-range molecular dynamics. *Journal of Computational Physics*, 117(1):1 – 19, 1995.

[183] Emmanuel Benazera. libcmaes: Multithreaded c++ 11 implementation of cma-es family for optimization of nonlinear non-convex blackbox functions, 2014.

[184] Nikolaus Hansen. The cma evolution strategy: A tutorial. *arXiv preprint arXiv:1604.00772v1*, 2016.

[185] Jian Qin, Gurdaman S. Khaira, Yongrui Su, Grant P. Garner, Marc Miskin, Heinrich M. Jaeger, and Juan J. de Pablo. Evolutionary pattern design for copolymer directed self-assembly. *Soft Matter*, 9:11467–11472, 2013.

[186] Gurdaman S. Khaira, Jian Qin, Grant P. Garner, Shisheng Xiong, Lei Wan, Ricardo Ruiz, Heinrich M. Jaeger, Paul F. Nealey, and Juan J. de Pablo. Evolutionary optimization of directed self-assembly of triblock copolymers on chemically patterned substrates. *ACS Macro Letters*, 3(8):747–752, 2014.

[187] Marc Z. Miskin, Gurdaman Khaira, Juan J. de Pablo, and Heinrich M. Jaeger. Turning statistical physics models into materials design engines. *Proceedings of the National Academy of Sciences*, 113(1):34–39, 2016.

[188] Heinrich M. Jaeger and Juan J. de Pablo. Perspective: Evolutionary design of granular media and block copolymer patterns. *APL Materials*, 4(5):053209, 2016.

[189] Karim R. Gadelrab, Adam F. Hannon, Caroline A. Ross, and Alfredo Alexander-Katz. Inverting the design path for self-assembled block copolymers. *Mol. Syst. Des. Eng.*, 2:539–548, 2017.

[190] Gurdaman Khaira, Manolis Doxastakis, Alec Bowen, Jiaxing Ren, Hyo Seon Suh, Tamar Segal-Peretz, Xuanxuan Chen, Chun Zhou, Adam F. Hannon, Nicola J. Ferrier, Venkatram Vishwanath, Daniel F. Sunday, Roel Gronheid, R. Joseph Kline, Juan J. de Pablo, and Paul F. Nealey. Derivation of multiple covarying material and process parameters using physics-based modeling of x-ray data. *Macromolecules*, 50(19):7783–7793, 2017.

[191] H. T. Baytekin, A. Z. Patashinski, M. Branicki, B. Baytekin, S. Soh, and B. A. Grzybowski. The mosaic of surface charge in contact electrification. *Science*, 333(6040):308–312, 2011.

[192] Nikolaus Hansen. Cma-es webpage. https://cma.gforge.inria.fr/cmaes$_s ourcecode_p age.html$, 2011.

[193] S. Salameh, J. Schneider, Jens Laube, A. Alessandrini, P. Facci, J. W. Seo, L. Colombi Ciacchi, and L. Mädler. Adhesion mechanisms of the contact interface of tio2 nanoparticles in films and aggregates. *Langmuir*, 28(31):11457–11464, 2012.

[194] Samir Salameh, Monique A. van der Veen, Michael Kappl, and J. Ruud van Ommen. Contact forces between single metal oxide nanoparticles in gas-phase applications and processes. *Langmuir*, 33(10):2477–2484, 2017.

[195] Jean-Paul Ryckaert, Giovanni Ciccotti, and Herman J.C Berendsen. Numerical integration of the cartesian equations of motion of a system with constraints: molecular dynamics of n-alkanes. *Journal of Computational Physics*, 23(3):327 – 341, 1977.

[196] Xujun Zhao, Jiyuan Li, Xikai Jiang, Dmitry Karpeev, Olle Heinonen, Barry Smith, Juan P. Hernandez-Ortiz, and Juan J. de Pablo. Parallel o(n) stokes' solver towards scalable brownian dynamics of hydrodynamically interacting objects in general geometries. *The Journal of Chemical Physics*, 146(24):244114, 2017.

[197] R John Ellis. Macromolecular crowding: an important but neglected aspect of the intracellular environment. *Curr. Opin. Struct. Biol.*, 11:114–119, 2001.

[198] Huan-Xiang Zhou, Germán Rivas, and Allen P Minton. Macromolecular crowding and confinement: biochemical, biophysical, and potential physiological consequences. *Annu. Rev. Biophys.*, 37(1):375–397, 2008.

[199] Huan-Xiang Zhou. Protein folding in confined and crowded environments. *Arch. Biochem. Biophys.*, 469(1):76–82, 2008.

[200] R John Ellis and Allen P Minton. Protein aggregation in crowded environments. *Biol. Chem.*, 387(5):485–497, 2006.

[201] Allen P Minton. Influence of macromolecular crowding upon the stability and state of association of proteins: Predictions and observations. *J. Pharm. Sci.*, 94(8):1668–1675, 2005.

[202] James A. Dix and A.S. Verkman. Crowding effects on diffusion in solutions and cells. *Annu. Rev. Biophys.*, 37(1):247–263, 2008.

[203] R Swaminathan, Cathy P Hoang, and AS Verkman. Photobleaching recovery and anisotropy decay of green fluorescent protein gfp-s65t in solution and cells: cytoplasmic viscosity probed by green fluorescent protein translational and rotational diffusion. *Biophysical journal*, 72(4):1900–1907, 1997.

[204] BR Terry, EK Matthews, and J Haseloff. Molecular characterization of recombinant green fluorescent protein by fluorescence correlation microscopy. *Biochemical and biophysical research communications*, 217(1):21–27, 1995.

[205] Michael C Konopka, Irina A Shkel, Scott Cayley, M Thomas Record, and James C Weisshaar. Crowding and confinement effects on protein diffusion in vivo. *J. Bacteriol.*, 188(17):6115–6123, 2006.

[206] Jeffrey Skolnick. Perspective: On the importance of hydrodynamic interactions in the subcellular dynamics of macromolecules. *J. Chem. Phys.*, 145(10):100901, 2016.

[207] Sean R. McGuffee and Adrian H. Elcock. Atomically detailed simulations of concentrated protein solutions: the effects of salt, ph, point mutations, and protein concentration in simulations of 1000-molecule systems. *J. Am. Chem. Soc.*, 128(37):12098–12110, 2006.

[208] Edmond Chow and Jeffrey Skolnick. Effects of confinement on models of intracellular macromolecular dynamics. *Proc. Natl. Acad. Sci. U.S.A.*, 112(48):14846–14851, 2015.

[209] George Barker Jeffery. On a form of the solution of laplace's equation suitable for problems relating to two spheres. *Proceedings of the Royal Society of London. Series A, Containing Papers of a Mathematical and Physical Character*, 87(593):109–120, 1912.

[210] GB Jeffery. On the steady rotation of a solid of revolution in a viscous fluid. *Proceedings of the London Mathematical Society*, 2(1):327–338, 1915.

[211] CW Oseen. Neuere methoden und ergebnisse in der hydrodynamik, akad. *Verlagsgesellschaft, Leipzig*, 1927.

[212] Margaret Stimson and George Barker Jeffery. The motion of two spheres in a viscous fluid. *Proceedings of the Royal Society of London. Series A, Containing Papers of a Mathematical and Physical Character*, 111(757):110–116, 1926.

[213] John Happel and Robert Pfeffer. The motion of two spheres following each other in a viscous fluid. *AIChE Journal*, 6(1):129–133, 1960.

[214] ME O'Neill. Exact solutions of the equations of slow viscous flow generated by the asymmetrical motion of two equal spheres. *Applied Scientific Research*, 21(1):452–466, 1969.

[215] HH Sherief, MS Faltas, and Shreen El-Sapa. A general formula for the drag on a solid of revolution body at low reynolds numbers in a microstretch fluid. *Meccanica*, 52(11-12):2655–2664, 2017.

[216] Horace Lamb. *Hydrodynamics*. University Press, 1924.

[217] John Happel and Howard Brenner. *Low Reynolds Number Hydrodynamics: with Special Applications to Particulate Media*. Prentice-Hall, Inc., Englewood Cliffs, New Jersey, 1965.

[218] Sangtae Kim and Seppo J Karrila. *Microhydrodynamics: principles and selected applications*. Courier Corporation, 2013.

[219] GK Batchelor. Slender-body theory for particles of arbitrary cross-section in stokes flow. *Journal of Fluid Mechanics*, 44(3):419–440, 1970.

[220] J. Happel and H. Brenner. *Low Reynolds Number Hydrodynamics*. 4th edition, 1986.

[221] WR Dean and ME O'Neill. A slow motion of viscous liquid caused by the rotation of a solid sphere. *Mathematika*, 10(1):13–24, 1963.

[222] Michael E O'Neill. A slow motion of viscous liquid caused by a slowly moving solid sphere. *Mathematika*, 11(1):67–74, 1964.

[223] ME O'Neill. A slow motion of viscous liquid caused by a slowly moving solid sphere: an addendum. *Mathematika*, 14(2):170–172, 1967.

[224] Arthur Joseph Goldman, Raymond G Cox, and Howard Brenner. Slow viscous motion of a sphere parallel to a plane wall—i motion through a quiescent fluid. *Chemical engineering science*, 22(4):637–651, 1967.

[225] C Pozrikidis. The motion of particles in the hele-shaw cell. *Journal of Fluid Mechanics*, 261:199–222, 1994.

[226] Peter Ganatos, Sheldon Weinbaum, and Robert Pfeffer. A strong interaction theory for the creeping motion of a sphere between plane parallel boundaries. part 1. perpendicular motion. *Journal of Fluid Mechanics*, 99(4):739–753, 1980.

[227] Peter Ganatos, Robert Pfeffer, and Sheldon Weinbaum. A strong interaction theory for the creeping motion of a sphere between plane parallel boundaries. part 2. parallel motion. *Journal of Fluid Mechanics*, 99(4):755–783, 1980.

[228] James W Swan and John F Brady. The hydrodynamics of confined dispersions. *Journal of Fluid Mechanics*, 687:254–299, 2011.

[229] Christian Aponte-Rivera and Roseanna N Zia. Simulation of hydrodynamically interacting particles confined by a spherical cavity. *Phys. Rev. Fluids*, 1(2):023301, 2016.

[230] O.A. Ladyzhenskaya. *The mathematical theory of viscous incompressible flow*. Gordon and Beach, New York, 1963.

[231] H. Power and L. C. Wrobel. *Boundary Integral Methods in Fluid Mechanics*. Computational Mechanics Publications, Southampton, 1995.

[232] Amit Kumar and Michael D Graham. Accelerated boundary integral method for multiphase flow in non-periodic geometries. *Journal Of Computational Physics*, 231(20):6682–6713, August 2012.

[233] Paul J Atzberger, Peter R Kramer, and Charles S Peskin. A stochastic immersed boundary method for fluid-structure dynamics at microscopic length scales. *Journal Of Computational Physics*, 224(2):1255–1292, 2007.

[234] V. N. Tsvetkov. *Acta Physicicochim (USSR)*, 16:132–147, 1942.

[235] Jose A Martínez-González, Xiao Li, Monirosadat Sadati, Ye Zhou, Rui Zhang, Paul F Nealey, and Juan J de Pablo. Directed self-assembly of liquid crystalline blue-phases into ideal single-crystals. *Nat. Commun.*, 8:15854, 2017.

[236] Howard Brenner. The slow motion of a sphere through a viscous fluid towards a plane surface. *Chemical engineering science*, 16(3-4):242–251, 1961.

[237] A. E. Cervantes-Martínez, A. Ramírez-Saito, R. Armenta-Calderón, M. A. Ojeda-López, and J. L. Arauz-Lara. Colloidal diffusion inside a spherical cell. *Phys. Rev. E*, 83:030402, Mar 2011.

[238] Mauricio D Carbajal-Tinoco, Ricardo Lopez-Fernandez, and José Luis Arauz-Lara. Asymmetry in colloidal diffusion near a rigid wall. *Physical review letters*, 99(13):138303, 2007.

[239] HB Eral, JM Oh, D Van Den Ende, F Mugele, and Michael HG Duits. Anisotropic and hindered diffusion of colloidal particles in a closed cylinder. *Langmuir*, 26(22):16722–16729, 2010.

[240] Michelle E. Staben, Alexander Z. Zinchenko, and Robert H. Davis. Motion of a particle between two parallel plane walls in low-reynolds-number poiseuille flow. *Phys. Fluids*, 15(6):1711–1733, 2003.

[241] R. B. Jones. Spherical particle in poiseuille flow between planar walls. *J. Chem. Phys.*, 121(1):483–500, 2004.

[242] S. Bhattacharya, J. Bławzdziewicz, and E. Wajnryb. Hydrodynamic interactions of spherical particles in suspensions confined between two planar walls. *J. Fluid Mech.*, 541:263–292, 2005.

[243] Binhua Lin, Jonathan Yu, and Stuart A. Rice. Direct measurements of constrained brownian motion of an isolated sphere between two walls. *Phys. Rev. E*, 62:3909–3919, Sep 2000.

[244] Binhua Lin, Jonathan Yu, and Stuart A. Rice. Diffusion of an isolated colloidal sphere confined between flat plates. *Colloids Surf, A*, 174(1):121 – 131, 2000.

[245] E. R. Dufresne, D. Altman, and D. G. Grier. Brownian dynamics of a sphere between parallel walls. *EPL*, 53(2):264, 2001.

[246] Nadine Tarantino, Jean-Yves Tinevez, Elizabeth Faris Crowell, Bertrand Boisson, Ricardo Henriques, Musa Mhlanga, Fabrice Agou, Alain Israël, and Emmanuel Laplantine. Tnf and il-1 exhibit distinct ubiquitin requirements for inducing nemo–ikk supramolecular structures. *J. Cell Biol.*, 204(2):231–245, 2014.

[247] Donald L Koch and Ganesh Subramanian. Collective hydrodynamics of swimming microorganisms: living fluids. *Annual Review of Fluid Mechanics*, 43:637–659, 2011.

[248] LK Hudson, J Eastoe, and PJ Dowding. Nanotechnology in action: Overbased nanodetergents as lubricant oil additives. *Advances in colloid and interface science*, 123:425–431, 2006.

[249] Ranko Richert. Geometrical confinement and cooperativity in supercooled liquids studied by solvation dynamics. *Physical Review B*, 54(22):15762, 1996.

[250] Joseph D Seymour, Justin P Gage, Sarah L Codd, and Robin Gerlach. Anomalous fluid transport in porous media induced by biofilm growth. *Physical Review Letters*, 93(19):198103, 2004.

[251] Ruben Z Waldman, Hao-Cheng Yang, David J Mandia, Paul F Nealey, Jeffrey W Elam, and Seth B Darling. Janus membranes via diffusion-controlled atomic layer deposition. *Advanced Materials Interfaces*, 5(15):1800658, 2018.

[252] AP Minton. Ap minton, biopolymers 20, 2093 (1981). *Biopolymers*, 20:2093, 1981.

[253] Alice B Fulton. How crowded is the cytoplasm? *Cell*, 30(2):345–347, 1982.

[254] Christine Selhuber-Unkel, Pernille Yde, Kirstine Berg-Sørensen, and Lene B Oddershede. Variety in intracellular diffusion during the cell cycle. *Physical biology*, 6(2):025015, 2009.

[255] Matthias Weiss, Markus Elsner, Fredrik Kartberg, and Tommy Nilsson. Anomalous subdiffusion is a measure for cytoplasmic crowding in living cells. *Biophysical journal*, 87(5):3518–3524, 2004.

[256] Dominique J Bicout and Martin J Field. Stochastic dynamics simulations of macromolecular diffusion in a model of the cytoplasm of escherichia coli. *The Journal of Physical Chemistry*, 100(7):2489–2497, 1996.

[257] Kristy L Kounovsky-Shafer, Juan P Hernandez-Ortiz, Konstantinos Potamousis, Gene Tsvid, Michael Place, Prabu Ravindran, Kyubong Jo, Shiguo Zhou, Theo Odijk, Juan J De Pablo, et al. Electrostatic confinement and manipulation of dna molecules for genome analysis. *Proceedings of the National Academy of Sciences*, 114(51):13400–13405, 2017.

[258] Vamsi K Kodali, Wouter Roos, Joachim P Spatz, and Jennifer E Curtis. Cell-assisted assembly of colloidal crystallites. *Soft Matter*, 3(3):337–348, 2007.

[259] Poornima Kolhar and Samir Mitragotri. Polymer microparticles exhibit size and shape dependent accumulation around the nucleus after endocytosis. *Advanced Functional Materials*, 22(18):3759–3764, 2012.

[260] SB Savage and CKK Lun. Particle size segregation in inclined chute flow of dry cohesionless granular solids. *Journal of Fluid Mechanics*, 189:311–335, 1988.

[261] John Mark Nicholas Timm Gray. Particle segregation in dense granular flows. *Annual Review of Fluid Mechanics*, 50:407–433, 2018.

[262] Vivek Sharma, Kyoungweon Park, and Mohan Srinivasarao. Shape separation of gold nanorods using centrifugation. *Proceedings of the National Academy of Sciences*, 106(13):4981–4985, 2009.

[263] Richard Caulkin, Xiaodong Jia, Michael Fairweather, and Richard A Williams. Geometric aspects of particle segregation. *Physical Review E*, 81(5):051302, 2010.

[264] Bakytzhan Kallemov, Amneet Bhalla, Boyce Griffith, and Aleksandar Donev. An immersed boundary method for rigid bodies. *Communications in Applied Mathematics and Computational Science*, 11(1):79–141, 2016.

[265] Andrew M Fiore, Florencio Balboa Usabiaga, Aleksandar Donev, and James W Swan. Rapid sampling of stochastic displacements in brownian dynamics simulations. *The Journal of chemical physics*, 146(12):124116, 2017.

[266] Brennan Sprinkle, Aleksandar Donev, Amneet Pal Singh Bhalla, and Neelesh Patankar. Brownian dynamics of fully confined suspensions of rigid particles without green's functions. *The Journal of chemical physics*, 150(16):164116, 2019.

[267] Paul A Lebwohl and Gordon Lasher. Nematic-liquid-crystal order—a monte carlo calculation. *Physical Review A*, 6(1):426, 1972.

[268] Gary L Hunter, Kazem V Edmond, and Eric R Weeks. Boundary mobility controls glassiness in confined colloidal liquids. *Physical Review Letters*, 112(21):218302, 2014.

[269] J. Happel and H. Brenner. *Low Reynolds Number Hydrodynamics*. Kluwer, Dordrecht, 1991.

[270] Sangtae Kim and Seppo J. Karrila. *Microhydrodynamics: principles and selected applications*. Butterworth-Heinemann, Boston, 1991.

[271] D. J. Jeffrey and Y. Onishi. Calculation of the resistance and mobility functions for two unequal rigid spheres in low-reynolds-number flow. *J. Fluid Mech.*, 139:261–290, 1984.

[272] D. J. Jeffrey. The calculation of the low reynolds number resistance functions for two unequal spheres. *Phys. Fluids A*, 4(1):16–29, 1992.

[273] A. Zsom, C. W. Ormel, C. Guettler, J. Blum, and C. P. Dullemond. The outcome of protoplanetary dust growth: pebbles, boulders, or planetesimals? II. introducing the bouncing barrier. *Astronomy & Astrophysics*, 513:A57, 2010.

[274] Hiroyuki Ohshima. Electrophoretic mobility of soft particles. *Journal Of Colloid And Interface Science*, 163(2):474–483, 1994.

[275] H Ohshima and T Kondo. On the electrophoretic mobility of biological cells. *Biophysical Chemistry*, 39(2):191–198, February 1991.

[276] Rosalind Allen, Jean-Pierre Hansen, and Simone Melchionna. Electrostatic potential inside ionic solutions confined by dielectrics: a variational approach. *Phys. Chem. Chem. Phys.*, 3:4177–4186, 2001.

[277] R. T. Bonnecaze and J. F. Brady. A method for determining the effective conductivity of dispersions of particles. *Proc. R. Soc. Lond. A*, 430(1879):285–313, 1990.

[278] R. T. Bonnecaze and J. F. Brady. The effective conductivity of random suspensions of spherical particles. *Proc. R. Soc. Lond. A*, 432(1886):445–465, 1991.

[279] R. T. Bonnecaze and J. F. Brady. Dynamic simulation of an electrorheological fluid. *J. Chem. Phys.*, 96(3):2183–2202, 1992.

[280] D. J. Klingenberg and Charles F. Zukoski. Studies on the steady-shear behavior of electrorheological suspensions. *Langmuir*, 6(1):15–24, 1990.

[281] D. J. Klingenberg, Frank van Swol, and C. F. Zukoski. The small shear rate response of electrorheological suspensions. i. simulation in the point–dipole limit. *J. Chem. Phys.*, 94(9):6160–6169, 1991.

[282] D. J. Klingenberg, Frank van Swol, and C. F. Zukoski. The small shear rate response of electrorheological suspensions. ii. extension beyond the point–dipole limit. *J. Chem. Phys.*, 94(9):6170–6178, 1991.

[283] Karl von Pfeil and Daniel J. Klingenberg. Nonlocal electrostatics in heterogeneous suspensions using a point-dipole model. *Journal of Applied Physics*, 96(9):5341–5348, 2004.

[284] G Bossis, A Meunier, and JD Sherwood. Stokesian dynamics simulations of particle trajectories near a plane. *Phys Fluids A-Fluid*, 3(8):1853–1858, Jan 1991.

[285] G. Bossis and J. F. Brady. The rheology of Brownian suspensions. *The Journal of Chemical Physics*, 91(3):1866, 1989.

[286] J. F. Brady, R. J. Phillips, J. C. Lester, and G. Bossis. Dynamic simulation of hydrodynamically interacting suspensions. *J. Fluid Mech.*, 195:257, 1988.

[287] L. Durlofsky, J. D. Brady, and G. Bossis. Dynamic simulation of hydrodynamically interacting particles. *J. of Flud Mech.*, 180:21, 1987.

[288] G Bossis and John F Brady. Self-diffusion of brownian particles in concentrated suspensions under shear. *J Chem Phys*, 87(9):5437–5448, Jan 1987.

[289] G Bossis and John F Brady. Dynamic simulation of sheared suspensions .1. generalmethod. *J Chem Phys*, 80(10):5141–5154, Jan 1984.

[290] LLoyd N. Trefethen and David III. Bau. *Numerical Linear Algebra*. SIAM, Philadelphia, 1997.

[291] W. H. Press, S. A. Teukolsky, W. T. Vetterling, and B. P. Flannery. *Numerical Recipes in Fortran 77*. Cambridge University Press, Cambridge, 2nd edition, 1992.

[292] M. Deserno and C. Holm. How to mesh up ewald sums. i. a theoretical and numerical comparison of various particle mesh routines. *J. Chem. Phys.*, 109(8):7678, November 1998.

[293] Juan Pablo Hernández-Ortiz, Hongbo Ma, Juan J De Pablo, and Michael D Graham. Concentration distributions during flow of confined flowing polymer solutions at finite concentration: slit and grooved channel. *Korea-Aust Rheol J*, 20(3):143–152, Jan 2008.

[294] R.G. Cox and H. Brenner. The slow motion of a sphere through a viscous fluid towards a plane surface: Ii small gap widths, including inertial effects. *Chem. Eng. Science*, 22:1753, 1967.

[295] A. J. Goldman, R. G. Cox, and H. Brenner. Slow viscous motion of a sphere parallel to a plane wall: Ii couette flow. *Chem. Eng. Science*, 22:653, 1967.